TU WIEN Informatics

Visualization and Analysis of X-ray Computed Tomography Data

HABILITATION THESIS

carried out in the years between 2010 and 2021 for the purpose of obtaining the

Venia Docendi (Right to Lecture)
in Computer Science

by

Dr. Christoph Heinzl

to the Faculty of Informatics

at the TU Wien

Vienna, 16th July, 2021

_____

Christoph Heinzl

_____

Acknowledgements

Abstract

Visualization and analysis of primary and secondary X-ray computed tomography (XCT) data has become highly attractive for boosting research endeavors in the materials science domain. On the one hand, XCT allows to generate detailed and cumulative data of the specimens under investigation in a non-destructive way. On the other hand, through the conception, the development, and the implementation of novel, tailored analysis and visualization techniques, in-depth investigations of complex material systems turned into reality, e.g., in the form of interactive visualization of spatial and quantitative data, uncertainty quantification and visualization, comparative visualization, ensemble analysis and visualization, visual parameter space analysis, and many others. Visual analysis of XCT data enables a detailed understanding of the internal structures and the characteristics of materials and thus facilitates studies on a multitude of phenomena, at multiple scales, in different dimensions, or even using different modalities. This was simply impossible before.

This habilitation thesis presents contributions to computer science in terms of novel methods and techniques as well as respective algorithms and data structures, which are advancing visual analysis and visualization for enabling insights into XCT data on material systems. The introduced methods and techniques focus on three distinct technical areas of visual analysis and visualization of XCT data. For each area, the problem statements, important research questions to be solved as well as the contributions of the habilitation candidate are discussed:

1. **Interactive visualization of spatial and quantitative data:** Visualization and analysis techniques are introduced in this thesis for exploring, encoding, connecting, abstracting elaborating, reconfiguring, filtering, and finally selecting in "rich" XCT data. To reveal insights into complex objects, MObjects (i.e., mean objects) is discussed as a novel aggregation and exploration technique, which computes average volumetric representations from selections of individual objects of interest. To analyze various of these mean objects and to compare them with regards to their individual characteristics, visual analysis techniques as presented in FiberScout facilitate a detailed exploration of primary spatial data together with derived quantitative data (i.e., secondary data).

2. **Visual parameter space analysis (vPSA):** The contributions towards vPSA focus on concepts for exploring and analyzing the space of possible parameter combinations of algorithms, models, and data processing pipelines as well as their effects on the ensemble of results. The presented methods and techniques visually guide users in finding adequate input parameter sets, leading to optimal output results. In particular, the vPSA of segmentation and reconstruction algorithms is investigated. Similarity Metrics are introduced for comparing features as well as their characteristics.

3. **Comparative visualization and ensemble analysis:** The comparison of larger sets of ensemble members as generated by vPSA is difficult, tedious, and error-prone, which is often exacerbated by subtle differences in the individual members. Here, techniques are presented to study the differences between multiple results regarding their visual representation as well as their characteristics. Dynamic Volume Lines is a novel technique for the visual analysis and comparison of large sets of 3D volumes using linearization methods combined with interactive data exploration. This technique is accompanied by a comparative visualization in the spatial domain to establish a link between the abstracted data and real world representations.

Finally, in terms of visualization theory and modeling, this thesis abstracts the characteristics of visual parameter space analysis in a holistic conceptual framework. It also classifies and frames the novel area of visual computing in materials science, identifying research gaps within this domain.

Contents

Introduction

This thesis presents a selection of my research in the field of visualization throughout the period of the last ten years. In this time my research focused on the question of how to visually analyze and explore "rich" X-ray computed tomography (XCT) data. The first chapter serves as introduction to this area, providing its classification as a big data problem together with a definition of "rich" XCT data. It outlines respective challenges in terms of rich XCT data analysis and visualization, framing the context of the core papers of this cumulative habilitation thesis. In the second chapter, these challenges are addressed and reflected in the context of high level related work (for the detailed related work, readers are referred to the core papers in Chapter 3). My research towards the identified research questions is presented and finally selected contributions towards computer sciences for solving these challenges are discussed. In the authorship statement, the core papers are listed and briefly described, indicating the contributions I made to each individual work. The thesis is completed with an outlook into open research questions, trends, and developments for future research.

1.1   Motivation and Challenges

Industrial X-ray Computed Tomography (XCT) is an imaging technique, which is used in a wide variety of diagnosis and (visual) analysis scenarios [Hei09]. What renders this technique highly advantageous and beneficial compared to others is its ability to generate detailed and cumulative data of the specimens under investigation in a non-destructive way [KH19]. Regarding its etymologic origin, tomography originally stems from Greek *"tomos"*, which means *"slice"* or *"section"*, and graphien, meaning *"to write"*. This etymologic consideration hints at the basic principle of XCT: Technology-wise XCT finds its foundation in X-ray radiation which non-destructively irradiates specimens in order to evaluate the attenuation of these X-rays by the specimen's matter in the form of radiographic projection images. Typically, not just a single but a large number of these radiographic projection images are recorded from different projection angles along a predefined scanning trajectory. The series of projection images is then reconstructed using a mathematical algorithm in order to generate 2D cross-sectional or 3D volumetric images of the scanned object [CDL18]. The reconstructed 2D images and 3D volumes are also referred to as *primary XCT data* and allow to generate a virtual (typically volumetric) representation of the object.

XCT as big data problem

Within the last 25 years of its increasing industrial use, XCT significantly evolved from a plain imaging technique to a true traceable metrology and characterization technique, which facilitates detailed measurements, analyses, and quantification [CDL18]. In fact, XCT's evolution is best explained by considering XCT based data generation and analysis as a big data problem: According to Patgiri and Ahmed [PA16], the big data paradigm is a game changer in virtually any area, such as materials science, (bio-)medicine, physics, aeronautics etc., where massive amounts of data are generated. In their work they summarize the concept of "V's" for characterizing big data problems starting from Volume, Variety, Veracity, Velocity, Value, Validity, Variability, Volatility, Virtual, Visualization, Visibility, to Complexity. Out of these characteristics, the first four V's are of utmost importance concerning the evolution of industrial XCT, which render XCT data analysis and visualization a true big data problem:

- **Volume:** In terms of volume, XCT used to generate data volumes of reasonable size in its early years which were ranging in the area of (several hundreds of) megabytes of 8 bit unsigned integer data. Currently, state of the art XCT devices generate volumes of 4096^3 voxels (i.e., volumetric elements) or more in 32 bit float in a single scan. These data sizes will be even increased, if special XCT modes are employed, such as stacked and tiled XCT scanning modes, virtual detector enlargements, or similarly, if spatio-temporal data are generated for analyzing ongoing processes in 4D-XCT data acquisition [AAS+16]). Such XCT data may yield sizes of (tens to hundreds of) terabytes of primary XCT data.

- **Variety:** Compared to early XCT imaging focusing on primary XCT data only, current XCT data analysis is facing increasingly heterogeneous data. First of all, XCT now offers different modalities to be considered. Aside the conventional absorption contrast images also phase contrast and dark field contrast [MFW+19], dual or multi energy XCT data [Hei09], or even spectral data [AFK+14] may be considered for data analysis. The different modalities do not necessarily feature the same extents and resolutions and may thus require additional interpolation or even registration steps. Secondly, in a lot of applications also secondary data is extracted using custom data analysis pipelines to generate abstract data on features of interest [WAL+14]. In the context of this thesis the term "feature" is used from an application perspective and thus refers to spatial objects (e.g., pores, fibers, inclusions etc.). *Secondary XCT data* is typically tailored to the respective data analysis scenario and specifically required to characterize individual features of interest. In case of fiber-reinforced composite materials, e.g., each fiber, each pore, or each void in the primary data is individually characterized by attributes such as volume, surface, aspect ratio, extent, center, shape factors, spherical coordinates, feature orientation etc., which are computed and made available together with primary XCT data for the analysis.

- **Veracity:** Regarding veracity, the (un-)certainty and quality of XCT data and respective analyses may be considered. Data veracity was neglected in XCT for a long time. In the advent of XCT transitioning from simple imaging to traceable metrology and characterization, the uncertainty prevalent in the data as well as information derived thereof came into focus [HKMG08]. Since then, investigations have been carried out, which were focused on the discovery and the characterization of influencing factors that contribute to uncertainty budgets in the generated results [SN10], as well as investigations on analyzing the uncertainty of primary and secondary XCT data [AHK+13].

- **Velocity:** In terms of data velocity, XCT is currently striving to move forward from a static, lab based data technique towards a fast, inline inspection technique. Fast XCT

acquisition and data analysis is thus increasingly introduced into industrial production lines in the form of a fully integrated inline XCT analysis, which is capable of facilitating XCT data generation and data evaluation within cycle time. To avoid compromising cycle times, inline XCT needs to be highly optimized to its target application. Using a low number of intelligently placed projection images to ensure fast data acquisition and / or limited angular views on the specimens of interest, investigations of well-known samples are facilitated within seconds through tailored analysis protocols [PJC$^+$17].

1.2 Visual Analysis of "Rich" XCT Data

In terms of XCT's application areas, especially materials science is strongly benefiting from XCT's characteristics, enabling non-destructive and highly detailed volumetric imaging of a wide variety of materials and material systems [HS17]. The combination of high resolution XCT imaging coupled with tailored analysis and visualization techniques has become a catalyst to accelerate research endeavors in this and other domains. Using visual computing and more specifically visual analysis, complex phenomena in multiple scales, multiple dimensions, and even multiple modalities can now be studied in a comprehensive and fully integrated manner. What is most important for such investigations of complex phenomena is to design, develop, and employ scalable solutions for the quantification, exploration, and analysis of *"rich" XCT* data.

Definition of "Rich" XCT Data: Rich XCT data significantly extends on slice-based or volumetric data from conventional XCT imaging. It may integrate one or more primary XCT datasets, recorded at different resolutions or using different XCT modalities, which are generated as direct outputs by the respective XCT device or modality. Rich XCT data may also contain derived spatial information such as segmentation masks or label images. Furthermore, rich XCT data may encompass quantitative information of features in the primary data, e.g., lists of derived attributes describing each feature of interest. Finally, ensembles of rich XCT data are required for studying time dependent phenomena. So in summary, rich XCT data is best characterized as complex ensemble of multi-dimensional, multi-modal, multi-scalar, and multi-variate data, which may vary over time or during an investigated process.

In recent years, a reasonable number of techniques has been introduced to provide novel insights through visual analysis of rich XCT data. Several workshops and discussion rounds [PSI17], [Dag19] as well as reports thereof [HKL$^+$19] analyzed these developments in order to frame the existing work as well as to identify current and future challenges in terms of visual analysis of rich XCT data. These workshops and discussion rounds were (co-)organized by the author and build an important pillar of this work. Specifically, the following challenges will be addressed in this thesis:

Challenge 1: Interactive Visualization of Spatial and Quantitative Data

As a result of the ever-increasing complexity of rich XCT data in combination with growing demands regarding their analysis, especially passive visualization and standard visualization techniques have reached their limits. While passive visualization does not incorporate interaction at all, also standard techniques do not necessarily feature the highly anticipated interaction techniques for in-depth analyses, in order to select, encode, abstract/elaborate, aggregate, reconfigure, connect, or explore data according to the classification proposed by Yi et al. [YKSJ07].

Interactive visualization techniques, however, strongly support the analysis process and respective techniques are therefore particularly helpful to support visual analysis processes. To interactively visualize spatial and quantitative data is thus a core challenge for analyzing and exploring either

rich XCT data ensembles, or single ensemble members thereof. A clear need is seen in structured design studies on integrated visual analysis tools [SMM12]. These need to be capable of handling rich XCT data and tailored to a specific application. These also need to guide users in their investigations to provide insights using meaningful and easy to understand visual metaphors. Especially for the visual analysis of time-varying data in dynamic processes, with materials under load or in different environmental conditions, such integrated tools are highly anticipated. Aside the visualization aspects, this challenge also encompasses preprocessing steps, e.g., for feature quantification, segmentation, and clustering, which are required to derive secondary data from primary XCT data in order to characterize features and their attributes.

Challenge 2: Visual Parameter Space Analysis

Visual parameter space analysis (vPSA) is dedicated to the challenge of systematically varying input parameters of models, algorithms, pipelines, or other data generation processes (i.e., sampling the input parameter space). In vPSA, this first sampling and data generation process is typically coupled with a second visual analysis process investigating the used inputs versus the generated outputs. The visual analysis of the generated output results is particularly helpful for the investigation of relations between the input parameter settings and their corresponding outputs by means of interactive visualization techniques [SHB$^+$14].

In terms of XCT, this challenge centers around vPSA techniques, which are required to sample and evaluate the high dimensional input parameter spaces in feature extraction, segmentation, and quantification algorithms (as well as data analysis pipelines), to understand their parametrization with respect to the generated outputs. Furthermore, finding potential correlations in the input parameters is of similar importance as finding parameters, which either show a strong or a negligible influence on the generated results. Such analyses need to reveal effects not only on primary, but also on derived secondary XCT data. Finally, respective methods need to guide users in finding adequate input parameter sets leading to optimal output results, i.e., optimal primary and secondary XCT data, for the defined analysis scenario.

Challenge 3: Comparative visualization and ensemble analysis

A comparison of many ensemble members is difficult, tedious, and error-prone, and often aggravated by just subtle differences in the individual members. Respective approaches may be classified using the taxonomy of Gleicher et al. [GAW$^+$11] for visual designs in comparative visualization. This taxonomy classifies techniques into three basic categories: juxtaposition, superposition, and explicit encoding.

The challenges of comparative visualization and ensemble analysis of large and complex data ensembles with numerous individual ensemble members are often linked with those of vPSA. Considering primary XCT data ensembles, the differences in terms of intensities of the voxels to be compared are typically very small and originate from various effects, such as detector efficiency, fluctuations of the X-ray source, or noise in the data, even for constant input parameters. Similarly, for secondary data, only small and slight changes in the extracted attributes may be observable and thus influencing the analysis. For this reason, evaluations of whether a particular parameter set provides improved results as compared to already studied parameters is a hard problem, especially for complex rich XCT data. This problem even exacerbates, if larger numbers of ensemble members or even the complete ensemble need to be compared in the analysis. Respective techniques for the visual analysis of large sets of rich XCT data are therefore required, employing novel comparative visualization techniques to generate insights into variations in the data as well as interesting areas.

Grand Challenge: Visualization Theory and Modeling

Aside the task-oriented challenges, this thesis also contributes to the grand challenge of visualization theory and modeling in attempts to structure and extract conceptual models from the existing body of work. Specifically, the properties of visual parameter space analysis are analyzed in order to generate a holistic conceptual framework, which is capable of summarizing, abstracting, and classifying the characteristics of visual parameter space analysis into a holistic conceptual framework. Secondly, to review, classify, and shape the area of visual computing in materials science, a state-of-the-art report outlines the benefits of materials science coupled with visual computing approaches. Both works are identifying research gaps within their domains.

In the following chapter, the core contributions of this thesis are outlined, providing solutions to the raised challenges. These contributions are arranged around the distinct technical areas of visual analysis and visualization of XCT data.

Contributions

After obtaining my PhD in 2009, I contributed to 34 peer-reviewed publications, 24 of which are journal articles, 6 are fully reviewed conference publications, and 4 are book chapters. One of these publications achieved a best paper award. The main part of my publications is published at top visualization conferences and journals. It should be noted, that papers which are accepted for the top visualization conferences typically appear as journal articles of a respective special issue on the conference. IEEE Vis, IEEE InfoVis and IEEE VAST papers are published in the IEEE Transactions on Visualization and Computer Graphics journal (impact factor (IF): 4.558). Papers presented at the EuroVis conference appear in the Computer Graphics Forum journal (IF: 2.116). Furthermore, I publish applications of the presented techniques as well as case studies in journals of the nondestructive testing (NDT) domain, such as Elsevier NDT&E International Journal (IF: 3.461), Springer Journal of Nondestructive Evaluation (IF: 1.950), Taylor&Francis Nondestructive Testing and Evaluation (IF: 1.424), and others. The peer-reviewed publications are complemented by a total of 60 other publications, such as conference contributions, short papers, posters.

The remainder of this chapter introduces the main contributions of the cumulative habilitation to the state-of-the-art at a high level. Regarding the detailed contributions of each individual publication the reader is referred to Chapter 3. Table 2.1 ff list all papers that are included as full texts of this thesis. The respective contributions were selected on the basis of their impact in the scientific community, the significance of the contributions the author of this thesis made to all of them, as well as how they fit in the overall scope of the thesis. The following sections are structured according to the challenges identified in the introduction of this thesis in Chapter 1.

2.1 Challenge 1: Interactive Visualization of Spatial and Quantitative Data

When we address a problem in terms of interactive visualization of spatial and quantitative data, we typically do a design study. While general concepts on visualization, analysis, and design are outlined by Munzner [Mun15], an efficient way for structuring such design studies is the methodology as introduced by Sedlmair et al. [SMM12]: This methodology consists of three major phases: (1) the precondition phase, (2) the core phase and (3) the analysis

phase. In the precondition phase (1), the stages of learning, winnowing, and casting focus on preparatory aspects regarding the actual visualization research. Here, we first need to learn about the visualization problem and the respective state-of-the-art before we can proceed and select promising collaborations for solving the problem. This phase is completed by casting the collaborators' roles in the visualization project. The core phase (2) of a design study contains the four additional stages of discovering, designing, implementing, and deploying, which are covering the actual design and implementation steps. We need to first discover what is most important by characterizing the problem and by abstracting the most relevant aspects in order to select methods based on close interaction with domain experts. Secondly, we need to design visualization methods for abstracting data, suitable visual encodings as well as interaction concepts before we can start with the actual implementation of prototypes, tools, and usability concepts. The deployment finalizes the core phase by releasing the software as well as gathering feedback. The last phase is the analysis phase (3) which is a reflection step to confirm, refine, or reject our hypotheses, as well as to propose guidelines of how to use the respective method. When all these steps have been completed the respective design study paper on the newly introduced method is written.

The related work in this area is diverse and comprises general concepts in the design of visualization techniques as discussed in Munzner's book on Visualization Analysis and Design [Mun15], interaction concepts as discussed by Yi et al. [YKSJ07], or respective methodologies as introduced by Sedlmair et al. [SMM12]. More tailored to the original area of this challenge is related work on the interactive visualization of spatial and quantitative data. For example, Radoš et al. [RSM+16] propose extensions to focus and context visualizations using novel linking and brushing techniques (i.e., the percentile brush and the Mahalanobis brush) for quantitative analyses. Mindek et al. [MMGB17] introduced a model for data sensitive visual navigation in medical visualization. Torsney-Weir et al. [TWSM17] suggested using 1D slices for multi-dimensional continuous functions in a system called Sliceplorer. Finally, related work can also be seen in visualization for materials science applications. In their approach to explore steel fibers in fiber reinforced sprayed concrete, Fritz et al. [FHG+09] quantify fiber properties such as fiber orientation and respective distributions based on a direction sphere histogram. Other approaches have demonstrated novel concepts in terms of feature-based tensor field visualization for fiber reinforced polymers as discussed by Zobel et al. [ZSS15] or in terms of exploring porous structures with illustrative visualizations by Grau et al. [GVTA10].

My research in terms of Challenge 1 focuses on the visual analysis of rich X-ray computed tomography data for advanced materials science applications as indicated in the introduction section. Here, the characterization and visual analysis of complex, heterogeneous materials are of utmost importance. Advanced composites and more specifically fiber reinforced polymers are promising candidate materials for a number of current and future applications. They facilitate the integration of highly anticipated industrial demands regarding cost efficient, function-oriented, fully integrated, and lightweight components. However, to generate such tailored, application specific materials and components, precise analyses are required. For composite materials, all individual parts of the respective material system are of interest, as they have a direct impact on the targeted specifications. The matrix component (i.e., epoxy resin matrix) keeps the reinforcements in place and acts as glue component. The reinforcements (i.e., fibers, arranged in different directions) are carrying the actual load. They need to be aligned in the load direction(s) in order to reach an optimal performance of the final component. In addition, also manufacturing induced errors and defects (e.g., pores in the matrix or inside the fiber bundles, inclusions of foreign materials, or general voids) may interfere with the targeted specifications. They may severely affect the overall strength and durability and thus cause material failure (e.g., cracks,
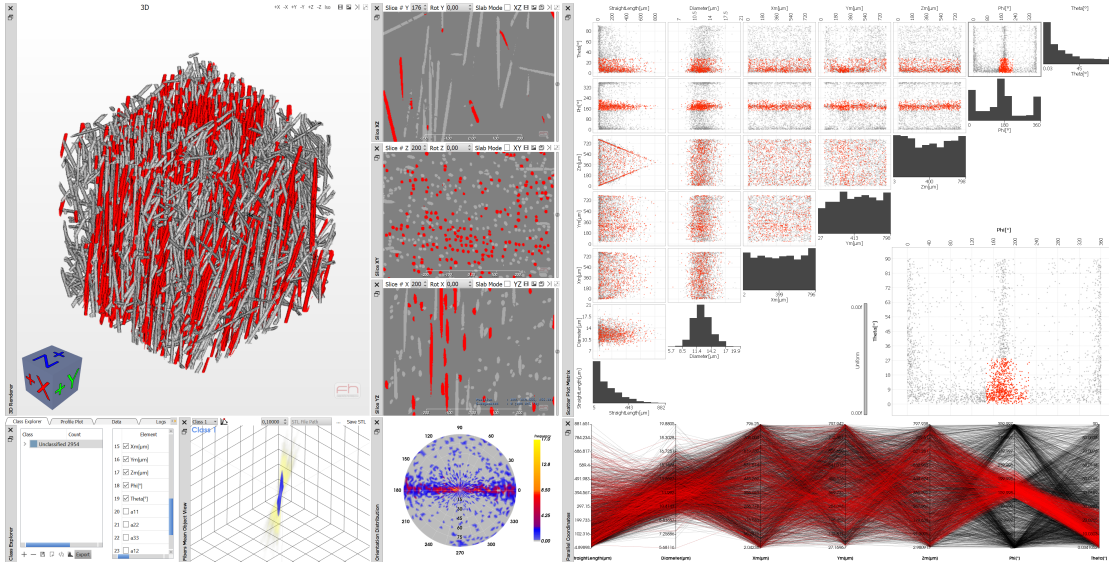
Figure 2.1: FiberScout [WAL+14] is an interactive visualization prototype for primary and secondary XCT data of fiber reinforced composites focusing on exploring and connecting data.

fractures, or delamination). In order to address the domain requirements we set up a number of research questions to provide insight. In this area we investigate the following research questions:

- What are the most important feature characteristics?

- What is the relationship between these?

- Can we visually connect features by their characteristics?

- What are suitable techniques to explore, filter, and connect feature sets?

- Which visual metaphors can be used to encode, abstract, or reconfigure sets of features from rich XCT data?

- Which interaction concepts support respective analysis workflows?

My contributions to computer science in the wake of these research questions are found in interactive visualization techniques as well as visualization pipelines for spatial and quantitative XCT Data [WAL+14], [WAG+16], [RGK+13], [RPK+12]. These techniques and pipelines are integrated in interactive visualization prototypes, e.g., as shown in Figure 2.1. According to Yi et al.'s taxonomy of interaction techniques [YKSJ07], we developed and introduced concepts for **exploring** rich XCT data (i.e., show me something else), for **encoding** (i.e., show me a different representation), for **connecting** (i.e., show me related items), for **abstracting and elaborating** (i.e., show me more or less detail), for **reconfiguring** (i.e., show me a different arrangement), for **filtering** (i.e., show me something conditionally), and finally for **selecting** (i.e., mark something as interesting) in rich XCT data. Some of these contributions are outlined in the following sections. All proposed techniques and methods have been thoroughly evaluated, typically by two groups of visualization (approx. 10 Master and PhD students) and domain experts (approx. 10 NDT practitioners and material scientists) respectively. The evaluations

were carried out using demonstrations followed by questionnaires. The results are presented using a five-point Likert scale.

Explore, Connect

FiberScout [WAL+14] is an interactive visualization prototype for primary and secondary XCT data of fiber reinforced composites (see Figure 2.1), which especially focuses on exploring and connecting data according to Yi et al.'s taxonomy. A parallel coordinate plot (PCP) displays all feature (i.e., fiber) attributes on parallel coordinate axes. Each individual feature is represented by a polyline, connecting these parallel coordinate axes at the value of the respective attribute. The PCP is employed to explore and connect features to initial feature classes of interest, which may be refined in a scatter plot matrix (SPLOM) subsequently. In contrast to the PCP, a SPLOM displays pairwise scatter plots of all possible combinations of feature attributes, which are arranged in a matrix. This single matrix based representation visualizes correlations in fiber attributes and facilitates a detailed (de-)selection of individual features as well as grouping of similar features through filtering and brushing operations. Combining PCP, SPLOM and a class explorer for storing feature classes of interest makes up the FiberScout core system for interactive visualization of spatial and quantitative data. All views and visual metaphors are linked with each other for data exploration. They are further complemented with 2D or 3D renderings of the original data, in order provide the spatial context of the fibers in the data. This way the data can be explored according to different aspects and hidden relations between the attributes or correlations of similar features and feature classes may be revealed. Although the focus is on exploration and connection of data, FiberScout also integrates interaction techniques for selecting (e.g., select individual items and groups of items), for encoding (e.g., encode the fibers' color according to their orientation), for reconfiguring (e.g., 2D projections of features such as porosity maps [RPK+12]), and filtering (e.g., filtering of fiber classes, refinements of initial classifications).

Encode

Often it is necessary to encode data for gaining overviews as well as hidden insights. Regarding encodings, the characteristics of the features of interest may already indicate potential directions for suitable visual metaphors. For instance, fibers typically feature a large aspect ratio, a circular cross-sectional shape, and a cylindrical overall structure. When integrating the characteristics of fibers in a visual metaphor encoding orientation, a beneficial way is to transform the Cartesian coordinates of the start and endpoints of the fibers into polar coordinates. Typically, only the orientation is of interest in this case, since there is no predefined starting point in symmetrical features such as fibers regarding a directional evaluation. In FiberScout [WAL+14], all fibers are represented by two angles for a polar coordinate representation (see Figure 2.2): one angle represents the polar angle θ from the zenith Z-direction and the other one measures the azimuth angle ϕ in the XY plane as measured from the X-direction. These polar coordinates are first plotted on a half sphere and subsequently visualized by azimuthal projection on a 2D plane in order to generate a polar plot. To avoid overplotting in case of high feature counts, the polar plot needs to be enhanced to a polar heatmap. For this reason, we discretized the half sphere into segments and computed the frequency of features within each segment. These frequencies are then color-coded and finally projected on a 2D plane using azimuthal projection. Fiber orientations with high frequencies as well as orientation clusters are revealed and encoded in a single plot of the complete dataset.
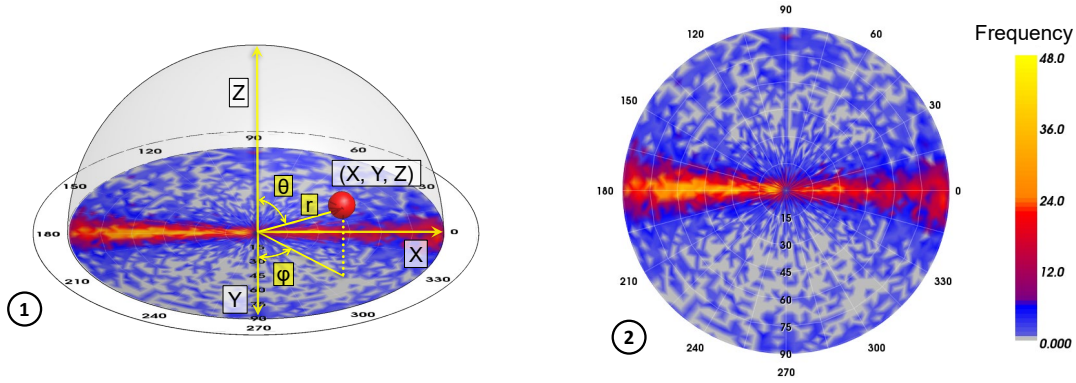
Figure 2.2: Encoding orientation in a polar heatmap. (1) Conversion from features characteristics in Cartesian coordinates to polar coordinates. (2) Representative polar heatmap of the global fiber orientation. ©2014 IEEE. Reprinted, with permission, from [WAL+14].

Abstract/Elaborate

Abstracting or elaborating interaction techniques show less or more detail of a complex problem [YKSJ07], which is specifically important when analyzing numerous features in 2D or 3D space. In such settings, the occlusion of large numbers of features of interest prevents from exploring overall structures. In case of fiber reinforced composites, respective visual analyses are used to evaluate the layered structure as well as to analyze and explore porous areas and large pores in the material system. A reasonable viewpoint therefore maximizes the pore overlap in the result image so that the layered structure of the sample is revealed and clearly visible. The best-viewpoint technique and the respective widget as presented by Reh et al. [RPK+12] falls in the category of abstract/elaborate. The goal of this technique is to rate the quality of viewpoints on a viewing sphere around the data volume. This is achieved by regular sampling of points on a parameterized sphere. At each position of this sphere, a histogram is aggregated from the projection of the segmented pore voxels on the viewing plane. These histograms are then subdivided into three classes of critical (strongly overlapping features), borderline (partly overlapping features) and uncritical (non overlapping features) pixels using user-specified thresholds. Based on the contributions of critical, borderline, and uncritical histogram bars, a quality value is computed and visualized on a spherical best-viewpoint widget. This way, the most suitable orientations are abstracted from the respective viewpoints and either directly color-coded or represented using cylinders on the surface of the sphere.

Reconfigure

Due to visual clutter when rendering higher numbers of objects, it is often difficult to get a sense of how average feature shapes manifest themselves. This undertaking becomes even impossible, when analyzing hundreds or thousands of individual objects in large datasets or if only specifically selected objects with respect to user-defined characteristics should be considered. Reh et al. [RGK+13] introduced a novel method of reconfiguring data for the purpose of exploring respective average objects (Figure 2.3). Here, segmentations of the features of interest (e.g., pores, voids, inclusions, or fibers) are detached from their spatial context and reconfigured to create MObjects (short for mean or average objects). In order to achieve this goal, all features need to be registered to each other based on their barycenter. We then aggregate the contributions of each feature to
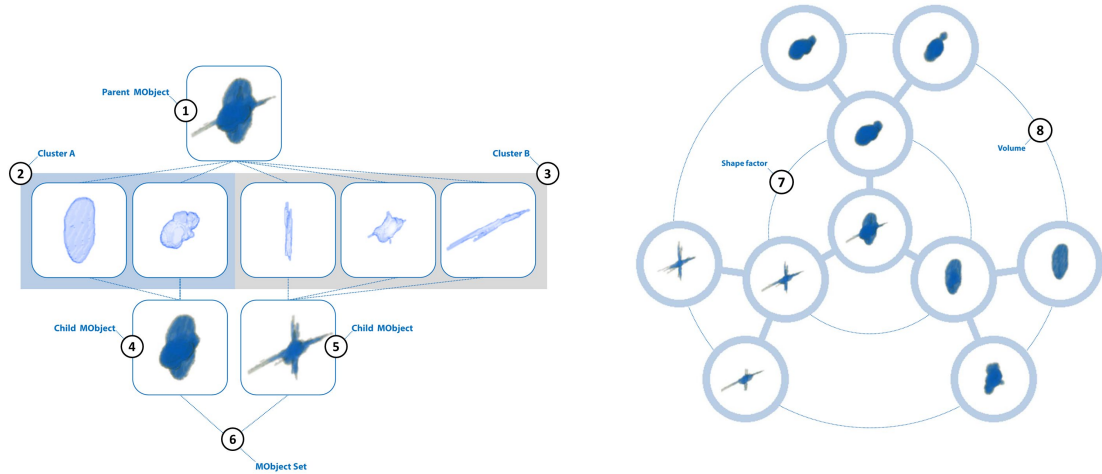
11

Figure 2.3: Reconfiguring spatial features using MObjects (i.e., mean objects). Right: All individual objects of the parent MObject (1) are subdivided into cluster A (2) and B (3). The resulting child MObjects (4 and 5) make up a MObject Set (6). Left: Concept of Radial MObject Set visualization for the exploration of sets of MObjects in terms of (7) shape factor and (8) pore volume. ©2013 IEEE. Reprinted, with permission, from [RGK+13].

the MObject. For this purpose, we walk through all voxels of the MObject and count, how many of the segmented features contain the considered voxel as part of the segmented structure. This is achieved by determining the distances of the considered voxels to their barycenters in X, Y, Z coordinates of each segmented feature. The respective voxels of the mean object at the same X, Y, Z distances to its barycenter are subsequently incremented. Using normalization to one, the aggregation into a mean object may be considered as a probability volume. Areas of high probability typically represent the center of the MObject, which means most of the segmented features contribute to this area. The probabilities are decreasing in surrounding areas. For the exploration of datasets with high numbers of features, the computation of a single mean object is typically insufficient. Users are interested in MObject Sets (short for mean object sets), e.g., with MObjects computed at specific regions, MObjects of features with similar shapes or with a specific volume range. To account for these needs, visualization concepts for the exploration of MObject Sets are required. We introduced two candidate visualization techniques, one of which presents MObject Sets in a radial layout and the other one in a parallel arrangement. Both visualization techniques allow to further subdivide parent MObjects into sets of child MObjects with respect to a specific characteristic (e.g., shape factor, volume, surface, position in space, etc.) as well as into the desired number of subdivisions and ranges of each characteristic. Through visual linking, all generated MObjects down the analysis path may be explored.

2.2   Challenge 2 & 3: vPSA, Comparative and Ensemble Visualization

Although each area is considered as a standalone topic in visualization, often visual parameter space analysis (vPSA) is accompanied by a comparative and/or ensemble visualization. Likewise in my field of research, these areas are strongly intertwined and therefore need to be considered together, which is why my contributions are combined in this subsection. This combination is explained as

follows: While vPSA integrates a systematic variation of the model input parameters in order to generate outputs for each combination of parameters (i.e., sampling the input parameter space), the generated outputs need to be compared [MHG10]. Furthermore, the respective relations between inputs and outputs need to be investigated [SHB$^+$14]. Typically, the data generated in this process is complex and contains collections of outputs generated from respective computations (i.e., ensemble data). Visualization can be of great help in the analysis.

The high-level related work in this area is spanning from vPSA, visual comparison and visualization of time-oriented data, comparative visualization techniques, to visualization techniques for ensemble data. Regarding the first topic, the reader is referred to Section 2.3 which contains a holistic conceptual framework we introduced for vPSA. For the second area, Aigner et al. [AMST11] discuss the visualization of time-oriented data, which requires suitable methods for reasoning using visual analysis due to the distinct characteristics of time. Gleicher et al. [GAW$^+$11] focused on visual comparison for information visualization. Regarding comparative visualization and respective techniques, the works of Gratzl et al. [GLG$^+$13] on the visual analysis of multi-attribute rankings, of Malik et al. [MHG10] on the comparative visualization for parameter studies of dataset series, and of Torsney-Weir et al. [TWMSK18] on the interactive visualization of shapes in multiple dimensions should be noted. Visualization techniques for ensemble data received much attention in recent years. This area is best outlined by the survey of Wang et al. [WHLS19] in terms of visualization and visual analysis of ensemble data. Notable works are focusing on comparative 3D ensemble visualization using multi-charts as introduced by Demir et al. [DDW14] or characterizing uncertainty in feature sets using contour boxplots for simulation ensembles as presented by Whitaker et al. [WMK13].

My research regarding Challenges 2 and 3 comprises visual parameter space analysis and comparative visualization techniques for rich XCT data ensembles originating from XCT data generation, (feature) reconstruction, and segmentation. In the field of reconstruction and segmentation, numerous algorithms and pipelines have been introduced for XCT data analysis. Yet, there is no unique optimal solution that fits all analysis problems. In addition, many influencing factors need to be considered concerning the quality of the respective results. Summarizing most of the previously presented approaches, these are sharing the persisting issue of finding suitable input parameters for generating reasonable outputs. In many daily data analysis operations, it remains largely unclear, which parameter values or even which parameter ranges of an algorithm generate suitable results. Sometimes it also remains unclear which algorithms should be preferred over others. A comparison of the generated results is therefore mandatory in order to evaluate the quality of the generated results and ideally, to derive optimized input parameters for new algorithm runs. In this kind of application, we typically deal with high numbers of ensemble members in XCT, which feature subtle differences between each other. So, we need to be able to analyze and compare reconstruction and segmentation results from different algorithms and pipelines. To tackle these requirements, we set up the following research questions:

- How to compare large, slightly changing data ensembles of spatial and abstract data?

- What is the relationship between the input parameter space and potential outputs of segmentation/registration algorithms?

- What are the trade-offs among the input parameters in terms of output accuracy, performance, and stability?

- What are the differences between features in terms of their spatial and quantitative characteristics?

- How to determine and visually encode the similarity of features?

My contributions to computer science in this area focus on vPSA, as well as the comparative and ensemble visualization [AHRG10], [WAG⁺16], [FMH16], [FEM⁺19], [WFG⁺19]. We have presented methods for **visual parameter space analysis**, exploring input parameter spaces with respect to the generated outputs, specifically of different segmentation and registration algorithms. Regarding **similarity metrics for vPSA** techniques, metrics are introduced in order to determine which object matches the predefined reference best in terms of their attributes, distances of characteristic points or overlap. Furthermore, regarding **comparative visualization**, techniques have been presented to study the differences between multiple results regarding their visual representation and their characteristics respectively. Finally, **ensemble visualization and analysis** using histogram heatmaps of ensemble data as well as Dynamic Volume Lines have been investigated. Some of these contributions are explained in the following sections. The proposed techniques and methods have been demonstrated on real world use cases and evaluated in respective case studies.

Similarity Metrics for vPSA

When comparing features as well as their characteristics, first a reference needs to be defined, against which all others can be correlated. Often a ground truth reference is used for such analyses or experiments, which is calibrated against a global reference standard for absolute comparisons. If such ground truth is not available, arbitrary feature samples may serve as reference for relative comparisons. In the following sections we focus on the latter case of relative comparisons and more specifically, on similarity metrics for fibers as generated in fiber reconstruction [FEM⁺19]. For comparing such fibers and their characteristics, similarity metrics are required to figure out, how fiber reconstruction results compare against each other and if a result is superior to another one. Such similarity metrics should return zero for a perfect match (i.e., the fibers are identical) and larger values, the less they are matching. Finally, similarity metrics should be invariant with respect to orientation (start and end points of single fibers may be interchanged), but not concerning scale or translation. By nature, features as well as datasets need to be considered as rigid. Three fiber similarity metrics have been identified. These metrics are based on fiber characteristics (1), point distances (2), and overlap (3).

Metrics of the first category measure similarity based on respective differences in terms of the fiber characteristics (1), e.g., differences in center points (X, Y, Z-coordinates), fiber lengths, as well as fiber directions defined by azimuth and elevation angles in a spherical coordinate system. Likewise, additional, or different characteristics could be considered. Attributes suitable for similarity metrics should be largely independent to account for the differences in the data. A straightforward metric of this first category determines the Euclidean distance in an n-dimensional space spanned by the used fiber characteristics. In the specific case of fibers and the selected characteristics, a 6-dimensional vector integrates the characteristics of a sample, yielding a 6-dimensional space. It contains the X, Y, Z-coordinates of the center point, the fiber length, and the azimuth and elevation angles of the fiber direction. This 6D vector serves as basis for the computation of respective Euclidean distances to other fibers within the 6D space. Unfortunately, as the individual fiber characteristics have different physical dimensions, they are not comparable. A methodological clean way for this kind of metric should therefore consider a normalization together with weighting factors for the individual characteristics.

Metrics based on point distances (2) consider critical points of the object of interest such as start points, centers, and end points. The computed sum of the Euclidean differences between these points serves as metric of this category. However, such a metric is not invariant towards

orientation, i.e., fibers which are perfectly matching, but having an inverted orientation would also end up with a high dissimilarity. To address this issue, the distances between start and end points need to be computed twice, once regularly and once with start and end points exchanged. Unfortunately, even with twice the computation of distances with start and end point exchanged accordingly, such a metric remains dependent on the fiber length. More sophisticated similarity metrics based on the squared average distances can circumvent this issue, returning a metric purely representing the geometric distance.

Overlap based metrics (3) typically sample points in the objects to be compared in order to evaluate their similarity, e.g., based on the Sørensen–Dice coefficient or the Jaccard index. We introduced a similar metric, which samples arbitrary points in only one object and measures, how many of those are contained in the other. The number of sample points contained is then divided by the total number of samples to account for the number of samples. What needs to be considered is the volume ratio between the two objects: a smaller object fully contained in a larger one would otherwise return a perfect match. In addition, the object with the smaller volume needs to be sampled and checked regarding its inclusion in the larger one, since the larger volumes can never be fully included in smaller ones. Overlap-based metrics represent best what users expect of a fiber dissimilarity measure, yet they are most expensive to compute.

Comparative Visualization

According to Gleicher et al. [GAW+11] there are three main approaches to compare data using visualization: (1) juxtaposition, (2) superposition and (3) explicit encoding. Using juxtaposition (1) a side-by-side visualization of the data is employed for the comparison. Juxtapositions typically do not scale well with the number of datasets. Furthermore, due to the side-by-side arrangement of the data, analyzing the differences even of only a few datasets may be a tedious and error prone task. Often juxtapositions are therefore used as overviews of the data and accompanied with additional visualization widgets, e.g., revealing statistics on similarity metrics. In FIAKER, Fröhler et al. [FEM+19] employ such a concept for a cumulative list view of output results generated by vPSA of fiber reconstruction algorithms (Figure 2.4 left image). This list view contains: the name of the result, volumetric renderings of the dataset, aggregated and weighted bar charts of the selected similarity metric, and histograms showing the distribution of the metric for visual comparison. Similarly to LineUp [GLG+13], FIAKER facilitates a quantitative ranking of the individual results with respect to the selected similarity metric. Side-by-side analysis in the sense of juxtaposition is here mainly used for the aggregated and weighted bar charts as well as the distribution histograms of the selected similarity metric. Volumetric renderings serve as miniature representations in the list and can be enlarged in the detail view for an in-depth analysis.

Comparative visualization using superposition (2) blends data over each other, which facilitates a direct comparison of data. Starting with the negative aspects and similarly to juxtaposition, superposition does not scale well with increasing number of datasets due to overplotting and visual clutter. On the positive side, a superposition may amplify cognition through direct in-place comparisons. Differences from reference to test data may immediately be revealed in the same display space due to the blending concept. Depending on the used visualization technique and due to transparency and color issues through blending, subtle differences in the datasets may be hidden. Fröhler et al. [FEM+19] used superposition in their detail view. By assigning individual colors to reference and test datasets/objects to be compared, differences are revealed for qualitative visual comparisons. A more sophisticated method of this category as well as of explicit encoding is explained in detail in the subsection on ensemble visualization, which is Dynamic Volume Lines by Weissenböck et al. [WFG+19].
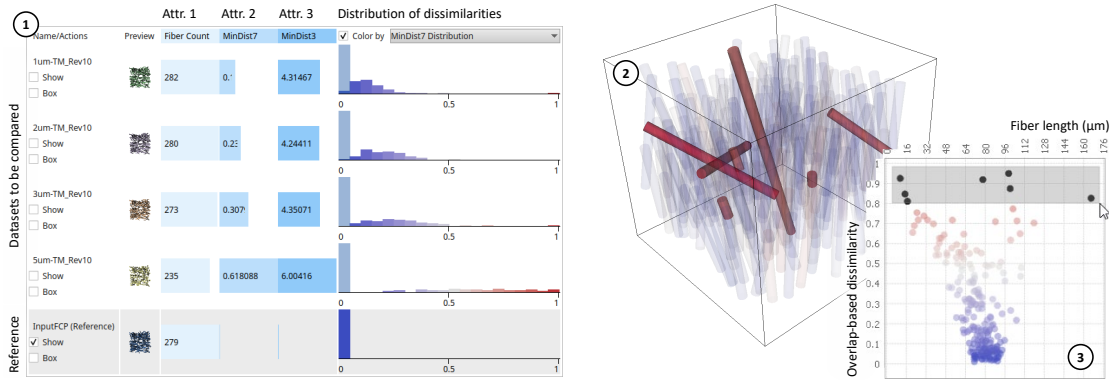
Figure 2.4: Comparative visualization using FIAKER. Left: Quantitative ranking of the individual results with respect to the selected similarity metric (1). Right: Explicit encoding of the features' dissimilarity to the reference using colors (2). Blue encodes low dissimilarity whereas red encodes high dissimilarity. Corresponding features with high dissimilarity in terms of overlap are selected (3) and shown opaque in the 3D rendering (image adapted from [FEM+19]).

The third category of comparative visualization approaches is called explicit encoding (3). For explicit encoding, similarity metrics such as differences of data values are employed and serve as basis for visualization. Respective visualization techniques of this category thus do not directly visualize the individual datasets or data values but rather focus on aggregated information thereof. For this reason, explicit encoding scales best with the number of datasets as compared to the other categories. In FIAKER, explicit encoding serves to compare datasets on the feature level. First a reference dataset is selected. Using the metrics as explained in the previous section, the similarity is computed feature-wise between reference and test dataset. For each feature, the similarity is then encoded using colors mapped to the computed similarity value. Such an encoding of similarity immediately reveals the matching quality (Figure 2.4 right image).

Ensemble Visualization and Analysis

The need of providing visual summaries for the comparison of many complex datasets is addressed in ensemble visualization. Such visual summaries often serve as interactive overviews of the complete ensembles and are supplemented by statistical information as presented in Ensemble-Vis by Potter et al. [PWB+09].
The comparison of members in large ensembles is particularly hard, if the ensemble members just slightly deviate from each other. This is the case in parameter studies of data analysis algorithms and pipelines generating rich XCT data ensembles. In Dynamic Volume Lines by Weissenböck et al. [WFG+19], we introduced a novel method for the interactive visual analysis and comparison of large ensembles of volumetric datasets (Figure 2.5). The core idea of this method is based on linearizing volumes to 1D line plots with the benefits of a high comparability and scalability. The abscissa of these line plots holds the indices of the volumetric elements, whereas the ordinate shows the actual values of the voxels. For volume linearization, conventional space filling curves may be employed, such as Z-curves, the Peano curve, or the Hilbert curve. The most obvious method is a scan line conversion, which extracts the indices and thus correlated data values line by line and subsequently slice by slice. This technique comes with the disadvantage of large jumps when reaching the end of one line and moving on to the start of the next (similarly as for slices), which would highly distract in analyzing the respective linearizations. In contrast,
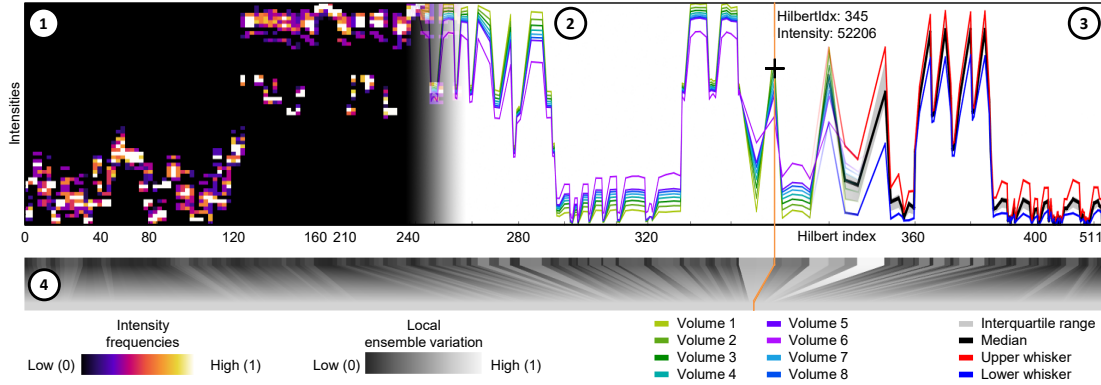
Figure 2.5: Ensemble visualization using Dynamic Volume Lines. The histogram heatmap (1) depicts sets of volumes in an overview visualization. 1D Hilbert line plots (2) serve as interactive detailed view. Functional boxplots (3) explicitly encode the descriptive statistics. All plots are non-linearly scaled based on the local ensemble variation. The scaling widget (4) depicts the ensemble variation on each level of detail. ©2019 IEEE. Reprinted, with permission, from [WFG+19].

the Hilbert space filling curve is a continuous fractal. Originally, it has been derived as variant from the Peano space-filling curves. The Hilbert space filling curve is used in Dynamic Volume Lines, as it allows to linearize volumes by traversing all points of a square, a cube, or more generally, an n-dimensional hypercube, while preserving locality in the traversal and largely avoiding jumps. Locality in this context means, that previous and next elements are typically neighboring the considered element. For comparing higher numbers of volumes using line plots, functional boxplots as introduced by Sun and Genton [SG11] are employed. Using functional boxplots, line plots are aggregated by computing and encoding descriptive statistic measures such as lower and upper whisker, the median, and the interquartile range.

A general problem which comes with any linearization technique, especially when applied to high resolution volume data, is the generation of line plots with extensive length (e.g., volumes with 1024^3 voxels return 1.073.741.824 indices; volumes with 2048^3 voxels return 8.589.934.592 indices), which means that the horizontal screen resolution of conventional display devices is not sufficient. Intelligent scaling is mandatory as valuable details might be lost through constant scaling procedures. Dynamic Volume Lines facilitate non-linear scaling by considering the maximal local ensemble variation in terms of intensities for every Hilbert index to derive a cumulative importance-function. The values of this importance function serve as compression factors of the line plot and control a nonlinear mapping of the distances between the Hilbert indices on the abscissa. The local compression factors become obvious in an interactive scaling widget, which depicts the local ensemble variations. This way an effective use of the available screen space is enabled and important areas (i.e., areas of high variance in the ensemble) are emphasized while less important areas (i.e., areas of little or no variance) are compressed or removed.

Intelligent scaling of line plots by local compression helps as visualization technique to focus on data segments of interest. In many cases this is still not enough for generating a complete overview of all indices in the entire volume. We therefore designed interactive histogram heatmaps of the intensity distributions as overview visualization technique in Dynamic Volume Lines, in order to fit the complete volume into a single cumulative chart within the available screen width. For this purpose, the horizontal axis of the line chart is subdivided into intervals of equal width. For each

interval a histogram of intensities is computed in order to finally construct the histogram heatmap (see Figure 2.5 (1)). In summary, the ensemble analysis is facilitated through a comprehensive interface, which integrates brushing and linking of the histogram heatmaps, line plots, and scaling widgets together with a spatial rendering of the original dataset indicating the selected voxels in 3D.

2.3 Grand Challenge: Visualization Theory and Modeling

Since its first dedicated conferences in the early 1990s, visualization significantly evolved as scientific field and also its self-conception as a mature scientific discipline. This evolution was accompanied and consolidated with state-of-the-art reports, position and white papers on its research as well as conceptual frameworks to guide future research efforts.

The related work in terms of visualization theory and modeling is found in general taxonomies of visualization and interaction: Shneiderman [Shn96] introduced in his task by data type taxonomy for information visualization the visual information seeking mantra, which has been seminal for numerous approaches in visualization. Kosara et al. [KHG03] and Yi et al. [YKSJ07] conducted reviews of visualization systems and their interaction capabilities. Quality metrics and visual comparisons are other very relevant concepts in their contributions to visualization theory and modeling. Here, quality metrics for complex and high-dimensional data visualization are of particular interest. Bertini et al. [BTK11] introduced a systematization of techniques that employ quality metrics supporting the visual exploration of patterns in high-dimensional data. Respective metrics are the foundation of all visual comparisons as discussed by Gleicher et al. [GAW$^+$11]. Finally, supporting techniques used for visual parameter space analysis and visual computing in materials science are considered as relevant. Corresponding techniques integrate visual interaction coupled with dimensionality reduction as addressed by Sacha et al. [SZS$^+$17]. Furthermore, Kehrer and Hauser [KH13] studied visualization and visual analysis of multifaceted scientific data as well as challenges arising from the heterogeneous nature of scientific data. Finally, Alsallakh et al. [AMA$^+$16] provide a systematic overview of visualization techniques for set relations.

My research towards contributions to visualization theory and modeling focuses on two distinct areas, which are explained as follows: Visual parameter space analysis (vPSA) has received much attention in the visualization community, e.g., in terms of image segmentation [TWSM$^+$11], weather forecasts [PWB$^+$09], disaster simulation [WFR$^+$10], and also in materials science [WAG$^+$16]. A state-of-the-art report is required to classify and guide research endeavors in this field. Similarly, but more recently, the topic of visual computing in materials science emerged, which is showing novel insights through tailored visual analysis techniques. Examples of this topic are found in terms of research on novel battery materials [GKL$^+$16], fiber reinforced composites [BWW$^+$17], or materials for fusion reactors [KJS$^+$14]. A structured literature review will help in understanding the body of work and thus framing future visualization research. In order to address these requirements, the following research questions are investigated:

- What are the data and the tasks, that visualization and visual computing are used for in materials science?

- Which visual metaphors and interaction concepts are used and why are they preferred over others?

- How to extract a common abstract framework characterizing vPSA across domains?

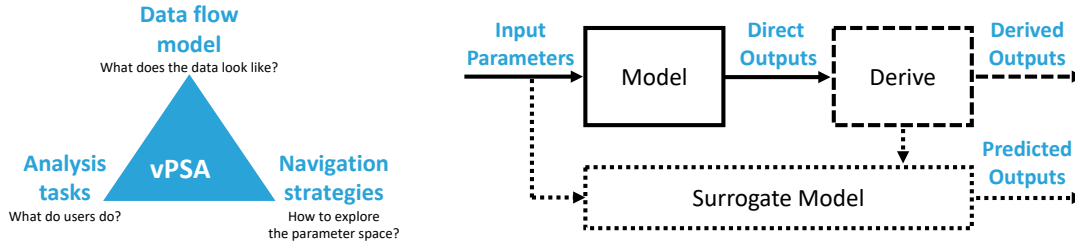- How to build up a higher-level understanding of vPSA?

Figure 2.6: Conceptual framework for the classification of vPSA approaches regarding data flow model, analysis tasks, and navigation strategies. vPSA data flow model abstracting vPSA problems. ©2014 IEEE. Reprinted, with permission, from [SHB+14].

- What are the open research challenges for future research endeavors?

My contributions to computer science in the context of these research questions generate in-depth insights into the research areas of visual parameter space analysis and visual computing in materials science [SHB+14], [HS17]. In terms of **visual parameter space analysis**, a conceptual framework as well as a unified set of definitions and terminology were derived based on a structured literature review of design studies in this area (Figure 2.6). Concerning **visual computing in materials science**, the current body of work was reviewed and classified in order to derive the intersection areas, the high-level tasks as well as to gain insights into the data, the visual metaphors and the interaction concepts they are employing. Some aspects of the respective contributions are explained in the following sections.

Visual Parameter Space Analysis

In various application domains visual parameter space analysis (vPSA) has shown great potential to support in using and validating algorithms, pipelines, and models. An application area of vPSA on reconstruction and segmentation pipelines was presented in the previous section.
In our report on vPSA (Sedlmair et al. [SHB+14]), we hypothesized that the presented domain-specific applications in parameter space analysis all share a common abstract framework, which characterizes the field. Therefore, our goal was to extract a generalized conceptual framework and provide directions on how to use it together with terminology and open research gaps. The report is based on more than 110 potentially interesting research papers. 21 of these were classified as highly relevant in order to illustrate our framework (see Figure 2.6).
First, a data flow model was proposed, which abstracts vPSA problems and characterizes recurring data manipulation operations. It includes the steps of sampling of the input parameter space, computing outputs based on the sampled inputs, deriving objective measures from outputs, and finally predicting outputs with cheaper surrogate models. Second, a classification of navigation strategies was presented. These navigation strategies integrate "informed-trial-and-error", which means the model is parametrized using prior knowledge coupled with iterative refinements. Further strategies are "local-to-global" and "global-to-local" navigation, which both require a precomputation of samples. While the local-to-global navigation strategy starts with a specific output in order to explore alternatives from there, global-to-local in contrast uses a global overview and then continues the drill down to details. Finally, "steering" an ongoing data generation process based on intermediate visualization results was identified as the fourth navigation strategy. Regarding typical analysis tasks in vPSA we identified the following topics in the highly relevant papers: "Optimization" tries to find the best parameters with respect to the given objectives.

"Partitioning" identifies types of different model behaviors. The analysis task of "Fitting" derives input parameters of the model based on actual measured data. "Outlier" detection seeks special samples. Ultimately, "uncertainty" and "sensitivity" determine the output's reliability as well as variations of outputs with respect to changes of the inputs.

Visual Computing in Materials Science

Recent achievements regarding high resolution data acquisition and visual computing enabled materials analysis to shift from plain imaging to detailed characterizations and traceable metrology. Similarly, precise material modeling and the ever-increasing computational power allows for detailed simulations of novel material systems. Furthermore, advanced manufacturing technologies paved the way towards the fabrication of tailored, lot-size-one materials and components.

In all these areas of materials science, visual computing is currently more important than ever. Visual computing allows to generate fundamentally new insights for the understanding, the discovery, the design, and the use of novel material systems, such as the discovery of novel battery materials [GKL+16] or the tailored design of composite materials [BWW+17]. A multitude of different phenomena may now be studied, at various scales, dimensions, or using different modalities.

In our state-of-the-art report on visual computing in materials science (Heinzl and Stappen [HS17]) the proximity of both fields, materials science and visual computing, is outlined. Starting with the definition of these fields, we systematically reviewed 241 potentially interesting research papers and based our findings on 88 papers which were classified as highly relevant. First, we investigated material systems for which visual computing is helpful. We found that visual computing is particularly beneficial in research on complex and advanced materials, such as composites, polymers, non-metal inorganic, biological or biomedical materials. A closer look at the tasks of visual computing in these areas revealed that especially the visual analysis of simulated data, the visual analysis of stress and deformation, the damage and risk analysis as well as the uncertainty quantification and visualization are frequently found and of great importance. Our study on data generation and data types revealed that in a growing number of cases, multi-modal, multi-dimensional, and multi-scale approaches are employed, invoking additional challenges regarding the aggregation, analysis, and exploration of heterogeneous data. Regarding the visual metaphors, mostly visual representations for spatial, for spatio-temporal as well as quantitative and derived data were required. These were accompanied by interaction techniques such as explore and reconfigure, linking and brushing, focus and context, and filtering. Finally, open high-level and low-level challenges were identified for future research.

2.4   open_iA

All the introduced visualization and analysis techniques in course of this habilitation thesis were implemented in open_iA [FWS+19], an open-source platform for visual analysis and processing of volumetric datasets, with a special focus on rich XCT data. The original concept of this framework dates back to 2009, as an attempt to integrate and consolidate the software engineering lessons learned during my PhD. open_iA is the result of (re-)structuring, integrating, and unifying all developments of my group in a common, reusable and platform independent software framework. This framework is implemented in C++ and builds upon Qt [Com21], a toolkit for graphical user interfaces and cross-platform applications, on VTK [Kit21c], a software system for manipulating and displaying scientific data, and finally ITK [Kit21b], a library for the analysis, processing, segmentation, and registration of scientific images. It is customizable through the cmake [Kit21a] build system and highly extensible through templates and modules, which may range from simple

image processing filters to highly sophisticated and fully integrated analysis and visualization tools. Figure 2.1 shows "FiberScout" as an exemplary module of open_iA. Its characteristics make the open_iA framework an ideal platform for rapidly developing novel visualization techniques and research prototypes for 2D, 3D and high dimensional data. Throughout the development of the framework, special attention was paid to advancing research prototypes from papers to ready-to-use software components, primarily for internal but also external collaborators. This extra work was worth the time and efforts on a longer perspective for our in house users and also to attract new partners from industry and academia regarding novel concepts and ideas. open_iA is the basis for all my running projects as well as all my scientific and industrial collaborations. In June 2016 open_iA was finally made available as open source on github [Wel21], which allowed to spark new collaborations in smaller student projects and also for larger industrial and academic activities. With its recent upgrades in terms of ONNX [Fou21], an open format to represent and integrate machine learning models, as well as OpenVR [Val21] for accessing VR hardware, the technological foundation of open_iA is set for future perspectives.

2.5 Future Perspectives

Materials science has shown a significant impact on our lives through the development of more durable and more economic, yet safer, healthier, environmentally friendlier and sustainable materials. Visual computing, and especially visualization and analysis of XCT, takes a large portion of these achievements. Some of the techniques introduced in this thesis have pioneered visual computing based materials science through the analysis and visualization of rich XCT data. But still there is a large number of open research questions yet to be answered. In the following list, the five most imminent research questions are summarized:

1. **How can visualization guide future analyses of rich XCT data?** For future rich XCT data analysis, we have to make sure, that our systems and tools indicate errors and identify wrongly used algorithms or parametrizations (i.e., "visual debugging"). We need to investigate if and how our methods and techniques can actively assist users throughout the visual analysis process. The exploitation of concepts such as guidance and knowledge-driven exploration will be of utmost importance in this area. Furthermore, we need to investigate, if current research trends such as immersive analytics, collaborative analytics, or cross virtuality analytics can have a substantial impact on guiding XCT data analysis or if they rather hinder analysis processes.

2. **How can visualization ensure the interpretability of rich XCT data despite the increasing complexity in terms of data and analysis pipelines?** Due to the increasing volume, velocity, veracity, and variety of rich XCT data, methods are required, which abstract rich XCT data in meaningful and easy to understand visual metaphors. For example, topology analysis can help in this effort to reveal complex internal structures such as crack networks. Yet, at the same time we need to ensure the interpretability of the derived visual metaphors in order to safeguard decision making processes. In addition, also novel analysis concepts such as machine learning (ML) need to be considered. Although ML is often helpful to reduce complexity or approximate models, respective techniques must be accompanied by visual tools to support the interpretability of ML and ML outputs.

3. **How can we balance automation vs. interactive visual analysis of rich XCT data in order to focus human expertise on areas where is really required?** An automation of data analysis tasks can be of great help to deal with the data's ever-increasing

complexity. Using automation, ambiguous and unclear areas in rich XCT data can be isolated, in order to make use of human knowledge and expertise in these areas. Moreover, many practices continue to require "the human in the loop" for decision making. Future tools should therefore feature smart defaults, but allow the user to explore, navigate and possibly refine data.

4. **For which tasks of rich XCT data analysis is a transition from interactive visual analysis to interactive steering beneficial?** Future applications of rich XCT data analysis will not only visualize the data with its corresponding reliability or uncertainty budgets. Methods will integrate predictive capabilities such as where to sample next or how to optimize parameters. We need to analyze if and for which scenarios interactive steering is helpful.

5. **Which specialization steps are necessary for interactive visualization to account for increasing data volumes and velocity in XCT?** XCT is a true big data problem. Many applications require a specialization of currently existing algorithms, pipelines, and techniques, especially when transitioning to inline XCT inspections. Yet, current techniques, which are originally designed for batch processing, need to be re-engineered to allow for interactive procedures, e.g., in terms of trend analysis, uncertainty or sensitivity analysis.

Following these questions, there are new research directions in visual analysis of rich XCT data, which have not been tackled in depth or at all. Some of these directions I target to address in my future research:

Topology analysis and visualization

For rich XCT data ensembles, a data-driven approach based on the structural features of the target dataset is essential for an effective visualization. Aside features of interest, also their topological structure reveals interesting information about the materials performance, aging status, and damage conditions. Topology analysis is an effective means for addressing these issues in scientific applications. The topology of structures in materials science applications will be of primary interest, e.g., for analyzing pore or crack networks, permeability, or electric or thermal conductibility. Meaningful and intuitive visualization techniques are required in terms of topology together with critical points, such as sources, sinks, or saddles. In addition to visualization also an empirical analysis regarding persistency is important, as topological analyses of real-world datasets extract many critical points due to noise or artefacts. Such minor critical points should be eliminated as they might hide an important global structure. The focus here will be on strategies to evaluate their importance and methods to reduce them effectively.

Fully integrated visualization pipelines

The tailored, fully integrated visual analysis of rich XCT data is of big interest. Due to the complexity and diversity of respective applications and analysis tasks, only very few approaches have been presented. Related thereto are general challenges in terms of designing, developing, and deploying scalable solutions for the quantification, exploration, analysis, and visualization of rich data. Features, characteristics, topologies as well as aggregations thereof need to be extracted from rich XCT data in spatial, temporal, or even higher dimensions, for a single or a multitude of samples. Two upcoming areas are of particular interest for future visualization pipelines which are machine learning (ML) and immersive analytics (IA). First, ML and more specifically deep convolutional neural networks (CNNs) proved to be able to identify and classify objects with

very high probabilities in various application areas. Various approaches have successfully applied deep CNNs, e.g., for segmentation, feature extraction, or reconstruction of XCT data. The target here is to find out, how visual computing in materials science can profit from ML concepts. In terms of feature extraction and quantification, enabling transfer learning between material systems could help in reducing training efforts. ML could be also employed for suggesting visual metaphors for novel data analysis concepts based on analysis task or data. Second, the benefits of immersive analytics (IA) for analyzing rich XCT data need to be evaluated. We need to answer, how immersive analytics can substantially support in terms of visual data analysis and exploration using novel interaction concepts and full immersion with our data. We have to clarify, if cross-virtuality analytics (XVA) is beneficial for rich XCT data. Cross-virtuality analytics in this sense refers to collaborative analyses along the reality-virtuality continuum as defined by Milgram et al. [MTUK95]. For IA and XVA, comparative and ensemble visualization techniques need to be advanced to ensure their applicability. In all our considerations we finally have to take into account, that more complex metrics for more complex data typically lead to more complex visualization techniques and steeper learning curves.

Interpretability and decision-making using visualization

Advanced material analysis and simulation coupled with novel and tailored visualization and visual analysis techniques, features the potential to address upcoming challenges in terms of understanding, discovery, design, and use of novel material systems. For example, advances in ML are allowing for fast approximations of complex phenomena. ML turned out to be particularly helpful in feature reconstruction, classification, or complexity reduction. However, as we learned from our own experiments, ML is only as good as its training. Without appropriate and careful training using suitable and sufficient training data, ML may generate erroneous or incomplete models, which can induce wrong results and decisions. The research questions to be answered here are how to safeguard appropriate outputs using visualization and how to explain the generated outputs. Uncertainty and sensitivity analysis and visualization will play a major role in this effort. New techniques are required to understand ML-based XCT data analysis together with analyzing the uncertainty prevalent in the generated results as well as the sensitivity regarding subtle changes of inputs or training parameters. Decision making using visualization of rich XCT data requires new visual metaphors. Extending on vPSA, sensitivity and uncertainty analysis, also the decisions taken and respective risks thereof need to be considered. A detailed understanding of the parameter space of data analysis pipelines, the sensitivity of inputs with respect to the generated outputs, as well as the uncertainty in the generated data is paramount for decision making. We need to answer the research question of how to support decisions based on rich XCT data by identifying and evaluating the risks contained in these decisions. For example, an optimal candidate material may be subjected to uncontrolled environmental conditions in production, such as increased humidity or temperature, and yield deteriorated specs. If other candidates are existing with similar specs, showing a more stable behavior and therefore a lower risk, these should possibly be preferred. In summary, as complexity and richness of the material specifications and respective analysis data increases, the topics of uncertainty, sensitivity and risk analysis will become indispensable components of all visual analysis solutions for decision making in materials science.

2.6   Authorship Statement

The following statement provides a concise overview on the author's contributions to the publications included in this habilitation thesis. These publications represent a snapshot of the research,

which has been conducted and published in a collaborative effort by the author together with other researchers between 2010 and 2020. Collaborations on the individual publications are highly characteristic for the scientific work in the visualization community. Single-author publications are exceptional and thus found only in very rare cases in our community. In Table 2.1ff, the contributions of the author to the respective publications are indicated. The contributions are classified based on **CRediT (Contributor Roles Taxonomy)**, a high-level classification scheme regarding the different roles for publishing research as presented by Brandt et al. [BAA$^+$15]. Significant contributions are indicated in bold and generated major input to fundamental parts of the work. Other contributions either provide input to well-defined smaller aspects or to parts where other co-authors played the leading role. These contributions are indicated in regular font. For most of the selected publications in this thesis I acted as the last author, with the respective PhD students I (co-)supervise being the first author. The two papers, which are not following this scheme, are those which I coauthored with senior researchers from different universities and research institutes. All papers have been published in projects, that were granted to me as principal investigator. They are reprinted in this thesis in the form they were accepted or published, following the publishers' policy for reproducing author's work.

Publications	Contributions
Bernhard Fröhler, Tim Elberfeld, Torsten Möller, Hans-Christian Hege, Johannes Weissenböck, Jan De Beenhouwer, Jan Sijbers, Johann Kastner, and **Christoph Heinzl**. A visual tool for the analysis of algorithms for tomographic fiber reconstruction in materials science. *Computer Graphics Forum*, 38(3):273–283, 2019. doi:10.1111/cgf.13688	**Conceptualization** **Methodology** Software Validation **Resources** Writing - Original Draft **Writing - Review & Editing** **Visualization** **Supervision** **Project administration** **Funding acquisition**

Table 2.1: Contribution statement 1/3

Publications	Contributions
Johannes Weissenböck, Bernhard Fröhler, Eduard Gröller, Johann Kastner, and **Christoph Heinzl**. Dynamic Volume Lines: Visual comparison of 3D volumes through space-filling curves. *IEEE Transactions on Visualization and Computer Graphics*, 25(1):1040–1049, 2019. doi:10.1109/TVCG.2018.2864510	**Conceptualization** **Methodology** Software Validation **Resources** Writing - Original Draft **Writing - Review & Editing** **Visualization** **Supervision** **Project administration** **Funding acquisition**
Christoph Heinzl, Stefan Stappen. STAR: Visual Computing in Materials Science. *Computer Graphics Forum* 36(3):647–666, 2017. doi:10.1111/cgf.13214	**Conceptualization** **Methodology** **Investigation** **Data Curation** **Writing - Original Draft** **Writing - Review & Editing** **Visualization** **Supervision** **Project administration** **Funding acquisition**
Arindam Bhattacharya, Johannes Weissenböck, Rephael Wenger, Artem Amirkhanov, Johann Kastner, **Christoph Heinzl**. Interactive Exploration and Visualization using MetaTracts extracted from Carbon Fiber Reinforced Composites. *IEEE Transactions on Visualization and Computer Graphics*, vol. 23(8):1988-2002, 2017. doi:10.1109/TVCG.2016.2582158	**Conceptualization** **Methodology** Software Validation **Resources** Writing - Original Draft **Writing - Review & Editing** **Visualization** **Supervision** **Project administration** **Funding acquisition**
Bernhard Fröhler, Torsten Möller, and **Christoph Heinzl**. GEMSe: Visualization-guided exploration of multi-channel segmentation algorithms. *Computer Graphics Forum*, 35(3):191–200, 2016. doi:10.1111/cgf.12895	**Conceptualization** **Methodology** Software Validation **Resources** Writing - Original Draft **Writing - Review & Editing** **Visualization** **Supervision** **Project administration** **Funding acquisition**

Table 2.2: Contribution statement 2/3

25

Publications	Contributions
Johannes Weissenböck, Artem Amirkhanov, Eduard Gröller, Johann Kastner, and **Christoph Heinzl**. PorosityAnalyzer: Visual analysis and evaluation of segmentation pipelines to determine the porosity in fiber-reinforced polymers. In *IEEE Conference on Visual Analytics Science and Technology (VAST)*, pages 101–110, 2016. doi:10.1109/VAST.2016.7883516	**Conceptualization** **Methodology** Software Validation **Resources** Writing - Original Draft **Writing - Review & Editing** **Visualization** **Supervision** **Project administration** **Funding acquisition**
Michael Sedlmair, **Christoph Heinzl**, Stefan Bruckner, Harald Piringer, and Torsten Möller. Visual Parameter Space Analysis: A Conceptual Framework. *IEEE Transactions on Visualization and Computer Graphics*, 20(12):2161-2170, 2014. doi:10.1109/TVCG.2014.2346321	**Conceptualization** **Methodology** **Investigation** **Data Curation** **Writing - Original Draft** **Writing - Review & Editing** **Visualization** **Funding acquisition**
Johannes Weissenböck, Artem Amirkhanov, Weimin Li, Andreas Reh, Alexander Amirkhanov, Eduard Gröller, Johann Kastner, and **Christoph Heinzl.** FiberScout: An interactive tool for exploring and analyzing fiber reinforced polymers. In 2014 *IEEE Pacific Visualization Symposium*, pages 153–160, March 2014. doi:10.1109/PacificVis.2014.52	**Conceptualization** **Methodology** Software Validation **Resources** Writing - Original Draft **Writing - Review & Editing** **Visualization** **Supervision** **Project administration** **Funding acquisition**
Andreas Reh, Christian Gusenbauer, Johann Kastner, Eduard Gröller, and **Christoph Heinzl**. MObjects–A Novel Method for the Visualization and Interactive Exploration of Defects in Industrial XCT Data. *IEEE Transactions on Visualization and Computer Graphics*, 19(12):2906–2915, 2013. doi:10.1109/TVCG.2013.177	**Conceptualization** **Methodology** Software Validation **Resources** Writing - Original Draft **Writing - Review & Editing** **Visualization** **Supervision** **Project administration** **Funding acquisition**

Table 2.3: Contribution statement 3/3

Bibliography

[AAS+16]   Alexandr Amirkhanov, Artem Amirkhanov, Dietmar Salaberger, Johann Kastner, Eduard Gröller, and Christoph Heinzl. Visual analysis of defects in glass fiber reinforced polymers for 4DCT interrupted in situ tests. *Computer Graphics Forum*, 35(3):201–210, 2016.

[AFK+14]   Artem Amirkhanov, Bernhard Fröhler, Johann Kastner, Eduard Gröller, and Christoph Heinzl. InSpectr: Multi-Modal Exploration, Visualization, and Analysis of Spectral Data. *Computer Graphics Forum*, 33(3):91–100, 2014.

[AHK+13]   Artem Amirkhanov, Christoph Heinzl, Christoph Kuhn, Johann Kastner, and Meister Eduard Gröller. Fuzzy CT Metrology: Dimensional Measurements on Uncertain Data. In *Proceedings of the 29th Spring Conference on Computer Graphics*, pages 81–90. Association for Computing Machinery, 2013.

[AHRG10]   Artem Amirkhanov, Christoph Heinzl, Michael Reiter, and Eduard Gröller. Visual Optimality and Stability Analysis of 3DCT Scan Positions. *IEEE Transactions on Visualization and Computer Graphics*, 16(6):1477–1486, November 2010.

[AMA+16]   Bilal Alsallakh, Luana Micallef, Wolfgang Aigner, Helwig Hauser, Silvia Miksch, and Peter Rodgers. The State-of-the-Art of Set Visualization. *Computer Graphics Forum*, 35(1):234–260, 2016.

[AMST11]   Wolfgang Aigner, Silvia Miksch, Heidrun Schumann, and Christian Tominski. *Visualization of Time-Oriented Data*. Human-Computer Interaction Series. Springer, London, 2011.

[BAA+15]   Amy Brand, Liz Allen, Micah Altman, Marjorie Hlava, and Jo Scott. Beyond authorship: attribution, contribution, collaboration, and credit. *Learned Publishing*, 28(2):151–155, 2015.

[BTK11]   Enrico Bertini, Andrada Tatu, and Daniel Keim. Quality Metrics in High-Dimensional Data Visualization: An Overview and Systematization. *IEEE Transactions on Visualization and Computer Graphics*, 17(12):2203–2212, 2011.

[BWW+17]   Arindam Bhattacharya, Johannes Weissenböck, Rephael Wenger, Artem Amirkhanov, Johann Kastner, and Christoph Heinzl. Interactive Exploration and Visualization Using MetaTracts extracted from Carbon Fiber Reinforced Composites. *IEEE Transactions on Visualization and Computer Graphics*, 23(8):1988–2002, 2017.

[CDL18]   Simone Carmignato, Wim Dewulf, and Richard Leach, editors. *Industrial X-Ray Computed Tomography*. Springer International Publishing, 1 edition, 2018.

[Com21]   The Qt Company. Qt Website, 2021. https://www.qt.io; Online; last accessed 08.06.2021.

[Dag19]   Schloss Dagstuhl. Dagstuhl-Seminar 19151 Visual Computing in Materials Sciences, 2019. https://www.dagstuhl.de/19151.

[DDW14]   Ismail Demir, Christian Dick, and Rüdiger Westermann. Multi-Charts for Comparative 3D Ensemble Visualization. *IEEE Transactions on Visualization and Computer Graphics*, 20(12):2694–2703, 2014.

[FEM+19]   Bernhard Fröhler, Tim Elberfeld, Torsten Möller, Hans-Christian Hege, Johannes Weissenböck, Jan De Beenhouwer, Jan Sijbers, Johann Kastner, and Christoph Heinzl. A Visual Tool for the Analysis of Algorithms for Tomographic Fiber Reconstruction in Materials Science. *Computer Graphics Forum*, 38(3):273–283, 2019.

[FHG+09]   Laura Fritz, Markus Hadwiger, Georg Geier, Gerhard Pittino, and Meister Eduard Gröller. A Visual Approach to Efficient Analysis and Quantification of Ductile Iron and Reinforced Sprayed Concrete. *IEEE Transactions on Visualization and Computer Graphics*, 15(6):1343–1350, 2009.

[FMH16]   Bernhard Fröhler, Torsten Möller, and Christoph Heinzl. GEMSe: Visualization-guided exploration of multi-channel segmentation algorithms. *Computer Graphics Forum*, 35(3):191–200, 2016.

[Fou21]   The Linux Foundation. ONNX Website, 2021. https://onnx.ai/; Online; last accessed 08.06.2021.

[FWS+19]   Bernhard Fröhler, Johannes Weissenböck, Marcel Schiwarth, Johann Kastner, and Christoph Heinzl. open_ia: A tool for processing and visual analysis of industrial computed tomography datasets. *Journal of Open Source Software*, 4(35):1185, 2019.

[GAW+11]   Michael Gleicher, Danielle Albers, Rick Walker, Ilir Jusufi, Charles D. Hansen, and Jonathan C. Roberts. Visual Comparison for Information Visualization. *Information Visualization*, 10(4):289–309, 2011.

[GKL+16]   Attila Gyulassy, Aaron Knoll, Kah Chun Lau, Bei Wang, Peer-Timo Bremer, Michael E. Papka, Larry A. Curtiss, and Valerio Pascucci. Interstitial and Interlayer Ion Diffusion Geometry Extraction in Graphitic Nanosphere Battery Materials. *IEEE Transactions on Visualization and Computer Graphics*, 22(1):916–925, 2016.

[GLG+13]   Samuel Gratzl, Alexander Lex, Nils Gehlenborg, Hanspeter Pfister, and Marc Streit. LineUp: Visual Analysis of Multi-Attribute Rankings. *IEEE Transactions on Visualization and Computer Graphics*, 19(12):2277–2286, 2013.

[GVTA10]   Sergi Grau, Eduard Vergés, Dani Tost, and Dolors Ayala. Exploration of porous structures with illustrative visualizations. *Computers & Graphics*, 34(4):398–408, 2010.

[Hei09]   Christoph Heinzl. *Analysis and Visualization of Industrial CT Data*. PhD Thesis, Institute of Computer Graphics and Algorithms, Vienna University of Technology, Favoritenstrasse 9-11/E193-02, A-1040 Vienna, Austria, 2009.

[HKL⁺19]   Christoph Heinzl, Robert Michael Kirby, Stepan V. Lomov, Guillermo Requena, and Rüdiger Westermann. Visual Computing in Materials Sciences (Dagstuhl Seminar 19151). *Dagstuhl Reports*, 9(4):1–42, 2019.

[HKMG08]   Christoph Heinzl, Johann Kastner, Torsten Möller, and Meister Eduard Gröller. Statistical Analysis of Multi-Material Components using Dual Energy CT. In Dietmar Saupe Oliver Deussen, Daniel Keim, editor, *VMV 2008, Vision, Modeling and Visualization*, pages 179–188, 2008.

[HS17]   Christoph Heinzl and Stefan Stappen. STAR: Visual computing in materials science. *Computer Graphics Forum*, 36(3):647–666, 2017.

[KH13]   Johannes Kehrer and Helwig Hauser. Visualization and Visual Analysis of Multifaceted Scientific Data: A Survey. *IEEE Transactions on Visualization and Computer Graphics*, 19(3):495–513, 2013.

[KH19]   Johann Kastner and Christoph Heinzl. X-Ray Tomography. In *Handbook of Advanced Nondestructive Evaluation*. Springer International Publishing, 2019.

[KHG03]   Robert Kosara, Helwig Hauser, and Donna L. Gresh. An Interaction View on Information Visualization. In *Eurographics 2003 - STARs*. Eurographics Association, 2003. ISSN: 1017-4656.

[Kit21a]   Kitware. CMake Website, 2021. https://cmake.org/; Online; last accessed 08.06.2021.

[Kit21b]   Kitware. ITK Website, 2021. https://itk.org/; Online; last accessed 08.06.2021.

[Kit21c]   Kitware. VTK Website, 2021. https://vtk.org/; Online; last accessed 08.06.2021.

[KJS⁺14]   Suk-Kwon Kim, Hyung Gon Jin, Kyu In Shin, Bo Guen Choi, Eo Hwak Lee, Jae-Sung Yoon, Yang-Il Jung, Dong Won Lee, and Duck-Hoi Kim. Manufacturing and Examination for ITER Blanket First Wall Small-Scale Mockups With KoHLT-EB in Korea. *IEEE Transactions on Plasma Science*, 42(5):1438–1442, 2014.

[MFW⁺19]   Lucas Da Cunha Melo, Bernhard Fröhler, Johannes Weissenböck, Johann Kastner, Torsten Möller, Hans-Christian Hege, Eduard Gröller, Jonathan Sanctorum, Jan De Beenhouwer, Jan Sijbers, and Christoph Heinzl. Tools for the Analysis of Datasets from X-Ray Computed Tomography based on Talbot-Lau Grating Interferometry. In *9th International Conference on Industrial Computed Tomography (iCT 2019)*, 2019.

[MHG10]   Muhammad Muddassir Malik, Christoph Heinzl, and Meister Eduard Gröller. Comparative Visualization for Parameter Studies of Dataset Series. *IEEE Transactions on Visualization and Computer Graphics*, 16(5):829–840, 2010.

[MMGB17]   Peter Mindek, Gabriel Mistelbauer, Eduard Gröller, and Stefan Bruckner. Data-sensitive visual navigation. *Computers & Graphics*, 67:77–85, 2017.

[MTUK95]   Paul Milgram, Haruo Takemura, Akira Utsumi, and Fumio Kishino. Augmented reality: A class of displays on the reality-virtuality continuum. In Hari Das, editor, *Photonics for Industrial Applications*, pages 282–292, Boston, MA, 1995.

[Mun15]   Tamara Munzner. *Visualization Analysis and Design.* AK Peters Visualization Series. CRC Press, 2015.

[PA16]   Ripon Patgiri and Arif Ahmed. Big Data: The V's of the Game Changer Paradigm. In *2016 IEEE 18th International Conference on High Performance Computing and Communications; IEEE 14th International Conference on Smart City; IEEE 2nd International Conference on Data Science and Systems (HPCC/SmartCity/DSS)*, pages 17–24, 2016.

[PJC+17]   Luis F. Alves Pereira, Eline Janssens, George D.C. Cavalcanti, Ren Tsang, Mattias Van Dael, Pieter Verboven, Bart Nicolai, and Jan Sijbers. Inline discrete tomography system: Application to agricultural product inspection. *Computers and electronics in agriculture*, 138:117–126, 2017.

[PSI17]   PSI. PSI Workshop VISA2017 on Visual Analysis of Dynamic Processes, 2017. https://www.psi.ch/visa2017.

[PWB+09]   Kristin Potter, Andrew Wilson, Peer-Timo Bremer, Dean Williams, Charles Doutriaux, Valerio Pascucci, and Chris R. Johnson. Ensemble-Vis: A Framework for the Statistical Visualization of Ensemble Data. In *2009 IEEE International Conference on Data Mining Workshops*, pages 233–240, 2009.

[RGK+13]   Andreas Reh, Christian Gusenbauer, Johann Kastner, Eduard Gröller, and Christoph Heinzl. MObjects–A Novel Method for the Visualization and Interactive Exploration of Defects in Industrial XCT Data. *IEEE Transactions on Visualization and Computer Graphics*, 19(12):2906–2915, 2013.

[RPK+12]   Andreas Reh, Bernhard Plank, Johann Kastner, Eduard Gröller, and Christoph Heinzl. Porosity Maps–Interactive exploration and visual analysis of porosity in carbon fiber reinforced polymers. *Computer Graphics Forum*, 31(3pt3):1185–1194, 2012.

[RSM+16]   Sanjin Radoš, Rainer Splechtna, Kresimir Matković, Mario Đuras, Meister Eduard Gröller, and Helwig Hauser. Towards Quantitative Visual Analytics with Structured Brushing and Linked Statistics. *Computer Graphics Forum*, 35(3):251–260, 2016.

[SG11]   Ying Sun and Marc G. Genton. Functional Boxplots. *Journal of Computational and Graphical Statistics*, 20(2):316–334, 2011.

[SHB+14]   Michael Sedlmair, Christoph Heinzl, Stefan Bruckner, Harald Piringer, and Torsten Möller. Visual parameter space analysis: A conceptual framework. *IEEE Transactions on Visualization and Computer Graphics*, 20(12):2161–2170, 2014.

[Shn96]   Ben Shneiderman. The eyes have it: A task by data type taxonomy for information visualizations. In *Visual Languages, 1996. Proceedings., IEEE Symposium on*, pages 336–343. IEEE, 1996.

[SMM12]   Michael Sedlmair, Mariah Meyer, and Tamara Munzner. Design Study Methodology: Reflections from the Trenches and the Stacks. *IEEE Transactions on Visualization and Computer Graphics*, 18(12):2431–2440, 2012.

[SN10]   Robert Schmitt and Christian Niggemann. Uncertainty in measurement for x-ray-computed tomography using calibrated work pieces. *Measurement Science and Technology*, 21(5):054008, 2010.

[SZS+17]   Dominik Sacha, Leishi Zhang, Michael Sedlmair, John A. Lee, Jaakko Peltonen, Daniel Weiskopf, Stephen C. North, and Daniel A. Keim. Visual Interaction with Dimensionality Reduction: A Structured Literature Analysis. *IEEE Transactions on Visualization and Computer Graphics*, 23(1):241–250, 2017.

[TWMSK18] Thomas Torsney-Weir, Torsten Möller, Michael Sedlmair, and Robert M. Kirby. Hypersliceplorer: Interactive visualization of shapes in multiple dimensions. *Computer Graphics Forum*, 37(3):229–240, 2018.

[TWSM+11] Thomas Torsney-Weir, Ahmed Saad, Torsten Moller, Hans-Christian Hege, Britta Weber, Jean-Marc Verbavatz, and Steven Bergner. Tuner: Principled Parameter Finding for Image Segmentation Algorithms Using Visual Response Surface Exploration. *IEEE Transactions on Visualization and Computer Graphics*, 17(12):1892–1901, 2011.

[TWSM17]   Thomas Torsney-Weir, Michael Sedlmair, and Torsten Möller. Sliceplorer: 1D slices for multi-dimensional continuous functions. *Computer Graphics Forum*, 36(3):167–177, 2017.

[Val21]   ValveSoftware.   OpenVR   GitHub   Repository,   2021. https://github.com/ValveSoftware/openvr; Online; last accessed 08.06.2021.

[WAG+16]   Johannes Weissenböck, Artem Amirkhanov, Eduard Gröller, Johann Kastner, and Christoph Heinzl. PorosityAnalyzer: Visual analysis and evaluation of segmentation pipelines to determine the porosity in fiber-reinforced polymers. In *IEEE Conference on Visual Analytics Science and Technology (VAST)*, pages 101–110, 2016.

[WAL+14]   Johannes Weissenböck, Artem Amirkhanov, Weimin Li, Andreas Reh, Alexander Amirkhanov, Eduard Gröller, Johann Kastner, and Christoph Heinzl. FiberScout: An interactive tool for exploring and analyzing fiber reinforced polymers. In *2014 IEEE Pacific Visualization Symposium*, pages 153–160, March 2014.

[Wel21]   CT   Vis   Group   Wels.   Open_ia   GitHub   Repository,   2021. https://github.com/3dct/open_iA; Online; last accessed 08.06.2021.

[WFG+19]   Johannes Weissenböck, Bernhard Fröhler, Eduard Gröller, Johann Kastner, and Christoph Heinzl. Dynamic Volume Lines: Visual comparison of 3D volumes through space-filling curves. *IEEE Transactions on Visualization and Computer Graphics*, 25(1):1040–1049, 2019.

[WFR+10]   Jürgen Waser, Raphael Fuchs, Hrvoje Ribičič, Benjamin Schindler, Günther Blöschl, and Meister Eduard Gröller. World Lines. *IEEE Transactions on Visualization and Computer Graphics*, 16(6):1458–1467, 2010.

[WHLS19]   Junpeng Wang, Subhashis Hazarika, Cheng Li, and Han-Wei Shen. Visualization and Visual Analysis of Ensemble Data: A Survey. *IEEE Transactions on Visualization and Computer Graphics*, 25(9):2853–2872, 2019.

[WMK13]   Ross T. Whitaker, Mahsa Mirzargar, and Robert M. Kirby. Contour Boxplots: A Method for Characterizing Uncertainty in Feature Sets from Simulation Ensembles. *IEEE Transactions on Visualization and Computer Graphics*, 19(12):2713–2722, 2013.

[YKSJ07]   Ji Soo Yi, Youn ah Kang, John Stasko, and J. A. Jacko. Toward a Deeper Understanding of the Role of Interaction in Information Visualization. *IEEE Transactions on Visualization and Computer Graphics*, 13(6):1224–1231, 2007.

[ZSS15]   Valentin Zobel, Markus Stommel, and Gerik Scheuermann. Feature-based tensor field visualization for fiber reinforced polymers. In *2015 IEEE Scientific Visualization Conference (SciVis)*, pages 49–56, 2015.
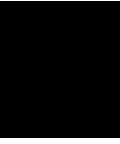
Core Publications

MObjects:
A Novel Method for the
Visualization and Interactive
Exploration of Defects in
Industrial XCT Data

Andreas Reh, Christian Gusenbauer, Johann Kastner, Eduard Gröller, Christoph Heinzl

MObjects—A Novel Method for the Visualization and Interactive Exploration of Defects in Industrial XCT Data

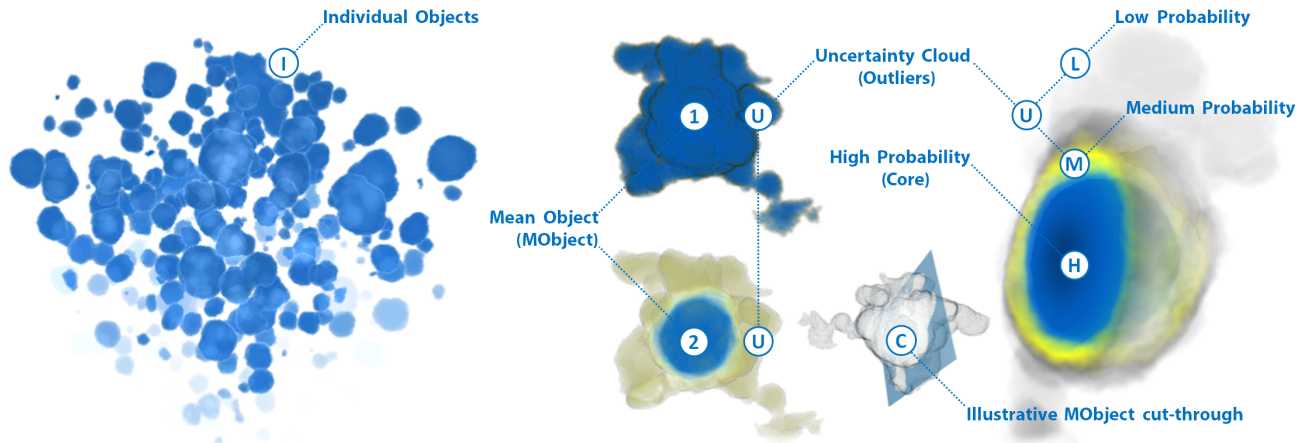Andreas Reh, Christian Gusenbauer, Johann Kastner, Eduard Gröller, and Christoph Heinzl

Fig. 1. From a set of individual objects (I) a MObject is calculated. MObjects are visualized by transfer functions based on the probability of each voxel of belonging to the MObject (1 and 2). The MObject cut-through (C) shows areas with high probability (H) in the center. Medium (M) and low (L) probabilities represent the uncertainty cloud (U) showing outliers of individual objects.

Abstract—This paper describes an advanced visualization method for the analysis of defects in industrial 3D X-Ray Computed Tomography (XCT) data. We present a novel way to explore a high number of individual objects in a dataset, e.g., pores, inclusions, particles, fibers, and cracks demonstrated on the special application area of pore extraction in carbon fiber reinforced polymers (CFRP). After calculating the individual object properties volume, dimensions and shape factors, all objects are clustered into a mean object (MObject). The resulting MObject parameter space can be explored interactively. To do so, we introduce the visualization of mean object sets (MObject Sets) in a radial and a parallel arrangement. Each MObject may be split up into sub-classes by selecting a specific property, e.g., volume or shape factor, and the desired number of classes. Applying this interactive selection iteratively leads to the intended classifications and visualizations of MObjects along the selected analysis path. Hereby the given different scaling factors of the MObjects down the analysis path are visualized through a visual linking approach. Furthermore the representative MObjects are exported as volumetric datasets to serve as input for successive calculations and simulations. In the field of porosity determination in CFRP non-destructive testing practitioners use representative MObjects to improve ultrasonic calibration curves. Representative pores also serve as input for heat conduction simulations in active thermography. For a fast overview of the pore properties in a dataset we propose a local MObjects visualization in combination with a color-coded homogeneity visualization of cells. The advantages of our novel approach are demonstrated using real world CFRP specimens. The results were evaluated through a questionnaire in order to determine the practicality of the MObjects visualization as a supportive tool for domain specialists.

Index Terms—3D X-ray computed tomography, carbon fiber reinforced polymers, porosity, parameter space analysis, MObjects

◆

1 INTRODUCTION AND MOTIVATION

Industrial research is continuously increasing efforts in designing new-tailored light-weight materials in order to meet the high demands regarding efficiency, environment, safety as well as comfort. Especially

- *Andreas Reh is with the University of Applied Sciences Upper Austria, Campus Wels, Austria. E-mail: andreas.reh@fh-wels.at.*
- *Christian Gusenbauer is with the University of Applied Sciences Upper Austria, Campus Wels, Austria. E-mail: christian.gusenbauer@fh-wels.at.*
- *Johann Kastner is with the University of Applied Sciences Upper Austria, Campus Wels, Austria. E-mail: johann.kastner@fh-wels.at.*
- *Eduard Gröller is with the Institute of Computer Graphics and Algorithms, Vienna University of Technology, Austria. E-mail: groeller@cg.tuwien.ac.at.*
- *Christoph Heinzl is with the University of Applied Sciences Upper Austria, Campus Wels, Austria. E-mail: christoph.heinzl@fh-wels.at.*

in the aeronautics industry a high demand for advanced composite materials is observable. Aircrafts of the future will be made of more than 50 % of these novel composite materials. Carbon fiber reinforced polymers (CFRPs) are currently considered as the most promising candidate since this material is outperforming the majority of conventional materials. As a result of the manufacturing process this material tends to have pores inside [25]. Pores in the material are typically inclusions of air. As they have an impact on the mechanical properties of the component, their determination and evaluation is an important task in quality control and a particular challenge for non-destructive testing (NDT) practitioners. Besides the characterization of individual pores, their spatial distribution in the tested component is a relevant factor. For example, a high concentration of pores in certain regions leads to different material characteristics as compared to a homogenous distribution of the pores.

The current state-of-the-art method for non-destructive porosity determination in aeronautics is ultrasonic testing. Characterization using ultrasonics is required by various aeronautic and automotive standards. The porosity is estimated from ultrasonic velocity and attenuation of sound waves using a calibration curve which is based on the contained
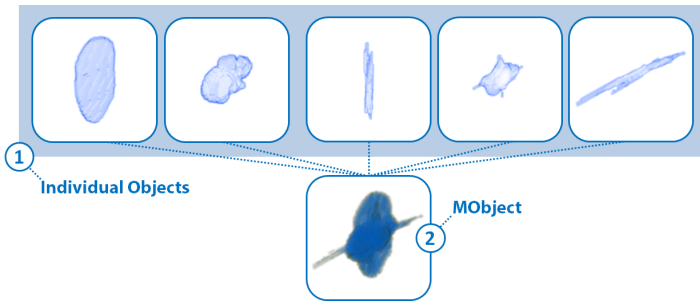
Fig. 2. Illustration of the MObject calculation showing pores of a CFRP dataset. (1) First the individual pores are spatially aligned according to their centers. (2) Second the MObject is calculated by summing up the voxels.

pores. Although the pores and their shape factors are strongly related to the manufacturing process, the same calibration curve is used for components from diverse manufacturing operations. This leads to inaccurate results. Active thermography is a complementary NDT method for porosity determination in CFRP components. For active thermography heat is induced with flashes of light and the propagation of the surface temperature is measured. As the heat propagation depends on the thermal diffusivity of the component, the heat conduction model is fundamental for the accuracy of the generated results [20]. The model is based on simulations, in which the sizes and shape factors of the pores play an important role, although they are not exactly known.

To avoid these drawbacks and to support NDT practitioners, we apply 3D X-Ray Computed Tomography (XCT). It is an NDT method with an increasing importance in the field of aeronautics. With XCT the tested component is placed on a rotary plate between an X-ray source and a detector. For a series of angular positions, 2D projection images are acquired and a 3D volumetric dataset is reconstructed. Due to the high spatial resolution, industrial XCT allows to detect a high number of pores *(individual objects)* inside. At first glance these pores have similar shapes and it is a difficult and tedious task to evaluate the data by identifying representative structures of interest in the dataset.

As a solution to this problem we introduce *mean objects (MObjects)*. The pores in the 3D dataset are examined individually (see Figure 2 (1)). To compute the MObject, the pores are spatially aligned according to their centers. The value of each voxel in the MObject is the sum of individual pores that overlap it (see Figure 2 (2)). By normalizing the MObject to 1, each voxel holds the *probability* of belonging to the MObject. Figure 1 illustrates our novel visualization approach showing individual objects (I) and the visualization with an illustrative MObject cut-through (C). A MObject is visualized by transfer functions based on the probability of each voxel in the MObject dataset (1 and 2). Areas with a high probability (H) represent the MObject *core* in the center. The surrounding medium and low probabilities (M and L) represent an *uncertainty cloud* (U) and correspond to *outliers* of individual objects. The calculated MObject of the whole dataset is then explored by a decomposition using interactive selection. The resulting set of MObjects is called *MObject Set*. With the help of the MObject Sets it is now possible to find *representative MObjects* in the dataset. For our specific application of CFRP analysis representative MObjects are structures of interest in the dataset. For example *representative mean pores* in a CFRP component are nodular and disc-shaped pores within the epoxy resin as well as long and thin micro pores in the fiber bundles. Although our approach can be used for all kinds of defects in material sciences, e.g., pores, inclusions, particles, fibers and even cracks, we will focus in this work on the evaluation of pores.

2 TASKS AND CONTRIBUTIONS

The previously introduced problem descriptions and their demands regarding material sciences lead us to the following tasks for the visualization and exploration of MObjects:

- **MObjects Visualization (Task 1):** A non-destructive testing (NDT) practitioner analyses visual representations of features or objects of interest inside a CFRP dataset regarding their individual properties, e.g., volume, dimensions, or shape factors. Due to the high number of pores the calculation and visualization of MObjects is the most important task.

- **Local MObjects Visualization (Task 2):** Besides individual pore properties, the spatial distribution of the pores is an important property of the investigated specimen. Non-destructive testing practitioners need a fast overview of the pore homogeneity. To achieve this goal, the dataset is divided into cells. For each cell a local MObject is calculated and visualized.

- **MObjects Exploration (Task 3):** Ultrasonic testing practitioners and active thermography experts are searching for MObjects as representatives of the structures of interest in the dataset. The MObjects are needed to improve the ultrasonic calibration curve and the simulations of the thermal diffusivity model. Therefore the MObject of a CFRP dataset is explored interactively.

In this paper we employ XCT to determine and visualize pores in CFRP specimens. MObjects of the segmented pores are calculated and visualized. To accomplish Task 1 - Task 3 visualization methods for the interactive exploration of MObjects are introduced. The main contributions of our work are:

- **MObjects Calculation and Visualization:** We calculate MObjects by clustering a set of individual pores. As the calculation produces probabilities for each voxel, we visualize an uncertainty cloud using transfer functions.

- **Homogeneity Visualization using Local MObjects:** For a fast homogeneity overview of the specimen we divide the dataset into regular sub-volumes. For each of these volumes we calculate a local MObject. We extend the homogeneity visualization with a color-coding of the sub-volumes regarding their individual properties.

- **Interactive Exploration of MObjects:** For the interactive exploration and visualization of pores in a CFRP dataset, we introduce two methods. In a *beginners mode* the MObjects are arranged in a radial design. All possible combinations of the user-defined properties are calculated and visualized. In the *expert mode*, the MObjects are arranged in parallel. They are constructed interactively from one level to the next in order to allow an in-depth exploration of the dataset. The resulting representative MObjects can be exported as volumetric datasets to serve as input for ultrasonic calibrations and active thermography simulations. Each voxel holds the probability of the MObject membership.

3 RELATED WORK

In our previous work [23] we introduced a drill-down approach to explore pores in a CFRP dataset. The main focus of this work was the determination of the quantitative porosity and the comparison with existing reference methods like ultrasonic testing, active thermography, and acid digestion. A fast porosity overview with the porosity maps visualization and an individual pore visualization with parallel coordinates was presented and showed satisfying results. However porosity in CFRP is still an interesting and important topic of research. Due to the possible high number of pores in the datasets, occlusions of pores may lead to evaluation problems using an individual pore visualization. We found out that analyzing the pores individually is insufficient in certain evaluation scenarios, e.g., if the mean characteristics of the pores are needed. In this paper, we developed the new MObjects approach which gives the user a fast visual overview of the average pores in the dataset. In the following sections we review the related work for our MObjects visualization and exploration pipeline.

3.1 Segmentation

The segmentation of the individual pores is an essential task. A survey on thresholding techniques by Sezgin and Sankur [24] shows the wide range of approaches and applications. All of these methods assign an object membership based on a density threshold, where no neighborhood information is taken into account. As we showed in our previous work [23] Otsu's thresholding technique [21] leads to satisfying results for industrial XCT data of CFRP specimens. It is an automatic threshold-selection method for bimodal histograms. The histogram is divided into two classes minimizing the intra-class variance and maximizing the inter-class variance. Thus the separability of the resulting classes in gray levels is maximized. As segmentation techniques are exchangeable in the presented workflow and not considered as core of this work, this area is not considered in more detail.

3.2 Parameter Space Analysis

The resulting set of segmented pores together with their properties like the volume, dimensions, and shape factors make up a new parameter space, which has to be explored *(MObjects Exploration - Task 3)*. A broad range of methods and applications for parameter space analysis exists. Design galleries by Marks et al. [19] present an interface with an automatically generated selection of different graphics or animations. These can be produced by varying the input parameters, e.g., opacity and color transfer functions for volume rendering. Ma [17] introduces Image Graphs, where the nodes in the graphs show result images. Each edge depicts the change of the rendering parameters between its connected nodes. Changes in the rendering parameters propagate through the graph. Bruckner and Möller [7] developed a system to assist graphics artists in generating special effects, e.g., smoke or explosions. Their visual exploration approach of the parameter spaces allows the user to find the appropriate parameters for the desired results. Torsney-Weir et al. [26] introduced Tuner, a system for parameter finding in image segmentation. Tuner systematically explores the parameter space in two stages. After sampling the parameter space, a statistical model for the estimation of the segmentation algorithm's response is applied. Based on this information the user can navigate through the parameter space to find areas with high response values. Amirkhanov et al. [2] presented a tool for the visual optimality and stability analysis of 3DCT specimen placements. For parameter space analysis a stability widget based on penetration-length calculation, radon-space analysis as well as placement-stability analysis is used. Another approach by Bruckner et al. [8] is realized in the BrainGazer software. The system is used for the exploration and analysis of neural circuits. Visual queries based on semantic and spatial relationships are applied to a database of fruit-fly brains. Berger et al. [5] presented an interactive approach to analyze a sampled parameter space. Other interesting papers concerning our work are available as well [28], [27] and [3].

3.3 Clustering

By calculating MObjects, we identify and group similar individual objects with respect to one of their properties. Therefore a cluster algorithm is used. Xu published a detailed survey on clustering algorithms [29]. We let the user decide on the number of clusters, e.g., a norm specifies the number of partitions which have to be made in an evaluation scenario. As the clustering algorithm is easily replaceable, simple k-means is taken for our approach of clustering individual objects. Clustering itself is considered to be out of scope for this work and is not discussed in more detail.

3.4 Hierarchical Visualization

The calculation of MObjects is based on the composition and decomposition of mean and individual objects. This leads us to hierarchical visualizations for the interactive exploration of the MObjects *(MObjects Exploration - Task 3)*. A combination of hierarchy visualization and scientific visualization was presented by Balabanian et al. [4]. Their method integrates visualizations for hierarchically organized volumetric datasets. A graph shows the hierarchy and the nodes display the corresponding 3D volumetric data. Brambilla et al. [6] introduced a hierarchical splitting scheme for the analysis of integral

surfaces. At each hierarchy level the cuts are chosen according to a surface complexity metric. Ip et al. [13] partition the histogram of a volumetric dataset into an exploration hierarchy using a normalized-cut multilevel segmentation approach. Inspired by these techniques, we introduce our MObject Set visualization. After a decomposition of the dataset's MObject, the user is able to explore the data in a graph, where the nodes show 3D representations of the MObjects.

3.5 Uncertainty Visualization

We calculate a new volumetric MObject dataset by aggregating individual objects of one cluster. Each voxel holds the probability of belonging to the newly generated MObject. These probabilities as well as the regions with elevated uncertainty are visualized *(MObjects Visualization - Task 1)*. Kniss et al. [14] present an approach for the interactive exploration of uncertainty including a risk and decision analysis. They render the results of the risk analysis into a unified probabilistic data space. As MObjects are aggregated from all considered individual objects, the approach by Kniss et al. [14] is not suitable for our visualization. Point-based probabilistic surfaces were introduced by Grigoryan and Rheingans [10]. They visualize surfaces with uncertainties using points as display primitives. Although their approach is useful for visualizing uncertainty on surfaces, we can not apply it to our data. Fout and Ma [9] present fuzzy volume rendering. By computing the posteriori uncertainty they provide a verifiable volume rendering. Heinzl et al. [11] compute a probability volume of multi-material components using a statistical analysis. Similarly we provide insight into the MObjects' data to show the core and the outliers. We also use transfer functions emphasizing a user-defined border of probability. They are suitable for visualizing the a priori-based uncertainty of an MObject.

3.6 Comparative Visualization

The issue of visualizing the pore homogeneity in the dataset *(Local MObjects Visualization - Task 2)* leads us to comparative visualization. Malik et al. [18] refer to a wide range of comparative visualization approaches. Additionally they propose a base tile pattern for a multi-image view for comparative visualization, which is an extension of the checkerboard-pattern approach and attribute blocks. Malik et al. compare 2D slices of volumetric datasets with different measurement parameters. Ahrens et al. [1] visualize differences between scientific simulations. These methods are not applicable to our segmented pores data. We divide the dataset into cells and calculate local MObjects for each cell. Furthermore we add a homogeneity visualization, where we color-code the cells based on the deviation of the local average from the global average.

3.7 Visualization of Multivariate Data

Parallel coordinates introduced by Inselberg [12] are a common visualization approach for displaying and filtering multivariate data. Kosara et al. [15] extended parallel coordinates and presented parallel sets for dealing with categorical data. Instead of individual data points, they show data frequencies between the axes and visualize the relations between categories. StratomeX by Lex et al. [16] was inspired by parallel sets, where datasets of genomic data are represented as columns and subtypes as bricks in the columns. Our MObject Set visualization in parallel alignment was inspired by these techniques *(MObjects Exploration - Task 3)*. Parallel coordinates can serve as classifiers for the selection of individual pores and parallel sets share the idea of clustered objects. Due to the usage of categories, both approaches are not applicable to volumetric datasets. They do not visualize the spatial relationship between as well as the appearance of the objects.

4 MObjects Visualization and Exploration Pipeline

In our work we want to identify representative structures of interest in an XCT dataset, e.g., pores in a CFRP component. We propose a pipeline for the visualization and interactive exploration of MObjects which is illustrated in Figure 3. In the data acquisition stage (1) 3D X-Ray Computed Tomography (XCT) data is generated (see Section 4.1). On the resulting volumetric dataset pre-processing steps (2), described
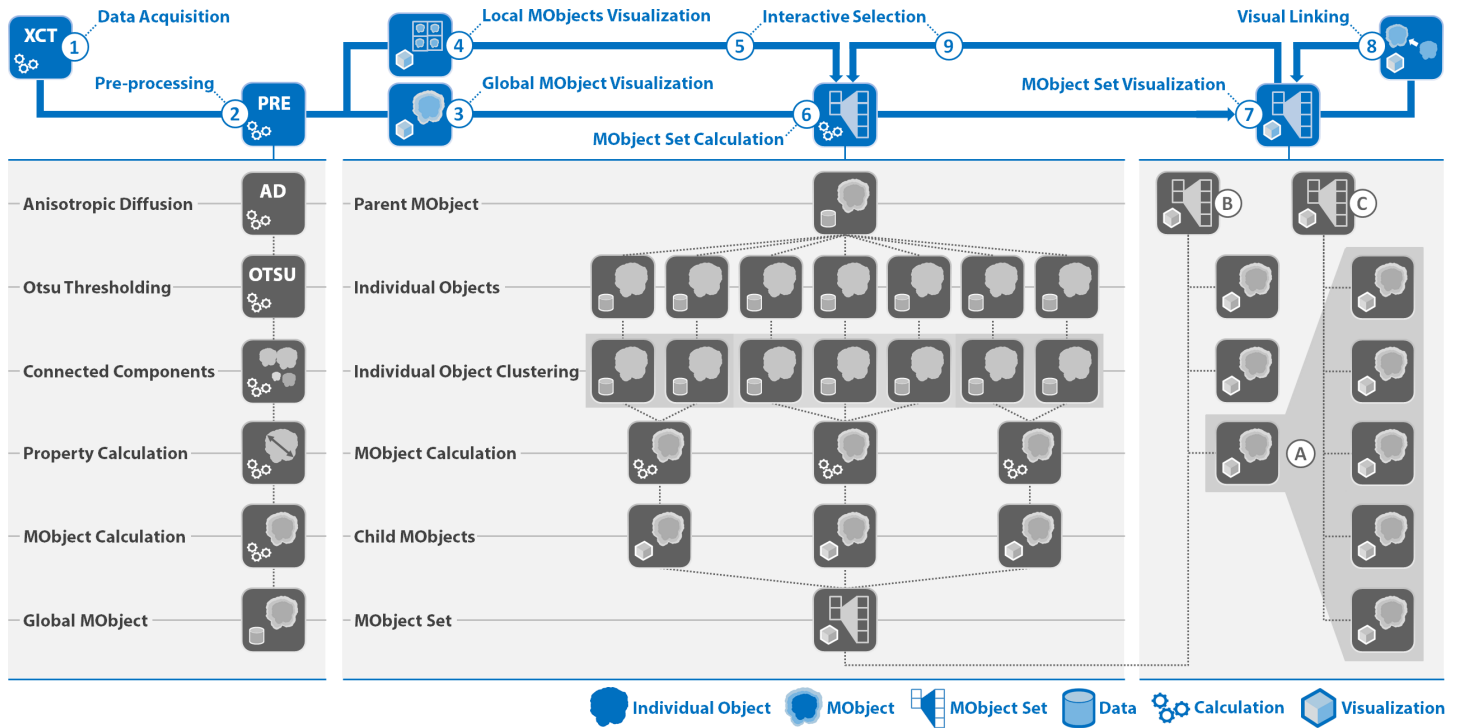
Fig. 3. Pipeline for the visualization and interactive exploration of MObjects in a dataset. The main pipeline is colored in blue, whereas the detailed steps are shown in gray.

in Section 4.2, are performed to calculate the resulting global MObject of the dataset. This MObject is considered as mean pore and represents the aggregation of all pores in the component. For further visualization of the MObject we propose two methods. In our first approach, the global MObjects visualization (3), the global MObject serves as input for further exploration. For a fast overview of the dataset we suggest a local MObjects visualization (4). The dataset is divided into cells and for each cell a local MObject is calculated and shown in combination with a color-coded homogeneity visualization. Through interactive selection (5) the subsequent exploration starts with one of the local MObjects instead of the global one.

All the individual objects in the MObject of interest are then clustered in the MObject Set calculation (6). The parent MObject is further subdivided into new child MObjects based on one of their calculated properties. For example the parent MObject is classified into two child MObjects based on the shape factors of the pores. The first MObject only contains nodular pores, whereas the second one consists of long and thin pores. The user is then able to interact with the resulting MObject Set visualization (7). Through visual linking (8) or interactive selection (9) an iterative calculation and visualization of the MObject Sets will be triggered upon each major change in the classification. By selecting a MObject (A) in a MObject Set (B) a new MObject Set (C) consisting of new child MObjects can be calculated from the selected parent MObject (A).

4.1 Data Acquisition

In this work, we use carbon fiber reinforced polymers (CFRP) specimens made of preimpregnated carbon fibers and epoxy resin. For the investigations plates with a size of 17 x 20 x 1 mm^3 were used. The voxel size of the datasets was 10.5 µm. The XCT scans were performed on a GE Phoenix|xray nanotom XCT system with a 180 kV nano focus tube. A tube voltage of 60 kV, a measurement current of 320 µA, and 500 ms integration time at the detector were used as scan parameters. Over-segmentation in the middle of the specimens may occur due to gray value modifications caused by beam hardening during the measurement. Therefore a beam hardening correction was applied during the reconstruction.

4.2 Pre-processing

Due to ambient noise in the scanned datasets, we apply *anisotropic diffusion* as described by Perona and Malik [22] for filtering the data. Anisotropic diffusion smoothes homogenous regions while preserving the edges. We use five iterations with a conductance of one and a time step of 0.0625 seconds. The *segmentation* of pores is done with the automatic threshold selection method for bimodal histograms by Otsu [21]. For the individual property calculation the objects are labeled after the segmentation by a *connected-components filter* using 26-connectivity neighborhoods. With the labeled objects we proceed through an individual *property calculation* stage which is the basis for our MObjects determination. A pore consists of a set of voxels within a regular volumetric grid. To enable interactive exploration and classification of objects the following properties for each individual pore are calculated:

- **Pore volume V_i:** The volume V_i of a pore i is the sum of all voxels in the dataset with the same label.

- **Dimensions a_i, b_i, c_i:** To calculate the extent of the pore along the x, y and z coordinate axes we perform the calculation on the discretized pore. For the extent along the x axis we determine the two voxels with minimal and maximal x coordinate values respectively. The extents a_i, b_i, c_i are then the differences between the maximal and minimal coordinates along the x, y and z axes of pore i.

- **Shape factor F_i:** The shape factor F_i of a pore i is defined as the ratio between the pore surface S_i and the pore volume V_i.

- **Directional shape factors $F_{(x/z)_i}, F_{(y/z)_i}, F_{(x/y)_i}$:** Mayr et al. [20] define the shape factors of typical ellipsoidal pores for each direction in space as follows: $F_{(x/z)_i} = a_i/c_i, F_{(y/z)_i} = b_i/c_i$ and $F_{(x/y)_i} = a_i/b_i$.

On the basis of these properties a MObject of the whole dataset is calculated in order to explore and visualize representative MObjects in a dataset.

5 VISUALIZATION

We introduce novel methods for the visualization and interactive exploration of MObjects which are based on a set of individual objects in a dataset. Besides the calculation and visualization of MObjects (see Section 5.1) we propose a homogeneity visualization of the dataset. It uses local MObjects and a color-coding of the grid-based sub-volumes. The approach is based on the deviation of average individual properties, e.g., the average pore volume in a cell (see Section 5.2). To explore MObjects we present two visualization approaches in Section 5.3 which use MObject Sets in radial and parallel arrangement. Furthermore we discuss interaction techniques for these two methods including visual linking.

5.1 MObject Visualization

For the visualization of a single MObject we introduce an uncertainty cloud surrounding the MObject core (see Section 5.1.1). We used transfer functions which are described in more detail in Section 5.1.2. To calculate a MObject all individual objects are spatially aligned by their centers. The center position can be calculated from the dimensions a_i, b_i, c_i of the individual objects or the barycenter of each individual object can be used. Both methods showed similar results for pores in CFRP datasets as pores typically have nodular, disc, or long and elongated shapes. In order to avoid additional calculations, we decided to use the dimension-based approach. When transferring the MObjects idea to other application areas, the centroid calculation has to be reconsidered according to the specific requirements. Although it is possible to rotate and register all individual objects in the calculation, we align them with their original orientation. This transformation without a rotation is important in the specific application area of CFRP analysis which we address in this work. Due to the layer structure of the material the MObject should clearly visualize the different orientations of the individual objects. For each voxel in the individual object dataset, the distances $\Delta x, \Delta y$ and Δz to the center are calculated. After the distance calculation for one voxel, the corresponding voxel in the MObject with the same distances $\Delta x, \Delta y$ and Δz to the center of the MObject is incremented. This step is done for each voxel of each individual object. To get the corresponding probabilities the resulting MObject dataset is normalized to 1.

5.1.1 Uncertainty Cloud

A MObject is a volumetric dataset, where each voxel holds the probability of belonging to the MObject. This information has to be visualized accordingly. We visualize an uncertainty cloud surrounding the MObject's core. Uncertainty cloud and core are based on the stored probabilities. A high probability at a specific position means
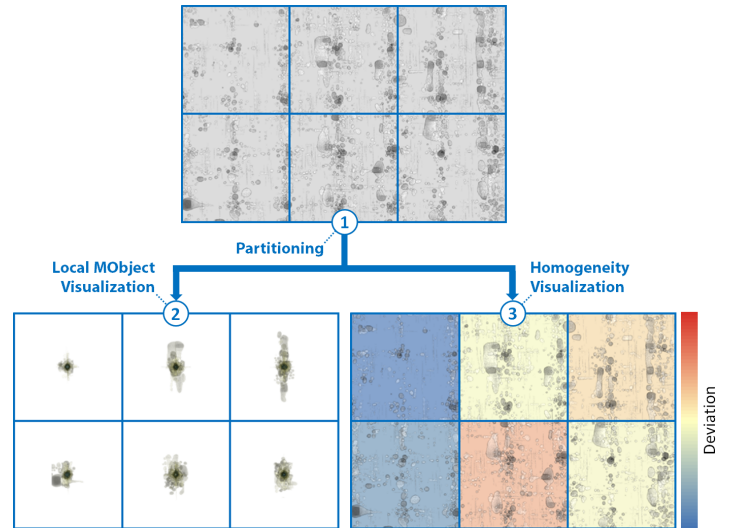
Fig. 5. Based on the partitioning (1) of the volume into cells, local MObjects (2) and a color-coded homogeneity visualization (3) is shown to the user. The color-coding illustrates the deviation of the average cell properties from the global average property. Red indicates the highest positive deviation, whereas blue shows the highest negative deviation.

that nearly all of the individual objects which were summed up to the MObject, include this location. In Figure 1 the uncertainty cloud (U) is illustrated. The probability in the core of the MObject is typically high (H). As the contribution of outliers to the MObject is low, they have a medium (M) or low (L) probability of belonging to the MObject.

5.1.2 Transfer Function Design

The uncertainty cloud is visualized using transfer functions. We apply colors for high probabilities (blue) to medium (yellow) and low probabilities (gray). Yellow-grey thus shows the outliers (see Figure 4). The step between high (blue) and medium (yellow) probabilities shows the membership of belonging either to the core or the outliers of the MObject. For the interactive visualization and adaptability to different applications, the user steers this visualization by an uncertainty filter σ. Figure 4 shows how the gray-yellow-blue gradient is shifted in the transfer function based on σ. Setting a low uncertainty filter, leads to a small uncertainty cloud and a visualization strongly representing the surface of the MObject (1). In the case of using a high uncertainty filter, one can clearly determine the core of the MObject and see the surrounding outliers (2). To emphasize the uncertainty cloud, we apply a lower opacity value at the position of σ in the transfer function.

5.2 Local MObjects Visualization

Pore homogeneity is an important criterion in material sciences. We already covered this topic with our porosity maps visualizing the porosity in a CFRP specimen [23]. As the homogeneity of the different pore properties is also helpful to find interesting regions for a further detailed analysis, this information has to be visualized in an easy to understand and intuitive way. We propose a homogeneity visualization using local MObjects and a comparative homogeneity visualization with color-coded cells. Figure 5 describes our approach in more detail. First the volumetric dataset is partitioned into sub-volumes (1). We refer to them as cells. The cell size depends on the biggest pore extents in the dataset as it should fit in a cell without overlapping. Based on this partitioning we implement two visualizations to convey homogeneity to the user. In our first method we visualize local MObjects (2). For each cell a MObject is calculated and centered in the cell. All pores whose centers are inside the cell are considered. The same transfer function is used for all local MObjects.

In our second approach the average pore properties and their deviations to the global average properties of the whole dataset are calcu-
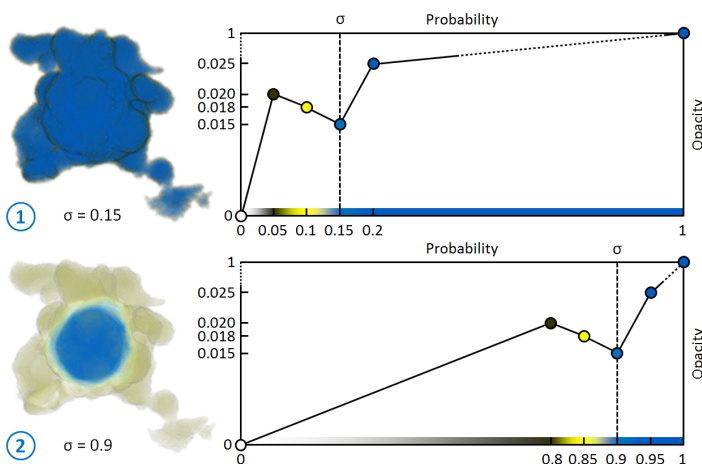

Fig. 4. (1) MObject showing a small uncertainty cloud using a low uncertainty filter $\sigma = 0.15$. (2) A high uncertainty filter $\sigma = 0.9$ leads to an uncertainty cloud showing the MObject's core and outliers.
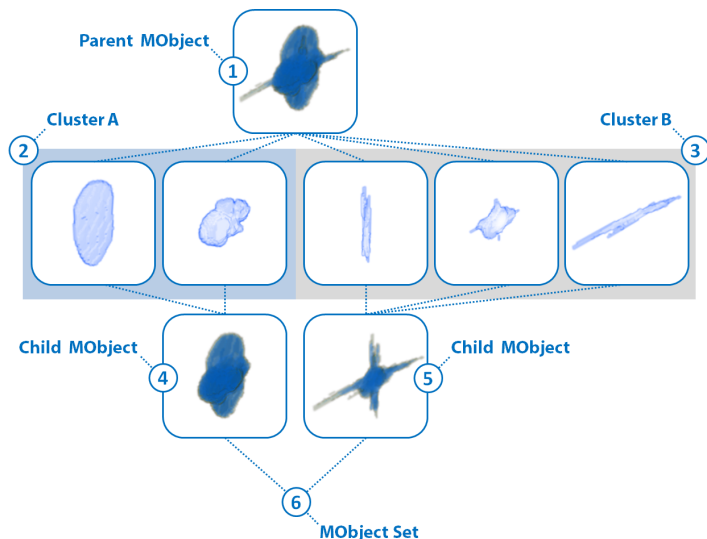
Fig. 6. Illustration of the MObject Set calculation showing pores of a CFRP dataset. All individual pores of the parent MObject (1) are divided into two clusters A (2) and B (3). The resulting child MObjects (4 and 5) make up a new MObject Set (6).

lated. The user is able to guide this comparative homogeneity visualization by selecting a property. Each cell is colored according to its deviation from the selected global property (3). For color-coding the cells we apply a diverging colormap from blue over yellow to red to show the negative and positive deviation of the average cell properties from the global average property of the specimen.

5.3 MObject Set Visualization

For the interactive exploration of MObjects in a dataset we provide a visual representation to the user. A parent MObject can be divided into a set of child MObjects which together make up a new MObject Set. All individual objects which belong to the parent MObject are clustered based on one of the calculated properties. For each cluster a new child MObject is calculated. The child MObjects together form a new MObject Set. The MObject Set may be explored interactively with a recursive selection and decomposition of the included child MObjects. Figure 6 illustrates this process using individual pores of a CFRP dataset. The parent MObject (1) is split up into the contained individual objects. First, these individual objects are clustered according to their shape factors into two clusters A (2) and B (3). Second, all in-

dividual objects in a cluster are aggregated to new child MObjects (4 and 5). These child MObjects make up a new MObject Set (6). For the clustering we provide two possibilities to the user:

- **Automatic Clustering:** The automatic clustering mode uses k-means clustering to assign the individual objects to classes. All the individual objects are classified into k clusters where each individual object belongs to the cluster with the closest mean. The user decides on the number k of clusters and which object property should be used for clustering.

- **User-defined Clustering:** If the user wants to select the cluster centers by himself, it is possible to override the automatic clustering. One reason may be that specific domain expert knowledge from previous analyses or a norm specifies the clustering for a certain property. In this case the user is able to modify the clustering done by the automatic approach using a simple dialog.

After clustering according to a certain property, a child MObject is calculated for each cluster out of all individual objects that belong to it. For the MObject Set visualization we propose then two modes. Section 5.3.1 describes the beginners mode where we introduce the radial MObject Set visualization. The expert mode with the parallel MObject Set visualization is described in Section 5.3.2.

5.3.1 Radial MObject Set Visualization (Beginners Mode)

For inexperienced users, setting the number of classes for clustering and specifying the sequence in which the properties shall be explored can be a challenging task. To give a better overview of the data and the resulting MObjects we provide a beginners mode for an interactive exploration of MObjects. Figure 7 (A) illustrates the MObject Set visualization in a radial arrangement. In most evaluation scenarios two properties are sufficient (e.g., pore volume and shape factor). The user selects the number of classes and the desired properties for the MObject Set calculations. The radial design allows to render all possible combinations between the properties (A-1) and (A-2) and not only one at a time (see parallel MObject Set visualization in Section 5.3.2). Based on this visualization, parameters for the expert mode can be found more easily. It further reduces the error rate of selecting undesired MObjects while exploring the data. Through interactive selection (A-3) the user is able to switch to the expert mode. There the MObject Sets (A-4) and (A-5) are displayed in parallel arrangement, according to the previously selected path.

5.3.2 Parallel MObject Set Visualization (Expert Mode)

The before described radial MObject Set visualization (see Section 5.3.1) leads to a fixed classification of the individual objects. Experienced users want to cluster the pores based on their properties in a
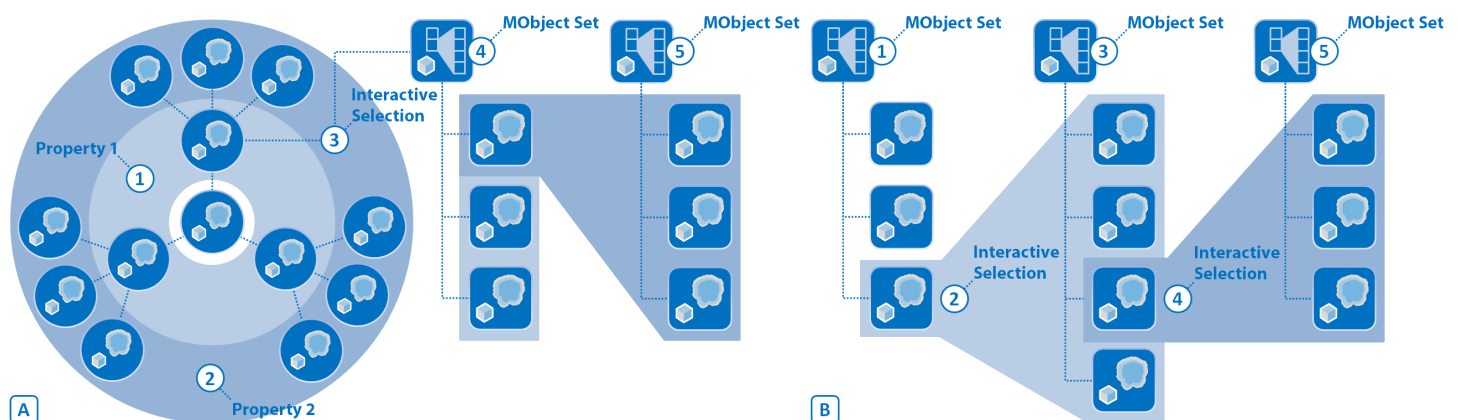

Fig. 7. (A) The radial MObject Set visualization shows all possible combinations between the properties (A-1 and A-2). (A-3) The user is able to switch to parallel alignment which shows MObject Sets (A-4 and A-5) along the selected path. (B) Parallel MObject Set visualization for a step by step exploration. MObject Sets (B-1, B-3 and B-5) are calculated and visualized after interactive selections (B-2 and B-4).

sequence that best fits their needs to extract the MObjects of interest. This sequence of properties may be different from case to case. To support this situation we present the parallel MObject Set visualization which is illustrated in Figure 7 (B). MObject Sets are calculated and visualized after interactive selections. All individual objects of the dataset are clustered based on a property and a user-defined number of clusters, e.g., three shape factor classes. The resulting MObjects are shown in a MObject Set (B-1). Through interactive selection of a MObject (B-2), the user is able to iteratively repeat the before described step of MObject Set calculation to explore the selected MObject. As a result a new child MObject Set (B-3) is calculated and visualized. As one would commonly use different properties as cluster criteria, it is possible to repeat the interactive selection step (B-4) to calculate another MObject Set (B-5) and finally explore the whole dataset to find the desired MObjects.

5.3.3 Scaling through Visual Linking

In our visualization all MObjects are rendered in individual frames of the same size. The MObjects are scaled to best fit their corresponding rendering frame. Our visual linking approach connects all MObjects along the selection path so that it becomes obvious where a child MObject is located inside the parent MObject. Furthermore the scaling of a considered MObject in the hierarchical relationship is represented. To do so, the transfer function for all MObjects except the selected MObject in the visualization is changed in a way, that only the surfaces of the MObjects are shown in grey with a high opacity. The selected MObject is then shown in all MObjects along the selection path. Figure 8 illustrates this approach using a parallel MObject Set visualization with two MObject Sets (A) and (B). When selecting a child MObject (1) visual linking shows the selected MObject inside the parent MObject (2) of the parent MObject Set (B).

6 RESULTS AND EVALUATION

The initial design of the MObjects visualization is motivated by a high demand of material characterizations in the aeronautics industry. Especially carbon fiber reinforced polymers (CFRP) show a great potential because of their increased stiffness and strength-to-weight ratio. As a result of the manufacturing process, CFRP tends to have pores inside. They can occur as nodular pores or crack-shaped delaminations in the epoxy resin or as long and thin micro pores inside the fiber bundles. In the following sections we show the local MObjects visualization including the color-coded homogeneity visualization (see Section 6.1) as well as the radial (see Section 6.2) and parallel (see Section 6.3) MObject Set visualization to explore a high number of individual pores. For the further evaluation we gathered user feedback from domain specialists through a questionnaire (see Section 6.4). The results show a CFRP dataset with a size of 1800 x 1600 x 100 voxel and a porosity of 1.94 %. The computational time including all preprocessing stages, the calculation of the global MObject and the local
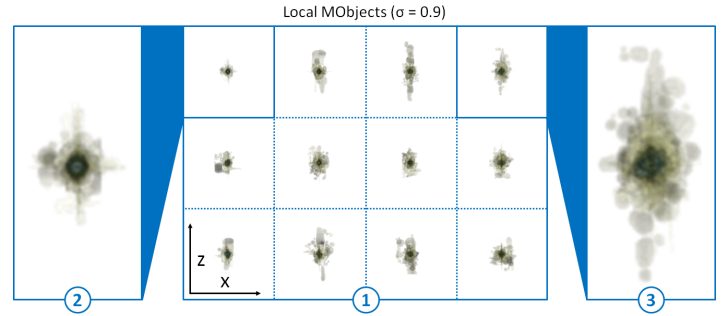

Fig. 9. (1) Local MObjects visualization using a high uncertainty filter $\sigma = 0.9$. (2 and 3) Enlarged visualization of two MObjects.

MObjects as well as the cell calculations for the color-coded homogeneity visualization was about 17 minutes on an Intel Xeon X5680 workstation with 48 GB RAM. We have integrated the pipeline in our framework iAnalyse. The MObject calculation and visualization stages are still non-optimized prototypes. As these prototypes are suitable to test the acceptability of our approach using real-world components, the major focus was not the optimization at this stage of the development. With reduced calculation times due to optimization we expect to be in the range of 1 minute and below which is acceptable in this application area.

6.1 Local MObjects Visualization

In our local MObjects visualization the CFRP dataset is partitioned into a 4 x 3 grid of cells. The number of rows and columns in the grid is calculated automatically depending on the biggest pore extents in the dataset. We ensure that the MObjects fit into the cells without overlapping. For each cell a local MObject is calculated and shown to the user (see Figure 9 (1)). The MObjects can be visualized using different uncertainty filters, e.g., $\sigma = 0.9$. Figure 9 (2 and 3) shows two enlarged MObjects from (1). As the MObjects' cores look similar, there is a homogenous distribution of small individual pores over the dataset in x direction, whereas big individual pores can be seen as outliers in (3). These outliers lead to an inhomogeneous porosity distribution in the specimen. Based on the given partitioning the user can switch to the comparative homogeneity visualization with color-coded cells as shown in Figure 10. Without coloring the cells (1) it is
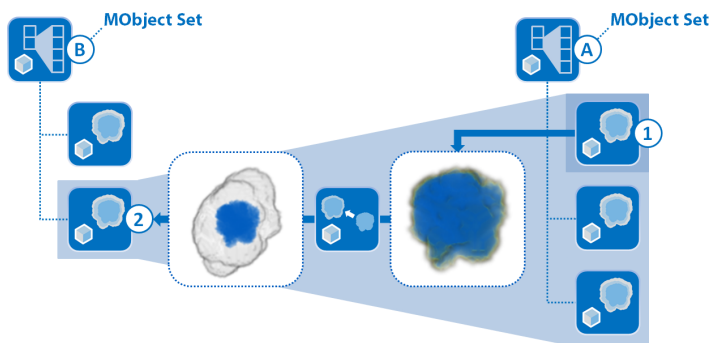

Fig. 8. Illustration of the visual linking approach. After selecting a MObject (1) in a MObject Set (A), visual linking shows the selected child MObject inside the parent MObject (2) of the parent MObject Set (B).
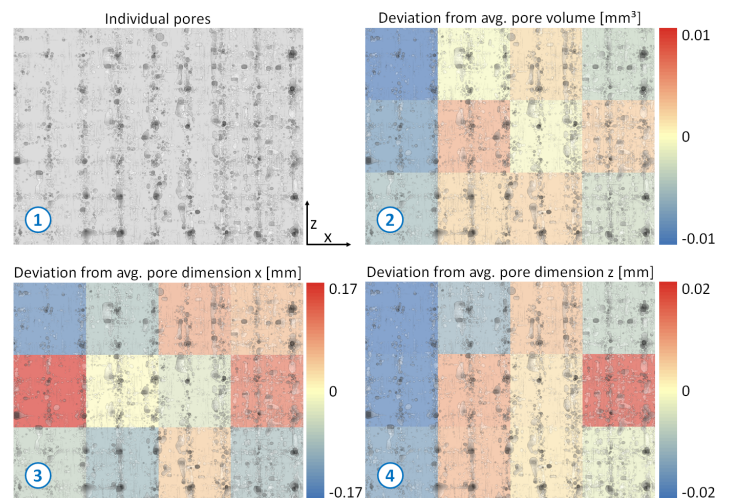

Fig. 10. (1) Visualization of the CFRP dataset. Homogeneity visualization of the deviation from the average pore (2) volume, (3) dimension x, and (4) dimension z in a 4 x 3 grid showing the CFRP dataset in the background.
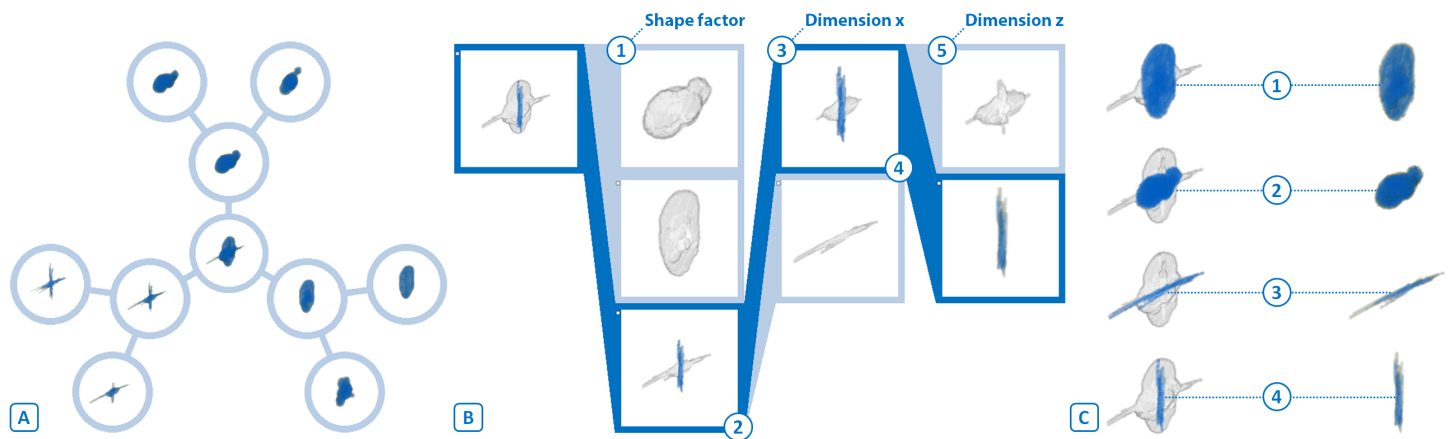
Fig. 11. (A) Radial MObject Set visualization of a CFRP dataset showing combinations of the properties shape factor and volume. (B) Parallel MObject Set visualization of a CFRP dataset showing the selected path and visual linking. (C) Representative mean pores of a CFRP dataset showing the visual linking visualization (left column) and the MObjects (right column). (C-1 and C-2) Nodular and disc-shaped pores. (C-3 and C-4) Long and thin micro pores in x and z direction.

hard to gain information about the pore homogeneity. By applying the color-coding, the user is able to see the homogeneity of one property. Our visualization shows the deviation of the average pore volume (2), dimension x (3), and dimension z (4) from the corresponding average global property. Further properties we can show are the shape factor and the dimension in y direction. Blue colors show a high negative deviation whereas red indicates a high positive deviation. In this example the homogeneity regarding the pore volume is particularly interesting. A trend can be seen, where in the left part of the specimen the average pore volume is significantly lower (2). Related to active thermography calculations, the homogeneity of the pore dimensions in x and z direction is of interest. Especially the homogeneity of the dimension in x direction (3) shows cells with a high deviation with respect to each other. For the homogeneity of the dimension in z direction (4) lower values in the left part of the specimen are visualized similar to the pore volume deviation.

6.2 Radial MObject Set Visualization

In the beginners mode the MObject Sets are arranged in a radial layout. The user can select the desired properties and the number of classes for the MObject Set calculations. The resulting visualization allows the user to see all possible combinations between the properties to get a better overview of the data and the resulting MObjects. Figure 11 (A) shows the radial MObject Set visualization for a CFRP dataset. The MObject of the whole dataset is shown in the center of the radial arrangement. The inner circle shows the MObject classifications based on three shape factor sub-classes. Each of these sub-classes is split up into two sub-classes according to pore volume. Hence all possible combinations of pore shape factor and volume are visualized in one view. Based on this information the user is able to draw conclusions about the individual pores. Using this detailed pore overview, it is easier to parameterize the expert mode (see Section 6.3).

6.3 Parallel MObject Set Visualization

The parallel MObject Set visualization shows MObject Sets in a parallel arrangement. The user can interactively explore the MObjects. The results of a CFRP dataset are depicted in Figure 11 (B) using visual linking. First the parent MObject is split into three user-defined shape factor classes (B-1). The three MObjects make up a new MObject Set. After the selection of the last MObject in this set (B-2), it is split into two classes based on the dimension in x direction (B-3). This step allows to separate the cross-shaped long and thin micro pores. Finally, the first class of the new MObject Set (B-4) is split into two classes based on the dimension in z direction (B-5). We used the parallel MObject Set visualization to find the representative mean pores in the CFRP dataset (see Figure 11 (C)). As a result of the manufacturing

process nodular and disc-shaped pores propagate in the epoxy resin (C-1) and (C-2). Long and thin micro pores occur in x and z direction due to the twill-weave pattern of the fiber layers (C-3) and (C-4).

6.4 Evaluation Questionnaire

For the evaluation, a questionnaire (see Table 1) was answered by 12 respondents of which make up two groups. The first group consists of domain experts of a company manufacturing aircraft components, including non-destructive testing (NDT) practitioners and various engineers of the CFRP production process. They use our visualizations for gaining new insights into their components in order to draw conclusions about the manufacturing process (*MObjects Visualization - Task 1*). Furthermore the domain experts use the MObject Set visualization to explore the pores. The resulting representative mean pores are used to improve ultrasonic calibration (*MObjects Exploration - Task 3*).

The second group of respondents consists of active thermography domain experts. They have a strong demand for a better understanding of the different pores in a CFRP component. Currently geometric primitives are used for mathematical simulations of a heat conduction model. Based on the MObjects exploration and the resulting representative MObjects, the domain experts take the mean pores of a real dataset as input for the heat conduction simulations. As their method

Table 1. Summary of the Evaluation Questionnaire

Task 1	Identification of deviating (not nodular) structures	
	in a 3D rendering	−
	in a MObject visualization	±
Task 2	Pore homogeneity identification of the dataset	
	in the individual pores visualization	∓
	in the local MObjects visualization	±
	in the color-coded homogeneity visualization	+
	Pore homogeneity identification in the cells	
	in the individual pores visualization	−
	in the local MObjects visualization	±
	in the color-coded homogeneity visualization	○
Task 3	Identification of the selected path and the different scalings through visual linking in a parallel MObject Set visualization	+
	Identification of representative pore classifications	
	in a 3D rendering	∓
	in a MObject visualization	+
	− poor, ∓ fair, ○ average, ± very good, + excellent	

assumes a homogenous distribution of the pores, the homogeneity visualization of the different pore properties is important *(Local MObjects Visualization - Task 2)*. These new possibilities aim to improve the simulations and finally the active-thermography method. The reference methods ultrasonic testing and active thermography only provide 2D images with lower resolutions. Due to the missing 3D information, we were not able to directly compare the MObjects visualization to existing NDT methods. As the common XCT visualization is a 3D rendering of the dataset, we compare our MObject visualizations to 3D renderings of segmented pores instead. Until now there has not been an averaging approach available to visually explore the characteristics of defects in XCT datasets in 3D.

The questionnaire focuses on the evaluation of the three tasks concerning the MObjects visualization *(MObjects Visualization - Task 1)*, the homogeneity visualization *(Local MObjects Visualization - Task 2)*, and the MObjects exploration and extraction of representative MObjects *(MObjects Exploration - Task 3)* in a dataset. A summary of the evaluation-questionnaire results is shown in Table 1.

MObjects Visualization (Task 1): Regarding the MObject visualization, the experts were shown 3D renderings of individual objects in isometric and xz views as well as 3D renderings of the corresponding MObject visualizations. Two different transfer function settings influence the visual depiction of the uncertainty cloud. In the questionnaire the respondents were asked whether they can identify deviating structures in the visualizations. As the used dataset mainly contains nodular pores, apart from a few elongated objects with a different shape factor, the respondents were asked to identify deviating structures like non-nodular outliers. The feedback confirms, that it is easier to find deviating structures in the MObject visualizations than in the 3D renderings showing the individual objects. This is due to the occlusion of the individual objects, so that deviating structures are hardly or not at all seen in a 3D rendering. Considering the answers about the different transfer function settings in the MObject visualizations, a slight trend is recognizable. Although the outliers can be clearly seen in both MObject visualizations ($\sigma = 0.15$ and $\sigma = 0.9$), due to perceptional reasons the respondents prefer a setting where the uncertainty cloud clearly separates the core from the outliers ($\sigma = 0.9$).

Local MObjects Visualization (Task 2): To evaluate the local MObjects visualization, we compared the visualization of segmented pores in a CFRP dataset, the corresponding visualization of local MObjects in a 4 x 3 grid, and the color-coded homogeneity visualization of the same dataset. The task for the respondents was to find the cells with lowest, highest positive and highest negative deviation of the pore properties in the segmented pores and the color-coded homogeneity visualization. It was nearly impossible for the participants to see the pore homogeneity in the segmented pores visualization whereas they were able to properly classify all cells in the color-coded homogeneity visualization. Regarding the local MObjects visualization the respondents were asked to find the MObjects with lowest and highest average pore properties in the dataset as well as the lowest and highest pore homogeneity in the cells. Generally the respondents judged our local MObjects visualization positively for perceiving the pore homogeneity inside the cells. To convey the pore homogeneity of the whole dataset across all the cells the color-coded homogeneity visualization was rated as a highly helpful visualization. Especially active thermography experts gain new homogeneity information out of our visualization to evaluate and evolve their method.

MObjects Exploration (Task 3): Another part of the questionnaire addressed the interactive MObjects exploration approach. The respondents rated as high the need of the exploration to find nodular, long and thin as well as crack-shaped objects. Furthermore they agreed that the classifications based on the pore volume, the dimensions and the shape factors are very interesting. There is a slight preference to take the shape factors as the most important property. For each property the experts typically split up a MObject into two to five sub-classes. All respondents were able to identify the selected path in a MObject Set visualization. The visual linking approach was positively received, as it allows to see the different scalings of the different MObjects along

the selected path. The last aspect of the evaluation comprises the exploration of representative mean pores in a CFRP dataset. The respondents were shown a 3D rendering of segmented pores in a CFRP specimen and the corresponding MObject visualization. They were hardly able to identify nodular, long and thin micro pores as well as cracks in the rendering of the segmented pores. On the other hand they positively valued the MObject visualization where it was easy for them to identify the different pore classifications. Furthermore we showed the respondents renderings of MObjects with different pore classifications. These were found with the MObjects exploration approach. The respondents agreed that the MObjects convey the typical pore structures in a CFRP dataset.

Further Feedback: NDT practitioners mentioned that the MObjects visualization may have considerable practical relevance in future inline XCT systems for 100 % testing in quality control. An automatic MObject evaluation tool may single out components with critical defects.

7 CONCLUSIONS AND FUTURE WORK

A novel method for the visualization and interactive exploration of MObjects was presented. We calculate MObjects from a set of individual objects and visualize them by applying transfer functions. As the MObjects dataset stores probabilities, the transfer function design is guided by a user-defined uncertainty filter. The approach includes the visualization of pore homogeneities as well. Local MObjects are visualized on a regular grid to show the pore homogeneity in individual cells. To visualize the pore homogeneity of the whole dataset, a color-coded homogeneity visualization was implemented which shows the deviation from the average pore properties. For the exploration with our MObject Set visualization we proposed a beginners mode in radial arrangement and an expert mode in parallel arrangement. Besides the interactive selection of MObjects, we introduced a scaling through visual linking approach along a selected path. Single MObjects hold probabilities for each voxel of belonging to the MObject and are visualized using transfer functions. They can be exported as volumetric dataset to drive subsequent calculations or simulations.

We have applied our techniques to cases of high practical relevance in the aeronautics industry. Representative pores of a CFRP dataset were found during interactive exploration of the MObjects. Based on these results NDT practitioners calculate the most appropriate ultrasonic calibration curve for each component to be tested in quality control. In active thermography the representative pores serve as input for the heat conduction simulations to improve the underlying model. Domain experts of a company manufacturing aircraft components and active thermography experts evaluated the MObjects approach with a questionnaire and found it to be a helpful tool with high practical relevance.

Although we focused on the evaluation of pores in this work, our approach can be used for all kinds of defects in material sciences. In the future we will apply our methods on cracks, inclusions, particles and fibers. Currently the number of classes into which a parent MObject is split up regarding a specific property is user-defined. This is based on the knowledge of the domain experts as well as norms specifying the number of partitions for certain properties. For future work the number of classes, a MObject is split up, can be chosen by an automatic approach.

REFERENCES

[1] J. Ahrens, K. Heitmann, M. Petersen, J. Woodring, S. Williams, P. Fasel, C. Ahrens, C.-H. Hsu, and B. Geveci. Verifying Scientific Simulations via Comparative and Quantitative Visualization. *Computer Graphics and Applications, IEEE*, 30(6):16–28, 2010.

[2] A. Amirkhanov, C. Heinzl, M. Reiter, and M. E. Gröller. Visual Optimality and Stability Analysis of 3DCT Scan Positions. *IEEE Transactions on Visualization and Computer Graphics*, pages 1477–1487, October 2010.

[3] C. Bajaj, V. Pascucci, and D. Schikore. The Contour Spectrum. In *Proceedings of IEEE Visualization '97*, pages 167–173, October 1997.

[4] J.-P. Balabanian, I. Viola, and E. Gröller. Interactive Illustrative Visualization of Hierarchical Volume Data. In *Proceedings of Graphics Interface 2010*, pages 137–144, June 2010.

[5] W. Berger, H. Piringer, P. Filzmoser, and E. Gröller. Uncertainty-Aware Exploration of Continuous Parameter Spaces Using Multivariate Prediction. *Computer Graphics Forum*, 30(3):911–920, June 2011.

[6] A. Brambilla, I. Viola, and H. Hauser. A Hierarchical Splitting Scheme to Reveal Insight into Highly Self-Occluded Integral Surfaces. *Journal of WSCG*, 20(1):5764, July 2012.

[7] S. Bruckner and T. Möller. Result-Driven Exploration of Simulation Parameter Spaces for Visual Effects Design. *IEEE Transactions on Visualization and Computer Graphics*, 16(6):1467–1475, October 2010.

[8] S. Bruckner, V. Šoltészová, E. Gröller, J. Hladůvka, K. Bühler, J. Yu, and B. Dickson. BrainGazer - Visual Queries for Neurobiology Research. *IEEE Transactions on Visualization and Computer Graphics*, 15(6):1497–1504, November 2009.

[9] N. Fout and K.-L. Ma. Fuzzy Volume Rendering. *IEEE Transactions on Visualization and Computer Graphics*, 18(12):2335–2344, December 2012.

[10] G. Grigoryan and P. Rheingans. Point-Based Probabilistic Surfaces to Show Surface Uncertainty. *IEEE Transactions on Visualization and Computer Graphics*, 10(5):564–573, September 2004.

[11] C. Heinzl, J. Kastner, T. Möller, and E. Gröller. Statistical Analysis of Multi-Material Components using Dual Energy CT. In *VMV 2008, Vision, Modeling and Visualization*, pages 179–188, October 2008.

[12] A. Inselberg. *Parallel Coordinates: Visual Multidimensional Geometry and Its Applications*. Springer-Verlag New York, Inc., Secaucus, NJ, USA, 2009.

[13] C. Y. Ip, A. Varshney, and J. F. Jaja. Hierarchical Exploration of Volumes Using Multilevel Segmentation of the Intensity-Gradient Histograms. *IEEE Transactions on Visualization and Computer Graphics*, 18(12):2355–2363, December 2012.

[14] J. Kniss, R. Van Uitert, A. Stephens, G.-S. Li, T. Tasdizen, and C. Hansen. Statistically quantitative volume visualization. In *Proceedings of IEEE Visualization 2005*, pages 287 – 294, oct. 2005.

[15] R. Kosara, F. Bendix, and H. Hauser. Parallel Sets: Interactive Exploration and Visual Analysis of Categorical Data. *IEEE Transactions on Visualization and Computer Graphics*, 12(4):558–568, July/August 2006.

[16] A. Lex, M. Streit, H.-J. Schulz, C. Partl, D. Schmalstieg, P. J. Park, and N. Gehlenborg. StratomeX: Visual Analysis of Large-Scale Heterogeneous Genomics Data for Cancer Subtype Characterization. *Computer Graphics Forum*, 31(3):1175–1184, 2012.

[17] K.-L. Ma. Image Graphs - A Novel Approach to Visual Data Exploration. In *Proceedings of IEEE Visualization '99*, pages 81–88, 1999.

[18] M. Malik, C. Heinzl, and E. Gröller. Comparative Visualization for Parameter Studies of Dataset Series. *IEEE Transactions on Visualization and Computer Graphics*, 16(5):829–840, September/October 2010.

[19] J. Marks, B. Andalman, P. A. Beardsley, W. Freeman, S. Gibson, J. Hodgins, T. Kang, B. Mirtich, H. Pfister, W. Ruml, K. Ryall, J. Seims, and S. Shieber. Design galleries: A General Approach to Setting Parameters for Computer Graphics and Animation. In *Proceedings of the 24th annual conference on Computer graphics and interactive techniques*, SIGGRAPH '97, pages 389–400, New York, NY, USA, 1997. ACM Press/Addison-Wesley Publishing Co.

[20] G. Mayr, B. Plank, J. Sekelja, and G. Hendorfer. Active thermography as a quantitative method for non-destructive evaluation of porous carbon fiber reinforced polymers. *NDT & E International*, 44(7):537–543, 2011.

[21] N. Otsu. A Threshold Selection Method from Gray-Level Histograms. *IEEE Trans. Systems, Man and Cybernetics*, 9:62–66, March 1979.

[22] P. Perona and J. Malik. Scale-Space and Edge Detection Using Anisotropic Diffusion. *IEEE Trans. Pattern Anal. Mach. Intell.*, 12:629–639, July 1990.

[23] A. Reh, B. Plank, J. Kastner, E. Gröller, and C. Heinzl. Porosity Maps - Interactive Exploration and Visual Analysis of Porosity in Carbon Fiber Reinforced Polymers. *Computer Graphics Forum*, 31(3):1185–1194, June 2012.

[24] M. Sezgin and B. Sankur. Survey over image thresholding techniques and quantitative performance evaluation. *J. Electronic Imaging*, 13(1):146–168, 2004.

[25] C. Soutis. Fibre reinforced composites in aircraft construction. *Progress in Aerospace Sciences*, 41(2):143–151, February 2005.

[26] T. Torsney-Weir, A. Saad, T. Moller, H. Hege, B. Weber, J. Verbavatz, and S. Bergner. Tuner: Principled Parameter Finding for Image Segmentation Algorithms Using Visual Response Surface Exploration. *IEEE Transactions on Visualization and Computer Graphics*, 17(12):1892–1901, December 2011.

[27] J. J. van Wijk and R. van Liere. HyperSlice: Visualization of scalar functions of many variables. In *Proceedings of IEEE Visualization '93*, pages 119–125, October 1993.

[28] J. Woodring and H.-W. Shen. Multiscale Time Activity Data Exploration via Temporal Clustering Visualization Spreadsheet. *IEEE Transactions on Visualization and Computer Graphics*, 15(1):123–137, January/February 2009.

[29] R. Xu. Survey of Clustering Algorithms. *IEEE Transactions on Neural Networks*, 16(3):645–678, May 2005.

Visual Parameter Space Analysis: A Conceptual Framework

Michael Sedlmair, Christoph Heinzl,
Stefan Bruckner, Harald Piringer, Torsten Möller

Visual Parameter Space Analysis: A Conceptual Framework

Michael Sedlmair, *Member, IEEE*, Christoph Heinzl, *Member, IEEE*, Stefan Bruckner, *Member, IEEE*,
Harald Piringer, and Torsten Möller, *Senior Member, IEEE*

Abstract—Various case studies in different application domains have shown the great potential of visual parameter space analysis to support validating and using simulation models. In order to guide and systematize research endeavors in this area, we provide a conceptual framework for visual parameter space analysis problems. The framework is based on our own experience and a structured analysis of the visualization literature. It contains three major components: (1) a data flow model that helps to abstractly describe visual parameter space analysis problems independent of their application domain; (2) a set of four navigation strategies of how parameter space analysis can be supported by visualization tools; and (3) a characterization of six analysis tasks. Based on our framework, we analyze and classify the current body of literature, and identify three open research gaps in visual parameter space analysis. The framework and its discussion are meant to support visualization designers and researchers in characterizing parameter space analysis problems and to guide their design and evaluation processes.

Index Terms—Parameter space analysis, input-output model, simulation, task characterization, literature analysis

✦

1 INTRODUCTION

Over the last decade, simulation models have become increasingly prevalent in a variety of application areas. In the visualization literature, for instance, case studies have shown how such simulation models were used to better understand weather and climate phenomena [56], the spread of infectious diseases [1], biological cell profiling [43, 57], and complex engineering and design problems [4, 18, 21, 37]. Structurally, all these examples are based on simulation models that define a set of *parameters* as inputs and are able to compute corresponding *outputs* for a particular parameterization.

From an abstract lens, many examples show recurring structures, tasks and goals. A typical goal is, for instance, the *optimization* of the output by identifying reasonable input parameter settings. Assessing the optimality of outputs often involves trading-off multiple contradicting objectives as well as qualitative judgments of complex data like time series [1, 37], segmented image data [69], animations [18], and 3D geometry [21]. Fully automatic optimization is then often too complex, expensive, or simply not clear how to achieve, and must be complemented by a human manually inspecting simulation outputs.

Traditional approaches of solving such problems were based on *informed trial and error* strategies. Based on prior knowledge and experience, the input parameters are set to a specific value. Then, the model is run and outputs are manually inspected. If the outputs are not satisfactory, the next iteration starts and the model is re-run with a different set of parameter values. A major drawback of this approach, however, is that model runs are often very expensive, that is, it takes minutes or even hours for single runs. In such cases, trial and error leads to severe and unwanted interruptions during the workflow.

To overcome these drawbacks, many researchers have recently proposed more structured workflows. To do so, interesting parts of the parameter space are coarsely sampled to generate input parameter sets. Then, the corresponding outputs are computed offline for all of these

sample settings, e.g., over-night or over the weekend. Finally, visualization approaches allow for exploring, investigating, and understanding the space of sampled inputs and their resulting outputs. Such approaches have become known as *visual parameter space analysis* techniques and offer an attractive possibility to deal with the complexity of the models while still keeping the human in the loop.

The current body of work in visual parameter space analysis comprises mostly tools and case/design studies from different application areas [1, 4, 14, 16, 37, 56, 57, 76]. In this paper, our goal is to take a step back from the current application-oriented lens on visual parameter space analysis and provide an abstract *conceptual framework*. The framework can be used to describe, discuss, and evaluate visual parameter space analysis solutions across different application domains, as well as to guide researchers in their design and evaluation decisions.

With our framework, we specifically make three primary contributions. First, we propose a *data flow model* (Section 4) that abstractly describes visual parameter space analysis problems and characterizes recurring data manipulation operations: sampling input parameters, deriving objective measures from outputs, and predicting outputs with cheaper surrogate models. Second, we present a classification of *four navigation strategies* (Section 5). We most importantly distinguish between local-to-global and global-to-local navigation strategies. In local-to-global strategies exploration starts from inspecting a specific sampled simulation run and then provides ways to navigate through other runs. In global-to-local strategies the exploration starts with an overview over all runs and then allows users to drill down into specific runs. Our third primary contribution is a characterization of *six typical analysis tasks* (Section 6) in visual parameter space analysis: optimization, partitioning, fitting, outliers, uncertainty, and sensitivity.

Our framework is based on our own experience working in visual parameter space analysis, collaborations with simulation experts, as well as a structured literature review of case/design studies in this area. This work additionally led us to identify three *open research gaps* to guide future work in this area (Section 8). Within the framework, we also offer a unified set of *definitions and terminology* facilitating research communication and progress. We consider these as secondary contributions of our work.

1.1 Definitions

The set of problems we are focusing on appears in the context of computational *input-output models*. We define input-output models broadly as any sort of function that maps a set of *input parameters* to a set of *outputs*. Together we simply refer to them as *variables*. Input-output models can therefore be, for instance, computational simulations, but most other types of algorithms also match these characteristics.

- *Michael Sedlmair is with the University of Vienna.*
  E-mail: michael.sedlmair@univie.ac.at.
- *Christoph Heinzl is with the University of Applied Sciences Upper Austria.*
  E-mail: Christoph.Heinzl@fh-wels.at.
- *Stefan Bruckner is with the University of Bergen.*
  E-mail: stefan.bruckner@uib.no.
- *Harald Piringer is with VRVis. E-mail: hp@vrvis.at.*
- *Torsten Möller is with the University of Vienna.*
  E-mail: torsten.moeller@univie.ac.at.

A typical goal of using such input-output models is to find an input parameter setting that leads to "good" output results. To achieve this goal, it is necessary to *sample* the model by setting the input parameters to specific values and compute the outputs corresponding to these inputs. One specific sample is also referred to as a simulation *run*; all samples/runs together are referred to as *sampled data*. In some application domains, this sampled data is also referred to as an *ensemble* [56]. Given that, we define *parameter space analysis* as follows:

> Parameter space analysis (PSA) is the systematic variation of model input parameters, generating outputs for each combination of parameters, and investigating the relation between parameter settings and corresponding outputs.

In some cases this process might be achieved fully automatically. Our focus is on how interactive visualization facilitates this analysis. We refer to this concept as *visual parameter space analysis (vPSA)*.

1.2 Example: Tuner

A typical example for visual parameter space analysis is the tool Tuner by Torsney-Weir et al. [69]. One of the *input-output models* in their case is a brain segmentation algorithm. As *input parameters*, this model takes a scanned image of the brain as well as a set of numerical control parameters that define how the algorithm operates. The *output* is a segmented brain image where different brain regions are marked, for instance, as background, skull, white matter, or grey matter.

Running the model with different settings of control parameters results in tremendous variations of the quality of the output segmentation. The goal is therefore to identify a parameter setting that leads to "good" segmentations. In this example, finding a "good" segmentation necessitates to subjectively trade off multiple objectives and fully automatic approaches are not suitable. Thus, Torsney-Weir et al. [69] suggested to coarsely *sample* the parameter space over night and then use methods of visual parameter space analysis to explore and analyze the *sampled data*, that is, instantiations of different input parameter settings and their corresponding output segmentations.

We will use Tuner as a running example for introducing our framework. More details will be discussed along the way, such as Figures 2, 3, 4 and 5 that refer to Tuner. We will also introduce other examples of visual parameter space analysis applications to further illustrate our abstract framework.

2 BACKGROUND

With the growing amount of published visualization research, building up a higher-level, more theoretical understanding of the work in our field becomes increasingly important. Towards that goal, this paper follows in the line of structured analyses of the visualization literature [11, 31, 39] . Bertini et al. [11], for instance, proposed a systematization and overview of quality measures and derived implications for future work. Here, we focus on a similar goal as Bertini et al. but for the area of visual parameter space analysis.

Our framework specifically focuses on problem abstraction, as well as strategies and tasks that occur in visual parameter space analysis. Many researchers have called for a stronger focus on such task and problem characterizations in visualization research [39, 47, 51, 70]. Following these calls, researchers have recently started to more actively focus on pure *problem characterization* papers. Kandel et al. [34], for instance, have studied analysts within the social and organizational context of companies. Kang and Stasko [35] characterize usage patterns and problems by conducting case studies with their text analysis tool Jigsaw. Earlier work from Tory and Staub-French characterizes visualization practices and collaboration patterns of building designers [72]. Our work follows a similar goal, that is, characterizing a specific set of problems. However, we have a different focus: while the above papers focus on specific application domains, we focus on a specific set of abstract problems, visual parameter space analysis, across application domains.

Previous work on *task characterization* has mostly focused on straightforward low-level tasks [2, 5, 36, 65], such as detecting outliers, or high-level goals [3, 41], such as hypothesis generation. Only

recently, researchers have started to characterize complex tasks that lie between these two extremes and that better reflect the needs of real users [17, 47, 58, 61]. Our work on tasks has similar goals. However while the previous work is targeted at generic visualization tasks, we focus on a specific set of data analysis challenges appearing around visual parameter space analysis. We argue that characterizing problems and tasks from more specific angles is indispensable for getting a more concrete understanding of users' needs in these areas.

We see our work between the extremes of narrow, domain-specific task characterizations as done in design studies [64], and generic task taxonomies. Notable examples along these lines are Lee et al.'s work on characterizing tasks for graph visualization [40], and Sedlmair et al.'s work on dimensionality reduction tasks [62].

3 METHOD

The framework is primarily based on our own experience conducting design studies in parameter space analysis and collaborating with simulation experts in different domains [4, 9, 10, 14, 18, 55, 69]. In these design studies, we started to identify and describe data and task characteristics. Here, we build on these domain-specific experiences, propose an abstract, domain-independent framework, and derive novel insights in terms of analysis strategies, tasks, and open research gaps.

To additionally ground our framework, we conducted a structured, in-depth analysis of the relevant research literature. Our assumption is that these research papers can be seen as a proxy for the problems, data and tasks of end users. From the visualization literature, we gathered an initial set of 112 research papers that we deemed potentially interesting. A closer analysis of these papers led us to a set of *21 core-relevant papers* [1, 4, 9, 10, 14, 16, 18, 21, 26, 37, 43, 44, 45, 46, 55, 56, 57, 68, 69, 73, 76]. This selection was based on a set of exclusion criteria that we defined. First, we specifically excluded papers *without concrete applications* of parameter space analysis. Without a close connection to a concrete application we cannot reliably argue about user tasks. Second, we excluded papers with *automatic analyses only* to keep the focus relevant to the visualization community. Third, we excluded papers that *did not match our definition* of parameter space analysis, as outlined in Section 1.1.

Similar to a machine learning approach, we split the 21 core papers into two groups, a "training" and a "validation" set. We selected and iteratively analyzed 14 papers (training set), with three major rounds of iterations. We used this first round of analysis to step-by-step improve and refine the initial conceptual framework that we developed based on our own experience and collaborations. This analysis specifically informed our characterization of exploration strategies (Section 5), analysis tasks (Section 6), and research gaps (Section 8). We then analyzed the remaining 7 papers to validate the robustness of our framework (validation set). In general, our analysis was inspired by open, axial and selective coding strategies as used in Social Science [19, 24]. Overall, each paper was coded by at least two authors (average 2.8 coders/paper). More details about the methodological approach can be found in the supplemental material.

In the following sections, we will use selected examples from the 21 core-relevant papers to illustrate our framework. Table 1 on page 7 summarizes the final categorization of these 21 papers.

4 DATA FLOW MODEL

Our first contribution is a data flow model that depicts how data is generated and manipulated in a visual parameter space analysis setting. Specifically, we characterize three key operations as part of this model: *sampling* the input parameter space, *derivation* of objective measures from the model output, and *prediction* of not-yet-computed (or unsampled) outputs using computationally cheap surrogate models.

4.1 Basic Input-Output Model

The focus of our work is on *input-output models*, such as computational simulation models or algorithms. For a more evocative abstraction of these models, we use a simple graphical representation depicting the data flow.
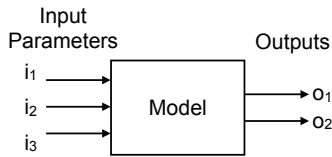
Fig. 1. Simple input-output model with 3 input parameters and 2 outputs.

Consider the simple example in Figure 1. This model takes three inputs and maps them to two outputs. The model might represent a hypothetical weather forecast model that takes current temperature, humidity, and pressure and based on them computes tomorrow's probability of rain, as well as the speed of the wind. Such models can come in very different forms. For instance, *stochastic* models [14, 74] yield different outputs for repeated runs with the same input parameter setting. On the other hand, *deterministic* models [18, 69] produce the same outputs whenever run with the same parameter setting.

In the simplest form, the inputs and outputs of a model come as real numbers. In that case, the model can be represented as a mapping $f : \mathbb{R}^m \to \mathbb{R}^n$, with $m = 3$ and $n = 2$ in the example of Figure 1. However, other data *types* are also common. We broadly classify input and output types into two groups: (1) *multi-variate/multi-dimensional*, and (2) *complex objects* [52]. This distinction is based on a semantic level, not on mathematical concepts.

As in the simple example above, inputs and outputs can come as a *set of semantically meaningful variables* (or dimensions) that are either quantitative, ordered, or categorical. In the literature examples we surveyed, we found that these sets of input/output variables rarely exceeded 100 variables. Moreover, in all cases these variables were semantically meaningful. That is, they were well chosen by the scientists or users that study a specific model. We propose to refer to these input parameters as *multi-dimensional* and to the output characteristics as *multi-variate*. This choice leans on common mathematical terminology [20] and allows us to distinguish between inputs and outputs. Further, we will not refer to these variables as high-dimensional as this is a term usually common in machine learning and statistics where the number of dimensions is in the thousands or millions, and where dimensions have no strong semantic meaning, such as pixel values in an image. Note, that we are not proposing a clear-cut number of variables/dimensions between multi- and high-dimensional, but argue that the strong or weak semantic meaning of dimensions/variables distinguishes these two.

Alternatively, inputs/outputs can come as (semantically) *complex objects*. For example, a 2D/3D image is a single complex object (despite the fact that they can be modelled mathematically as $N \times N$ pixels, or N^2 dimensions). Images cannot be easily described with a single quantitative/ordered/categorical variable. The semantic unit is the complex object itself. Other examples are animations, performance graphs, social networks, or robot behaviors, just to name a few.

Naturally, both can coexist in a model. Consider the running example on image segmentation from the introduction (Tuner). Here, a brain segmentation algorithm takes a scanned image of the brain as input and returns a segmented image as output where different colors mark the individual brain regions, as illustrated in Figure 2.
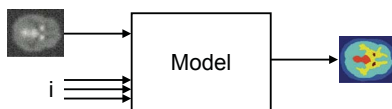

Fig. 2. Model with a complex object in addition to numerical variables as input and a complex object as output. Example from Torsney-Weir et al. [69].

Both the unsegmented 2D input image, as well as the segmented 2D output image are semantically complex objects. Additionally, the model takes some quantitative input parameters that can be adjusted to control the segmentation process. This example highlights the existence of different *classes of input parameters*. To better characterize these differences, we adopt a classification from the statistics community that separates input parameters into three classes [60]:

- *Control parameters* are parameters the user can directly manipulate. These parameters are of primary interest to parameter space analysis problems, such as the three numerical inputs in the example above (Figure 2).

- *Environmental parameters* are parameters that can be measured in the real world, such as the un-segmented brain scan image in the example. They are often prone to small changes and, hence, are modeled as random variables. Therefore, these are parameters that often cannot be directly controlled by the user.

- *Model parameters* are implicit parameters often needed for the numerical realization of the model such as setting certain thresholds, grid spacings or convergence criteria. They might be important during the model building but are mostly hidden during the usage of a model.

4.2 Sampling

At the heart of visual parameter space analysis is the systematic sampling of the input parameter space, and the generation of respective outputs for each sample point (a specific setting of input parameters). Figure 3 shows the sampling process by means of the segmentation example. Each of the parameter settings leads to a different segmentation output.
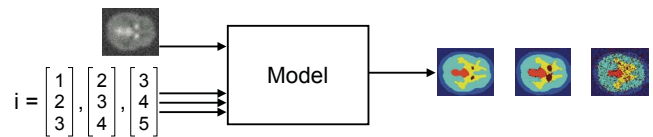

Fig. 3. Sampling a model. Here, 3 different samples are generated by running the model with 3 different input settings.

Most of the papers we analyzed used either regular or stochastic sampling strategies. Regular Cartesian sampling—also known as full-factorial designs in the statistics literature—was the most favored approach. In the case of random sampling, uniform random sampling is used. Some strategies also employ Latin Hypercube approaches. While these sampling strategies allow an overview of behaviors in the parameter space, few tools we analyzed directly supported sampling strategies from within the tools [10, 44, 69, 76]. We refer to this direct integration as *integrated sampling* that allows users themselves to trigger and refine sampling processes, for instance, to generate additional samples or adapt sampling strategies.

4.3 Derivation

It is common that the output of a model is a complex object (18/21 of our analyzed examples). For an effective parameter space analysis, many outputs will have to be studied together requiring an efficient summary, specifically for complex objects. In such cases, the user of the model might want to derive *objective measures* that summarize the essential characteristics of the complex model output. We refer to them as *derived outputs*. Consider the segmentation example again. Figure 4 shows that for each segmented output image, a set of scalar objective measures is computed. In this example, the objective measures are computed by comparing the segmented image to a ground-truth, hand-segmented image. The measures quantify how much the segmented areas differ between the output and the ground-truth image.

Alternatively, the use of pair-wise similarity (or distance) metrics allows an easier comparison of different outputs visually or algorithmically. The distance metric can then be used to provide an overview with distance-based visualization techniques such as MDS plots [29].
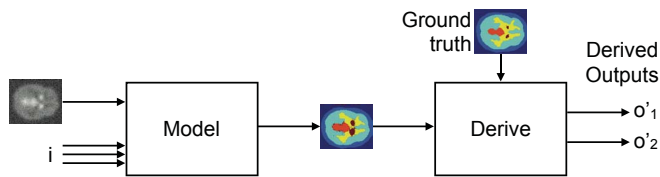
Fig. 4. Derive additional variables. In this case, the segmented output image from the algorithm is compared to a ground truth, hand-segmented image. Differences are quantified as derived outputs.

Fig. 6. Our problem abstraction summarized as a data flow model. Dashed and dotted lines indicate the optionality of the additional *derivation* and *prediction* steps.

4.4 Prediction

Sampling a model provides discrete combinations of inputs and outputs. Consider a simple model with 2 input parameters and 1 output. Data from sampling this model 100 times could be easily visualized in a scatterplot with the 2 inputs being the axes, the 100 samples are drawn as points, and the output is mapped to a color-scale which is used to encode each sample point.

However, often the model user is interested in seeing outputs at locations that have not been sampled. If sampling is cheap these points can be just computed on the fly. However, usually generating samples is computationally expensive and would therefore interrupt the analysis process. In these cases, cheap surrogate models [60] can be leveraged to *predict* outputs that have not been sampled by the real model. Moreover, surrogate models might allow one to predict all un-sampled areas and to reproduce the actual continuous-to-continuous mapping between inputs and outputs. Creating continuous spaces from discrete samples is, in the signal processing community, referred to as approximation or interpolation [20]; in the statistical community this is known as regression and prediction [13].

To illustrate this prediction step, let us once again come back to the segmentation example from above. Predicting the two derived objective measures from the three input control parameters leads to a continuous-to-continuous mapping which now can be represented with Hyperslices [75] instead of discrete scatterplots. The three input parameters are mapped to the dimensions, and the two outputs are mapped to orange-white and purple-white color scales, as illustrated in Figure 5. The continuous mapping makes it possible to understand the entire space of relations between in- and outputs, without restricting it to a selected set of sample points.
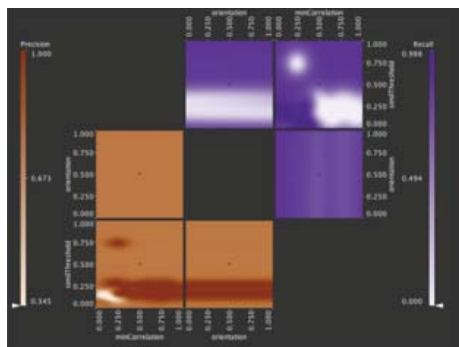

Fig. 5. Hyperslices of the image segmentation algorithm. The 3 input parameters are mapped to the axes. 2 derived outputs are encoded on a white-purple, and a white-orange color scale. Courtesy of Torsney-Weir et al. [69].

4.5 Summary: Data Flow Model

The complete data flow can now be summarized as in Figure 6. The actual input-output model takes multi-dimensional input parameters that can be controlled by the user, and produces *direct outputs* that can either be multi-variate or complex objects. From these direct outputs further *derived outputs* may be extracted. This pipeline can be
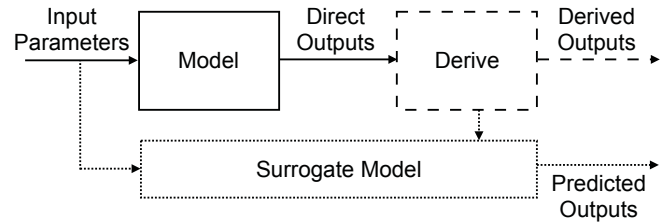
replaced with a surrogate model taking the same input parameters but now computing *predicted outputs*. Hence, the actual output space contains direct outputs but can include derived and predicted outputs as well. While there is alternative terminology that could describe this problem space, we hope that this data flow model is evocative enough through all areas of visualization research that it will be accepted as a common language.

Note, that this summary depiction reflects a typical scenario. In the real world, more complex scenarios do appear as well, including multiple serial, parallel, or nested derivation steps. However, these can be represented by simply recombining the elementary components of the pipeline. Another interesting question related to this data flow pipeline is where to draw the "line" between the model and derive step. If a model returns multi-variate outputs, oftentimes these have already been "derived" within the model. We argue that this depends on the person who looks at the model and the stage of development. A distinction we find helpful is between visualization researchers and domain experts: direct outputs are what visualization researchers get from domain collaborators, although they might be internally derived; derived outputs are those which visualization researchers actively develop or help developing.

5 NAVIGATION STRATEGIES

When data has been generated via sampling, derivation, and/or prediction, this data needs to be presented to the user for exploration and analysis. Based on our literature analysis, we classify four distinctive strategies of how this data was made available for navigation.

5.1 Informed Trial and Error

Traditionally, parameter space analysis was conducted with *informed trial and error* strategies. Based on prior knowledge, a user (1) runs a model with a specific setting of input parameters creating one sample, (2) inspects the outputs of this sample, and (3) re-runs the model with a refined set of parameter settings if the outcome was not satisfactory. This sequential process can be effective if the simulation output can be produced in real-time. Given that model computations are usually expensive, the informed trial and error strategy, however, has tremendous interruption costs: the user has to wait for minutes, or even hours for new samples to be produced. Usually, this time to find the right parameters is not reported. One simply finds a statement along the lines of "We have found the following parameter settings to yield good results ...". The well known SIFT algorithm [42] serves as a good example. It is a specific feature detector for computer vision applications which works well when a number of parameters are set to specific values. Since no systematic determination has been reported in the paper, it is likely that finding these parameter settings has been done following the wide-spread, traditional trial and error strategy.

5.2 Local-to-Global

To allow for real-time interaction rates despite high model computation costs, researchers have suggested to pre-compute samples before the actual parameter space analysis process. The expensive pre-computation can be done, for instance, over night. The column "no. of samples" in Table 1 on page 7 shows the numbers of samples used in

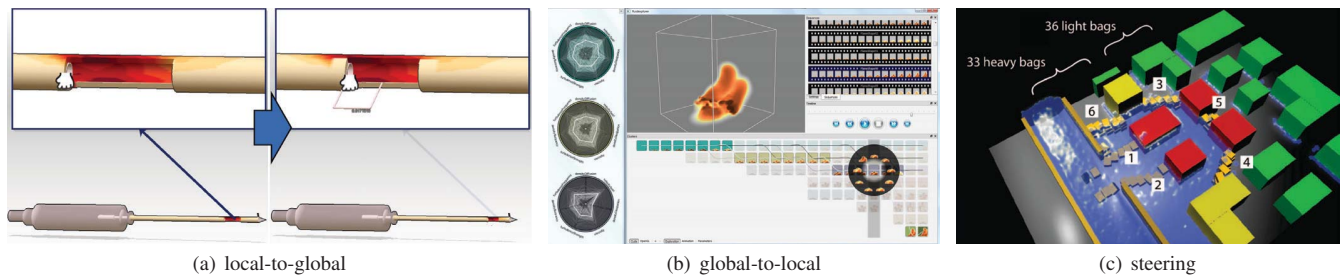(a) local-to-global   (b) global-to-local   (c) steering

Fig. 7. Examples for different navigation strategies: **(a) Local-to-global**: The user can interactively manipulate the size of the cutting window (input parameters), which is then updating the overlaid stress field heatmap (output). Courtesy of Coffey et al. [21]. **(b) Global-to-local**: The view at the top-right and the view at the bottom show overviews of all simulated explosion (outputs) using representative thumbnail images. Upon selecting one specific explosion its animation can be inspected in the top-mid view. The circular parallel-coordinate plots on the left show the respective input parameter settings. Courtesy of Bruckner and Möller [18]. **(c) Steering**: The user can interactively place sand sacks (input parameters) while a flooding simulation is running (output). Courtesy of Waser et al. [76].

the papers we analyzed. Based on the tradeoff between computational costs on the one hand and analysis accuracy on the other hand, the number of generated samples ranges often between 100 and 1000.

Given this set of precomputed sample points, we identified different characteristic strategies of how they were visually represented and navigated in analysis tools. The local-to-global strategy starts with showing one specific output and lets the user explore alternatives from there. Consider, for instance, a visual parameter space analysis example supporting the design of a medical biopsy device, as shown in Figure 7(a) [21]. Here, a virtual CAD device is used to explore various characteristics such as the length of the tissue cutting window or the outer radius of the cannula, which are the inputs to a simulation model. The simulation output, a scalar stress field, is directly mapped as a heatmap onto the CAD virtual device. The navigation through the pre-computed design space starts with showing a very specific sample, that is, specific device characteristics and a specific stress field. A user can now interactively change the device characteristics (inputs), and in doing so updates the stress field heatmap (output). Step-by-step the user can interactively infer global structures from local searches.

5.3 Global-to-Local

Global-to-local navigation strategies are similarly based on the precomputation of a large set of sample points. However, instead of starting with a specific sample and navigate alternatives from there, the goal is to start with an overview over all pre-computed samples and then drill-down into more details. In that sense, this strategy is closer to Shneiderman's venerable mantra "Overview first, zoom and filter, then details on demand" [65].

Consider, for instance, how Bruckner and Möller used visual parameter space analysis to support visual effect designers in finding desired explosion animations [18]. Sampling the animation algorithms with different parameter settings, they present interactive thumbnails of clustered animations as shown in Figure 7(b). In doing so, they first reveal the breadth of possible animations to the user, and then support drilling down, identifying and refining good animation candidates.

5.4 Steering

In some cases, a user might want to change the input parameter settings while a simulation runs. We refer to this strategy as *steering*. While the above strategies focus on changing and analyzing control parameters in a systematic way, steering often addresses environmental and model parameters.

We refer to steering environmental parameters as *simulation steering*, which for instance can be found in real-time simulators such as flight or driving simulators. World Lines by Waser et al. [76] is a prime example for this category. As shown in Figure 7(c), their system lets the user place different barriers to contain flooding of a city while the water is rising. Different possible performances can be compared. Users can evaluate alternative scenarios for the assessment of potential hazards by actively steering the simulation while it runs.

On the other hand, steering model parameters refers to on-the-fly adjustment of numerical or other aspects of the computational realization of the model. Examples include changing the grid size or time-stepping parameters. Adjusting these parameters is known as *computational steering* [50].

It is worthwhile to notice that, while we differentiate between local-to-global and steering, others have used the word steering to express local-to-global search [45]. We argue that these two strategies are fundamentally different as one is based on pre-computation or re-sampling (local-to-global), while the other is inherently tied to adjusting parameters during simulation runtime (steering).

6 ANALYSIS TASKS

So far, we have characterized how *data* can be produced from their underlying models, and how *visualization* can support different ways of navigating this data. A third important component is understanding the *tasks* that users eventually want to engage in when doing visual parameter space analysis.

In general, tasks regarding input-output models are often coarsely classified as model building, model validation, and model usage [22]. Our work on visual parameter space analysis primarily focuses on *model validation and usage* tasks for which a computational model already needs to exist. In model validation, modellers question the behavior of the model itself and try to derive formative insights on how to make it better, or summatively judge its performance. In model usage, analysts/scientists use a more or less trusted model without primarily questioning its validity. Visual parameter space analysis of the model can then be used for various purposes. It might be used to guide *design and engineering* processes, for instance, of a biopsy device as discussed above [21]. In *policy making*, decisions can be informed by simulating different "possible futures" [14]. Similarly, a model might be used to study *scientific* phenomena such as bird moving patterns that would otherwise be hard or impossible to study [10]. Or, it simply might be used for *training* purposes emulating real systems in a simulation [76]. While there is no clear-cut line between model validation and usage, we found it a helpful distinction when discussing visual parameter space analysis problems.

With the goal of providing better guidance for visualization researchers and designers, we intended to characterize visual parameter space analysis tasks on a more fine-granular level. Based on our own work and the literature review, we describe a set of six recurring analysis tasks: *optimization, partitioning, fitting, outliers, uncertainty, and sensitivity*. These tasks essentially cross-cut both model validation and usage. Note that it is very common that several of these analysis tasks co-occur in real application scenarios.

6.1 Optimization: *"Find the best parameter combination given some objectives."*

One of the most common tasks is to find an input parameter setting that leads to satisfying output results. Oftentimes objective functions

can be formulated and numerical measures be derived from the direct outputs respectively. If the objective can be summarized in a single scalar there is a multitude of numerical optimization strategies that can be employed [15].

However, when there are *multiple competing objectives* finding the best output often relies on *subjective human judgement*, a promise that visual parameter space analysis holds. Consider the example of a segmentation algorithm design as supported by our running example Tuner [69]. On the one hand, 12 derived objective measures need to be balanced. On the other hand, it is necessary to subjectively analyze the performance of the segmentation as the objective measures are not fully capturing the expert knowledge.

In some cases optimization might even be a completely subjective process. Consider the above mentioned example of Fluid Explorer in Figure 7(b): in this example, the optimization heavily relies on qualitative assessment of the outputs, the animated explosions. The users are primarily interested in exploring the output space in order to identify a realization that most closely represents their envisioned goals. A similar example is Marks et al.'s venerable work on Design Galleries [44]. Both approaches rely on presenting thumbnails of images or animations which are organized according to a similarity measure.

6.2 Partitioning: *"How many different types of model behaviors are possible?"*

The goal of a partitioning task is to find a partitioning—or clustering, or segmentation—of the output space and relate that back to input parameter settings. In doing so, it is possible to understand what different types of outputs can be expressed by the existing model. A good example is Bergner et al.'s work clustering different fuel cell performance graphs (model outputs), followed by mapping their cluster IDs back into the input space [10]. The input space is shown as a 2D-dimensional scatterplot with the sample points colored according to clusters in the output space. This representation reveals "shapes" of input parameter settings that lead to similar output results.

6.3 Fitting: *"Where in the input parameter space would actual measured data occur?"*

During building and validating a model, it is of interest to see how and whether real measured data can be expressed by the model. In that sense, fitting represents an inverse problem: given model outputs only, what input parameters would yield this behavior? This is also akin to regression analysis in statistics or approximation and interpolation methods in signal processing. While mathematically, this could be formulated as an optimization problem, the user might need a different mind-set and therefore a different visual encoding and interaction design. Improving the understanding of differences between model and reality helps to fit the model more closely to the underlying real world system that is simulated. HyperMoVal [55] is an example that specifically focuses on the validation of regression models. HyperMoVal seeks to support the fitting task by simultaneously plotting the regression model together with known validation data. This approach allows users to analyze how well model outputs align with the real system.

6.4 Outliers: *"What outputs are special?"*

The abstract task of finding outliers can have different specific meanings in model usage and validation. When using a more or less trusted model, it can refer to detecting anomalies in simulations, for instance, to understand interesting and unique phenomena in weather forecast models [56]. On the other hand, when building and validating a model, it can refer to identifying implausible outputs that would not have been possible in an underlying real system. The aforementioned example of HyperMoVal [55], for instance, reports on a case study where an outlier turned out to be an implausible validation sample.

6.5 Uncertainty: *"How reliable is the output?"*

Understanding uncertainties in model usage and validation can come in different forms [22]. In our literature analysis, we specifically identified:

- Aleatoric/statistical uncertainty (lack of knowledge modelled through random variables, often found in environmental variables): "How much do (non-deterministic) runs with the same parameter settings differ?"
- Structural uncertainty: "How much does the model differ from reality?" (a form of epistemic uncertainty)
- Prediction uncertainty (of surrogate models): "How accurate are predicted outputs?" (a form of epistemic uncertainty)

Understanding and integrating uncertainty into scientific, engineering and design processes has gained considerable attention [22]. Yet, the visualization and communication of uncertainty is done cautiously in many systems. Consider, for instance, decision making tools such as Vismon [14], a visual tool for fisheries data analysis. In the Vismon project, the managers and stakeholders (the users of the system) were already overwhelmed with the complexity of the data they need to consider. Hence, the system was developed to bring aspects of uncertainty to the forefront only when explicitly requested by the user. This trend could change as the literacy about sources and quantification of uncertainty sweeps through the different application areas.

6.6 Sensitivity: *"What ranges/variations of outputs to expect with changes of input?"*

Mathematically, sensitivity might be expressed as an uncertainty of the input parameter value, and is therefore often considered a subfield of uncertainty quantification [22]. However, while some of the mathematical approaches of quantifying uncertainty might be applicable to sensitivity analysis, the semantic understanding and articulation of sensitivity is different. Hence, we find it helpful to articulate it as a separate analysis task. In the tools we have studied, sensitivity was never merged or considered a form of uncertainty. In analyzing sensitivity one distinguishes between *global* and *local* sensitivity [59], however, we have only found support for local sensitivity in the tools we have surveyed. Specifically, we have found sensitivity to be cross-cutting through most other analysis tasks:

- Optimization: The question arising is the stability of the output for slight changes of the optimal input parameters. Users are willing to choose a less optimal solution, if it is guaranteed that the solution is stable to small changes of input parameters (specifically, environmental parameters that cannot be directly controlled by the user)
- Partitioning: The question arising here is one of stability of partitions, i.e., how quickly or slowly does one partition change to another when changing the inputs?
- Fitting: Given some specific measured data, the question is how large a range of inputs will yield the model output representing the data measured.

For analyzing sensitivity, it might be useful to *predict* outputs with surrogate models. Reproducing a partial or full continuous-to-continuous mapping between inputs and outputs supports a better understanding of local neighborhoods surrounding points of interests, which in turn is crucial for sensitivity analysis. This approach is, for instance, used in our running example Tuner, in which sensitivity analysis was identified as an important task. Figure 5 shows how Hyper-Slices were used to navigate the continuous-to-continuous mapping between inputs and predicted outputs.

7 DISCUSSION

Table 1 shows the final result of our iterative analysis of the 21 papers. The cells mark how we classified these papers according to our framework. Naturally, the papers we analyzed were not written with our theoretical lens in mind, necessitating interpretation and in-depth discussions in their analysis. We see our main contribution in summarizing, abstracting, and classifying different characteristics of visual parameter space analysis into a holistic conceptual framework based on these 21 papers.

After reviewing our framework's relation to other theoretical visualization models, we provide guidance on how to use the framework, and discuss its focus and limitations.

	No. of Applications presented	Data Flow Model (Sec. 4)			Navigation Strategies (Sec. 5)			Analysis Tasks (Sec. 6)							Additional details on Model/Data														
		Integr. Sampling	Derivation	Prediction	Local-to-Global	Global-to-Local	Steering	Optimization	Partitioning	Fitting	Outliers	Uncertainty	Sensitivity		Input						Direct Outs			Sampling Strategy				No. of Samples	
Afzal et al. [1]	2	*					*																						Afzal et al.: Epidemic modeling and response evaluation [1]
Amirkhanov et al. [4]	1	*									*																		Amirkhanov et al.: 3DCT ScanPositions [4]
Berger et al. [9]	1										P																		Berger et al.: Uncertainty-Aware Exploration [9]
Bergner et al. [10]	3	*		*			*	*	*	*		*																	Bergner et al.: Partitioning for Computer Simulations [10]
Booshehrian et al. [14]	1										A	*																	Booshehrian et al: Vismon — Fisheries Management [14]
Brecheisen et al. [16]	3	*		*			*													not reported									Brecheisen et al.: Parameter Sensitivity for DTI Fiber Tracking [16]
Bruckner & Möller [18]	1	*					*																						Bruckner & Möller: Visual Effects Design [18]
Coffey et al. [21]	2						*																						Coffey et al.: Design by Dragging [21]
Guo et al. [26]	1			*			*																						Guo et al.: Multivariate Linear Trend Discovery [26]
Konyha et al. [37]	2						*	*			*																		Konyha et al.: Interactive VA of Families of Function Graphs [37]
Luboschik et al. [43]	1	*					*			A																			Luboschik et al.: Simulation trajectories [43]
Marks et al. [44]	3	*					*																						Marks et al.: Design galleries [44]
Matkovic et al. [45]	2						*				*																		Matkovic et al.: Common Rail Injection System [45]
Matkovic et al. [46]	1		*				*																						Matkovic et al.: Families of Data Surfaces [46]
Piringer et al. [55]	1		*				*			S																			Piringer et al.: HyperMoVal [55]
Potter et al. [56]	1									A	*																		Potter et al.: Ensemble-Vis [56]
Pretorius et al. [57]	2		*	*																									Pretorius et al.: Image Analysis [57]
Spence et al. [68]	1							*																					Spence et al.: Visualization for functional design [68]
Torsney-Weir et al. [69]	2	*					*			*	P	*																	Torsney-Weir et al.: Tuner [69]
Unger et al. [73]	1			*			*			*	*	*																	Unger et al.: Validation of Geoscientific Simulation Models [73]
Waser et al. [76]	1	*									*																		Waser et al.: World Lines [76]

Table 1. The table summarizes the 21 application/design study papers we analyzed in terms of our framework. A cell is marked with yellow when a certain aspect of our *data flow model* is supported by the application. Blue marks indicate the main *navigation strategy* a certain tool follows. Green marks the *analysis tasks* that are primarily supported. Secondary data operations/strategies/tasks are labeled with an asterisk (*). We label a cell as secondary if a strategy or task was not explicitly targeted by the authors but might still be feasible with their tool. In the uncertainty column we further differentiate between aleatoric (A), structural (S), and prediction uncertainty (P), as described in Section 6. Grey shows additional information relevant to visual parameter space analysis.

7.1 Relation to Other Visualization Models

Our framework can be best contextualized using Munzner's Nested Model [51]. The Nested Model organizes the visualization design and validation process into four levels: (1) domain problem characterization, (2) problem/data/task abstractions, (3) visual encoding/interaction design, and (4) algorithm design. Our work in general, and the data flow model (Section 4) and analysis tasks (Section 6) in particular, focus mainly on the abstraction layer (level 2). We ground these abstractions in a thorough analysis (literature analysis and firsthand experience) of domain problems (level 1). We also connect the framework upwards to visual encoding/interaction design (level 3) by characterizing navigation strategies (Section 5).

We also sought to organize our tasks and strategies using the multilevel task typology proposed by Brehmer and Munzner [17]. This typology is organized as why, how and what and presents a set of abstract tasks living in these categories. While we found the general categories of why and how helpful in guiding our analysis, we could not directly match our framework into this typology. Our work addresses analysis tasks specific to visual parameter space analysis that have not been discussed in their typology. We see this fact as a confirmation on the many calls for more work on problem and task analyses [17, 47, 51]. Understanding the richness and variety of visualization problems, and putting them together into a theoretical underpinning remains a major challenge of our community.

7.2 Framework Usage

Our framework can be used in three different ways: (1) descriptive—for describing a significant range of visual parameter space analysis problems and solutions; (2) evaluative—to help assess design alternatives; and (3) generative—to support creating new ideas [7, 8].

Descriptive Usage The terminology we proposed, the data flow model, as well as the analysis task characterizations can be used to abstractly describe domain problems for which visual parameter space analysis solutions are generated. We refined and validated our framework by describing visual parameter space analysis applications from 21 papers, and are therefore confident that the framework will be descriptive for many other application examples as well.

We anticipate three major benefits when describing visual parameter space analysis work through our abstract lens. First, it will help in problem-driven research, such as design studies [64], to abstractly characterize the problem and translate domain knowledge into actionable design decisions. Second, technique-driven researchers can use it to clearly characterize their goals and assumptions. Third, the framework then can facilitate the communication between researchers. Specifically, it will allow for an easier mapping between problem-driven and technique-driven work. Additionally, it will allow to compare and relate findings *across different application domains*, accelerating progress in visual parameter space analysis research in general.

Evaluative Usage The navigation strategies and analysis tasks we characterized will help to better assess multiple alternatives in designing visual parameter space analysis tools.

Consider the example of deciding between *local-to-global* and *global-to-local* navigation strategies. Global-to-local starts with a broad overview over many/all possible model outcomes, while local-to-global starts from a specific output and then allows the interactive exploration of alternatives. From that perspective global-to-local seems more powerful in many cases. However, this decision might interact with other factors. For instance, deep immersion into specific decisions might outweigh global exploration of alternatives in certain situations. Also, such decisions depend on how complex the model output is and how easy/hard it is to computationally *derive* objectives and/or visually provide an evocative overview.

As intrinsically true for all conceptual frameworks, these identified strategies are naturally a simplification of the reality. For real tools we found that aspects of local-to-global and global-to-local navigation were often combined with different views supporting different strategies. We marked these combinations with an asterisk in Table 1.

However, having a clear characterization of strategies and tasks helps to better reason about choices and eventually make more informed design decisions.

Generative Usage   Finally, our framework can also be used to generate and inspire new ideas. We believe that the framework is concrete enough to depict visual parameter space analysis problems and solutions, yet general enough to inspire other areas as well.

While we use our input-output data flow model to reason about simulations and algorithms it could, for instance, be similarly used to describe and analyze the visualization process itself. The idea would be to generate, that is, *sample* many different visual encodings and then use *derived* quality measures to spot interesting ones. Some of the pioneering work in visualization includes the study of transfer functions for volume rendering (Design Galleries [44], visualization spreadsheets [32], parallel-coordinate-style interfaces [71], Vis-Trails [6]), the analysis of the rendering pipeline [38], graphs [33], and the analysis of multi-variate data projections [66, 77]. Our framework gives a new theoretical lens to think about this line of work and might be used to generate new ideas that have not been thought of with the traditional perspective.

7.3   Focus and Limitations

Our work is grounded in our own experience working in visual parameter space analysis, as well as a structured analysis of 21 core-relevant papers. This approach comes with standard limitations of qualitative theory building [19]. Selecting and coding papers, as well as generating the framework was inevitably shaped by our previous experience.

To keep the effort of our in-depth literature analysis manageable, we selected 21 core-relevant papers with a specific focus based on our definition of visual parameter space analysis. Nevertheless, there are many other papers that are closely related to our endeavor, which is reflected in the larger set of 112 papers that we initially gathered (see supplemental material for a full list).

For instance, we specifically focused on visualizing relations of inputs and outputs sampled from computational models. However, also *measured data* often comes in a similar form of two groups of related variables. In statistics, they are usually called independent (analogous to our inputs), and dependent variables (outputs). Consider, for instance, Guo et al.'s work on sensitivity analysis, which is a task that also appears in our framework. Their focus is on previously measured data. The example in their paper relies on a benchmark dataset of measured diamond weight, color, clarity, and cut (independent var.), and their relation to price (dependent var.) [27].

We further selected core-relevant papers with a focus on the investigation of input-output relations. Other visualizations of simulation data focus mainly on representing the *output space*. Nocke et al., for instance, primarily look at solutions of how to visualize complex outputs from climate simulations [54]. Given the complexity of representing even individual climate simulation outputs, they only marginally focus on input-output relations. Smith et al. address the question of morphing between shape objects resulting from computational design models, such as car CAD models [67]. Their work is closely related to our *prediction* strategy.

We mainly focused on model validation and usage tasks of an existing computational model. We did not explicitly include other *model building* tasks, such as feature extraction, selection, or transformation. Consider, for instance, Mühlbacher's and Piringer's work that discusses how visualization can support building regression models [49].

Finally, we specifically set out to study *visual* parameter space analysis. While this focus was intentional, we believe that our framework might be useful for more general parameter space analysis scenarios with a less substantial role of visual encodings as well. We also believe that the framework is general enough to be useful for the closely-related areas discussed above, although these lines of work were not part of our core literature analysis. Naturally, all possible generalizations cannot be tested in a single paper. Validating, refining, and extending our framework to include other problem areas is an interesting step for future work.

8   RESEARCH GAPS AND FUTURE WORK

Through our practical and theoretical work on visual parameter space analysis, we additionally identified three research gaps that are described in the following. We believe that these gaps provide ample opportunity for future work.

8.1   Data Acquisition Gap

As described above, the visual parameter space analysis pipeline starts with *sampling* the parameter space. All following analysis steps rise and fall with this crucial first step. However, only a few current tools directly support sampling from within the tool (4/21 papers address it as a primary goal). Reasons for not supporting sampling might include potential engineering and organizational hurdles when integrating the model with the visualization tool [63], high computational costs of the sampling process, and the fact that proper sampling of multi-dimensional spaces is not trivial. Given that model computations are usually expensive, sampling multi-dimensional spaces and categorical parameters pose challenges. Often, it is not clear which sampling strategy to utilize and simple uniform random sampling becomes the default, without a deeper understanding of its implications. For instance, not every instance of a random distribution truly assures a uniform covering of the space [53].

While such decisions might not pose any challenges to domain scientists with a strong mathematical background, they do for others without this background. Ingram et al. classified the latter as middle-ground users [28]. These users would tremendously benefit from easy-to-use visual parameter space analysis tools that integrate the sampling step and help reveal underlying sampling assumptions and implications.

8.2   Data Analysis Gap

Integrating computational analysis methods into the visualization pipeline also poses a major challenge for future work. While the *predict* step in our pipeline refers to the challenge of building good surrogate models, the *derive* step deals with how to derive good objective measures. While domain knowledge is crucial to be successful, there are a number of general strategies that have been developed in the data analysis communities of statistics and machine learning. Yet, they are similarly important for visual analysis.

18/21 of our analyzed papers described models with complex objects as direct outputs. For those, deriving is a crucial step to open up more sophisticated visual analysis approaches. Deriving fosters more holistic and powerful global-to-local analysis strategies. Deriving also better supports most of the tasks we characterized in our work, such as multi-objective optimization, partitioning, or sensitivity analysis.

The actual model in our pipeline is usually a black box to us as visualization researchers (and also might be to the domain experts themselves). In contrast, we argue that we need to better understand methods for deriving and predicting. Making these steps a white box to us will allow us to better support a much richer set of analyses steps, and help to make them accessible to middle-ground users as in the DimStiller project [28].

The visualization community is already very active in this area, for instance, by focusing on quality measures for multi-variate data representations [11, 66, 77]. Also, many examples we analyzed already utilize derived measures (15/21 papers). Given the richness of potential model outputs, however, we deem this only as a starting point for an important area of future work.

8.3   Cognition Gap

Another major challenge is how to facilitate the cognitive understanding of and navigation through multi-dimensional spaces. As humans we are inherently 3D plus time beings. Naturally, understanding higher dimensions seems inherently impossible. While this challenge is shared with general multi-dimensional visualization, visual parameter space analysis comes with specific characteristics that are important to understand.

Consider, for instance, multi-objective optimization. Pareto front visualizations have been found to be helpful for such endeavors [69].

A Pareto front basically connects all solutions where no objective measure can be improved without degrading another one, and therefore gives useful constraints for output space navigation. Yet, while visual Pareto fronts are straight-forward in 2D [69], it is not clear how to visually depict or even efficiently compute them in higher dimensions. Vismon [14], for instance, samples specific multi-dimensional options for direct comparison, not taking advantage of a higher-dimensional Pareto front.

It is also not clear how many objectives in an optimization problem can be cognitively handled by humans. Is this number, for instance, following the general 7 ± 2 rule of capacity limits in human information processing [48]? A possible approach might be Gleicher's work on generating projections according to the users' needs [25]. Here the user builds an analysis system one dimension at a time, allowing the gradual increase of complexity.

8.4 Other Areas of Future Work

Beyond these gaps, conducting research in visual parameter space analysis gives ample opportunity to study many previously identified visualization challenges. *Scalability* considerations are inherently part of many computational model analyses necessitating out-of-core, parallel, and cluster computing solutions [12]. On the other hand, the rich set of potential visual and computational analysis methods for parameter space analysis problems calls for good concepts of user *guidance* [28]. Sophisticated *provenance* approaches [23] could help in this regard to better track what parts of the parameter space have already been explored and which not. Especially policy making examples such as Vismon [14], inherently involve multiple stakeholders, giving ample opportunity to study *collaboration* processes [30]. Eventually, we also need a stronger focus on *user evaluation* [39]. Analyzing the current literature revealed that most parameter space analysis applications were evaluated with usage scenarios. These scenarios make clear how data could be analyzed, but leave out how users actually used these tools themselves. Some notable exceptions, such as Pretorius [57], give richer usage descriptions, where actual users used the tool and reported anecdotal evidence [51].

Finally, we want to echo previous calls on the importance of problem-driven work such as case and design studies [47, 64]. Our work is grounded in the first-hand experiences reported in 21 of such application papers. Deriving our higher-level theoretical framework would not have been possible without this problem-driven work.

9 CONCLUSION

We have presented a conceptual framework that characterizes the data flow, navigation strategies, and analysis tasks in visual parameter space analysis problems. We hope that our work will establish a useful abstraction of otherwise domain-specific concepts and will propel the fascinating area of visual parameter space analysis to a fruitful area of further visualization research.

REFERENCES

[1] S. Afzal, R. Maciejewski, and D. Ebert. Visual analytics decision support environment for epidemic modeling and response evaluation. In *IEEE Conf. on Visual Analytics in Science and Technology (VAST)*, pages 191–200, 2011.

[2] R. A. Amar, J. Eagan, and J. T. Stasko. Low-level components of analytic activity in information visualization. In *IEEE Symp. on Information Visualization (InfoVis)*, pages 111–117, 2005.

[3] R. A. Amar and J. T. Stasko. Knowledge precepts for design and evaluation of information visualizations. *IEEE Trans. on Visualization and Computer Graphics*, 11(4):432–442, 2005.

[4] A. Amirkhanov, C. Heinzl, M. Reiter, and E. Gröller. Visual optimality and stability analysis of 3DCT scanpositions. *IEEE Trans. on Visualization and Computer Graphics*, 16:1477 –1487, 2010.

[5] N. Andrienko and G. Andrienko. *Exploratory analysis of spatial and temporal data.* Springer Berlin, Germany, 2006.

[6] L. Bavoil, S. Callahan, P. Crossno, J. Freire, C. Scheidegger, C. Silva, and H. Vo. VisTrails: Enabling interactive multiple-view visualizations. In *IEEE Conf. on Visualization*, pages 135–142, 2005.

[7] M. Beaudouin-Lafon. Designing interaction, not interfaces. In *Conf. on Advanced Visual Interfaces (AVI)*, pages 15–22. ACM, 2004.

[8] B. B. Bederson and B. Shneiderman. *The craft of information visualization: readings and reflections (Chapter 8).* Morgan Kaufmann, 2003.

[9] W. Berger, H. Piringer, P. Filzmoser, and E. Gröller. Uncertainty-aware exploration of continuous parameter spaces using multivariate prediction. *Computer Graphics Forum*, 30(3):911 – 920, 2011.

[10] S. Bergner, M. Sedlmair, T. Möller, S. Nabi Abdolyousefi, and A. Saad. ParaGlide: Interactive parameter space partitioning for computer simulations. *IEEE Trans. on Visualization and Computer Graphics*, 19(9):1499–1512, 2013.

[11] E. Bertini, A. Tatu, and D. Keim. Quality metrics in high-dimensional data visualization: An overview and systematization. *IEEE Trans. on Visualization and Computer Graphics*, 17(12):2203–2212, 2011.

[12] J. Beyer, A. Al-Awami, N. Kasthuri, J. W. Lichtman, H. Pfister, and M. Hadwiger. ConnectomeExplorer: Query-guided visual analysis of large volumetric neuroscience data. *IEEE Trans. on Visualization and Computer Graphics*, 19(12):2868–2877, 2013.

[13] C. M. Bishop. *Pattern Recognition and Machine Learning.* Springer-Verlag New York, Inc., 2006.

[14] M. Booshehrian, T. Möller, R. M. Peterman, and T. Munzner. Vismon: Facilitating analysis of trade-offs, uncertainty, and sensitivity in fisheries management decision making. *Computer Graphics Forum*, 31(3):1235–1244, 2012.

[15] S. Boyd and L. Vandenberghe. *Convex Optimization.* Cambridge University Press, 2009.

[16] R. Brecheisen, A. Vilanova, B. Platel, and B. ter Haar Romeny. Parameter sensitivity visualization for DTI fiber tracking. *IEEE Trans. on Visualization and Computer Graphics*, 15(6):1441–1448, 2009.

[17] M. Brehmer and T. Munzner. A multi-level typology of abstract visualization tasks. *IEEE Trans. on Visualization and Computer Graphics*, 19(12):2376–2385, 2013.

[18] S. Bruckner and T. Möller. Result-driven exploration of simulation parameter spaces for visual effects design. *IEEE Trans. on Visualization and Computer Graphics*, 16(6):1467–1475, 2010.

[19] K. Charmaz. *Constructing grounded theory. A practical guide through qualitative analysis.* Sage Publications, Inc, 2006.

[20] W. Cheney and W. Light. *A Course in Approximation Theory.* American Mathematical Society, 2009.

[21] D. Coffey, C.-L. Lin, A. Erdman, and D. Keefe. Design by dragging: An interface for creative forward and inverse design with simulation ensembles. *IEEE Trans. on Visualization and Computer Graphics*, 19(12):2783–2791, 2013.

[22] Committee on Mathematical Foundations of Verification, Validation, and Uncertainty Quantification; Board on Mathematical Sciences and Their Applications, Division on Engineering and Physical Sciences, National Research Council. *Assessing the Reliability of Complex Models: Mathematical and Statistical Foundations of Verification, Validation, and Uncertainty Quantification.* The National Academies Press, 2012.

[23] J. Freire, D. Koop, E. Santos, and C. T. Silva. Provenance for computational tasks: A survey. *Computing in Science and Engineering*, 10(3):11–21, 2008.

[24] D. Furniss, A. Blandford, and P. Curzon. Confessions from a grounded theory PhD: Experiences and lessons learnt. In *ACM Trans. Computer-Human Interaction (ToCHI)*, pages 113–122, 2011.

[25] M. Gleicher. Explainers: Expert explorations with crafted projections. *IEEE Trans. on Visualization and Computer Graphics*, 19(12):2042–2051, 2013.

[26] Z. Guo, M. O. Ward, and E. A. Rundensteiner. Model space visualization for multivariate linear trend discovery. In *IEEE Conf. on Visual Analytics in Science and Technology (VAST)*, pages 75–82, 2009.

[27] Z. Guo, M. O. Ward, E. A. Rundensteiner, and C. Ruiz. Pointwise local pattern exploration for sensitivity analysis. In *IEEE Conf. on Visual Analytics in Science and Technology (VAST)*, pages 131–140, 2011.

[28] S. Ingram, T. Munzner, V. Irvine, M. Tory, S. Bergner, and T. Möller.

Dimstiller: Workflows for dimensional analysis and reduction. In *IEEE Conf. on Visual Analytics in Science and Technology (VAST)*, pages 3–10, 2010.

[29] S. Ingram, T. Munzner, and M. Olano. Glimmer: Multilevel MDS on the GPU. *IEEE Trans. on Visualization and Computer Graphics*, 15(2):249–261, 2009.

[30] P. Isenberg, N. Elmqvist, J. Scholtz, D. Cernea, K.-L. Ma, and H. Hagen. Collaborative visualization: Definition, challenges, and research agenda. *Information Visualization*, 10(4):310–326, 2011.

[31] T. Isenberg, P. Isenberg, J. Chen, M. Sedlmair, and T. Möller. A systematic review on the practice of evaluating visualization. *IEEE Trans. on Visualization and Computer Graphics*, 19(12):2818–2827, 2013.

[32] T. Jankun-Kelly and K.-L. Ma. Visualization exploration and encapsulation via a spreadsheet-like interface. *IEEE Trans. on Visualization and Computer Graphics*, 7(3):275–287, 2001.

[33] T. Jankun-Kelly, K.-L. Ma, and M. Gertz. A model and framework for visualization exploration. *IEEE Trans. on Visualization and Computer Graphics*, 13(2):357–369, 2007.

[34] S. Kandel, A. Paepcke, J. M. Hellerstein, and J. Heer. Enterprise data analysis and visualization: An interview study. *IEEE Trans. on Visualization and Computer Graphics*, 18(12):2917–2926, 2012.

[35] Y.-A. Kang and J. T. Stasko. Examining the use of a visual analytics system for sensemaking tasks: Case studies with domain experts. *IEEE Trans. on Visualization and Computer Graphics*, 18(12):2869–2878, 2012.

[36] P. R. Keller and M. M. Keller. *Visual cues: practical data visualization (Appendix B)*. IEEE Computer Society Press, 1993.

[37] Z. Konyha, K. Matkovic, D. Gracanin, M. Jelovic, and H. Hauser. Interactive visual analysis of families of function graphs. *IEEE Trans. on Visualization and Computer Graphics*, 12(6):1373–1385, 2006.

[38] J. Kronander, J. Unger, T. Möller, and A. Ynnerman. Estimation and modeling of actual numerical errors in volume rendering. *Computer Graphics Forum*, 29(3):893–902, 2010.

[39] H. Lam, E. Bertini, P. Isenberg, C. Plaisant, and S. Carpendale. Empirical studies in information visualization: Seven scenarios. *IEEE Trans. on Visualization and Computer Graphics*, 18(9):1520–1536, 2012.

[40] B. Lee, C. Plaisant, C. S. Parr, J.-D. Fekete, and N. Henry. Task taxonomy for graph visualization. In *Proc. BELIV*, pages 1–5. ACM, 2006.

[41] Z. Liu and J. T. Stasko. Mental models, visual reasoning and interaction in information visualization: A top-down perspective. *IEEE Trans. on Visualization and Computer Graphics*, 16(6):999–1008, 2010.

[42] D. G. Lowe. Object recognition from local scale-invariant features. In *IEEE Conf. on Computer Vision*, volume 2, pages 1150–1157 vol.2, 1999.

[43] M. Luboschik, S. Rybacki, F. Haack, and H.-J. Schulz. Supporting the integrated visual analysis of input parameters and simulation trajectories. *Computers & Graphics*, 39(0):37 – 47, 2014.

[44] J. Marks, B. Andalman, P. A. Beardsley, W. Freeman, S. Gibson, J. Hodgins, T. Kang, B. Mirtich, H. Pfister, W. Ruml, K. Ryall, J. Seims, and S. Shieber. Design Galleries: A general approach to setting parameters for computer graphics and animation. In *Proc. SIGGRAPH*, pages 389–400, 1997.

[45] K. Matkovic, D. Gracanin, M. Jelovic, and H. Hauser. Interactive visual steering—rapid visual prototyping of a common rail injection system. *IEEE Trans. on Visualization and Computer Graphics*, 14(6):1699–1706, 2008.

[46] K. Matkovic, D. Gracanin, B. Klarin, and H. Hauser. Interactive visual analysis of complex scientific data as families of data surfaces. *IEEE Trans. on Visualization and Computer Graphics*, 15(6):1351–1358, 2009.

[47] M. Meyer, M. Sedlmair, P. S. Quinan, and T. Munzner. The nested blocks and guidelines model. *Information Visualization*, pages 1–16, 2013.

[48] G. A. Miller. The magical number seven, plus or minus two: Some limits on our capacity for processing information. *Psychological review*, 63(2):81, 1956.

[49] T. Mühlbacher and H. Piringer. A partition-based framework for building and validating regression models. *IEEE Trans. on Visualization and Computer Graphics*, 19(12):1962–1971, 2013.

[50] J. D. Mulder, J. J. van Wijk, and R. van Liere. A survey of computational steering environments. *Future generation computer systems*, 15(1):119–129, 1999.

[51] T. Munzner. A nested model for visualization design and validation. *IEEE Trans. on Visualization and Computer Graphics*, 15(6):921–928, 2009.

[52] T. Munzner. *Visualization Analysis and Design (Chapter 2)*. A K Peters Visualization Series. Taylor and Francis / CRC Press, 2014. to appear.

[53] H. Niederreiter. *Random number generation and quasi-Monte Carlo methods*. Society for Industrial and Applied Mathematics, 1992.

[54] T. Nocke, M. Flechsig, and U. Böhm. Visual exploration and evaluation of climate-related simulation data. In *Winter Simulation Conf.*, pages 703–711, 2007.

[55] H. Piringer, W. Berger, and J. Krasser. HyperMoVal: Interactive visual validation of regression models for real-time simulation. In *Computer Graphics Forum*, pages 983–992, 2010.

[56] K. Potter, A. Wilson, P.-T. Bremer, D. Williams, C. Doutriaux, V. Pascucci, and C. Johnson. Ensemble-Vis: A framework for the statistical visualization of ensemble data. In *IEEE Conf. on Data Mining Workshops*, pages 233–240, 2009.

[57] A. Pretorius, M.-A. Bray, A. Carpenter, and R. Ruddle. Visualization of parameter space for image analysis. *IEEE Trans. on Visualization and Computer Graphics*, 17(12):2402–2411, 2011.

[58] R. E. Roth. An empirically-derived taxonomy of interaction primitives for interactive cartography and geovisualization. *IEEE Trans. on Visualization and Computer Graphics*, 19(12):2356–2365, 2013.

[59] A. Saltelli, M. Ratto, T. Andres, F. Campolongo, J. Cariboni, D. Gatelli, M. Saisana, and S. Tarantola. *Global Sensitivity Analysis: The Primer*. John Wiley & Sons, Ltd, 2008.

[60] T. J. Santner, B. J. Williams, and W. I. Notz. *The Design and Analysis of Computer Experiments*. Springer-Verlag, 2003.

[61] H.-J. Schulz, T. Nocke, M. Heitzler, and H. Schumann. A design space of visualization tasks. *IEEE Trans. on Visualization and Computer Graphics*, 19(12):2366–2375, 2013.

[62] M. Sedlmair, M. Brehmer, S. Ingram, and T. Munzner. Dimensionality reduction in the wild: Gaps and guidance. Technical Report TR-2012-03, Dept. of Computer Science, University of British Columbia, 2012.

[63] M. Sedlmair, P. Isenberg, D. Baur, and A. Butz. Information visualization evaluation in large companies: Challenges, experiences and recommendations. *Information Visualization*, 10(3):248–266, 2011.

[64] M. Sedlmair, M. Meyer, and T. Munzner. Design study methodology: Reflections from the trenches and the stacks. *IEEE Trans. on Visualization and Computer Graphics*, 18(12):2431–2440, 2012.

[65] B. Shneiderman. The eyes have it: A task by data type taxonomy for information visualizations. In *IEEE Symp. on Visual Languages*, pages 336–343, 1996.

[66] M. Sips, B. Neubert, J. P. Lewis, and P. Hanrahan. Selecting good views of high-dimensional data using class consistency. *Computer Graphics Forum*, 28(3):831–838, 2009.

[67] R. Smith, R. Pawlicki, I. Kokai, J. Finger, and T. Vetter. Navigating in a shape space of registered models. *IEEE Trans. on Visualization and Computer Graphics*, 13(6):1552–1559, 2007.

[68] B. Spence, L. Tweedie, H. Dawkes, and H. Su. Visualization for functional design. In *IEEE Symp. on Information Visualization (InfoVis)*, pages 4–10, 1995.

[69] T. Torsney-Weir, A. Saad, T. Möller, H.-C. Hege, B. Weber, and J.-M. Verbavatz. Tuner: Principled parameter finding for image segmentation algorithms using visual response surface exploration. *IEEE Trans. on Visualization and Computer Graphics*, 17(12):1892–1901, 2011.

[70] M. Tory. User studies in visualization: A reflection on methods. In *Handbook of Human Centric Visualization*, pages 411–426. Springer, 2014.

[71] M. Tory, S. Potts, and T. Möller. A parallel coordinates style interface for exploratory volume visualization. *IEEE Trans. on Visualization and Computer Graphics*, 11(1):71–80, 2005.

[72] M. Tory and S. Staub-French. Qualitative analysis of visualization: A building design field study. In *Proc. BELIV*, pages 7:1–7:8. ACM, 2008.

[73] A. Unger, S. Schulte, V. Klemann, and D. Dransch. A visual analysis concept for the validation of geoscientific simulation models. *IEEE Trans. on Visualization and Computer Graphics*, 18(12):2216–2225, 2012.

[74] A. Unger and H. Schumann. Visual support for the understanding of simulation processes. In *IEEE Pacific Visualization Symp.*, pages 57–64, 2009.

[75] J. J. van Wijk and R. van Liere. HyperSlice: Visualization of scalar functions of many variables. In *IEEE Conf. on Visualization*, pages 119–125, 1993.

[76] J. Waser, R. Fuchs, H. Ribicic, B. Schindler, G. Blöschl, and E. Gröller. World lines. *IEEE Trans. on Visualization and Computer Graphics*, 16(6):1458–1467, 2010.

[77] L. Wilkinson, A. Anand, and R. L. Grossman. Graph-theoretic scagnostics. In *IEEE Symp. on Information Visualization (InfoVis)*, pages 157–164, 2005.

FiberScout:
An Interactive Tool for Exploring and Analyzing Fiber Reinforced Polymers

Johannes Weissenböck, Artem Amirkhanov, Weimin Li, Andreas Reh, Alexandr Amirkhanov, Eduard Gröller, Johann Kastner, Christoph Heinzl

FiberScout: An Interactive Tool for Exploring and Analyzing Fiber Reinforced Polymers

Johannes Weissenböck*
University of Applied
Sciences Upper Austria -
Wels Campus

Artem Amirkhanov†
University of Applied
Sciences Upper Austria -
Wels Campus

Weimin Li‡
University of Applied
Sciences Upper Austria -
Wels Campus

Andreas Reh§
University of Applied
Sciences Upper Austria -
Wels Campus

Alexander Amirkhanov¶
Ufa State Aviation Technical
University, Ufa, Russia

Eduard Gröller‖
Vienna University of
Technology, Institute of
Computer Graphics and
Algorithms, Vienna, Austria

Johann Kastner**
University of Applied
Sciences Upper Austria -
Wels Campus

Christoph Heinzl††
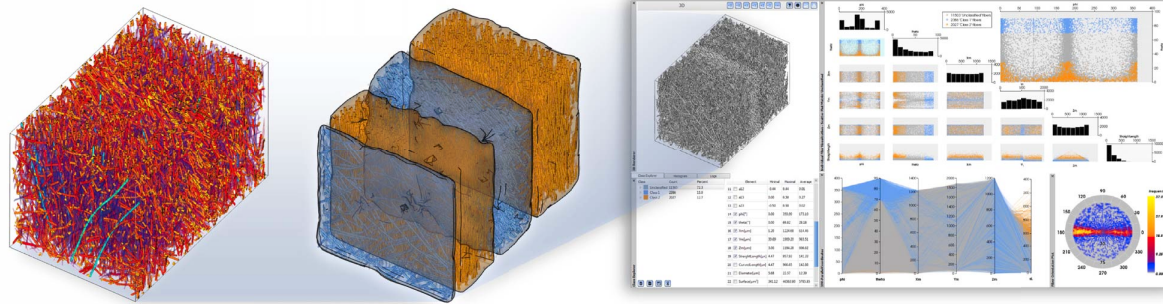University of Applied
Sciences Upper Austria -
Wels Campus

Figure 1: Glass fiber reinforced polymer (GFRP) visualized using the *FiberScout* system.

ABSTRACT

Advanced composites such as fiber reinforced polymers are promising candidate materials for future components as they allow integrating the continuously rising demands of industry regarding cost-effectiveness, function-orientation, integration and weight. The most important structures of fiber reinforced polymers are the individual fibers, as their characteristics (stiffness, strength, ductility, durability, etc.) to a large extent determine the properties of the final component. The main contribution of this paper is the introduction of a new system for interactive exploration and visual analysis of fiber properties in X-ray computed tomography data of fiber reinforced polymers. The presented tool uses parallel coordinates to define and configure initial fiber classes. Using a scatter plot matrix linked to the parallel coordinates the initial classification may be refined. This allows to analyze hidden relationships between individual fiber properties. 2D and 3D views depict the resulting fiber classifications. By using polar plots an intuitive rendering of the fiber orientation distribution is provided. In addition, two modules of higher abstraction are proposed: The Blob visualization creates a hull around fibers with similar characteristics. The fiber metadata visualization allows to calculate overlays for 2D and 3D views containing regional information of particular material characteristics. The proposed system has been evaluated by two groups of domain experts. Applying the presented concepts the user feedback shows that the domain experts are now able to efficiently perform tasks as classification of fibers, visualization of fiber lengths and orientations, and visualization of fiber regions. The insights gained can be forwarded to the design office as well as to material development and simulation, in order to speed up the development of novel composite components.

Index Terms: I.3.6 [Computer Graphics]: Methodology and Techniques—Interaction techniques

1 INTRODUCTION

In modern industry a clear trend evolved of moving industrial research towards new cost-effective, function-oriented, highly integrated and light-weight components. This novel trend is mainly caused by growing demands in terms of efficiency, environment, safety as well as comfort. Especially the aviation industry and more recently also automotive, leisure and other industries have found a promising candidate class of materials meeting these high demands in advanced composite materials.

Advanced composite materials and more specifically fiber reinforced polymers (FRPs) make up a growing proportion in high tech industrial products. For example, in next-generation aircrafts, more than 50% of the complete aircraft will be made of fiber reinforced polymers [24]. Due to the increasing share of advanced composite materials also the demand for non-destructive testing (NDT) methods is rapidly growing [20]. As the characteristics of individual fibers in FRP components contribute to a great ex-

---

*e-mail: johannes.weissenboeck@fh-wels.at
†e-mail: artem.amirkhanov@fh-wels.at
‡e-mail: li.weimin@fh-wels.at
§e-mail :andreas.reh@fh-wels.at
¶e-mail: alexander.msg@gmail.com
‖e-mail: groeller@cg.tuwien.ac.at
**e-mail: johann.kastner@fh-wels.at
††e-mail: christoph.heinzl@fh-wels.at

tent to the final characteristics in terms of stiffness, strength, ductility and durability, the domain experts are highly interested in non-destructive, qualitative and quantitative analyses. For example, quantities such as fiber orientation distribution (FOD), fiber length distribution (FLD) or fiber content are highly important parameters for the prediction of tensile strength of short-fiber reinforced polymers [6, 28]. Therefore, getting insight into the characteristics of individual fibers without destroying the specimen is crucial for domain experts to improve and optimize the material as well as the design of new parts.

Industrial 3D X-Ray computed tomography (XCT) has rapidly evolved in the field of non-destructive testing within recent years and is now increasingly applied for quality control and metrology. State of the art industrial XCT devices are capable of generating high resolution volume data at voxel sizes of 1 μm or even below. The main benefit of high resolution XCT volume data for NDT practitioners is to get a comprehensive and highly detailed analysis of the test specimen. However, due to the high information content of the volume data, data exploration and visualization has become a big challenge.

When analyzing an FRP sample the domain experts are interested in how the fibers are distributed according to length and orientation. Depending on the given lengths and how the fibers are aligned experts can then estimate and verify the material properties. They are looking for fiber layers (different by their orientation), resulting from the manufacturing process. Furthermore, it is important for the experts which fiber characteristics a spatial subregion has. These insights can be used for subsequent simulations. In addition another question for material experts is, how the individual fiber properties relate to each other and which regularities can be derived from them. Currently, the domain experts are using specific software products such as *VG Studio Max* and its *Materials Fiber Composite Analysis Module* [29] to examine FRP materials. With this module, local and global orientations as well as concentrations of fibers can be displayed in a 3D view and a 2D slice view. But it is not possible to search for specific fiber properties within a sample and there is no visual highlighting or classification for fibers. In addition, no dependencies between the individual fiber characteristics can be investigated and no visualizations on a higher abstraction level are provided.

Based on the domain-specific requirements the following tasks for fiber characterization and fiber visualization using XCT have been identified:

Task 1: Classification of fibers. The most important task is to identify and visualize classes of individual fibers in XCT scans of FRP samples. The domain experts need interactive visualization techniques to define and configure fiber classes in accordance to their specific properties and to individually render each class.

Task 2: Visualization of fiber lengths and orientations. Fiber lengths and fiber orientations contribute to a large extent to the characteristics of the final components such as strength or stiffness. Therefore the domain experts need visualization techniques to render the fiber length and orientation distribution in the dataset.

Task 3: Visualization of fiber regions. The domain experts require a quick and easy solution to identify and visualize regions with similar fiber characteristics. A hull has to be determined, which is enclosing regions of fibers with similar characteristics and clearly differentiate themselves from other regions. The domain experts need a method to analyze the manufacturing process in order to determine modifications in the layer structure of the material. Furthermore, methods are required to quickly explore the data and to identify relationships between individual fiber characteristics.

In order to address the tasks identified by the domain experts, we introduce the *FiberScout*, a system to visualize and explore XCT scans of fiber reinforced composites. The analysis work flow starts with an XCT scan of the specimen and thus the generation of data.

In a preprocessing step a label image is calculated from the original gray value image, which is used as basis for all developed techniques. The main contributions of this work are found in the designed techniques and their domain specific integration as well as in the solutions for tasks 1 - 3 identified by domain specialists (see Figure 2):

Parallel coordinates and scatter plot matrix to classify fibers. In order to analyze the internal micro-structure of the specimen, parallel coordinates and a scatter plot matrix classify the fibers according to fiber characteristics. The scatter plot matrix is used to refine the classification results from the parallel coordinates in a further step. Furthermore, the scatter plot matrix allows to reveal hidden relationships between fiber characteristics.

Polar plots to render fiber orientations. The fiber orientation distribution (FOD) is computed on a half sphere and visualized using the azimuthal projection of the northern hemisphere on a 2D plane. A spherical color map is integrated to color code the orientations of fibers in 3D as specified by the domain experts.

Blob visualization and fiber metadata visualization to render fiber classes. In order to address the problem of occlusion and clutter when rendering datasets with high fiber content, a smooth hull (blob) is extracted and rendered. It shows regions of fibers with similar characteristics or fiber bundles. Each identified region is visualized as a single blob. Furthermore regional meta information of the fiber data is computed for the fiber metadata visualization to quickly explore the dataset.

In the subsequent section we review the related work on fiber analysis and fiber visualization. In Section 3 the data generation, the datasets and the data preprocessing are described. In Section 4, the visualization techniques to address task 1-3 are introduced. Section 5 presents the evaluation of the visualization results. Finally, we conclude and point out potential future work in Section 6.
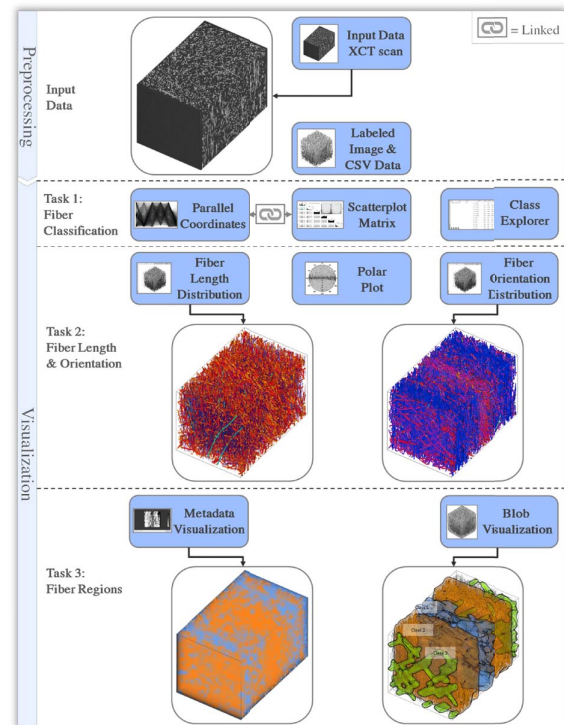

Figure 2: Overview of the *FiberScout* visualization techniques.

154

2 RELATED WORK

The related work for the proposed techniques is mainly found in the visualization and analysis of material systems, parameter space exploration as well as visual data exploration techniques.

2.1 Visualization and Analysis of Material Systems

Initial visualization techniques for non-destructive testing using industrial XCT data have been first introduced by Huang et al. [10]. A method for visualizing a pre-computed feature volume with a time series of domain parameters using 3D transfer functions was presented by Hadwiger et al. [8]. Based on this method, Fritz et al. [5] introduced an approach to explore steel fiber reinforced sprayed concrete and to quantify fiber properties such as fiber orientation. They use a direction sphere histogram to visualize the fiber orientation distribution. Furthermore direction transfer functions in the orientation domain are used to visualize fiber orientations with user specified colors. The field of application of Fritz' work is in comparison to our application area of FRPs a completely different one. We can calculate far more individual fiber characteristics of FRPs and we can represent each characteristic in charts. Furthermore, we can search for fibers with a highly specific set of fiber features and classify them. Besides these differences, we employ several abstract representations to visualize fiber characteristics and the defined fiber classes.

Regarding orientation visualization, Robb et al. [21] presented a method to calculate the local orientation of a fiber using a Gaussian orientation space. Altendorf and Jeulin [1] compute the local directions in continuous space by analyzing the mathematical morphology of images. A disadvantage of the local orientation analysis is that a single fiber may have various orientations, as the calculation is done on a pixel or voxel-basis. This is not suitable for visualizing fibers as a whole object in our visualization pipeline.

The algorithm described by Salaberger et al. [22] and Teßmann et al. [27] is used to extract individual fibers in our visualization pipeline. Tests included in their work demonstrated that the methods produces results with accuracies of more than 95% correctly detected fibers (mainly depending on the fiber content). Based on this implementation further algorithms are applied for the calculation of fiber properties (e.g., fiber orientation, fiber length, fiber diameter, fiber volume). Fiber orientations are then visualized in 3D space with a domain specific spherical color map based on the work of Yamrom et al. [31].

2.2 Parameter Space Exploration

Parallel coordinates [11] and scatter plots [30] are popular techniques for visualizing high-dimensional data sets. For example, Craig et al. [4] use coordinated parallel views to query micro array time-course data. The queries done in the coordinated parallel view are then linked to a scatter plot. They conclude that the coordinated parallel view is more appropriate for revealing details in the data and supporting the discovery of less dominant patterns. S-style axis layout parallel coordinates are used by Qu et al. [19] to highlight wind directions for analyzing the air pollution problem in Hong Kong. This approach is suitable for revealing correlations between 1D directions and other variables. However for analyzing 3D directions together with spatial information conventional parallel coordinates are more convenient. Kuang et al. [15] did a comparison of scatter plots and parallel coordinates. They found that parallel coordinates show advantages in low dimensionality and low density datasets, while scatter plots outperform parallel coordinates in higher dimensionality and higher density datasets. Parallel coordinates and a scatter plot matrix are integrated in our visualization pipeline. We combine the two techniques using *linking* and *brushing* [14], in order to explore the data in a more interactive way. The advantages of these two techniques are exploited and hidden correlations between individual characteristics are easier to detect.

2.3 Visual Exploration

Regarding clustering methods, Zhou et al. [33] introduced splatting of the individual lines in parallel coordinates to reveal strong correlations between the dimensions and to detect trends. In addition Zhou et al. [32] proposed a novel method using parallel coordinates for multi-dimensional transfer function design. Guo et al. [7] present an effective transfer function (TF) design for multivariate volumes, providing tightly coupled views of parallel coordinates plots. Li et al. [16] showed a novel approach for space deformation to simulate a magnification lens on versatile volume datasets and textured solid models. Tatu et al. [26] employ interestingness-guided subspace search algorithms to detect a candidate set of subspaces. The result of a *k-means* [13] algorithm turned out to generate robust consequences for initial automatic classifications. Therefore, in our proposed work we follow this approach for the determination of fiber classes with similar characteristics. Jackson et al. [12] present a tangible interface which allows a 3D interactive exploration of thin fiber structures to understand patterns in fiber orientation inside a volume.

3 DATA GENERATION AND PREPROCESSING

This section briefly explains how the industrial X-ray computed tomographic data is generated (see Section 3.1), which datasets are used (see Section 3.2), and how the preprocessing step performs calculations on fiber characteristics and individual fiber extractions (see Section 3.3).

3.1 Data Generation

Industrial X-ray computed tomography (XCT) provides a 3D volumetric representation of the scanned specimen. The specimen is placed on a rotary table between an X-ray source and a detector. The specimen is penetrated by X-rays. It attenuates the incident X-rays according to material properties and penetration thickness [9]. The detector converts the radiation intensity into digital projection images, which are finally reconstructed into a 3D volume data.

3.2 Dataset Descriptions

The two glass fiber reinforced polymer (GFRP) specimens to test the fiber visualization pipeline are $614 \times 961 \times 600$ and $608 \times 1411 \times 500$ voxels in size with a resolution of 2 μm and 3 μm respectively. We will subsequently call them *dataset1* (see Figure 3A) and *dataset2* (see Figure 3B). The carbon fiber reinforced polymer (CFRP) specimen we investigated in this work has a size of $600 \times 500 \times 600$ voxels and is scanned with a resolution of 1 μm. We will subsequently call it *dataset3*. All specimens are scanned with a GE phoenix|X-Ray Nanotom 180.
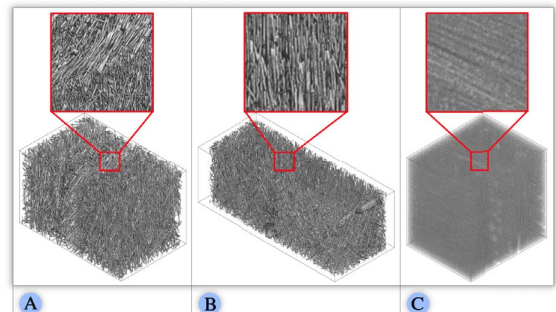

Figure 3: 3D rendering of the datasets used in this paper. (A) GFRP specimen (*dataset1*), 15916 fibers. (B) GFRP specimen (*dataset2*), 21751 fibers. (C) CFRP specimen (*dataset3*), 22656 fibers.

155

Characteristic	Description	Unit
a_{11}, a_{22}, a_{33}	The main diagonal elements of the fiber orientation tensor [25]	-
φ, θ	Spherical coordinates of a fiber orientation	°
X_i, Y_i, Z_i	Cartesian coordinates of the ith fiber center point, $0 \leq i \leq m-1$	μm
sL	Straight length of a fiber	μm
diameter	Diameter of a fiber	μm
volume	Volume of a fiber	μm^3

Table 1: Most significant fiber characteristics, identified by the domain experts.

3.3 Preprocessing

In the preprocessing step the fiber characterization pipeline (FCP) according to Salaberger et al. [22] is applied to the scanned XCT volume data of the fiber reinforced polymer (FRP) specimens. In the first step of this pipeline Gaussian blurring is applied to reduce noise in the original volume data. In the second step the gradient magnitude is computed, which is used as input for the computation of the Hessian matrix at each voxel. Using the Hessian matrix, the gray value differences of a voxel compared to its neighboring voxels are detected, which allows to deduce the main orientation of fibers. The Hessian matrix also determines the medial axis of the individual fibers as originally proposed by Teßmann et al. [27]. The intermediate results of the pipeline are the extracted individual fibers of the dataset given by their corresponding start and end points. The characteristics of the extracted fibers are computed at the same time as the individual fibers are extracted. Finally a labeling filter is applied to all the extracted fibers. In the labeled image every voxel of an individual fiber is mapped to a unique label identification. In total, 25 fiber characteristics for each fiber are available. The most significant fiber characteristics for further analysis are shown in Table 1.

4 VISUALIZATION

For understanding the micro structures of fiber reinforced polymers, visualization techniques such as direct volume rendering of the extracted fibers do not satisfy the requirements of the domain specialists. This is due to clutter and occlusion. To overcome this problem, the *FiberScout* system (see Figure 1 on the right) with its visual fiber exploration techniques (Section 4.1) has been developed allowing interactive data exploration, clustering and classification. Therefore, parallel coordinates (Section 4.1.1) are linked to a scatter plot matrix (Section 4.1.2), the fiber class explorer (Section 4.1.3) as well as to 2D and 3D views. Furthermore, visualization techniques have been developed to give insight into the clustered fiber data at a higher level of abstraction. These widgets and techniques include the fiber orientation distribution (Section 4.2), the fiber length distribution (Section 4.3), the blob visualization (Section 4.4), and the fiber metadata visualization (Section 4.5).

4.1 Visual Fiber Exploration

Right after loading the dataset into the visualization pipeline, an *overview* of the data is presented in parallel coordinates (PC), in a scatter plot matrix (SPM) as well as in a 3D view. Following the visual information-seeking mantra described by Shneiderman [23], the data is divided into subclasses *(zoom and filter)*, which are displayed in turn in parallel coordinates and the scatter plot matrix.

The clutter and occlusion problem of the visualization may be considerably reduced using additional user-specified queries to the data (*details on demand*). Furthermore, the views of PC and SPM are linked together. Changes done in the parameter space will immediately be applied to the data (3D view and slice views) so that the user is able to get a real-time feedback when querying the data. This concept supports interactivity and makes the visual exploration process clearer and simpler.

4.1.1 Parallel Coordinates for Fibers

Parallel coordinates (PC) [11] is a powerful visualization technique using high-dimensional geometry for the analysis of multivariate data. Unlike in the Cartesian coordinate system, the axes are set up in parallel and equidistant to each other. A point in n-dimensional space is represented by a polyline crossing the n parallel axes. The position of the intersection on the jth axis corresponds to the value of the jth coordinate of the point. In the end each multidimensional point is represented by a polyline through the parallel axes. In the proposed approach parallel coordinates are used to initially classify fibers according to their individual characteristics. The number of fibers in a specimen ranges from several hundreds to hundreds of thousands and more and thus results in cluttering and occlusion. As too many lines are drawn between the parallel axes, the exploration process becomes very inefficient. Following the nested model for visualization design and validation [18] we examined our implementation and explored Axis Order Selection for parallel coordinates [19]. If axes representing fiber characteristics with hidden correlations are placed near to each other, the relationships between these characteristics are likely to become apparent. We then found that we will lose other potential correlations between the rest of the characteristics. After studying the coordinated parallel views for exploratory analysis of micro array time-course data [4], we took an approach which links a scatter plot matrix to enhance and refine the classification results of the PC.

4.1.2 Scatter Plot Matrix for Fibers

In addition to parallel coordinates a scatter plot matrix (SPM) [30] is used to visualize and reveal relationships such as dependencies, patterns and even outliers among all of the fiber characteristics. Additionally the scatter plot matrix serves as a refinement tool for the selection obtained using parallel coordinates. The scatter plot matrix used in our visualization pipeline consists of $n(n-1)/2$ scatter plots organized in a matrix. n represents the number of fiber characteristics used in the SPM. To avoid redundancy only the region below the main diagonal of the SPM is filled. A histogram of each fiber characteristic is shown in the main diagonal. Below this main diagonal a scatter plot is drawn for each pair of the characteristics. In the upper right corner an enlarged view of the selected scatter plot is displayed. In the enlarged view, and in the small charts as well, selections are done by drawing rectangles which will mark the selected data in red (*brushing*). These selections will be applied to all other scatter plots, the parallel coordinates as well as the 3D view (*linking*). In order to suggest initial classes of fibers a *k-means* algorithm [13] is used. The fiber characteristics depicted in the enlarged view are taken as input data for the automatic clustering. The total number of classes is specified by the user. Results of the classification can then be transferred to the *Fiber Class Explorer* or further refined in the parallel coordinates or the scatter plot matrix.

4.1.3 Fiber Class Explorer

The fiber class explorer lists all created classes of fibers and allows to add, modify or remove classes of interest. For each class the user may assign individual names and colors. In addition, for each class statistical information such as number of fibers (*Count*), the percentage of the fiber count (*Percent*), the *minimal*, the *maximal* and the *average* values of all fiber characteristics within a class are
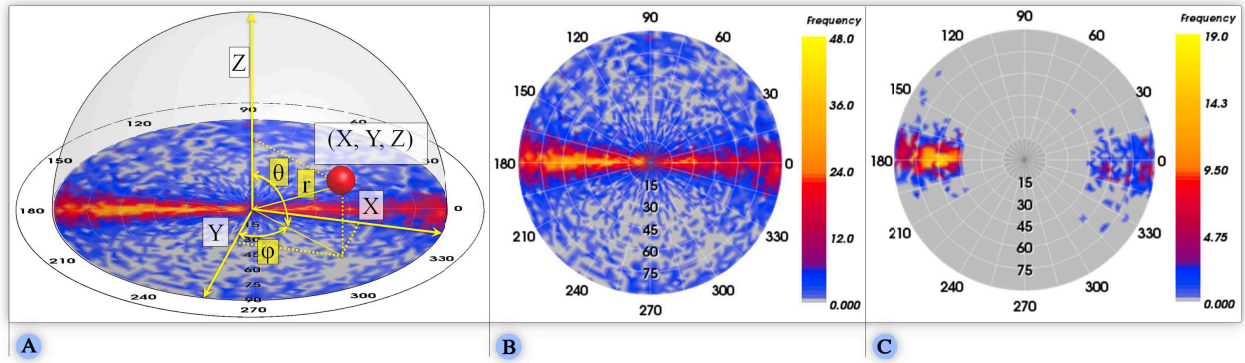
Figure 4: Fiber orientation distribution (FOD) in a PC plot. (A) Construction of the fiber orientations from Cartesian coordinates. (B) Global FOD (*dataset1*). (C) FOD of a single class (*dataset1*).

calculated. By clicking on a class of interest its elements are revealed and the individual properties of each fiber may be explored. It is also possible to check the 25 fiber characteristics individually. The checked features will be updated in the SPM and the PC immediately.

4.2 Fiber Orientation Distribution (FOD)

To visualize the fiber orientation, spherical coordinates are used. Figure 4A shows the construction of the fiber orientation from Cartesian coordinates. Here θ represents the polar angle measured from the zenith Z-direction. The azimuth angle φ lies in the XY-plane and is measured from the X-direction. Because of symmetry it is possible to depict all fiber orientations on a half sphere by specifying $\theta \in [0, \pi/2]$ and $\varphi \in [0, 2\pi)$. We discretize the northern half sphere with a user defined resolution and compute the frequency

Figure 5: Visualization of the individual fiber orientations. (A) The spherical color map. (B) A direct volume rendering of the fibers using color-coded orientations (*dataset2*).

of each discretized direction. This builds up the fiber orientation distribution (FOD). The azimuthal projection is later used to generate a 2D image of the FOD. Figure 4B depicts the global FOD of *dataset1*. The annotations around the outer circle represent the azimuthal angle and the annotations inside represent the polar angle. The color bar ranges from gray to yellow where gray encodes low frequency and yellow encodes high frequency. Gray is used to depict the orientations where no fibers are headed. In addition to the global FOD, we allow the computation of the orientation distribution for each manually defined class. The main orientations in both Figure 4A and Figure 4B are easily visible as yellow spots. A strong prevalence along the horizontal axis is present. The visualization of the FOD, which defines the mechanical loading capacity, is of great interest to the domain experts. We therefore applied a spherical color map (see Figure 5A) where the colors are mapped to the spatial fiber orientations. In order to highlight the X, Y and Z-direction of a dataset, we mapped these directions to red, green and blue respectively. Figure 5B shows a direct volume rendering of fibers by color coding the orientations with the spherical color map. This visualization allows easy identification of the fiber classes by their color.

4.3 Fiber Length Distribution (FLD)

In addition to fiber orientation visualization, an automatic algorithm is applied to classify and visualize the fibers according to their length. The calculation of the fiber length distribution (FLD) is very important for the experts to quickly represent the layout of short or long fibers in the volume. Thus conclusions about the loading capacity of the material can be drawn. Figure 6A shows the 3D rendering of a fiber length distribution and Figure 6B shows the corresponding histogram.

4.4 Blob Visualization

For the domain experts, it is important to gain a quick overview of the shape of each fiber class and the layer structure in order to analyze the material build-up of the final component. Due to the issues of overlap and occlusion the separation of the different fiber classes is frequently problematic using techniques like direct volume rendering. This task is becoming challenging especially for datasets with a very high fiber density that contains thousands of fibers. Based on the defined fiber classes in the *Class Explorer* we introduce a blob visualization (see Figure 7) by applying methods of implicit modeling as proposed by Bloomenthal et al. [3].

A blob in our application case is defined as a closed contour surface surrounding all fibers of a class. It provides the domain experts with an enclosure of the class and shows the spatial location
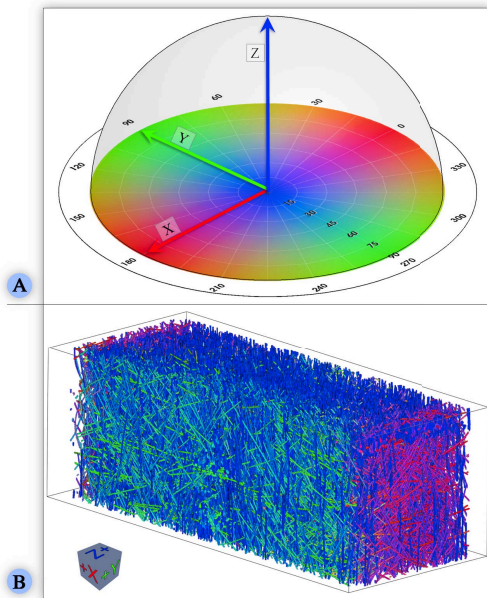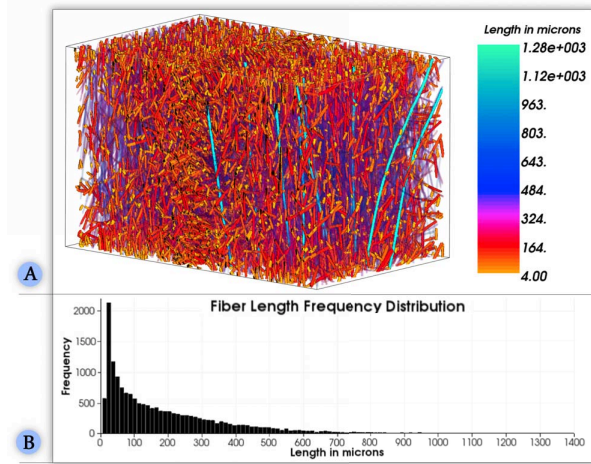
157

Figure 6: Visualization of the different fiber lengths. (A) 3D rendering of the fiber length distribution with the corresponding color map. (B) Fiber length distribution of *dataset1* shown in Figure 6A.
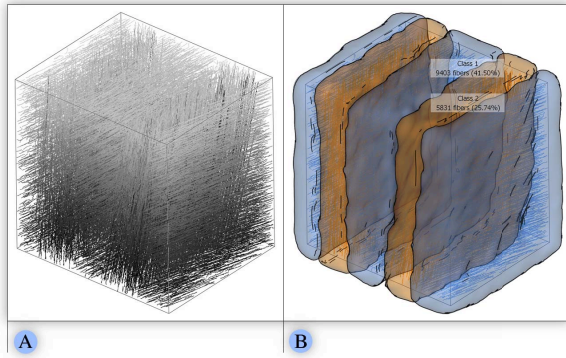

Figure 7: Blob visualization of *dataset3*. (A) 3D view of the dataset with unclassified fibers in gray. (B) 3D view of the blue and orange class with labeled blobs (*blue* Class 1, 9403 fibers (41.50%) and (*orange* Class 2, 5831 fibers (25.74%)).

and shape of the class within the data. To construct the blob surface we apply a distance-field based approach which is remotely similar to the metaballs method proposed by Blinn et al. [2]. For every fiber of the class we specify a line segment so that the start and the end points of a line segment correspond to the start and the end points of a fiber. This provides an approximation for straight and slightly curved fibers. Taking all line segments we can define the shape of a blob by the following distance function defined in 3D space:

$$\min_{i=1..m} d_i \leq threshold$$

where *m* is the number of line segments, d_i is the Euclidean distance to the given line segment and *threshold* is a parameter defining the blob size. To obtain a mesh of the blob surface we uniformly sample the distance function on a grid and then apply the marching cubes algorithm [17] with a corresponding threshold value. In some cases blobs determined from different fiber classes may overlap, which results in unclear or cluttered representations. To solve this issue we have modified the algorithm in a way that it removes overlapping by adjusting the blob shapes (see Figure 7A and 7B). We resolve

conflicts for those points belonging to more then one blob using the following approach: the point belongs to the closest blob with the closest fiber. For all the other blobs we set the distance function to infinity so that they do not include the point. This way the point will belong to the blob with the closest fiber, and the areas where blobs overlap will become separated based on the corresponding Voronoi diagrams. We further allow the user to define the minimal distance separating any pair of blobs. If the minimal separating distance is introduced, the point in an overlapping area is not assigned to any of the blobs if the difference between their distance functions in this point is greater than the separation distance. Each blob in the 3D view is marked with a label containing the name of the class and short class statistics: the number of fibers in the class and the percentage from the total fiber count. In order to enhance the shape perception of the blob, the user can enable a silhouette rendering mode. This mode shows the outline of the blob and highlights its sharp edges using black lines.

4.5 Fiber Metadata Visualization

As described in Task 3, domain users need a method to explore the data in order to find regions of interest (ROI). Due to the high information content, visualizations based on the original volume data are often not efficient. In order to provide a higher level overview of the fiber characteristics' distribution in the data we use a fiber metadata visualization approach. We subsample the original volume data with a user specified scaling-factor which results in a meta-volume, i.e., a volume made up of larger cells, typically 5 to 20 voxels each. We then calculate local characteristic values based on the fibers which at least partially lie in each cell of the meta-volume. The average value of each fiber characteristic is calculated from all fibers of a cell. The individual fiber characteristics are used as input data for calculating the meta-volume. We visualize the meta-volume as a context for the original volume data in the 3D
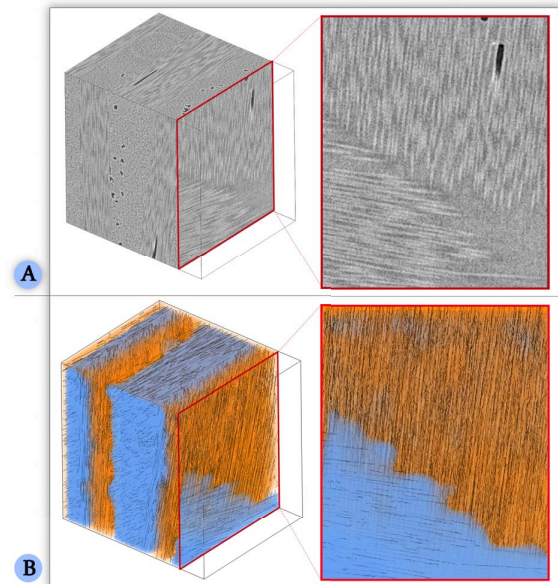

Figure 8: Fiber metadata visualization of *dataset3* in detail. (A) Left: 3D view of the original volume data set with a red border slice. Right: Slice view of the original dataset. (B) Left: 3D view of the meta-volume overlaid on the original volume data. Right: Slice view of the semi-transparent meta-volume overlaid on the original volume data with a linear blending.

158

view using multi-channel volume rendering (see Figure 8A) as well as overlaying in the 2D slice views. Figure 8B on the left, shows a meta-volume color coded according to the fiber orientation angle θ. An opacity indicator takes care of the overall adjustment regarding the opacity between the overlaid meta-volume and the original volume data in the slice views. Figure 8B on the right, shows the slice view of the meta-volume overlaid on the original volume data. The metadata visualization allows the user to pick a fiber characteristic of interest and to visualize the characteristic's distribution as a context. It enables a better visual exploration of the data by facilitating the identification of regions with similar or different fiber characteristics.

5 RESULTS AND EVALUATION

The generated results are demonstrated on different types of FRPs, i.e., one carbon fiber reinforced polymer and two glass fiber reinforced polymer specimens (see Section 5.1). A questionnaire to evaluate all presented methods was prepared and filled out by domain experts. The results outline the usability of the presented methods from the perspective of domain experts (see Section 5.2).

5.1 Visualization Results

Original Volume Data: As shown in in Figure 2 (input data), fiber classes or fiber orientations of *dataset1* are difficult to identify.
Visual Fiber Exploration Method: After the visual exploration process, the user is able to apply a multi-class rendering process to the manually defined classes. All fibers are colored according to their specific fiber class color in the parallel coordinates, scatter plot matrix and the 3D renderer. Figure 1 on the right and in the middle (blob visualization combined with multi-class rendering) depicts the manually defined classes for *dataset1*. All the classes can be clearly identified.
Orientation Identification: Figure 5 depicts the 3D view of the extracted fibers (*dataset2*) color coded according to the spherical color map (Figure 5A). The fiber orientations can be clearly identified. The color coding is applied to the 3D view and the 2D slices.
Fiber Length Distribution: An automatic algorithm is applied to classify and visualize the fibers according to their length. Figure 6 shows the color coding of the extracted fibers (*dataset1*) with respect to fiber length.
Blob Visualization: To provide the domain experts with an enclosure of all their defined classes, we applied the concept of blob visualization. This allows the domain experts to gain a quick overview of the specimens layer structure and the shape of the fiber classes. Figure 7 illustrates the blob visualization based on *dataset3*.
Fiber Metadata Visualization: A 3D view of the meta-volume (*dataset3*) color coded according to the fiber characteristic θ is shown in Figure 8 on the left. Orange represents a θ value between $0°$ and $10°$ and indicates that the fiber orientation is aligned to the Z-axis. Blue represents a θ value between $80°$ and $90°$ and denotes fibers which are aligned orthogonally to the Z-direction. The slice views (see Figure 8 on the right) with reduced opacity information clearly indicate a layer structure of the specimen.

5.2 Evaluation and User Feedback

The necessity of individual and interactive fiber visualizations originates from the requirement of non-destructive testing (NDT). During *FiberScout* development over a period of more than 18 months, improvements of the fiber visualization pipeline were constantly done together with the NDT practitioners. In order to get feedback on the *FiberScout* system, we designed an evaluation questionnaire with regard to the tasks defined by the domain experts (see Section 1). The questionnaire is structured so that the experiences of the participants with XCT are collected first. Then it is determined how suitable PC and SPM is for classifying the fibers. In addition,
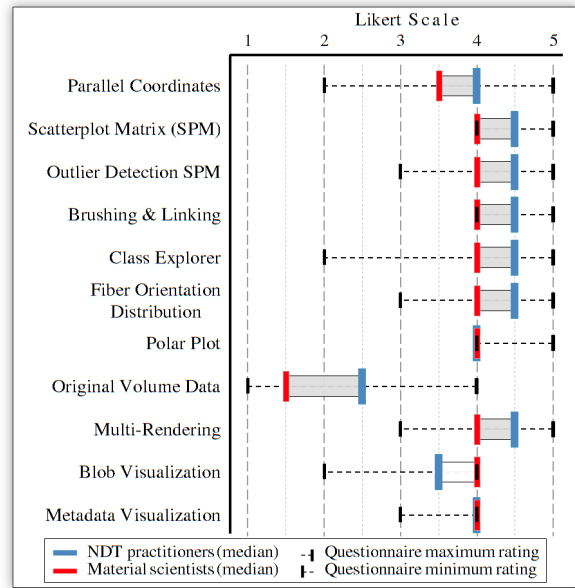

Figure 9: Averaged results of the evaluation questionnaire.

the usefulness of the statistical information of the fiber class explorer is determined. After that we tried to find out how the FOD is applicable for displaying fiber orientations. It is then checked if the fiber classes can be well distinguished by the blob visualization. Finally, it is determined how well metadata visualization suffices to indicate general fiber orientations. To evaluate the questionnaire we choose four NDT practitioners, who are familiar with X-ray computed tomography and its visual representations, and four material scientists, which are experienced in analyzing fiber reinforced polymers. The averaged and weighted results of the evaluation questionnaire are depicted in Figure 9. The red line represents the results of the material scientists while the blue one displays the results of the NDT practitioners. We use a Likert scale ranging from 1 to 5 to represent the user experience, varying from poor to excellent. The fiber visualization pipeline on the whole received good feedback from the domain experts. The SPM was considered as best suited for clustering fiber characteristics. By linking the SPM and PC the relationships between the fiber characteristics can be easily revealed. Outliers in the SPM are obvious to be detected. In addition the participants pointed out that further material phenomena such as porosity are easily observable. The orientation visualization is simple and self-explanatory. The main fiber orientation can be easily determined using the polar plot for the FOD. Both the NDT practitioners and the material scientists reckon that it is difficult to generate useful information of fiber characteristics using the original volume data. Blob and metadata visualization also provide valuable results for separating fiber classes. Furthermore, a difference in the results between NDT practitioners and material scientists is found in the outlier detection using the blob visualization. NDT practitioners perceive that it is obvious and simple to detect outliers, while the material scientists score this technique low.

6 SUMMARY AND CONCLUSIONS

We presented the *FiberScout*, a visualization system for the visual analysis of fiber characteristics in fiber reinforced polymers. The user feedback shows overall good results from domain experts, especially concerning clustering with the help of the SPM with *brushing & linking* and the visualization of the fiber orientation distribu-

159

tion. The metadata visualization allows the user to quickly explore the data and find regions of interest. The blob visualization is an appreciated technique to represent regions with the same characteristics in a volume. One shortcoming of the current implementation is that the analysis is limited to approximately 100.000 fibers. In case of one million fibers, the calculation times would last much longer. This fact could be counteracted by parallelizing appropriate code sections. Another problem relates to the PC and the SPM which are cluttered if too many fiber features are selected. For future work, the calculation of additional statistics and the selection of individual fibers in the 3D view can be mentioned. The experts indicated that combining the porosity information and the fiber characteristics of a specimen would be important for them in the future.

ACKNOWLEDGEMENTS

REFERENCES

[1] H. Altendorf and D. Jeulin. 3D Directional Mathematical Morphology for Analysis of Fiber Orientations. *Image Analysis & Stereology*, 28(3), 2009.

[2] J. F. Blinn. A Generalization of Algebraic Surface Drawing. *ACM Trans. Graph.*, 1(3):235–256, July 1982.

[3] J. Bloomenthal and B. Wyvill. Interactive Techniques or Implicit Modeling. *SIGGRAPH Comput. Graph.*, 24(2):109–116, March 1990.

[4] P. Craig, J. Kennedy, and A. Cumming. Coordinated Parallel Views for the Exploratory Analysis of Microarray Time-course Data. In *Proceedings of the Coordinated and Multiple Views in Exploratory Visualization*, CMV '05, pages 3–14, Washington, DC, USA, 2005. IEEE Computer Society.

[5] L. Fritz, M. Hadwiger, G. Geier, G. Pittino, and M. E. Gröller. A Visual Approach to Efficient Analysis and Quantification of Ductile Iron and Reinforced Sprayed Concrete. *IEEE Transactions on Visualization and Computer Graphics*, 15(6):1343–1350, 2009.

[6] S.-Y. Fu and B. Lauke. Effects of Fiber Length and Fiber Orientation Distributions on the Tensile Strength of Short-Fiber-Reinforced Polymers. *Composites Science and Technology*, 56(10):1179–1190, 1996.

[7] H. Guo, H. Xiao, and X. Yuan. Multi-Dimensional Transfer Function Design based on Flexible Dimension Projection embedded in Parallel Coordinates. In *Proceedings of the 2011 IEEE Pacific Visualization Symposium*, PACIFICVIS '11, pages 19–26, Washington, DC, USA, 2011. IEEE Computer Society.

[8] M. Hadwiger, L. Fritz, C. Rezk-Salama, T. Höllt, G. Geier, and T. Pabel. Interactive Volume Exploration for Feature Detection and Quantification in Industrial CT Data. *IEEE Transactions on Visualization and Computer Graphics*, 14(6):1507–1514, 2008.

[9] C. Heinzl. *Analysis and Visualization of Industrial CT Data*. PhD thesis, Institute of Computer Graphics and Algorithms, Vienna University of Technology, 12 2009.

[10] R. Huang, K.-L. Ma, P. McCormick, and W. Ward. Visualizing Industrial CT Volume Data for Nondestructive Testing Applications. In *Proceedings of the 14th IEEE Visualization 2003 (VIS'03)*, pages 547–554, Washington, DC, USA, 2003. IEEE Computer Society.

[11] A. Inselberg and B. Dimsdale. Parallel Coordinates: A Tool for Visualizing Multi-Dimensional Geometry. In *Proceedings of the 1st conference on Visualization '90*, VIS '90, pages 361–378, Los Alamitos, CA, USA, 1990. IEEE Computer Society Press.

[12] B. Jackson, T. Y. Lau, D. Schroeder, K. C. Toussaint, and D. F. Keefe. A Lightweight Tangible 3D Interface for Interactive Visualization of Thin Fiber Structures. *Visualization and Computer Graphics, IEEE Transactions on*, 19(12):2802–2809, 2013.

[13] T. Kanungo, D. Mount, N. Netanyahu, C. Piatko, R. Silverman, and A. Wu. An Efficient k-Means Clustering Algorithm: Analysis and Implementation. *IEEE Transactions on Pattern Analysis and Machine Intelligence*, 24(7):881–892, Jul 2002.

[14] D. A. Keim. Information Visualization and Visual Data Mining. *IEEE Transactions on Visualization and Computer Graphics*, 8(1):1–8, 2002.

[15] X. Kuang, H. Zhang, S. Zhao, and M. McGuffin. Tracing Tuples Across Dimensions: A Comparison of Scatterplots and Parallel Coordinate Plots. *Comp. Graph. Forum*, 31:1365–1374, June 2012.

[16] B. Li, X. Zhao, and H. Qin. 4-Dimensional Geometry Lens: A Novel Volumetric Magnification Approach. *Computer Graphics Forum*, 2013.

[17] W. Lorensen and H. Cline. Marching Cubes: A High Resolution 3D Surface Construction Algorithm. In *ACM SIGGRAPH Computer Graphics*, volume 21, pages 163–169, 1987.

[18] T. Munzner. A Nested Model for Visualization Design and Validation. *IEEE Transactions on Visualization and Computer Graphics*, 15(6):921 –928, nov.-dec. 2009.

[19] H. Qu, W.-Y. Chan, A. Xu, K.-L. Chung, K.-H. Lau, and P. Guo. Visual Analysis of the Air Pollution Problem in Hong Kong. *IEEE Transactions on Visualization and Computer Graphics*, 13(6):1408–1415, Nov. 2007.

[20] C. Red. Aviation Outlook: Composites in General Aviation 2011-2020. *High-Performance Composites*, May 2012.

[21] K. Robb, O. Wirjadi, and K. Schladitz. Fiber Orientation Estimation from 3D Image Data: Practical Algorithms, Visualization, and Interpretation. In *Proceedings of the 7th International Conference on Hybrid Intelligent Systems*, HIS '07, pages 320–325, Washington, DC, USA, 2007. IEEE Computer Society.

[22] D. Salaberger, K. A. Kannappan, J. Kastner, J. Reussner, and T. Auinger. Evaluation of Computed Tomography Data from Fibre Reinforced Polymers to Determine Fibre Length Distribution. In *International Polymer Processing*, volume 3, pages 283–291, 2011.

[23] B. Shneiderman. The Eyes Have It: A Task by Data Type Taxonomy for Information Visualizations. In *Proceedings of the 1996 IEEE Symposium on Visual Languages*, VL '96, pages 336–343, Washington, DC, USA, 1996. IEEE Computer Society.

[24] J. Sloan. Carbon Fiber Market: Cautious Optimism. Composites world (accessed on 02.09.2013 18:37), 3 2011. http://www.compositesworld.com/articles/carbon-fiber-market-cautious-optimism.

[25] M. Stommel, M. Stojek, and W. Korte. *FEM zur Berechnung von Kunststoff- und Elastomerbauteilen*. Carl Hanser Verlag, 2011.

[26] A. Tatu, F. Maas, I. Farber, E. Bertini, T. Schreck, T. Seidl, and D. Keim. Subspace Search and Visualization to make Sense of Alternative Clusterings in High-Dimensional Data. In *IEEE Conference on Visual Analytics Science and Technology (VAST)*, pages 63–72, 2012.

[27] M. Teßmann, S. Mohr, S. Gayetskyy, U. Hassler, R. Hanke, and G. Greiner. Automatic Determination of Fiber-Length Distribution in Composite Material using 3D CT Data. *EURASIP J. Adv. Signal Process*, 2010:1:1–1:9, Feb. 2010.

[28] C. L. Tucker and E. Liang. Stiffness Predictions for Unidirectional Short-Fiber Composites: Review and Evaluation. *Compos Sci Technol*, 59:655–671, 1998.

[29] VGStudioMAX. VolumeGraphics - VGStudioMAX 2.2. http://www.volumegraphics.com/, 2013.

[30] P. C. Wong and R. D. Bergeron. 30 Years of Multidimensional Multivariate Visualization. In *Scientific Visualization, Overviews, Methodologies, and Techniques*, pages 3–33, Washington, DC, USA, 1997. IEEE Computer Society.

[31] B. Yamrom, J. A. Sutliff, and A. P. Woodfield. Visualizing Polycrystalline Orientation Microstructures with Spherical Color Maps. In *Proceedings of the conference on Visualization '94*, VIS '94, pages 46–51, Los Alamitos, CA, USA, 1994. IEEE Computer Society Press.

[32] X. Zhao and A. Kaufman. Multi-Dimensional Reduction and Transfer Function Design using Parallel Coordinates. In *Proceedings of the 8th IEEE/EG international conference on Volume Graphics*, VG'10, pages 69–76, Aire-la-Ville, Switzerland, 2010. Eurographics Association.

[33] H. Zhou, W. Cui, H. Qu, Y. Wu, X. Yuan, and W. Zhuo. Splatting the Lines in Parallel Coordinates. *Comput. Graph. Forum*, pages 759–766, 2009.

GEMSe:
Visualization-Guided Exploration of Multi-channel Segmentation Algorithms

BERNHARD FRÖHLER, TORSTEN MÖLLER, CHRISTOPH HEINZL

GEMSe: Visualization-Guided Exploration of Multi-channel Segmentation Algorithms

B. Fröhler[1,2], T. Möller[2], and C. Heinzl[1]

[1]University of Applied Sciences Upper Austria, Research Group Computed Tomography, Wels, Austria
[2]University of Vienna, Faculty of Computer Science, Visualization and Data Analysis Research Group, Vienna, Austria

Abstract

We present GEMSe, an interactive tool for exploring and analyzing the parameter space of multi-channel segmentation algorithms. Our targeted user group are domain experts who are not necessarily segmentation specialists. GEMSe allows the exploration of the space of possible parameter combinations for a segmentation framework and its ensemble of results. Users start with sampling the parameter space and computing the corresponding segmentations. A hierarchically clustered image tree provides an overview of variations in the resulting space of label images. Details are provided through exemplary images from the selected cluster and histograms visualizing the parameters and the derived output in the selected cluster. The correlation between parameters and derived output as well as the effect of parameter changes can be explored through interactive filtering and scatter plots. We evaluate the usefulness of GEMSe through expert reviews and case studies based on three different kinds of datasets: A synthetic dataset emulating the combination of 3D X-ray computed tomography with data from K-Edge spectroscopy, a three-channel scan of a rock crystal acquired by a Talbot-Lau grating interferometer X-ray computed tomography device, as well as a hyperspectral image.

Categories and Subject Descriptors (according to ACM CCS): I.3.8 [Computer Graphics]: Applications—- I.4.6 [Image Processing and Computer Vision]: Segmentation—Pixel classification

1. Motivation

Many scientific disciplines such as material sciences [CCK*14], medicine [GFL04] or geosciences [KLF*15] attempt to gain novel insights by acquiring and analysing two- or three-dimensional datasets from a specimen of interest. In most cases, image analysis techniques focus on data acquired by one scanning modality returning a single data value for each spatial location. However, data from single scanning modalities may return unclear or ambiguous responses, or may not deliver all information that is needed. Material scientists, for example, often require the exact topological details of a specimen along with minuscule structural deficiencies as well as information on its chemical composition [AFK*14]. To address these demands, the analysis strategies are increasingly adapted to measuring the same scene or specimen using multiple techniques, resulting in a so-called multi-modal dataset, where multiple measurement values are available per dataset location. At times a single scanning modality can also result in multiple measurement values per dataset location. Here, we will use the term multi-channel to refer to any dataset or image where multiple values are available per spatial position.

Image segmentation, the process of partitioning an image into regions sharing common properties, is a very important step of the image analysis workflow in many domains. In industrial applications it is for example essential in quantifying features of interest, such as voids or defects, or constituent components of a material system like fibers, particles or their surrounding material. Many different segmentation algorithms have been developed, typically tailor-made for a specific target domain. Adapting and parameterizing segmentation pipelines to new modalities or to different inputs is time-consuming and non-trivial. Typically no segmentation expert is at hand to lend her expertise to the domain scientist. Often, there is also no objective measure available and therefore no automatic optimization can be performed. Thus, domain experts can only determine whether a segmentation result is meaningful through visual inspection.

Considering multiple channels of information during segmentation leads to complex algorithms with many input parameters which require careful tuning. Domain scientists, being no segmentation experts, typically have no guidance available for this tuning procedure. The traditional way to determine the influence of the segmentation pipeline's parameters on the result is to manually perform iterative trial and error steps.

We therefore see a strong need for approaches to evaluate the input parameter space and the result space of segmentation algorithms for multi-channel images. A tool implementing these methods will allow domain experts to arrive at optimal segmentation

results for their multi-channel images without ground truth information available and without having advanced expertise in image segmentation. We developed and implemented GEMSe to address this problem. The main contributions of our work are found in the following points:

- Methods for exploring and analyzing the input parameter and result space of a segmentation pipeline.
- Implementing these methods in GEMSe, which guides users towards choosing adequate segmentation parameter values leading to optimal results for a specific kind of dataset.
- Evaluation of the usability of GEMSe in various case studies of different application domains.

2. Related Work

Visually supporting segmentation algorithms of 3D data has been one of the most researched topics in the visualization community. The typical approach is through defining a transfer function [HKRs*06]. For an overview of different transfer function approaches we refer the reader to a recent survey [AD10]. However, transfer functions suffer from two problems. On the one hand they are not very intuitive to use. On the other hand, they are not able to properly segment very complex modalities.

The area of computer vision in general and medical imaging in particular have been focused on developing very sophisticated segmentation algorithms. One of the most widely used approaches today is the random walker algorithm [Gra05]. Hence we are using this algorithm in our approach. However, we are not limited to this algorithm and it could be exchanged with any other. Visually supporting such a segmentation pipeline has also been studied in the visualization community. Saad et al. [SMH10, SHM10] were some of the first to provide visual support to explore the capabilities of the random walker algorithm. Their focus was to use the probabilistic features of the algorithm in order to find anomalies in the segmentation that might uncover tumor tissue. Praßni et al. [PRH10] as well as Top et al. [THA10] introduced approaches to use the segmentation uncertainty to query the user for input where the labeling is too uncertain.

However, in this work we are not focusing on the uncertainty information of the algorithm thus far. Instead we are dealing with the problem of finding good parameter settings for the segmentation algorithm to perform well. Systematically exploring the parameter space of algorithms has become an important research topic in the visualization community over the last few years. Sedlmair et al. [SHB*14] present a recent overview and taxonomy of the approaches in the literature. Using this approach, Tuner [TWSM*11] as well as Paramorama [PBCR11] are possibly the two approaches most closely related to our work.

Tuner was developed for medical image segmentation experts to help them fine-tune a particular energy model. Hence, it required a ground-truth segmentation or at least one objective quality measure in order to function properly. However, in our approach we aim to support domain experts (that are not necessarily algorithmic experts in segmentation) and we do not require any ground truth or objective measure. Instead we navigate the user through segmentation space and rely on visual inspection to help find proper

segmentations. Hence, the interfaces of Tuner and GEMSe have no resemblance (although they provide similar functionality).

Paramorama [PBCR11] on the other hand lets the user browse through a large collection of segmented images. A specialized layout algorithm allows users to manually compare the label images in one or more clusters. While they require using uniform sampling on a fixed cartesian grid, which does not scale well, we can employ any sampling method. They cluster by parameter values whereas we cluster by result similarity.

The major difference of our approach to all these previous work is that we (a) provide a general segmentation framework for many different image modalities, and (b) that we are focusing on multi-channel data. To the best of our knowledge, none of the previous work has these capabilities.

3. Problem Characterization

The main challenge this work addresses is analyzing the input parameter space of segmentation algorithms for multi-channel data and the set of potential label images that they can produce. This problem can be categorized as visual parameter space analysis, as systematized by Sedlmair et al. [SHB*14]. The input is a multi-channel, two- or three-dimensional dataset with an arbitrary number of channels per location. We will use the word *image* to denote conventional 2D images as well as 3D volumes. Our segmentation pipeline furthermore takes a parameter set as input, consisting of various numeric or categorical parameters. A detailed description of the particular parameter set we investigated is given in Section 4.1. The output of one segmentation run is referred to as label image, which is a single-channel image. As derived output, we calculate the count of connected components in the label image, and record the time required by the segmentation algorithm. We used the count of connected components, or *object count*, mainly because it was used by the domain scientists we worked with, but also because it was used in the Paramorama tool [PBCR11]. Measuring the performance is intended for a trade-off analysis between result suitability and algorithm speed.

We sample over the parameter space of this model, resulting in a collection of label images, henceforth referred to as ensemble. Each label image is linked to the parameter set that produced it and its derived output. We provide a global-to-local approach to explore this ensemble.

3.1. Tasks

Through collaborating with domain scientists working on segmenting industrial multi-channel datasets and analyzing their current workflow and analysis needs, the following tasks to be solved were identified:

- **T1**: Get an overview over the possible results produced by the algorithm.
- **T2**: Analyze the influence of input parameters on the output images and their correlation to derived output.
- **T3**: Find stable parameter combinations which produce suitable segmentation results as determined by visual inspection.

In terms of Sedlmair et al. [SHB*14], T1 and T2 fall into the partitioning category, as they are applied to get an insight into what variation of results can be achieved. T3 is a combination of optimization and sensitivity analysis – users first want to arrive at ranges of parameter values producing suitable results, and then identify those regions where the results are insensitive to slight parameter changes.

4. GEMSe Design

For a given multi-channel image we first perform preprocessing as schematized in Figure 1. The analysis work is subsequently done through the main interface of GEMSe as shown in Figure 2.
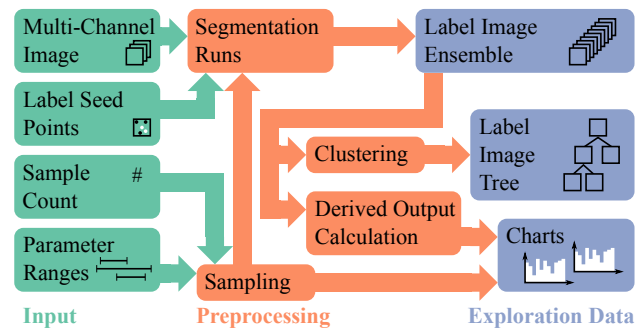
4.1. Preprocessing

Figure 1: *Overview over input, preprocessing pipeline and the data explored by GEMSe.*

As depicted in Figure 1, preprocessing starts by sampling the parameter space of a segmentation pipeline. For this purpose users can either use default parameter ranges or refine ranges if they already have a preconception of where suitable results are more likely to occur, for example from a previous sampling run. We assemble parameter sets according to the chosen sampling method and parameter ranges. The result of a single run of the segmentation pipeline is referred to as label image. We perform one segmentation run for each parameter set, resulting in an ensemble of label images. We calculate the object count as the count of connected components of all resulting label images, a simple derived output which can help in determining the segmentation quality, as will be shown in our case studies. On the ensemble we finally perform hierarchical clustering using maximum linkage [FLPZ51]. For that we initially set up each label image as leaf cluster and calculate pairwise similarities as sum of the dice metric [Dic45] calculated for each label. These preprocessing steps typically take a long time (in the range of several hours to days depending on the used hardware) and are therefore performed in advance and detached from the result exploration.

For segmentation, we have adopted a multi-channel segmentation framework around the Support Vector Machine (SVM) classification algorithm and the Extended Random Walker (ERW) segmentation algorithm [Gra05]. Our current sampling tool uses this SVM+ERW-based segmentation pipeline but could be easily adapted to run any other segmentation pipelines or algorithms.

Common parameters

SVM	C_{svm}	soft classification penalty
	γ_{svm}	Gaussian RBF kernel width parameter
	n_{svm}	number of channels to consider
ERW	β_{erw}	normalization neighborhood weight
	γ_{erw}	weight of prior model vs. neighborhood
	m_{erw}	max. number of iterations in linear solver

Modality-specific parameters

ERW	pca_i	number of PCA components considered for channel i
	w_i	channel i weight in neighborhood information
		$i \in [1..N]$, N = number of image channels
	$dist_i$	Distance metric used for channel i

Table 1: *Parameters to our custom segmentation framework.*

We have chosen both algorithms because they are successfully used in many application domains, for example in medical sciences [GFL04] and the geosciences [KLF*15]. In this setup, there are six common parameters and two to three additional parameters per data modality in use to our segmentation pipeline, which are summarized in Table 1. In addition to input parameters, the SVM takes seed points for each label as input. We use the same set of seed points, predetermined by the user, for each segmentation run of the same dataset at the moment.

4.2. Result Exploration Interface

Figure 2 shows the main interface of GEMSe. Its layout is partially fixed, meaning that the single views cannot be moved around, but they can be resized to enlarge areas of interest. We initially considered a vertically panning screen similar to Bederson and Meyer's Pad++ system [BM98], so that we would not be limited to the size of a single screen, and to better separate the different analysis layers. We found the downsides of such an approach, namely the lack of overview and the confusion of the user having to switch through many screens, to outweigh the benefits and therefore discarded that idea.

In our interface there are seven linked views. A *cluster tree view* (Figure 2a) displays the hierarchy resulting from our clustering, the *cluster example view* (Figure 2d) displays characteristic images from the selected cluster, the *detail view* (Figure 2b) shows a large version of the currently selected image, the *slice view* (Figure 2c) enables switching between the three possible axis-aligned slice views as well as changing the currently shown slice, the *histogram view* (Figure 2g) shows histograms for input parameters and derived outputs, the *scatterplot view* (Figure 2f) correlates input parameters with derived outputs, and finally the *favorite bar* (Figure 2e) keeps track of preferred images. All interactions in an image view are instantaneously propagated to all other image views for better comparison. Label images are color-coded using a qualitative scheme from ColorBrewer [HB03]. the datasets we studied so far only required 2-7 labels, so we do not see a problem in the limitation to a maximum of twelve colors.

The *cluster tree view* (Figure 2a) shows an interactive tree view of the cluster hierarchy. Visual appearance and interaction methods resemble those from the folder view in a file explorer such as Windows Explorer. For each cluster a node with the number of con-
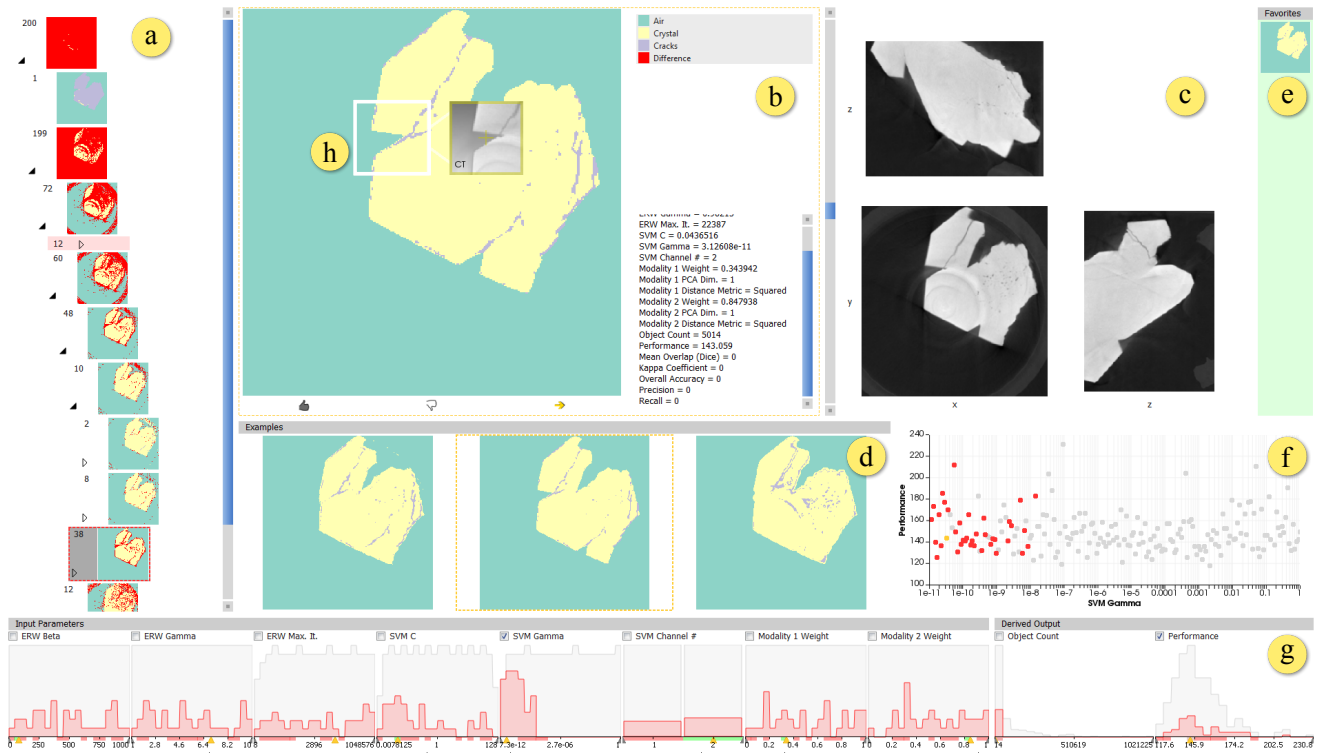
Figure 2: *Main interface of GEMSe: (a) cluster tree view, (b) detail view, (c) slice view, (d) cluster example view, (e) favorite bar, (f) scatterplot view, (g) histogram view, (h) magic lens showing original image*

tained samples is shown alongside a *cluster representative* image. For a leaf node in our hierarchy, the representative is the label image contained in it. For internal nodes, this image should give an overview over amount and location of differences in the label images of this cluster. Our first idea was to show the medoid of the label images in the cluster. Another option we considered was to calculate an average image from all the masks. A medoid, being a single label image, same as an average image, can not give an adequate impression of the range of images contained in the cluster. An average *label image* is furthermore not meaningful, since it does not necessarily represent any single member of the cluster. We therefore implemented a visual metaphor following similar ideas as the homogeneity view introduced by Malik et al. [MHG10]. All pixels which have the same label in all samples retain that labeling, and all other pixels are replaced with a marker color not used for labeling. This directly visualizes the regions of the image in which a cluster contains variation. The system tries to minimize the space used by the tree. It automatically hides the preview images of parent and sibling nodes when expanding a tree node as well as nodes that are marked as unsuitable. The cluster tree view is mainly addressing task T1. Since selections of a node in the cluster tree view result in linked updates in all other views, it also acts as main interaction hub. Task T3 is mainly solved through the interaction of all views, therefore the cluster tree view plays a vital role in addressing it.

The *cluster example view* (Figure 2d) shows a number of exemplary label images from the currently selected cluster. These are se-

lected so that they represent the variation in the cluster, supporting the overview task T1. The number *n* of label images to be shown is determined based on the available space. Following the idea of Krishnamachari and Abdel-Mottalebof [KAM99], we choose leafs from a parent cluster in the same relation as the number of leafs in each child cluster. In case we need to choose a single item from a cluster which is no leaf, a random child is picked. This is executed recursively, and will lead to *n* images, or less if the number of leafs in the selected cluster is smaller than *n*.

Depending on the previous interaction, the *detail view* (Figure 2b) shows an enlarged version of either the cluster representative selected in the cluster tree view, or a label image selected in the cluster example view. The border color of the view indicates the current state, red indicating a cluster representative, yellow a single label image. Next to the image additional detail information about the parameter sets producing the label images in this cluster, and the cluster ID are displayed as can be seen on the right side of Figure 2b. Comparison to the original images is enabled through a magic lens (Figure 2h). Additionally, users are presented with interaction elements to positively or negatively rate a segmentation result, and to navigate towards a specific label image, as can be seen in the bottom of Figure 2b.

In the *histogram view* (Figure 2g), we followed the idea of scented widgets [WHA07] and implemented histograms for all parameters and derived outputs which are connected to filter sliders on the axes. The view is designed to address task T2, the analysis of

correlations between clusters of label images and input parameters or derived output. By default our histograms show the result count on the vertical axis over the respective parameter or derived output on the horizontal axis. The horizontal axis is scaled linearly or logarithmically depending on the way the parameter was sampled. The data of the whole result space is shown in gray, data of the selected cluster is shown in red, the same color that is used for highlighting a selected cluster in the cluster tree view. When a single example image is selected, its parameters are marked with yellow arrows on the horizontal axis.

The *slice view* (Figure 2c) is intended for navigation through the whole image. The original image is shown for comparison with label images in the form of three axis-aligned slicer images, as domain experts are used to such slice views. Selecting one of the three small slicers changes the slice axes for all previews. Providing a 3D view was considered in the design process of GEMSe, but we observed that the domain scientists we collaborated with tended to rarely use 3D visualizations of the dataset, and preferred slice views due to their better interpretability. The *favorite bar* (Figure 2e) is used for collecting intermediate results for later reference. With it we address the issue that when analyzing any large collection, it is easy to get lost or to loose track of previous findings. The *scatterplot view* (Figure 2f) shows a correlation of two attributes marked in the histogram view, intended for addressing task T2. The data points of the currently selected cluster, potential filter ranges and example image selections are highlighted here as well.

Ensemble members or whole clusters can be marked as suitable or unsuitable. This results in a color-coding on the x-axes of the parameter histograms, which enables the correlation of input parameter ranges to segmentation quality.

5. Implementation

We implemented GEMSe as a standalone application in a custom C++ application framework built on top of the Qt framework, using VTK [SML06] and ITK [YAL*02] libraries for visualization and image processing. The sampling of the segmentation parameter space, resulting in the ensemble of segmentation masks, was implemented inside the same framework. For the segmentation framework we used the libSVM library [CL11], our extended random walker calculation is built on top of the Eigen v3 linear algebra library [GJ*10]. The source code of our tool will be made available on https://github.com/3dct.

6. Evaluation

We applied two different types of evaluation to our prototype. First we conducted usability interviews to refine visualization and interaction methods. This lead to an improved version of our tool, addressing the main concerns raised during these interviews. We subsequently used this improved tool in several real world as well as synthetic scenarios.

6.1. Usability Evaluation

GEMSe was developed in constant collaboration with domain experts in material science. Our design was therefore heavily influenced by their input. To evaluate and improve its usefulness on
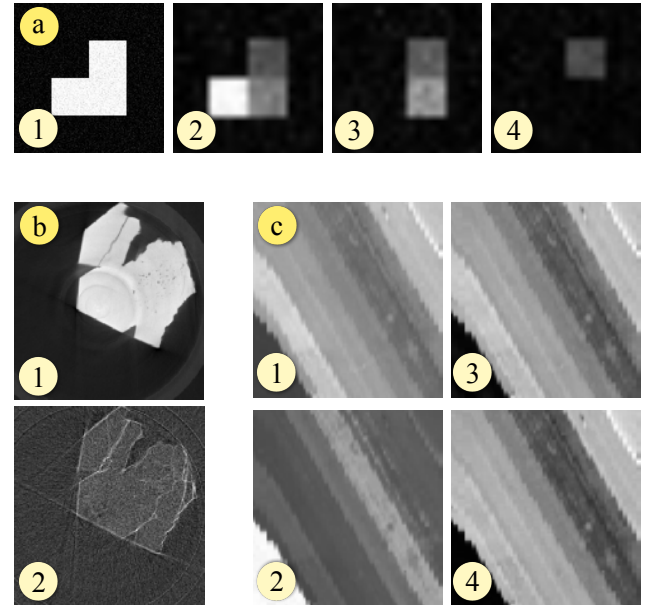

Figure 3: *Datasets used in our case studies: Attenuation image (a1) and three K-Edge element maps (a2-a4) of the synthetic K-Edge dataset. Attenuation image (b1) and dark field image (b2) of the middle slice along x-y-axis of the rock crystal TLGI-XCT scan. Channels 26(c1), 46(c2), 125(c3) and 176(c4) from the SalinasA hyperspectral dataset.*

a broader scale, we asked five visualization professionals to take a look at our tool. Following the best practices established by Nielsen [Nie00], we performed approximately one-hour long interviews over the course of four weeks. We used the small synthetic dataset as shown in Figure 3a for the evaluation. We first introduced each user to our tool. Then we encouraged them to interact with the tool to get acquainted with the modes of interaction. During this phase, our users implicitly addressed task T1 from Section 3.1, namely to get an overview over the possible results. Subsequently we posed two explicit exercises for them to solve through the help of our tool: The first exercise consisted of finding out what was the determining factor for the small amount of obviously unsuitable label images in the synthetic example as shown in Figure 5(a5), a specific instance of task T2. The second, more open-ended exercise was to find the visually most satisfying segmentation result and deducing reasonable and stable parameters for segmenting this dataset, basically task T3. We observed our users in performing these tasks and took notes on how they were doing. Additionally, we encouraged them to comment on their current thoughts. For all sessions we recorded screen captures and the conversation. We used this feedback to improve our software prototype, in order to arrive at the most effective ways of visualization and interaction.

Users started their exploration with the root node of the hierarchical clustering selected. To get an overview over the possible results, three of our users navigated down in the tree hierarchy, checking cluster representatives and continuing in the direction of the result which matched their expectation most. Interest-

ingly, the benefits of the cluster example view were controversial. Two users reported that they found the view tremendously helpful and used it as their main navigation cue, chose the label image that they found most suitable, and navigated towards that image. Two users did not use it at all and commented that they found it confusing. We think this suggests different interaction preferences in our users, both of which our tool supports. For the first exercise, finding the parameter responsible for a cluster of unsuitable label images, most of our users observed the histogram view while switching between clusters. Within at most one minute all of our users spotted the parameter γ_{erw} mainly responsible for the difference. Most users required encouragement by the interviewer to employ filtering, facilitated through the slider handles below the histograms, which could also have helped solving this exercise. Once aware, our users commented very positively on this feature, especially the immediate feedback in the cluster hierarchy. There, the number of masks matching the current filter is shown alongside the number of all masks in that cluster, and clusters with all contained label images outside of the filter range are minimized. The scatterplot view, which would allow detailed correlation analysis, was also only used after a reminder by the interviewer. It was not perceived as that helpful. It might not be required at all, but might be used more if it had permanent visibility and deeper integration into the linked views.

For our second exercise, users continued their exploration as they did while getting an overview. They typically arrived at a broad range of parameters suitable for the dataset within a few minutes. We received as common feedback that it was perceived as hard to arrive at a final stable parameter region. A part of these users missed methods to compare the parameter ranges in which favorites were located. The second remark in this direction was that it is hard to spot whether there are any bigger differences left in a cluster. Some users commented that it would be useful to zoom in on a particular subtree, for example when it has become clear that good results are only to be found in one particular cluster. During these usability sessions we had one large original image next to the detail view. One common suggestion was to allow a more direct comparison between the label images and the original image. The cluster representative in general was perceived very helpful in determining the variation inside a cluster. When comparing siblings in the hierarchy, we made the observation that the cluster representative can have a slight misleading effect. Users tended to interpret a representative showing many differences as generally worse than one with less differences. The full picture only unravels however when considering the number of label images inside the cluster, as well as the location of differences and the number of label images that contributed to one particular difference. Two of our users suggested to provide filtering capabilities directly in the result space. Their argument was that from looking at the original they already formed a mental image of how the resulting label image should look like. They thus wanted to restrict the shown results to the ones having specific label values at certain positions, and excluding those results which exhibited, for example, noise artifacts.

Based on the feedback from these interviews, we introduced several improvements into GEMSe. To allow better comparison to the original, we implemented a magic lens for overlaying the original data in the detail view directly, as shown in Figure 2h. To im-

	Rock Crystal	Synthetic	Salinas
Size	285x300x216	120x120x8	83x86
Channels	3	4	214
Labels	3	4	6
# of Samples	200	100	500
SVM C	$0.01..100^l$	-	$10^{-5}..10,000^l$
γ_{svm}	$10^{-11}..1^l$	-	$10^{-11}..0.01^l$
SVM n	1..2	-	1..224
β_{erw}	0.1..1,000	$0.1..1,000^l$	0.1..10,000
γ_{erw}	1..10	0.1..10	1..10
m	$10..1,000,000^l$	-	10..10,000
w	0..1	0.25..1/0..0.75	-

Table 2: *Properties and sampling ranges of datasets used in our case studies. ^{l} indicates a logarithmic sampling scale.*

prove the navigation towards a final suitable parameter range we introduced a coloring of the parameter axes in regions of good and bad label images. Clusters can be marked as suitable or unsuitable through interaction elements in the detail view. These markings determine a coloring of the histogram axes in the histogram view. We calculate the ratio of these suitable to unsuitable label images for each histogram bin. If there are only suitable label images in a bin, then it is marked green, and red if there are only unsuitable ones, as shown in Figure 4(l, o). In between we map to grey and reduce the opacity, so that an equal distribution will result in no coloring.

6.2. Case Studies

We have successfully used our tool on several datasets from different domains. In the following paragraphs we will present three of them. The details of these datasets are shown in Table 2.

6.2.1. Talbot-Lau grating interferometer X-ray computed tomography data

Our main source of test datasets is Talbot-Lau Grating Interferometry X-ray Computed Tomography (TLGI-XCT), which generates three data channels: the attenuation as known from conventional X-ray computed tomography, the differential phase contrast which is related to the index of refraction and a dark-field contrast reflecting the total amount of radiation scattered at small angles. We supplied our tool to two domain experts working with phase contrast datasets. We analyze the *Rock Crystal* dataset here, which depicts a quartz structure with several cracks and pores inside. In this case we used attenuation and dark field image, a slice of each is shown in Figure 3b. The attenuation image alone can not resolve all cracks. The dark field image can, but typically over-emphasizes them and also shows high signal near the border of the crystal. The main goal was to segment all cracks and pores in the crystal.

Starting with getting an overview according to task T1, the root cluster as seen in Figure 2a shows variations of segmentation labels for nearly every pixel of the image. The second child cluster of this root is the minimized top cluster in Figure 4a. Its first child a1, currently selected, looks promising, where most of the air is correctly labeled (in green), as well as a big portion of the crystal is labeled as such (in yellow). Its child node a2 shows solid round structures labeled as cracks, which are also visible in the cluster
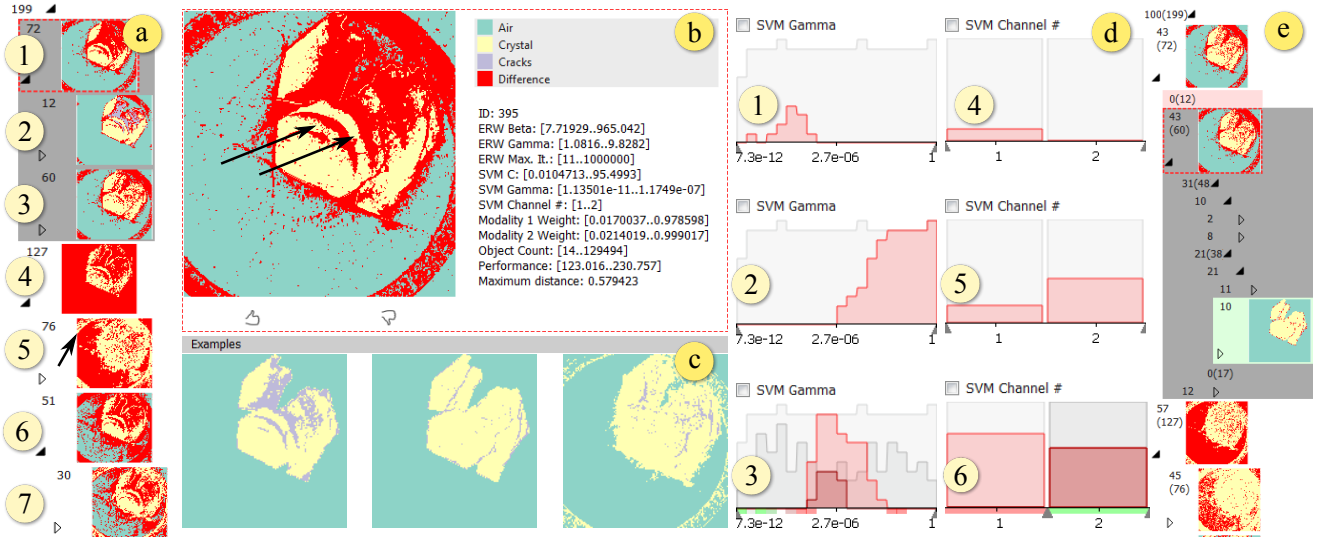
Figure 4: *GEMSe with the rock crystal dataset loaded. Clusters (a1-7) show an overview of the result ensemble. For the selected cluster a1, the enlarged representative is shown in the detail view (b) along with exemplary label images (c) from that cluster. Histograms d1-d3 show the distribution of γ_{svm} for clusters (a2, a5, a6). Histograms d4-d6 show the distribution of the number of channels used in SVM for clusters (a2, a3, a4). The filter set in d6 affects the cluster tree view (e), also clusters rated suitable and unsuitable are highlighted here, and their parameter ranges are color-mapped accordingly in histograms d3 and d6.*

representative in the detail view Figure 4b and marked there with arrows. These are not actual crack structures but unwanted artifacts. We therefore want to determine the parameter causing these to be wrongly labeled, an instance of task T2. A look at the histogram for the number of considered SVM channels d4 for cluster a2 reveals that all masks in it were produced using only one data channel. This could be a hint that considering all datasets for SVM will lead to results without these artifacts. Cluster a3, the sibling of a2, does not show these artifacts. Its SVM channel histogram d5 indicates that some masks in that node were also produced using only one data channel, but significantly more used data available in both channels. To determine this correlation more closely, we filter for a high SVM channel number in histogram d6 of cluster a4. The cluster tree view in Figure 4e shows the filtered cluster representatives, which are calculated only from matching label images. There, the artifacts are not visible anymore.

When looking at the node a5 we see that it contains masks which all over-segment the crystal label, and in addition show a large ring artifact which should be labeled as air, marked with an arrow. The corresponding γ_{svm} histogram d2 shows high values in this cluster. γ_{svm} influences the width of the bell-shaped surfaces in the Gaussian RBF kernel used for separation in SVM. The underlying gray plot representing the distribution in the whole result set shows that the majority of masks with an SVM gamma parameter in the upper third of the range are contained in this cluster. Its sibling a6, where the ring artifact is still visible but less pronounced, shows values in the middle of the range with the corresponding histogram d3. Histogram d1 for node a2, whose representative does not show the large ring artifact, was produced using low γ_{svm} values. For suitable results, γ_{svm} must therefore be selected from the lower end of

the range. The threshold between suitable and unsuitable results, as determined through interactive filtering, is at approximately 10^{-9}.

For further refinement of the parameter ranges, as required by task T3, we rate clusters using the interaction elements shown below the detail image in 4b. Rated clusters are highlighted in the cluster tree view in Figure 4e and on the axes of histograms d3 and d6. For γ_{erw}, the weight factor of the prior model in the ERW, we determine through filtering that very low values are producing noisy results. Values higher than 1.1 result in well-suited label images. Higher values of the parameter C_{svm}, allowing soft margins but penalizing wrongly classified points in the SVM, tend to slightly over-segment the crystal. For the other parameters the situation is less clear, with this sampling we could not determine a direct correlation with a suitable segmentation outcome. One possibility would be to re-sample these with fixed values for the most influential parameters γ_{svm} and n_{svm}. The best label image we could find had parameters $\beta_{erw} = 85.38$, $\gamma_{svm} = 6.98$, $C_{svm} = 0.044$, $\gamma_{svm} = 3.13 \times 10^{-11}$ and $n_{svm} = 2$.

6.2.2. Synthetic K-Edge Data

K-Edge absorptiometry is a new scanning modality in X-ray computed tomography devices, which is enabled by a new generation of X-ray detectors in computed tomography (CT) devices [FNMA06]. The X-ray attenuation image from a conventional CT device can provide high contrast, but typically limited information on the elemental composition. K-Edge absorptiometry delivers elemental concentrations at the cost of a higher noise level and reduced resolution. In our synthetic dataset shown in Figure 3a, the whole specimen is modeled to have the same average attenuation value, and three K-Edge absorptiometry images each give the concentration

of a single element. The sampling here was done with a limited segmentation framework using a fixed prior model derived from thresholding instead of SVM, thus the SVM parameters do not have ranges listed in Table 2.

In the cluster representative of the root node as shown in Figure 5(a1) every pixel has the difference marker color. The first overview conclusion, solving task T1 is therefore that inside this cluster there is not a single pixel with a consistent label throughout all images. Looking at the two child nodes, we see a division between one larger, homogeneous and well-segmented cluster of images in a2 and another node a5 showing highly varying results. Starting a correlation analysis task T2, the γ_{erw} parameter histogram b2 for node a5 reveals that those images were all generated with low γ_{erw} values. For node a2 on the other hand the γ_{erw} values are all higher as shown in the histogram in b1. Apparently low settings of γ_{erw} deliver invalid results for this kind of dataset. The exact threshold value is determined using the filtering controls. Figure 5(b3) illustrates this with a filter interval which masks out all images in node a5 while still matching all label images of node a2, as can be seen in the updated cluster tree view 5(c).

Inspecting the object count histogram 5(d) for node a1 shows that while most label images contain four objects, some have a significantly higher object count. Filtering for a high object count, and using the slice view to change the slice axis, it turns out that in some label images noise lead to separate objects. The histograms reveal that these result from using one PCA dimension and a low γ_{erw} value near the threshold defined before. Adjusting the γ_{erw} filter to a threshold of approximately 1 results in the images with high object count being filtered out. This conclusion can be drawn from the scatter plot in 5(e). For T3, we have already identified that γ_{erw} is the parameter with most influence on the suitability of a segmentation in this case. The PCA dimension turns out to have no direct correlation with the noise – there are label images using only one PCA dimension and no noise. When completely filtering out the noise we arrive at a threshold for γ_{erw} of 3.3. Further analysis shows that a minor influence on noisy pixels also came from β_{erw}. For the modality weights, we could not determine a clear correlation to the segmentation quality for this dataset. Very low values of weights were however only sampled in regions of a problematic γ_{erw} value. Re-sampling with suitable γ_{erw} values might provide additional information.

Using this dataset, we also performed a detailed comparison to Paramorama [PBCR11]. For this specific test we employed uniform sampling. This is the only sampling strategy supported by Paramorama, as its interface is tailored to it through their parameter tree, which is splitting the parameter space hierarchically. In contrast to the test datasets provided for Paramorama, we are facing a higher number of parameters for our synthetic dataset: Six for our overall algorithm and three for each of the two modalities. Even when only two different values per parameter are sampled, $2^{12} = 4096$ segmentation masks are generated. When loading this ensemble in Paramorama, even with the relatively large amount of samples there is no chance to determine a specific threshold between suitable and unsuitable results for the γ_{erw} parameter. The only thing to be determined is that the lowest value results in unsuitable masks, while the highest value produces suitable masks.

With our tool and using the latin hypercube sampling strategy, we could easily determine a narrow range for this threshold with only 100 samples.

6.2.3. Hyperspectral Data

We also tested our tool on the hyperspectral *SalinasA* dataset [VMV] (Figure 3c). It can demonstrate the functionality of our tool even for a high number of channels, and when ground truth is available. The main goal here was to verify the robustness of our segmentation pipeline with ground truth data. For that we calculate objective measures (dice coefficient, overall accuracy and kappa coefficient) as additional derived output for each of our sampling result and show it in the histogram view as shown in Figure 6b-d. By filtering for the highest dice metric scores, we can easily navigate to the best segmentation result. The magic lens proves to be very useful in this case by showing the result in comparison to the ground truth, as can be seen in Figure 6a. Our best result achieves an overall accuracy of 0.8 and only slightly lower kappa coefficient of 0.79 in our ensemble, using an approximate 2 % of the image pixels randomly chosen as seed points. As a general rule values over 0.8 are regarded as strong classification results [CG08]. Considering that we are using a general segmentation framework for multi-channel data not finetuned for hyperspectral data, and without even having refined the sampling to the most suitable ranges, this is a very good result. A very recent segmentation framework also based on the ERW and tuned for hyperspectral images by Kang et al. [KLF*15], achieves an overall accuracy of 0.88 and a kappa coefficient of 0.87 applied on a larger part of the same dataset, using 2% of the pixels as training points.

Figure 7 shows a summary of the ranges used for the most influential parameters in all three case studies. In each instance 5-10 positive and negative examples were ranked, the axis shows the resulting coloring. For the SVM channels, we can see that considering a higher number typically causes better results for both Salinas A and rock crystal dataset. Considering the mixed coloring at the higher end for the Salinas A dataset, we can see that highest values however do not necessarily improve the results. An SVM C somewhere above 0.354 needs to be chosen for the Salinas A dataset, where for the rock crystal dataset the best value is clearly closer to the minimum of 0.0078, values around 1 are not well-suited. γ_{svm} values around 10^{-7} produce suitable results for Salinas A, while for the rock crystal dataset best results from choosing it nearer to 10^{-12}.

7. Conclusion and Outlook

We presented GEMSe, a tool for the exploration of the parameter- and result space of multi-channel, multi-dimensional image segmentation algorithms. Three tasks were identified in collaboration with domain experts: getting an overview over the space of potential results, analyzing correlations between input parameters and output, and finding stable parameter regions producing suitable label images. Our case studies conducted together with domain experts show the suitability of our methods for these tasks. Our cluster tree view was perceived as very helpful in solving the overview task. While the cluster representative image was shown to provide
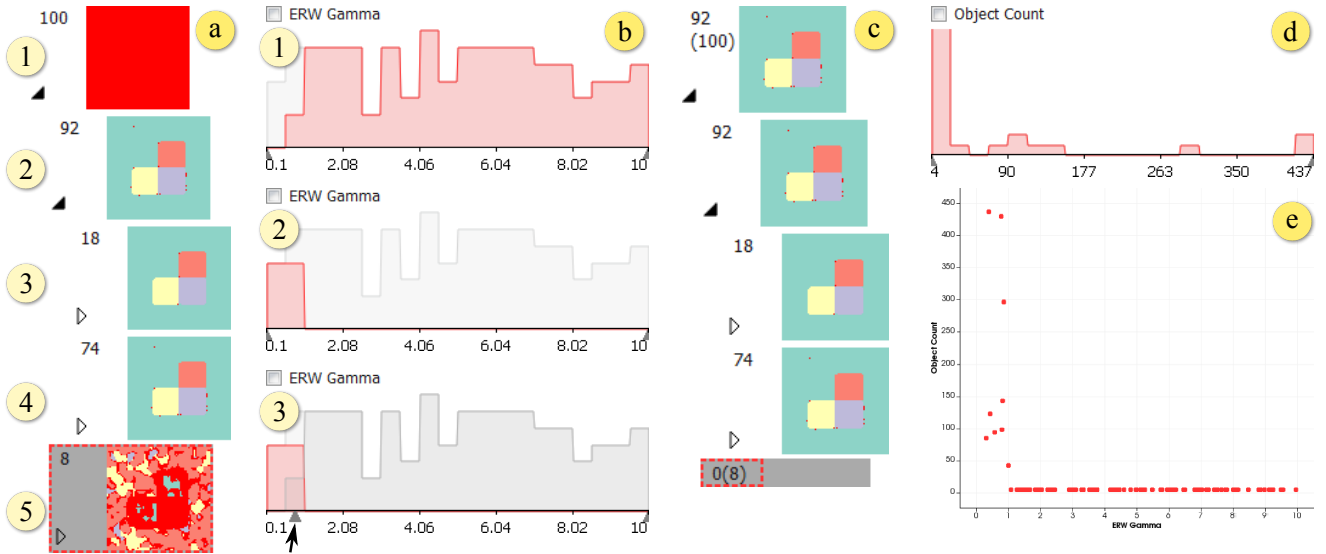
Figure 5: *Cluster view (a) of the synthetic K-Edge dataset. Histogram b1 shows the γ_{erw} distribution of node a2, b2 that of a5, b3 demonstrates the filtered histogram, (c) the resulting cluster tree view. Histogram (d) shows the object count for node a1, the scatterplot (e) correlates γ_{erw} (x-axis) to the object count (y-axis).*
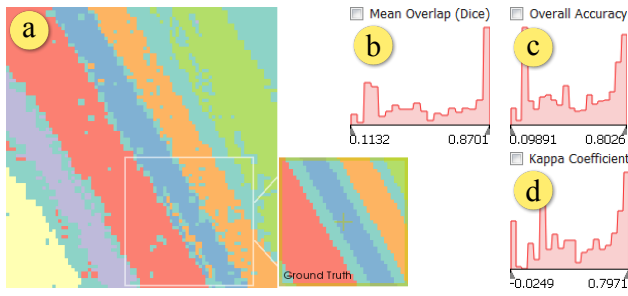

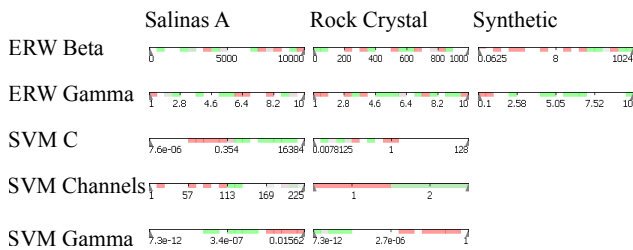**Figure 6:** *(a) label image with best kappa value, the ground truth is shown in the magic lens for comparison. (b-d) objective measure histograms.*

Figure 7: *Comparison of ranked parameter ranges for all case studies.*

insight into the cluster variation, there is a need for researching further methods of representing a cluster, for example through a scale encoding the number of differences for each voxel. Linked Histograms and filtering have proven to be successful for analyzing the correlations between input parameters and output, as shown in Section 6.2.1 and Section 6.2.2. Finding stable parameter regions, at least for the most influential parameters, was shown to be successful through our rating, axis coloring and filtering interactions. As can be seen in Figure 7 different modalities require different parameter settings. Hence, there is a need for GEMSe in helping practitioners find these settings without the help of segmentation experts. Future work could look further into the multi-channel aspect, for example through integrating image fusion for comparison visualizations, or through evaluating multiple different segmentation algorithms at once. The segmentation pipeline we employed can produce a probabilistic result, another promising area for future work is incorporating information on the segmentation uncertainty, which these probabilistic results give access to. Regarding clustering, one could investigate ways to combine clustering by result similarity as we have applied here, with clustering or splitting by parameter values, or perform dimensionality reduction instead of clustering.

Acknowledgements

References

[AD10] ARENS S., DOMIK G.: A survey of transfer functions suitable for volume rendering. In *IEEE/ EG Symposium on Volume Graphics* (2010), Westermann R., Kindlmann G., (Eds.), The Eurographics Association. `doi:10.2312/VG/VG10/077-083`. 2

[AFK*14] AMIRKHANOV A., FRÖHLER B., KASTNER J., GRÖLLER E., HEINZL C.: InSpectr: Multi-Modal Exploration, Visualization, and Analysis of Spectral Data. *Computer Graphics Forum 33*, 3 (2014), 91–100. `doi:10.1111/cgf.12365`. 1

[BM98] BEDERSON B., MEYER J.: Implementing a zooming user interface: Experience building pad++. *Software-Practice & Experience 28*, 10 (Aug. 1998), 1101–1135. `doi:10.1002/(SICI)1097-024X(199808)28:10<1101::AID-SPE190>3.0.CO;2-V`. 3

[CCK*14] CHIFFRE L. D., CARMIGNATO S., KRUTH J.-P., SCHMITT R., WECKENMANN A.: Industrial applications of computed tomography. *CIRP Annals - Manufacturing Technology 63*, 2 (2014), 655–677. `doi:10.1016/j.cirp.2014.05.011`. 1

[CG08] CONGALTON R. G., GREEN K.: *Assessing the accuracy of remotely sensed data: principles and practices*, 2nd ed. CRC press, 2008. `doi:10.1111/j.1477-9730.2010.00574_2.x`. 8

[CL11] CHANG C.-C., LIN C.-J.: LIBSVM: A library for support vector machines. *ACM Transactions on Intelligent Systems and Technology 2*, 3 (May 2011), 27:1–27:27. `doi:10.1145/1961189.1961199`. 5

[Dic45] DICE L. R.: Measures of the amount of ecologic association between species. *Ecology 26*, 3 (1945), 297–302. 3

[FLPZ51] FLOREK K., LUKASZEWICZ J., PERKAL J., ZUBRZYCKI S.: Sur la liaison et la division des points d'un ensemble fini. *Colloquium Mathematicae 2* (1951). 3

[FNMA06] FIRSCHING M., NIEDERLOHNER D., MICHEL T., ANTON G.: Quantitative material reconstruction in CT with spectroscopic X-ray pixel detectors – a simulation study. In *Nuclear Science Symposium Conference Record, 2006. IEEE* (Oct. 2006), vol. 4, pp. 2257–2259. `doi:10.1109/NSSMIC.2006.354363`. 7

[GFL04] GRADY L., FUNKA-LEA G.: Multi-label image segmentation for medical applications based on graph-theoretic electrical potentials. In *Computer Vision and Mathematical Methods in Medical and Biomedical Image Analysis* (Prague, Czech Republic, May 2004), ECCV 2004 Workshops CVAMIA and MMBIA, Springer, pp. 230–245. `doi:10.1007/978-3-540-27816-0_20`. 1, 3

[GJ*10] GUENNEBAUD G., JACOB B., ET AL.: Eigen v3. http://eigen.tuxfamily.org, 2010. Online. Retrieved March 10, 2016. 5

[Gra05] GRADY L.: Multilabel random walker image segmentation using prior models. In *Proceedings of the 2005 IEEE Computer Society Conference on Computer Vision and Pattern Recognition* (June 2005), vol. 1, pp. 763–770. `doi:10.1109/CVPR.2005.239`. 2, 3

[HB03] HARROWER M., BREWER C. A.: ColorBrewer.org: An online tool for selecting colour schemes for maps. *The Cartographic Journal 40*, 1 (2003), 27–37. `doi:10.1179/000870403235002042`. 3

[HKRs*06] HADWIGER M., KNISS J. M., REZK-SALAMA C., WEISKOPF D., ENGEL K.: *Real-time Volume Graphics*. A. K. Peters, Ltd., Natick, MA, USA, 2006. 2

[KAM99] KRISHNAMACHARI S., ABDEL-MOTTALEB M.: Image browsing using hierarchical clustering. In *Proceedings of the IEEE International Symposium on Computers and Communications* (1999), pp. 301–307. `doi:10.1109/ISCC.1999.780837`. 4

[KLF*15] KANG X., LI S., FANG L., LI M., BENEDIKTSSON J. A.: Extended random walker-based classification of hyperspectral images. *IEEE Transactions on Geoscience and Remote Sensing 53*, 1 (Jan. 2015), 144–153. `doi:10.1109/TGRS.2014.2319373`. 1, 3, 8

[MHG10] MALIK M. M., HEINZL C., GRÖLLER E.: Comparative visualization for parameter studies of dataset series. *IEEE Transactions on Visualization and Computer Graphics 16*, 5 (Sept. 2010), 829–840. `doi:10.1109/TVCG.2010.20`. 4

[Nie00] NIELSEN J.: Why you only need to test with 5 users. http://goo.gl/uLD01, Mar. 2000. Online. Retrieved March 26, 2015. 5

[PBCR11] PRETORIUS A. J., BRAY M.-A., CARPENTER A. E., RUDDLE R. A.: Visualization of parameter space for image analysis. *IEEE Transactions on Visualization and Computer Graphics 17*, 12 (Dec. 2011), 2402–2411. `doi:10.1109/TVCG.2011.253`. 2, 8

[PRH10] PRASSNI J.-S., ROPINSKI T., HINRICHS K.: Uncertainty-aware guided volume segmentation. *IEEE Transactions on Visualization and Computer Graphics 16*, 6 (2010), 1358–1365. `doi:10.1109/TVCG.2010.208`. 2

[SHB*14] SEDLMAIR M., HEINZL C., BRUCKNER S., PIRINGER H., MÖLLER T.: Visual parameter space analysis: A conceptual framework. *IEEE Transactions on Visualization and Computer Graphics 20*, 12 (Dec. 2014), 2161–2170. `doi:10.1109/TVCG.2014.2346321`. 2, 3

[SHM10] SAAD A., HAMARNEH G., MÖLLER T.: Exploration and visualization of segmentation uncertainty using shape and appearance prior information. *IEEE Transactions on Visualization and Computer Graphics (Proceedings Vis 2010) 16*, 6 (10 2010), 1365–1374. `doi:10.1109/TVCG.2010.152`. 2

[SMH10] SAAD A., MÖLLER T., HAMARNEH G.: ProbExplorer: Uncertainty-guided exploration and editing of probabilistic medical image segmentation. *Computer Graphics Forum (Proceedings EuroVis 2010) 29*, 3 (6 2010), 1113–1122. `doi:10.1111/j.1467-8659.2009.01691.x`. 2

[SML06] SCHROEDER W., MARTIN K., LORENSEN B.: *The Visualization Toolkit*, 4th ed. Kitware, 2006. 5

[THA10] TOP A., HAMARNEH G., ABUGHARBIEH R.: Spotlight: Automated confidence-based user guidance for increasing efficiency in interactive 3d image segmentation. In *Medical Image Computing and Computer-Assisted Intervention Workshop on Medical Computer Vision (MICCAI MCV)* (2010), pp. 204–213. `doi:10.1007/978-3-642-18421-5_20`. 2

[TWSM*11] TORSNEY-WEIR T., SAAD A., MÖLLER T., HEGE H.-C., WEBER B., VERBAVATZ J.-M.: Tuner: Principled parameter finding for image segmentation algorithms using visual response surface exploration. *IEEE Transactions on Visualization and Computer Graphics 17*, 12 (2011), 1892–1901. `doi:10.1109/TVCG.2011.248`. 2

[VMV] VEGANZONES M. Á., MARQUÉS I., VILCHES B. A.: Hyperspectral remote sensing scenes. http://www.ehu.eus/ccwintco/index.php?title=Hyperspectral_Remote_Sensing_Scenes. Online. Retrieved March 26, 2015. 8

[WHA07] WILLETT W., HEER J., AGRAWALA M.: Scented widgets: Improving navigation cues with embedded visualizations. *IEEE Transactions on Visualization and Computer Graphics 13*, 6 (Nov. 2007), 1129–1136. `doi:10.1109/TVCG.2007.70589`. 4

[YAL*02] YOO T. S., ACKERMAN M. J., LORENSEN W. E., SCHROEDER W., CHALANA V., AYLWARD S., METAXAS D., WHITAKER R.: Engineering and algorithm design for an image processing api: a technical report on itk - the insight toolkit. *Studies in health technology and informatics* (2002), 586–592. 5

PorosityAnalyzer: Visual analysis and evaluation of segmentation pipelines to determine the porosity in fiber-reinforced polymers

Johannes Weissenböck, Alexandr Amirkhanov, Eduard Gröller, Johann Kastner, Christoph Heinzl

PorosityAnalyzer: Visual Analysis and Evaluation of Segmentation Pipelines to Determine the Porosity in Fiber-Reinforced Polymers

Johannes Weissenböck*
University of Applied Sciences
Upper Austria, Wels, Austria

Artem Amirkhanov†
University of Applied Sciences
Upper Austria, Wels, Austria

Eduard Gröller‡
TU Wien, Vienna, Austria and
VrVis Research Center, Austria

Johann Kastner§
University of Applied Sciences
Upper Austria, Wels, Austria

Christoph Heinzl¶
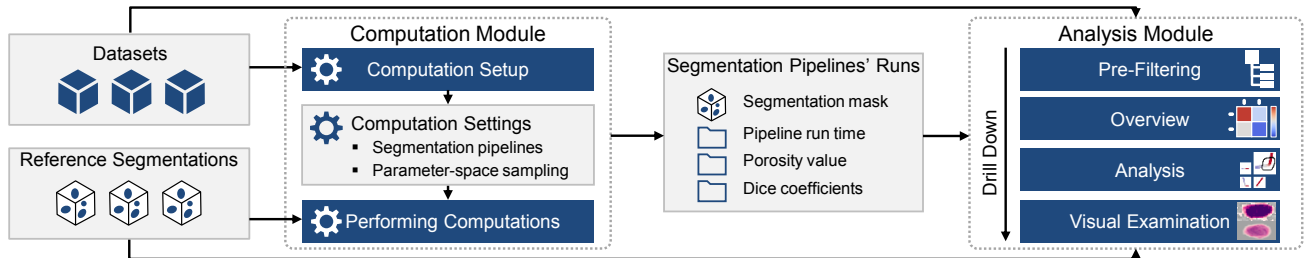University of Applied Sciences
Upper Austria, Wels, Austria

Figure 1: Overview of the *PorosityAnalyzer* workflow (gray boxes: input and intermediate data, dark blue boxes: stages of the workflow).

ABSTRACT

In this paper we present *PorosityAnalyzer*, a novel tool for detailed evaluation and visual analysis of pore segmentation pipelines to determine the porosity in fiber-reinforced polymers (FRPs). The presented tool consists of two modules: the computation module and the analysis module. The computation module enables a convenient setup and execution of distributed off-line-computations on industrial 3D X-ray computed tomography datasets. It allows the user to assemble individual segmentation pipelines in the form of single pipeline steps, and to specify the parameter ranges as well as the sampling of the parameter-space of each pipeline segment. The result of a single segmentation run consists of the input parameters, the calculated 3D binary-segmentation mask, the resulting porosity value, and other derived results (e.g., segmentation pipeline runtime). The analysis module presents the data at different levels of detail by drill-down filtering in order to determine accurate and robust segmentation pipelines. Overview visualizations allow to initially compare and evaluate the segmentation pipelines. With a scatter plot matrix (SPLOM), the segmentation pipelines are examined in more detail based on their input and output parameters. Individual segmentation-pipeline runs are selected in the SPLOM and visually examined and compared in 2D slice views and 3D renderings by using aggregated segmentation masks and statistical contour renderings. *PorosityAnalyzer* has been thoroughly evaluated with the help of twelve domain experts. Two case studies demonstrate the applicability of our proposed concepts and visualization techniques, and show that our tool helps domain experts to gain new insights and improve their workflow efficiency.

Index Terms: I.3.6 [Computer Graphics]: Methodology and Techniques—Interaction techniques

---

*e-mail: johannes.weissenboeck@fh-wels.at

†e-mail: artem.ogre@gmail.com

‡e-mail: groeller@cg.tuwien.ac.at

§e-mail: johann.kastner@fh-wels.at

¶e-mail: christoph.heinzl@fh-wels.at

1 INTRODUCTION

Fiber-reinforced polymers (FRPs) have become of great practical importance in modern-day industries because of their specific properties, their versatile processing, and application possibilities. As described in a market report [1], the aeronautics, automotive, energy, and leisure industries are increasingly focusing on these high-tech materials. Components, which are made of conventional materials (e.g., aluminum, steel), can be replaced by these new materials without impairing the functionality, while improving specific properties (e.g., reduced weight) or even extending their functionalities. For example, the proportion of fiber-reinforced composites in newly designed commercial aircrafts has increased to more than 50 %wt. (percentage by weight) [28]. In order to fulfill the high demands and quality standards in the field of aeronautics, industrial cone-beam X-ray computed tomography (XCT) is increasingly used to measure FRP specimens. With XCT it is possible to non-destructively identify and characterize material features such as pores or fibers accurately, which is highly important for the domain experts as pores and fibers have a strong influence on the functional and strength properties of the component. For example, in order to predict a component's behavior, experts are particularly interested in deriving pore characteristics as pore number, size, shape, and distribution. However, the most important global characteristic of a material that contains pores is its porosity value. The porosity value is defined as the ratio in percent of the total cumulative volume of all pores in the specimen to the specimen's volume.

In material testing and quality control the porosity value is often used for deciding whether an expensive component passes a quality control check or whether it is rejected. There exist various destructive and non-destructive methods for the porosity determination in FRPs. Destructive methods include wet-chemical analysis using acid digestion and materialography in combination with microscopic analysis [6]. Non-destructive methods, for example, are ultrasonic testing and active thermography [17]. However, these methods are often not as accurate as desired in critical areas of the specimen. In contrast, modern XCT scanning devices are capable of delivering high resolution results down to a few microns. When XCT is used for a precise porosity determination, the scan parameters, the reconstruction methods, the image processing, and especially the segmentation algorithms play a decisive role.

101

2 DOMAIN BACKGROUND AND MOTIVATION

The porosity determination of FRPs by means of XCT is difficult, since typical industrial components are composed of various materials. The wide variety of material combinations causes differences in image quality regarding noise, sharpness, and artifacts. Therefore, the XCT experts are required to adjust the parameters of their segmentation methods for every material type.

To determine the porosity of an XCT scanned FRP specimen, the domain experts are mainly using global threshold segmentation algorithms to extract the pores from the rest of the specimen (fibers and matrix) [29]. The advantage of global-thresholding segmentation-methods is the high processing speed and the small number of parameters to tune. A representative of this family is the Otsu segmentation algorithm [21]. This histogram-based segmentation method has no parameters. But usually XCT datasets are suffering from noise, artifacts (e.g., beam hardening), and low resolution. Therefore, global-thresholding segmentation-methods might produce a significant number of misclassified voxels, which leads to an incorrect porosity value of the specimen. This problem can be solved by using smoothing filters to reduce the noise and more advanced segmentation methods. But these algorithms typically require additional parameters to specify. Tuning these input parameters to find an appropriate parameter preset is essential.

Typically, domain experts start this task by empirically setting initial parameters to the best of their knowledge and experience. The result is then visually compared side-by-side to a reference segmentation, which comes from the same dataset. Depending on the result, the parameters are adapted. This iterative process is terminated as soon as the domain expert considers the correspondence between result and reference as sufficient. In addition, the comparison of the results is further hampered by the different outcomes which originate from different reference methods. During this procedure, it is important to record the parameter combinations and the corresponding results to evaluate and compare them later. This trial-and-error approach is not only time consuming, tiring, and often frustrating, but also generates modest results in many cases.

Taking all the factors mentioned above into account, it follows that there is a high demand for tools to set up segmentation pipelines, to perform all necessary computations in batches, to manage and organize the resulting data, and to support the visual analysis of the data. With such tools available, domain experts can be much more efficient in making a well-justified selection of the segmentation pipeline for XCT-scanned FRP specimens. Moreover, it enables the domain experts to base their decision-making on a detailed analysis of various aspects of pore segmentation pipelines and domain-specific requirements. Based on the demands of the domains experts we identified the following tasks:

Task 1: Set up a segmentation pipeline where the parameter ranges of all filters are adjustable and run the segmentation pipelines in a batch process.

Task 2: Analyze and evaluate the candidate pipelines and compare them with each other.

Task 3: Explore segmentation pipeline parameter trade-offs concerning accuracy, performance, and stability.

Task 4: Generate accurate, robust, and reproducible results using a specific segmentation pipeline preset for a class of datasets.

In order to fulfill these domain-specific demands we present the *PorosityAnalyzer*, an interactive tool to visually analyze and explore segmentation pipelines for porosity determination in FRPs. The workflow of the *PorosityAnalyzer* is shown in Figure 1. The input data are: a list of XCT-scanned FRP datasets and a list of reference segmentations for these datasets. The data acquisition is described in Section 4.

Our tool is divided into two modules: the *computation module* and the *analysis module*. The computation module allows users to set up and execute distributed off-line computations of porosity segmentation pipelines (see Section 5). In the computation setup phase the parameter spaces of the segmentation algorithms for the chosen datasets are sampled and the resulting settings are stored. The computations are then performed, resulting in sets of segmentation-pipeline runs. For each run the segmentation mask, porosity value, run time, and Dice coefficients describing the similarity between a segmentation mask and a reference segmentation mask [9] are calculated and stored. These computation results are used as input for the analysis module (see Section 6), which provides tools for visualization, exploration, and visual analysis of the segmentation pipelines. The analysis module consists of four levels: pre-filtering, overview, analysis, and visual examination. During a drill-down approach the user performs a visual analysis and an examination of the data on each level by selecting the most interesting data portion and passing it on to the next level. This allows a thorough visual analysis from the data overview to the most detailed representations.

The main contributions of our work are in the *visual knowledge discovery*, in the *interactive visualization techniques* on multiple levels-of-detail, and in the *fulfillment of the domain-specific requirements* for the analysis of pore segmentation pipelines for XCT scanned FRP specimens.

3 RELATED WORK

The related work of the *PorosityAnalyzer* lies in the areas of 3D image segmentation, visualization of multidimensional data, and visual parameter-space analysis. A broad survey of 3D image segmentation methods is presented by Wirjadi [33]. Gleicher et al. [12] provide a detailed survey on methods for information visualization and visual comparison. Scatter plots are often used as a visualization tool for statistical, non-spatial, and multi-dimensional data [7]. A scatter plot matrix (SPLOM) organizes all possible combinations of 2D scatter plots in one layout for providing an overview on multidimensional data, studying the correlations between data dimensions, and locating clusters of data points. Elmqvist et al. [10] introduced novel SPLOM navigation techniques using transitions for an intuitive multidimensional visual data exploration. Gavrilescu et al. [11] extended interface elements, such as sliders or transfer function editors, with plots showing the magnitude of change in a rendered image. This provides visual cues on the resulting effects that would occur if a certain parameter is changed. We utilized a similar approach with *parameter-range sliders* (see Section 6.3).

The related research in the area of porosity analysis and pore visualization in FRPs is given in the approaches by Reh et al. Porosity maps [25] provide an overview of pore locations and density. A mean-object visualization [24] aggregates all the pores in the specimen in order to cluster pores by shape and size, and provides a global overview of pore shapes in the data. Ushizima et al. [31] proposed geometric and topological descriptors to enhance the estimation of material permeability in complex porous micro structures. Their analysis framework combines image processing, multi-scale topological analysis, and the visualization of pore bodies.

Visual parameter-space analysis has a great potential to support the validation and the use of simulation models. Sedlmair et al. [26] developed an abstract conceptual framework for visual parameter-space analysis problems to guide and systematize research endeavors in this area. The authors' framework covers a broad range of tools and design studies from different application fields. Their classification is based on three major components: a data flow model abstractly describing analysis problems independent of the application domain, a set of four navigation strategies supporting the parameter-space analysis with visualization tools, and a characterization of six analysis tasks. Our work fits into this framework and fulfills the following classification criteria: it is a data

102

flow model with an integrated sampling step, utilizing derived measures. The navigation strategy is global-to-local. The application area is engineering and the analysis tasks are optimization, partitioning, and sensitivity investigation.

Another related work in the field of visual parameter-space analysis was done by Piringer et al. [22] who use multiple 2D and 3D projections of an n-dimensional space for regression-model simulations in car engine design. Their approach compares known and predicted results as well as results of multiple models, analyzes regions with a bad fit, and assesses the physical plausibility of models. Berger et al. [4] extend this work for uncertainty-aware exploration of continuous parameter-spaces. They guide the user to potentially interesting parameter regions and visualize the model predictions' uncertainty in 2D scatter plots and parallel coordinates. Coffey et al. [8] utilize a local-to-global approach for exploring large design spaces in simulation-based engineering, the design of visual effects, and other tasks that require tuning parameters of computationally intensive simulations. Pretorius et al. [23] developed a plug-in for the CellProfiler biomedical-image analysis-framework that regularly samples continuous parameters of an image processing pipeline. Paramorama, a visual analysis tool, is used to study relationships between the input parameter-space and image-based outcomes. Results are hierarchically-clustered based on the parameter values and can be queried and laid-out side-by-side for a visual comparison. Bergner et al. [5] introduced ParaGlide, a visualization system for a systematic interactive exploration of parameter spaces of multi-dimensional simulation models.

The Tuner tool by Torsney-Weir et al. [30] is somewhat similar to *PorosityAnalyzer* and also addresses the problem of parameter-finding in image segmentation algorithms and finding optimal algorithm presets. The parameter space of the evaluated algorithm is parsed, and off-line computations are performed. Dice coefficients are utilized to evaluate the quality of the segmentation results compared to the ground-truth segmentations. Finally a Pareto panel and HyperSlice [32] views are used for the visual analysis and navigation. In comparison to Tuner, there is a list of important differences that sets our work apart. First, the potential users of Tuner are segmentation-algorithm developers, i.e., people who are familiar with all the implementation details and inner workings of segmentation algorithms. *PorosityAnalyzer's* main users are domain experts, i.e., segmentation-algorithm consumers, who are required to solve specific tasks involving segmentation algorithms. Second, the goal of Tuner is to find optimal parameter settings for one segmentation algorithm. The main goal of *PorosityAnalyzer* is to evaluate and compare many different segmentation pipelines in order to find the optimal pipeline and preset. Third, optimizations in Tuner are based on a ground-truth segmentation mask. We are mainly interested in evaluating segmentation pipelines based on the domain specific criterion of the porosity value. In addition, we consider the reference segmentation mask and run time of the algorithm. Fourth, Tuner is designed to work with one algorithm and one dataset at a time with the possibility to switch datasets sequentially. One important design principle of *PorosityAnalyzer* is to provide off-line computations and visual analysis for multiple segmentation pipelines and multiple datasets at once. Fifth, there is a clear distinction in how the sensitivity analysis is performed. Tuner is using uncertainty/gain values provided by a Gaussian process model. Interactive sensitivity analysis is performed in the following way: as the user changes a particular parameter value all plots dependent on it change interactively, which reflects the algorithm's sensitivity to this parameter. *PorosityAnalyzer* mainly uses box plots, histograms, statistical contours for porosity segmentations, and parameter-range sliders (PRS) to evaluate a segmentation pipeline's sensitivity and robustness. Finally, in the investigation phase we are utilizing a SPLOM in the analysis module, while Tuner is relying on the HyperSlice visualization.
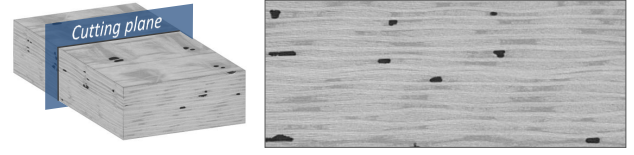

Figure 2: A typical 3D volume dataset with pores (black) from the aeronautic industry (E5_high, left: 3D volume, right: 2D slice).

Table 1: Characteristics of the FRP datasets used in this work.

Dataset Name	XYZ Dimensions in Voxels	Resolution in μm	Reference Porosity
E3_low	749x304x1396	10.0	0.965%
E4_low	711x302x1423	10.0	0.394%
E5_high	756x262x1472	10.0	6.668%
E6_high	835x298x1653	11.5	6.819%
E7_high	842x288x1706	11.5	8.657%
WChem_low	1365x421x1674	10.0	0.501%
PorePhantom	173x230x140	11.0	6.123%

4 DATA ACQUISITION

Our domain experts mainly deal with fiber-reinforced polymers (FRPs). In this work we use seven carbon fiber-reinforced polymer (CFRP) specimens which were measured with a GE phoenix—X-Ray Nanotom 180 XCT device. A typical CFRP dataset (E5_high) is shown in Figure 2. Due to the different methods for reference-porosity determination we categorized the datasets into two classes. In the subsequent sections, we will refer to these classes as: *aeronautic industry* and *wet chemical analysis* scans. The specimens are named accordingly (*Ex_*, and *WChem_low*). In addition, we investigated the *PorePhantom* dataset where the pores were artificially included by the domain experts. Table 1 provides an overview of the used datasets.

5 COMPUTATION MODULE: SETUP OF PORE SEGMENTATION PIPELINES

According to the domain-specific requirement, *to be able to batch-process various segmentation pipelines* (see Task 1, Section 2), we designed a computation module which provides a graphical user interface (GUI) for connecting segmentation pipeline filters within the user-defined parameter-spaces in a simple way. The core of the computation module is the batch processing of the created segmentation pipelines and the data storing of the calculated results. Starting from an identical database (XCT datasets of the FRP specimens), the module can be run on different computers simultaneously, in order to distribute the computation load. For this purpose we designed a file and folder structure for storing the results of the individual computers in a shared folder (see Figure 3).

Each segmentation-pipeline run of the batch process stores the information about the used computer (e.g., CPU type), the assembled segmentation pipeline and its parameters, the calculated results (e.g., run-time, the porosity value), and the binary segmentation masks. In the background, this module takes care of the proper filter linkage by setting the necessary intermediate connection steps (e.g., ensuring correct data types). Thus, the required user-input is kept very small. To set up a batch computation, the user has to specify the locations where the data are stored. The batch-computation settings-file (see Figure 4A) contains all the previously investigated pipelines. The pipelines in the file will be automatically loaded to the segmentation-pipeline batch-table (see Figure 4C). Once the paths and the folders are specified, the different segmentation pipelines can be created (see Figure 4B).
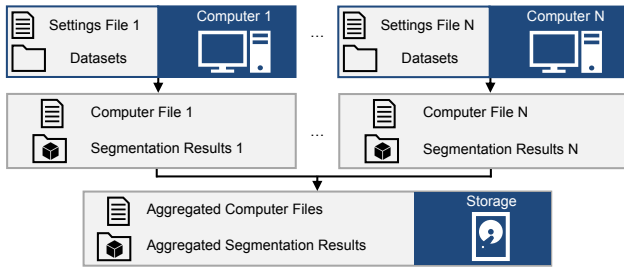
103

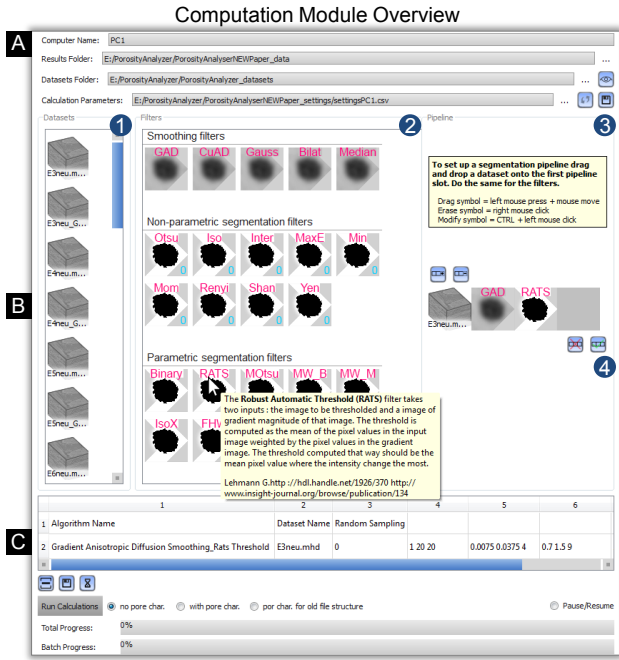Figure 3: Underlying file and folder structure of the *PorosityAnalyzer*.

Figure 4: The computation module to set up and batch-process segmentation pipelines. Folder and file paths (A). Drag and drop area (B) to assemble a segmentation pipeline (datasets (1), filters (2), pipeline (3)). Accepted pipelines (4) are shown in the batch table (C).

We initially pursued a text-based approach to create a segmentation pipeline. The individual filters of a pipeline and their parameter ranges were manually entered in the columns of the batch table. The involved experts criticized this approach because of the cumbersome, complicated, and error-prone data entry. In order to overcome these problems, we opted for a drag-and-drop interface to set up the segmentation pipelines. A segmentation pipeline may consist of any number of steps. To set up a pipeline, a dataset icon from the dataset list (1) is selected and positioned into the first slot of the pipeline (3). This drag and drop process is repeated for the desired number of filters/steps (2) to build a functional segmentation pipeline. After the pipeline assembly is completed, the parameter-space sampling is specified for each filter. For this purpose the filter icons in the pipeline can be clicked and the corresponding parameter-space dialog (PSD) opens. Here, the sampling method (regular sampling or random sampling) for each step and the corresponding parameter ranges are specified. In the case of regular sampling the user defines the n-dimensional grid granularity by simply specifying the range and the number of samples of each filter parameter. n is the number of input parameters, which is in the range from zero to seven for the pipelines we tested. This

causes the parameter step-size to be fixed to the ratio between the parameter range and the number of samples. In the case of random sampling the samples are selected arbitrarily inside a user defined parameter range.

The first version of the PSD was designed as a simple input interface for defining the parameter ranges of a filter. However, this dialog was not well accepted by the domain experts with the argumentation that it does not preserve the context of the pipeline's dataset, which makes the parameter-range specification difficult. Therefore, we provide within the PSD an XY-slice of the dataset, additional dataset information (e.g., dimension, resolution), the corresponding gray-value histogram (with labeled air/pore and material peaks), and a filter description. The created pipelines can be added (4) to the segmentation-pipeline batch-table (see Figure 4C). Pressing the "Run Calculations" button executes the defined segmentation pipeline on the machine. By repeating this process on other machines, the calculation of different segmentation pipelines can be distributed. The calculated results of the different batch-processed segmentation pipelines serve as input for the analysis module (see Section 6).

The *PorosityAnalyzer* primarily uses the Insight Segmentation and Registration Toolkit (ITK) 4.6 [14] and its filter implementations. In our demonstrator framework we used five smoothing, nine non-parameterized segmentation [2], and ten parameterized segmentation filters. A detailed list of the implemented filters is presented in Table 2.

Table 2: Applied filters in the *PorosityAnalyzer* tool.

	Filter Name	Abbreviation	Reference
Smoothing filters	Gradient Anisotropic Diffusion	GAD	[14]
	Curvature Anisotropic Diffusion	CAD	[14]
	Recursive Gaussian	Gauss	[14]
	Bilateral	Bilat	[14]
	Median	Median	[14]
Non-parametric segmentation filters	Otsu Threshold	Otsu	[2]
	IsoData Threshold	Iso	[2]
	Intermodes Threshold	Inter	[2]
	Maximum Entropy Threshold	MaxE	[2]
	Minimum Threshold	Min	[2]
	Moments Threshold	Mom	[2]
	Renyi Threshold	Renyi	[2]
	Shanbhag Threshold	Shan	[2]
	Yen Threshold	Yen	[2]
Parametric segmentation filters	Binary Threshold	Binary	[14]
	Robust Automatic Threshold Selection	RATS	[16]
	Multiple Otsu	MOtsu	[20]
	Watershed (Beucher)	MW_B	[3]
	Watershed (Meyer)	MW_M	[3]
	Confidence Connected	Confi	[14]
	Connected Threshold	Conn	[14]
	Neighborhood Connected	Neigh	[14]
	IsoX Threshold	IsoX	–
	Maximum Distance	Fhw	[15]

6 ANALYSIS MODULE: VISUAL ANALYSIS AND EVALUATION OF PORE SEGMENTATION PIPELINES

The analysis module provides exploration and analysis methods for the large number of results generated by applying multiple segmentation pipelines with varying presets to a set of different datasets. The overall purpose of this module is to provide the functionality needed by the domain experts to efficiently and conveniently perform their analysis.
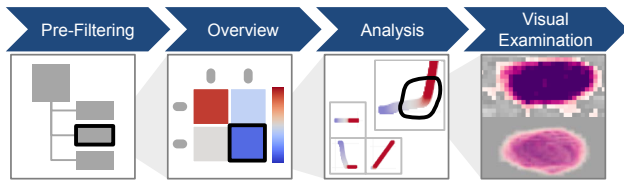
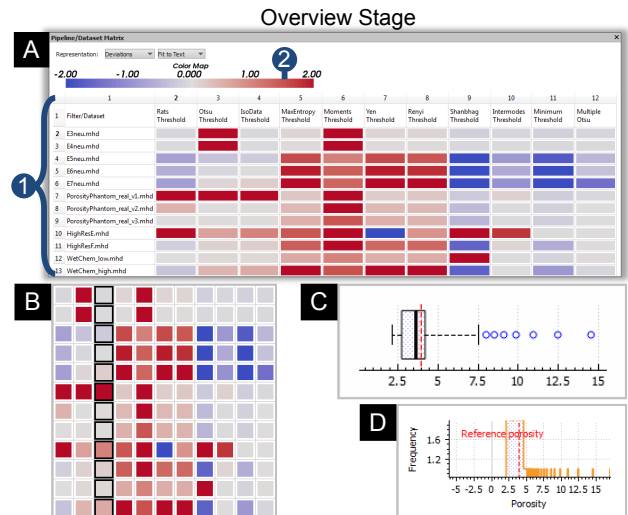Figure 5: Data representation stages of the analysis module.

Figure 6: The overview comparative matrix (A) in *deviation* mode (1) with the deviation color map (2). Collapsed deviation comparative matrix with selected "IsoData Threshold" column (B), box plot visualization (C), histogram visualization (D).

In order to enable an intuitive visual-analysis workflow for segmentation data, we follow the "overview first, zoom and filter, details-on-demand" design principle [27]. The data are analyzed on four levels-of-detail: *tree view* (pre-filtering stage), *overview comparative matrix* (overview stage), *scatter plot matrix* (SPLOM) and *parameter-range sliders* (PRS) (analysis stage), and *comparative visualizations* using 2D slices and 3D views (visual examination stage). Figure 5 depicts the four data representation stages. In each stage a portion of the data can be selected. First, the user loads all generated segmentation data and pre-filters particular segmentation pipelines and datasets if necessary (see Section 6.1). The *overview comparative matrix* shows the deviations of the segmentation pipelines' porosity values from the porosity values of the reference methods (see Section 6.2). Here, the user selects a pipeline/dataset combination and analyzes it on the level of the individual segmentation runs (see Section 6.3). Finally, the user visually verifies and compares the selected segmentation runs side-by-side by means of 2D slices and 3D views (see Section 6.4). By using the interconnected data representation stages, the requirements of the domain experts, i.e., *analysis, evaluation and comparison of the candidate pipelines* as well as *segmentation pipeline parameter trade-off analysis* (see Task 2 and 3, Section 2) are met.

Initially, the individual views of each stage were displayed hierarchically in tab views. With the separation into the tab views the domain experts experienced problems as the context to the previously selected data is lost. Therefore, we decided to present all views of the individual stages at the same time. When selecting data in one view the data in all other views are automatically updated. All views can be positioned and resized individually. In the following subsections we describe each stage of the *PorosityAnalyzer* visual-analysis workflow starting from an overview to more detailed representations.

6.1 Pre-Filtering Stage

After loading the segmentation data into the analysis module we provide a collapsible and expandable side-panel for pre-filtering the data. The loaded segmentation data are presented in a *tree view*. Here, the top-level tree-items can be grouped either by the segmentation-pipeline name or by the dataset name. If the top-level items are grouped by dataset name, the second level items will be grouped by segmentation pipeline name and vice-versa. Expanding the second-level tree-items reveals all the available information about the individual runs for the chosen segmentation pipeline/dataset combination. The user can pre-filter the data by selecting the segmentation pipelines or datasets. The contents of the *tree view* and the *overview comparative matrix* (see Section 6.2) are dynamically updated, whenever the filter settings are modified.

6.2 Overview Stage

Since the domain experts are primarily interested in the porosity value of a dataset, we first calculate statistical informations for the resulting porosity values of all runs of each segmentation pipeline/dataset combination and their deviations from the reference porosity values. Based on these statistical values, we provide a high-level overview visualization, to allow domain experts a first

judgment concerning the robustness of the porosity values (delivered by the evaluated segmentation pipelines) as well as concerning the accuracy of the resulting porosities.

The segmentation data from the pre-filtering stage are visualized in the *overview comparative matrix*, which shows segmentation pipelines in columns and datasets in rows (see Figure 6A (1)). The *overview comparative matrix* has three visualization modes: deviation, box plot, and histogram. The deviation mode color-codes the median deviations of each segmentation pipeline/dataset combination (to the reference porosity values) using a diverging cool/warm perceptually-uniform color map (2). Originally proposed by Moreland [18]. Columns of the *overview comparative matrix* can be expanded to fit to the lengths of the segmentation-pipeline names or collapsed (see Figure 6B). In addition to the deviation mode, we want to show more details on the distribution of the porosity values. Therefore, the box-plot mode was designed to render a matrix of box plots. For example, Figure 6C shows a box plot for the "RATS Threshold" applied to the WetChem_low dataset. A box plot shows the statistical properties (lower and upper whisker, first and third quartiles, median, and outliers) of the porosity values of a segmentation pipeline. The reference porosity value is indicated with a vertical red dashed line and outliers are depicted with blue circles. Similarly, the histogram mode depicts one porosity-value histogram per segmentation pipeline inside a matrix cell. Figure 6D shows a histogram for the "RATS Threshold" applied to the WetChem_low dataset. In the *overview comparative matrix,* a cell, a column, or a row may be selected. Figure 6B shows a selected column of the "IsoData Threshold". After the selection is made, the segmentation data are forwarded to the analysis stage where they are presented in the SPLOM and PRS (see Section 6.3).

6.3 Analysis Stage

The analysis stage is designed to provide tools and methods for a detailed visual analysis of the segmentation-pipeline runs. Figure 7 shows the user interface for the visual analysis of segmentation data. Here, the central view is a scatter plot matrix (SPLOM) (1), which visualizes all the input and output parameters of each segmentation-pipeline run. Including the run time, porosity value, deviation from the reference porosity, index of the dataset, and Dice coefficients [9]. To assist the visual analysis, any of these parame-
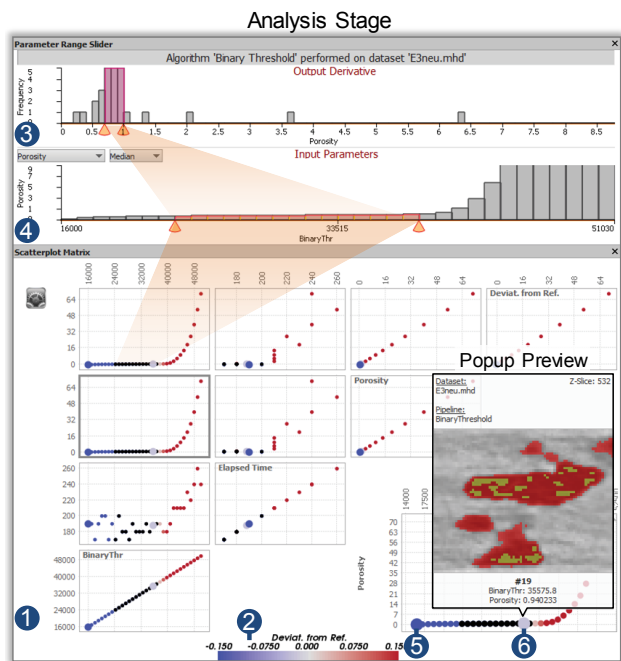
Figure 7: A SPLOM with the parameters of a segmentation pipeline (1). A parameter of choice (*Deviat. from. Ref.*) is color-coded (2). The porosity frequency histogram with a selected porosity range (3). A *parameter-range slider* with a selected range of the parameter *BinaryThr* (4). The SPLOM *popup preview*, which compares two different segmentation results (5) and (6).
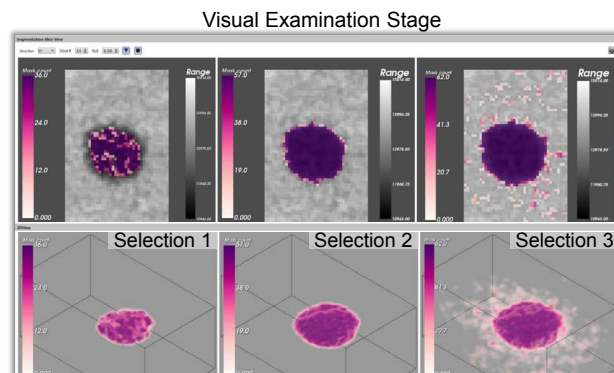

Figure 8: Side-by-side comparison of three selections of aggregated segmentation masks (left: under-segmentation, middle: close to optimal segmentation, right: over-segmentation).

ters can be color-coded using a perceptually-uniform color-map (2). Furthermore, a trade-off analysis is facilitated by the SPLOM.

The reasons why a scatter plot matrix was implemented are: a SPLOM is often used to make correlations, trends, and outliers visible in multi-dimensional data [19] and our experts are familiar with this visual representation. When we presented the SPLOM to the experts, they mentioned that it is difficult to interpret the data points without seeing the underlaying segmentation data. In order to increase the understanding of the segmented data and their parameters, we present the segmentation result in a *popup preview* if the user hovers over a data point in the SPLOM. The *popup preview* shows the original data superimposed with the segmentation result. A region of interest (ROI) widget is connected to the *popup preview* and shows the corresponding dataset slice-wise. By specifying a rectangular region in the ROI widget, cutouts in a dataset slice are defined and displayed in the *popup preview*. To compare the segmentation results of two data points in the SPLOM, one data point can be fixed. When hovering over another one, the differences in pore regions are displayed color-coded in the *popup preview*. Figure 7 depicts a dark blue fixed data point (5) and a light blue compared data point (6). The *popup preview* shows a ROI of the dataset E3_low. The yellow overlay indicates those voxels that are the same in both segmentations, the newly added voxels are color-coded in red, removed ones are color-coded in blue.

Domain experts consider it as important to assess the sensitivity of the variations in input parameters when evaluating a segmentation pipeline. Therefore, the *parameter-range sliders* (PRS), were implemented which operate on the histogram plots of the output parameters (porosity/porosity deviations) and the input parameters of the corresponding segmentation pipeline. By selecting a range in the output-parameter histogram (3) the corresponding range of the input-parameter histogram (4) is highlighted (yellow). Mean or median values are chosen in the input-parameter histogram. These

values are calculated by keeping an input parameter constant and accumulating porosity or porosity deviation values for all combinations of the remaining input parameters. The expert can select a subset of pipeline runs by using either the SPLOM through specifying an arbitrary polygon in one of the scatter plots or the PRS by specifying parameter ranges using two handles on each slider. The selection made in the PRS is interactively synchronized with the SPLOM. Multiple selections can be managed and organized using a selections view. Every selection from the list can be chosen, and dynamically loaded at any time. When a selection is loaded, *pre-filtering*, *overview*, and *analysis* views automatically restore the state they had when the selection was made. This makes it easy to go back to a previous point in time during the analysis workflow. The user can visually examine each selection's segmentation masks, or compare segmentation masks of multiple selections to each other with 2D slices and 3D views (see Section 6.4).

6.4 Visual Examination Stage

Usually, our domain experts visually examine the result of a segmentation algorithm by going through the volume and randomly investigating some 2D slices with specific features. We provide the visual examination stage to compare the segmentation results of multiple selections using 2D slices and 3D views. If a comparison of multiple selections is performed, the corresponding 2D slices and 3D renderings for each selection are placed side-by-side (see Figure 8). If the user interacts with a 2D slice view (e.g., zooming, panning) or a 3D rendering (e.g., zooming, translation, or rotation) of one selection, the interaction results will automatically synchronize with the views of the other selections. This approach of linked views, ensures that the ROIs for all the selection views under examination remain the same. Thus, the comparison of the segmentation results is facilitated.

The different visual representations of the selected data in the 2D slice view are presented in Figure 9. The raw XCT data (see Figure 9A) is shown in the 2D slice view to provide the proper context for the visualizations of the segmentation data. Additional context and reference are provided by overlaying the segmentation mask of the reference method (see Figure 9B). The opacity of the reference segmentation-mask overlay can be changed by the user from transparent to opaque. In order to convey an overview on how the selected pipeline runs segment the pores, we show an aggregated segmentation-masks overlay with adjustable opacity (Figure 9C). First, for each voxel we calculate how many segmentation masks classify this specific voxel as a pore. Then we encode the number of masks for each voxel using a perceptually-uniform, color-blind-safe color map chosen with ColorBrewer [13]. Such a representation shows which areas are segmented, and how many runs
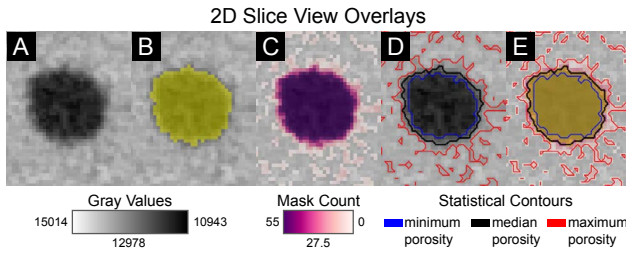
106

2D Slice View Overlays

Figure 9: 2D slice view overlays: gray value data (A), reference segmentation mask (B), aggregated segmentation masks (C), statistical contours (D), and all features in combination (E).

segment these areas as pores. It is not capable of showing where exactly the segmentation contours are located. On the other hand, showing segmentation contours for every run in the selection might lead to an excessively cluttered visualization, which is hard to interpret even for experienced domain experts. Therefore, only contours are shown for three representative segmentation runs (see statistical contours in Figure 9D), i.e., the runs with minimum (blue), median (black), and maximum (red) porosity values. This allows the domain experts to evaluate the potential extent of the selected runs' segmentations. The colors for the statistical contours were selected in such a way that they do not overlap with the colors from the reference and aggregated segmentation masks. Every visualization layer can be toggled on/off and displayed on top of each other, allowing the user to effectively combine the various depictions (Figure 9E). For the visual analysis scenarios where the perception of the pore shape is crucial but 2D does not provide enough context, a 3D view is provided to the user. Aggregated segmentation masks can be rendered in 3D using volume rendering (see Figure 8, 3D view).

7 EVALUATION AND DOMAIN FEEDBACK

The *PorosityAnalyzer* system was developed over a period of 16 months. During this time we closely worked together with the domain experts. To evaluate the tool, a questionnaire with respect to the domain-specific tasks was compiled. The evaluation questionnaire uses a five-point Likert scale to rate the techniques and concepts. The scale ranges from one (poor) to five (excellent) respectively. In total, ten domain experts participated. Most of them work with XCT data on a daily basis, have a good knowledge of fiber reinforced polymers (FRPs), and are well acquainted with porosity determination of FRPs. The experience of the participants in the field of XCT ranges from 1 year up to 11 years; in the field of FRPs from 1 year up to 13 years, and in the field of porosity determination of FRPs from 1 year up to 8 years. Figure 10 presents the results of the evaluation questionnaire.

The questionnaire first, determined how suitable the computation module and the parameter-spaces dialog (PSD) are for setting up the segmentation-pipelines by showing videos of the workflow. Overall we got a good feedback from the domain specialists in this respect. It was mentioned that the segmentation-pipeline setup by drag and drop is convenient and the automatic loading of the relevant dataset file is very comfortable. Locating the desired dataset among many others often takes a long time in commercial software. The domain experts noted that a selection of predefined segmentation pipelines (material dependent) would be helpful. The batch processing of the segmentation pipelines was lauded. With the currently used software this is only possible by instantiating the program several times, setting up the different segmentation pipelines and processing them.

To evaluate the overview visualizations of the analysis module the domain experts had to solve domain related tasks, like comparing and rating the pipelines to the reference one. Overall they
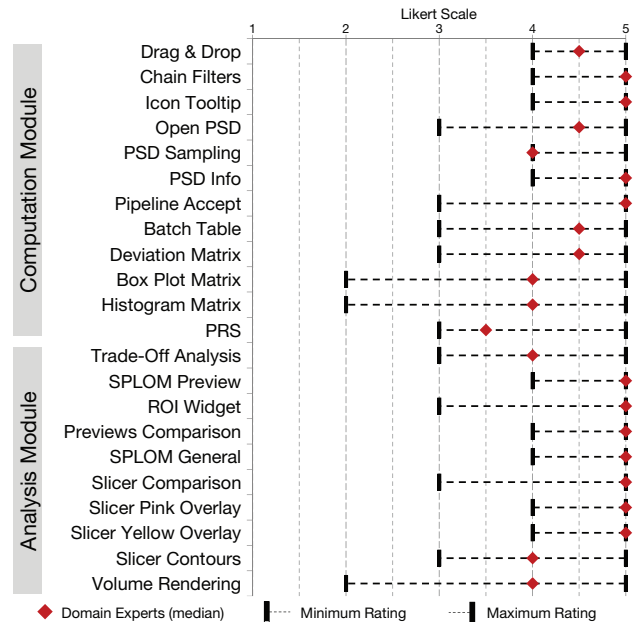

Figure 10: Results of the questionnaire with a five-point Likert scale ranging from one to five respectively, i.e., from poor to excellent.

performed very well, except in the case of the *overview comparative matrix* in box-plot mode, where they could not identify the correct pipeline. One feature that may have caused confusion was the use of different plot scales. We then checked the concept of the *parameter-range sliders* (PRS) for selecting suitable parameter ranges. Concerning the SPLOM for selecting parameters and allowing the experts a trade-off analysis, we got quite good feedback. Especially, the SPLOM *popup preview* to preserve the context of the segmentation results and the ROI widget were perceived as beneficial. We got excellent feedback on the 2D slice views for comparing segmentation results and overlaying those slice views with aggregated segmentation masks, reference mask, and statistical contours. The representation of aggregated segmentation masks as 3D volume renderings was generally received well by the domain experts, however some prefer the 2D slice views.

In addition to the questionnaire, we conducted an independent qualitative interview with two domain experts who are familiar with porosity determination of XCT scanned FRP specimens. In this interview we explained and discussed the computation and analysis module of the *PorosityAnalyzer* tool. Each module was then tested by the domain experts themselves. They created different segmentation pipelines in the computation module and evaluated previously calculated segmentation results by using the different data representation stages of the analysis module. In general, both experts pointed out that the *PorosityAnalyzer* simplifies their work significantly (e.g., by keeping track of the segmentation results) and makes the porosity determination of FRPs more efficient, as shown in the case studies in Section 8, or even enables analysis possibilities, which are hard to achieve with the currently used commercial software (e.g., comparing segmentation pipelines with color-coded 2D slice view overlays).

8 CASE STUDIES

In this section we present two case studies that reflect the domain-specific requirements and present the capabilities of our tool. First, we conduct a *porosity determination of non-parametric segmentation-pipelines* and second, we focus on the *influence of edge-preserving smoothing when determining the porosity*.

8.1 Porosity Determination of Non-Parametric Segmentation-Pipelines

Our domain experts often use a non-parametric segmentation algorithm called "Otsu Threshold", because it is fast and has no parameters to specify. However, our experts found out that the "Otsu Threshold" sometimes fails or provides unsatisfying results. Therefore, we included into the *PorosityAnalyzer* eight other non-parametric segmentation algorithms and compared those to the "Otsu Threshold". Figure 11A shows the *overview comparative matrix* in deviation mode (see Section 6.2) for the aeronautic datasets E3_low - E7_high (see Table 1). Datasets E3_low and E4_low have a low porosity, datasets E5_high-E7_high have a much higher porosity. All algorithms segmented the datasets E3_low and E4_low in approximately five seconds. The *overview comparative matrix* in deviation mode shows that the "Otsu Threshold" has a high deviation for the low porosity datasets. This relationship is illustrated in Figure 11B and Figure 11C. All other segmentation pipelines except "Moments Threshold" have a low deviation from the reference. The *overview comparative matrix* in deviation mode shows that the "IsoData Threshold" works for both kinds of datasets (low and high porosity). Table 3 shows the results. From the domain-specific perspective the "IsoData Threshold" is most suitable for the aeronautic industry datasets E3_low - E7_high as it delivers robust, accurate, and fast results for these dataset types (see Task 4, Section 2). Assembling and analyzing the 45 tested pipelines with the *PorosityAnalyzer* tool takes about 20 minutes compared to the conventional method of the domain experts, which takes about three and a half hours.
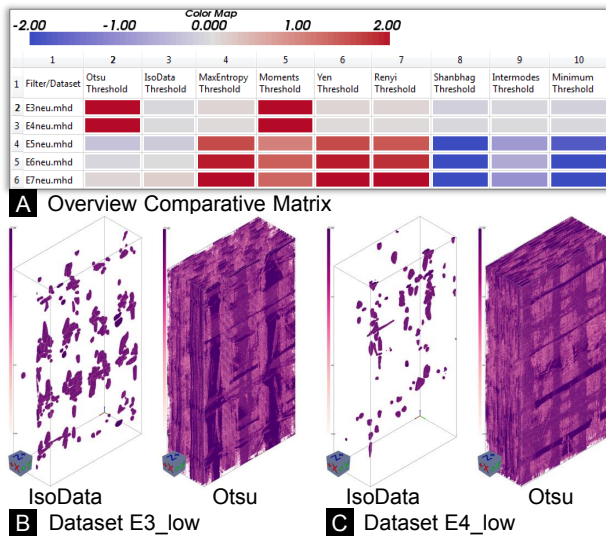

A Overview Comparative Matrix

B Dataset E3_low   **C** Dataset E4_low

Figure 11: *Overview comparative matrix* in deviation mode (A); comparison of aggregated segmentation masks in 3D of "IsoData Threshold" and "Otsu Threshold" for datasets E3_low (B) and E4_low (C).

Table 3: Accuracy results, i.e., deviations from the reference, for the "Isodata Threshold" and the "Otsu Threshold" performed on the datasets E3_low and E4_low.

		Dataset Name	
		E3_low	E4_low
"Isodata Threshold"	Dev. from Ref.	-0.0554 %	-0.0224 %
"Otsu Threshold"	Dev. from Ref.	21.03 %	66.65 %

8.2 Influence of Edge-Preserving Smoothing on Porosity Determination

In order to determine the porosity of an FRP specimen, the domain experts apply a global threshold to the raw XCT data [29]. Typically, in their daily work, domain experts do not use smoothing filters. However, the use of global methods without smoothing has the disadvantage that noise is segmented as well. Therefore, the domain experts wanted to know, how the pore segmentation behaves if smoothing filters are used to eliminate noise. To show the effect of smoothing filters, we have assembled two segmentation pipelines, which operate on the *PorePhantom* dataset (see Section 4). The gray values of this 16-bit dataset lie between 0 and 65535. One pipeline uses gradient anisotropic diffusion (GAD), an edge-preserving smoothing method, the other pipeline does not. Both pipelines use the "Binary Threshold" (see Table 2) to segment the pores. For a moderate smoothing of the data, we used the following GAD filter parameters: iterations 30, timestep 0.6874, and conductance 1. The parameter range of the "Binary Threshold" filter was set to 20000-45000 with a step size of 1000 gray values. This parameter range includes all the relevant gray values between pore gray values and material gray values. Figure 12A presents the resulting porosities of the individual segmentation runs for the pipeline without GAD smoothing (upper points) and with GAD smoothing (lower points). The porosities without GAD smoothing rise faster with increasing the "Binary Threshold" than the porosities with GAD smoothing. The smoothing with GAD enlarges the flat region of the porosities in the middle. A closer look at both porosity values, close to the reference segmentation (reference porosity is 6.123%), shows that the porosity difference is very small (porosity without GAD is 6.122%, with it is GAD 6.0931%). The *popup preview* visualizes this difference. The data point without GAD was fixed and compared with the data point with GAD (see Figure 12B, *popup preview*). Identical segmentation areas are color-coded in yellow, different ones in blue. The blue difference voxels are not included in the segmentation with GAD (compared point). The domain experts would not classify the "lengthy" blue region as a pore. They would classify it rather as noise. In addition, we superimposed the segmentation masks without GAD and with GAD (purple voxels and black median contour) with the reference segmentation (yellow voxels) and compared them in a 2D slice view (see Figure 13A, B, and C). The segmentation without GAD almost matches the reference segmentation except for a very few voxels (see Figure 13B). However, both segmentations identify the noisy voxels as pores. The segmentation with GAD is largely identical to the reference segmentation, but does not segment the noisy voxels (see Figure 13C). The influence of the noise is illustrated in the 3D views (see Figures 13D and E). We therefore conclude that the used reference segmentation method is not optimal, as it contains noise.

To find an optimal parameter set for the *GADSmoothing_BinaryThreshold* segmentation pipeline, we sampled the input parameter space of the GAD filter as follows: iterations 10–80, step size 10; timestep 0.6874; conductance 0.6–2.0, step size 0.1. The
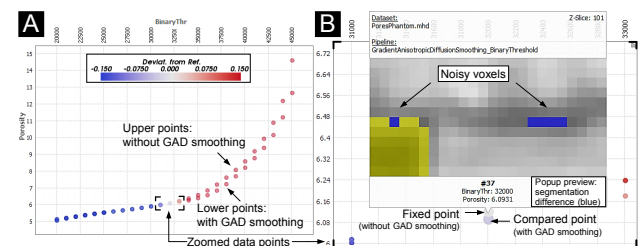

Figure 12: Comparison of the segmentation pipelines with GAD smoothing filter and without. Resulting porosities and gray value thresholds (A). *Popup preview* with voxel differences (B).
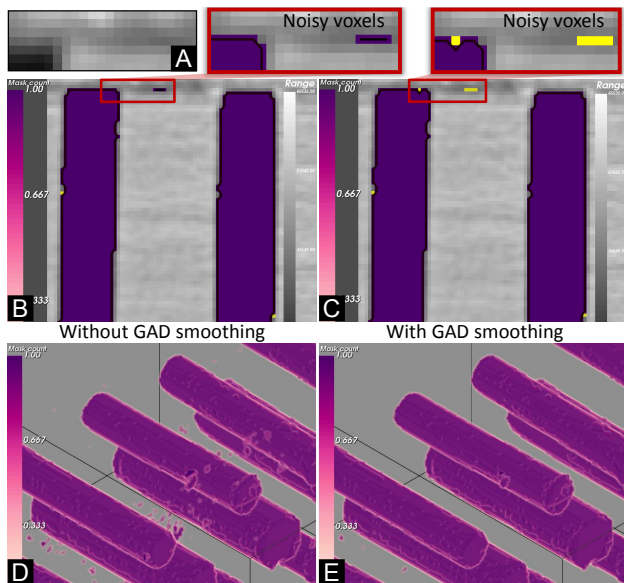
Figure 13: Cutout of the raw XCT data (A). 2D slice (B, C) and 3D (D, E) view comparison of the segmentation masks without GAD (noisy voxels segmented) and with GAD smoothing (no noisy voxels segmented; yellow noisy voxels in the zoom-in result from the reference).
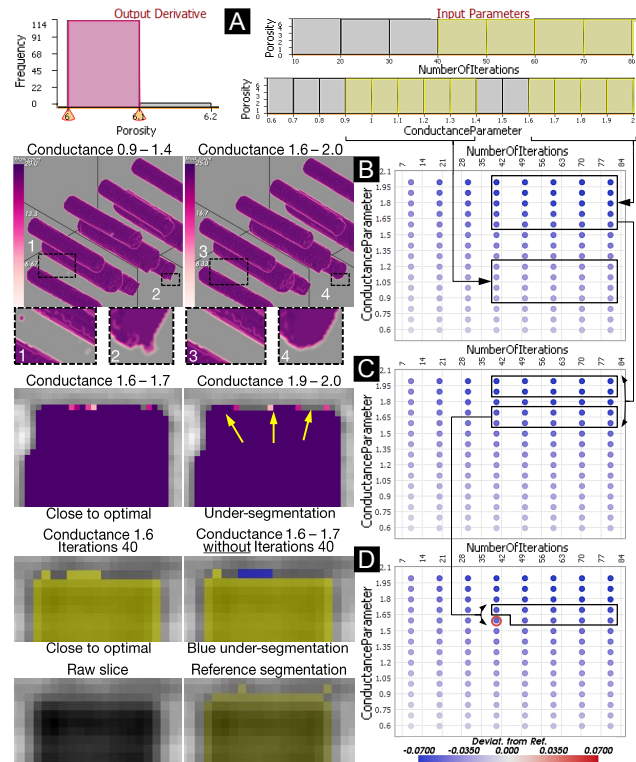

Figure 14: PRS with a selected porosity and the proposed GAD filter input parameters (A). 3D aggregated segmentation masks (B). 2D slice comparison (C). *Popup preview* comparison (D).

"Binary Threshold" was set to the same threshold value as for the reference segmentation (32011). For an initial selection of the input parameters, we used the *parameter-range sliders* (PRS). We selected the porosity bin with the highest segmentation frequency in the output parameter histogram (porosity range 6–6.1%). The PRS automatically marked the corresponding input parameter ranges (iterations 40–80; conductance 0.9–1.4 and 1.6–2) with yellow (see Figure 14A). These ranges were selected, saved to the selections view, and loaded to the SPLOM. The scatter plot in Figure 14B shows the selected ranges. The aggregated segmentation masks of these segmentation classes are illustrated in the 3D view. The comparison of the two classes in 3D shows that the segmentations with conductance 0.9–1.4 contain noise, while the segmentations with conductance 1.6–2 do not (see Figure 14B, 3D details). Therefore, we focused on the segmentation class with conductance 1.6–2. We divided this class into two classes, one with conductance 1.6–1.7 and one with conductance 1.9–2 (see Figure 14C, scatter plot). When examining the 2D slices of the aggregated segmentation masks, we found that the segmentations with conductance 1.9–2 start under-segmenting the data (see Figure 14C, exemplary 2D slices). We discarded the segmentations with conductance 1.9–2 and further investigated the remaining class with conductance 1.6–1.7 (see Figure 14D, scatter plot). By using the *popup preview*, we were able to compare the differences of the individual segmentations. All the segmentations start to under-segment the data except one segmentation with conductance=1.6 and iterations=40 (see Figure 14D, exemplary 2D slices). This segmentation pipeline shows a porosity value of 6.0715%. When comparing the reference segmentation (porosity 6.123%) with the found segmentation, it can be seen that the reference method over-segments the data. For this specimen type, we propose a data preprocessing with the GAD filter (iterations=40, timestep=0.6874, conductance=1.6), for a precise porosity determination (see Task 3, Section 2). Assembling and analyzing the 120 segmentations of the *GADSmoothing_BinaryThreshold* segmentation pipeline takes about one hour with the *PorosityAnalyzer* tool. With traditional methods a systematic evaluation of this number of segmentation masks would not be possible within reasonable time.

9 SUMMARY AND CONCLUSIONS

We presented the *PorosityAnalyzer*, a novel tool for the detailed evaluation and visual analysis of pore-segmentation pipelines in fiber-reinforced polymers. The computation module was developed to conveniently set up and execute distributed off-line computations. The analysis module is used for examining the resulting data. We demonstrated how a number of visualization techniques can be applied for the visual analysis of data on multiple levels-of-detail. These visualizations include the *overview comparative matrix*, the *scatter plot matrix* with the *popup preview*, the *parameter-range sliders*, 2D slices with overlays, and 3D views. The tool allows the domain experts to improve their workflow, obtain important insights into porosity segmentation-pipelines, and automate tedious manual operations. We present two use cases, indicating how *PorosityAnalyzer* can be employed to compare, analyze, and obtain insights into segmentation pipelines applied to a range of different datasets. We evaluated the tool with a questionnaire and a qualitative interview to get feedback from the domain experts. The feedback has shown that our tool makes it easier to compare established as well as new segmentation techniques and reduces the required time to compare various segmentation algorithms.

109

REFERENCES

[1] Market Report: Global Carbon Fiber Composite Market. Acmite Market Intelligence, July 2014.

[2] R. Beare. Histogram-based thresholding - some missing methods. 2011. http://www.insight-journal.org/browse/publication/811, accessed on 31.03.2016.

[3] R. Beare and G. Lehmann. The watershed transform in ITK - discussion and new developments. 2006. http://www.insight-journal.org/browse/publication/92, accessed on 31.03.2016.

[4] W. Berger, H. Piringer, P. Filzmoser, and E. Gröller. Uncertainty-Aware Exploration of Continuous Parameter Spaces Using Multivariate Prediction. *Computer Graphics Forum*, 30(3):911–920, 2011.

[5] S. Bergner, M. Sedlmair, T. Möller, S. N. Abdolyousefi, and A. Saad. ParaGlide: Interactive Parameter Space Partitioning for Computer Simulations. *IEEE TVCG*, 19(9):1499–1512, 2013.

[6] E. Birt and R. Smith. A review of NDE methods for porosity measurement in fibre-reinforced polymer composites. *Insight - Journal of The British Institute of Non Destructive Testing*, 46(11):681–686, 2004.

[7] W. C. Cleveland and M. E. McGill. *Dynamic Graphics for Statistics*. CRC Press, Inc., 1st edition, 1988.

[8] D. Coffey, C.-L. Lin, A. G. Erdman, and D. F. Keefe. Design by Dragging: An Interface for Creative Forward and Inverse Design with Simulation Ensembles. *IEEE TVCG*, 19(12):2783–2791, 2013.

[9] L. R. Dice. Measures of the Amount of Ecologic Association Between Species. *Ecology*, 26(3):297–302, 1945.

[10] N. Elmqvist, P. Dragicevic, and J. Fekete. Rolling the Dice: Multi-dimensional Visual Exploration using Scatterplot Matrix Navigation. *IEEE TVCG*, 14(6):1539–1148, 2008.

[11] M. Gavrilescu, M. M. Malik, and E. Gröller. Custom Interface Elements for Improved Parameter Control in Volume Rendering. In *14th International Conference on System Theory and Control*, pages 219–224, 2010.

[12] M. Gleicher, D. Albers, R. Walker, I. Jusufi, C. D. Hansen, and J. C. Roberts. Visual Comparison for Information Visualization. *Information Visualization*, 10(4):289–309, 2011.

[13] M. Harrower and C. A. Brewer. ColorBrewer.org: An Online Tool for Selecting Colour Schemes for Maps. *The Cartographic Journal*, 40(1):27–37, 2003.

[14] H. J. Johnson, M. McCormick, L. Ibáñez, and The Insight Software Consortium. *The ITK Software Guide*. Kitware, Inc., fourth edition, 2014. http://www.itk.org/ITK/resources/software.html, accessed on 31.03.2016.

[15] J. Kastner, B. Plank, D. Salaberger, and J. Sekelja. Defect and porosity determination of fibre reinforced polymers by x-ray computed tomography. In *2nd International Symposium on NDT in Aerospace*, 2010.

[16] G. Lehmann. Robust automatic threshold selection. 2006. http://www.insight-journal.org/browse/publication/134, accessed on 31.03.2016.

[17] G. Mayr, B. Plank, J. Sekelja, and G. Hendorfer. Active thermography as a quantitative method for non-destructive evaluation of porous carbon fiber reinforced polymers. *NDT & E International*, 44(7):537–543, 2011.

[18] K. Moreland. Diverging Color Maps for Scientific Visualization. In *Advances in Visual Computing*, volume 5876 of *Lecture Notes in Computer Science*, pages 92–103. 2009.

[19] T. Munzner. *Visualization Analysis and Design*. A K Peters/CRC Press, 2014.

[20] H.-F. Ng. Automatic thresholding for defect detection. In *IEEE 1st Symposium on Multi-Agent Security and Survivability*, pages 532–535, 2004.

[21] N. Otsu. A threshold selection method from gray-level histograms. *IEEE Transactions on Systems, Man and Cybernetics*, 9(1):62–66, 1979.

[22] H. Piringer, W. Berger, and J. Krasser. HyperMoVal: Interactive Visual Validation of Regression Models for Real-Time Simulation. *Computer Graphics Forum*, 29(3):983–992, 2010.

[23] A. J. Pretorius, M.-A. Bray, A. E. Carpenter, and R. A. Ruddle. Visualization of Parameter Space for Image Analysis. *IEEE TVCG*, 17(12):2402–2411, 2011.

[24] A. Reh, C. Gusenbauer, J. Kastner, E. Gröller, and C. Heinzl. MObjects–A Novel Method for the Visualization and Interactive Exploration of Defects in Industrial XCT Data. *IEEE TVCG*, 19(12):2906–2915, 2013.

[25] A. Reh, B. Plank, J. Kastner, E. Gröller, and C. Heinzl. Porosity Maps – Interactive Exploration and Visual Analysis of Porosity in Carbon Fiber Reinforced Polymers. *Computer Graphics Forum*, 31(3):1185–1194, 2012.

[26] M. Sedlmair, C. Heinzl, S. Bruckner, H. Piringer, and T. Möller. Visual Parameter Space Analysis: A Conceptual Framework. *IEEE TVCG*, 20(12):2161–2170, 2014.

[27] B. Shneiderman. The Eyes Have It: A Task by Data Type Taxonomy for Information Visualizations. In *Proceedings of the 1996 IEEE Symposium on Visual Languages*, pages 336–343, 1996.

[28] J. Sloan. Carbon fiber market: Cautious optimism. Composites world, High-Performance Composites, March 2011. http://www.compositesworld.com/articles/carbon-fiber-market-cautious-optimism, accessed on 31.03.2016.

[29] R. Stoessel, D. Kiefel, R. Oster, B. Diewel, and L. Llopart Prieto. μ-computed tomography for 3d porosity evaluation in carbon fiber reinforced plastics (CFRP). *International Symposium on Digital Industrial Radiology and Computed Tomography*, page 7, 2011.

[30] T. Torsney-Weir, A. Saad, T. Möller, H.-C. Hege, B. Weber, J. Verbavatz, and S. Bergner. Tuner: Principled Parameter Finding for Image Segmentation Algorithms Using Visual Response Surface Exploration. *IEEE TVCG*, 17(12):1892–1901, 2011.

[31] D. Ushizima, D. Morozov, G. H. Weber, A. G. C. Bianchi, J. A. Sethian, and E. W. Bethel. Augmented topological descriptors of pore networks for material science. *IEEE TVCG*, 18(12):2041–2050, December 2012.

[32] J. J. van Wijk and R. van Liere. Hyperslice: Visualization of scalar functions of many variables. In *Proceedings of the 4th Conference on Visualization '93*, pages 119–125, 1993.

[33] O. Wirjadi. *Survey of 3D Image Segmentation Methods*. Berichte des Fraunhofer ITWM: Fraunhofer-Institut für Techno- und Wirtschaftsmathematik. ITWM, 2007.

110

Interactive Exploration and Visualization Using MetaTracts extracted from Carbon Fiber Reinforced Composites

Arindam Bhattacharya, Johannes Weissenböck, Rephael Wenger,
Artem Amirkhanov, Johann Kastner, Christoph Heinzl

Interactive Exploration and Visualization Using MetaTracts extracted from Carbon Fiber Reinforced Composites

Arindam Bhattacharya, Johannes Weissenböck, Rephael Wenger, Artem Amirkhanov, Johann Kastner, and Christoph Heinzl, *Member, IEEE*

Abstract—This work introduces a tool for interactive exploration and visualization using MetaTracts. MetaTracts is a novel method for extraction and visualization of individual fiber bundles and weaving patterns from X-ray computed tomography (XCT) scans of endless carbon fiber reinforced polymers (CFRPs). It is designed specifically to handle XCT scans of low resolutions where the individual fibers are barely visible, which makes extraction of fiber bundles a challenging problem. The proposed workflow is used to analyze unit cells of CFRP materials integrating a recurring weaving pattern. First, a coarse version of integral curves is used to trace sections of the individual fiber bundles in the woven CFRP materials. We call these sections MetaTracts. In the second step, these extracted fiber bundle sections are clustered using a two-step approach: first by orientation, then by proximity. The tool can generate volumetric representations as well as surface models of the extracted fiber bundles to be exported for further analysis. In addition a custom interactive tool for exploration and visual analysis of MetaTracts is designed. We evaluate the proposed workflow on a number of real world datasets and demonstrate that MetaTracts effectively and robustly identifies and extracts fiber bundles.

Index Terms—MetaTracts, fiber bundle extraction, analysis and visualization, carbon fiber reinforced polymers, X-ray computed tomography, interactive visual exploration and analysis

✦

1 INTRODUCTION AND MOTIVATION

THE development of novel materials and components which integrate function orientation and efficiency are increasingly becoming a key objective of modern industry. Carbon fiber reinforced polymers (CFRPs) allow a quick integration of these demands and have become the material of choice for an ever growing number of applications. CFRPs are rapidly replacing conventional materials such as aluminum and steel, e.g., CFRPs show desirable characteristics such as high specific stiffness, high specific strength and high corrosion resistance. Moreover, CFRP materials show these characteristics at considerably lower weight. At the same time, highly complex and integrated components, which were previously impossible to manufacture, may now be produced from CFRPs. Primary structures and highly loaded components in aeronautics are a common example.

Typical carbon fiber reinforced polymer components, specifically CFRP laminates with endless carbon fibers consist of two main components: first a matrix, which acts as a bonding element and second, the reinforcements, which

help in achieving the desired characteristics. Various production processes are used to manufacture CFRP laminates. Most of these processes start with the reinforcement element, weaving individual carbon fiber bundles (yarn) into sheets of carbon fiber cloth in a predefined pattern. These sheets of woven carbon fiber cloth are also referred to as fabric and form the geometrical structure associated with the CFRP materials. Depending on the requirements of the final component, fabrics may be stacked in multiple layers in similar or different orientation. Both the alignment of fabrics and the weaving pattern of the individual carbon fiber bundles strongly influence the properties of the CFRP laminate. Resins are then integrated in the material system to fill the gaps in the fabric forming the matrix component. The main function of the matrix is to act as a bonding between the individual carbon fiber bundles. After curing, the production process of the CFRP laminate is finished.

The rapid expansion in utilization of CFRPs, the complexity of both the material system and the final components has generated a strong demand towards non-destructive testing (NDT) techniques for quality control [1]. The most widely used method for NDT is ultrasonic testing (UT). While UT provides a quick and cost-efficient overview of the material, it generally lacks resolution and may generate arbitrary results, e.g., due to the geometry of the component. Industrial 3D X-ray computed tomography (XCT, also referred to as 3DXCT or cone beam XCT) is increasingly applied for non-destructive testing of fiber reinforced polymers [2]. In contrast to UT, XCT generates a highly detailed 3D volumetric representation of the scanned specimen. In cone beam XCT geometry, the specimen is placed on a rotary table between X-ray source and detector. The X-rays

- *A. Bhattacharya and R. Wenger are with the Ohio State University, Columbus, OH 43210.*
  E-mail: arindamb86@gmail.com, wenger@cse.ohio-state.edu.
- *J. Weissenböck, A. Amirkhanov, J. Kastner, and C. Heinzl are with the University of Applied Sciences Upper Austria, Wels 4600, Austria.*
  E-mail: {johannes.weissenboeck, artem.amirkhanov, johann.kastner, christoph.heinzl}@fh-wels.at.
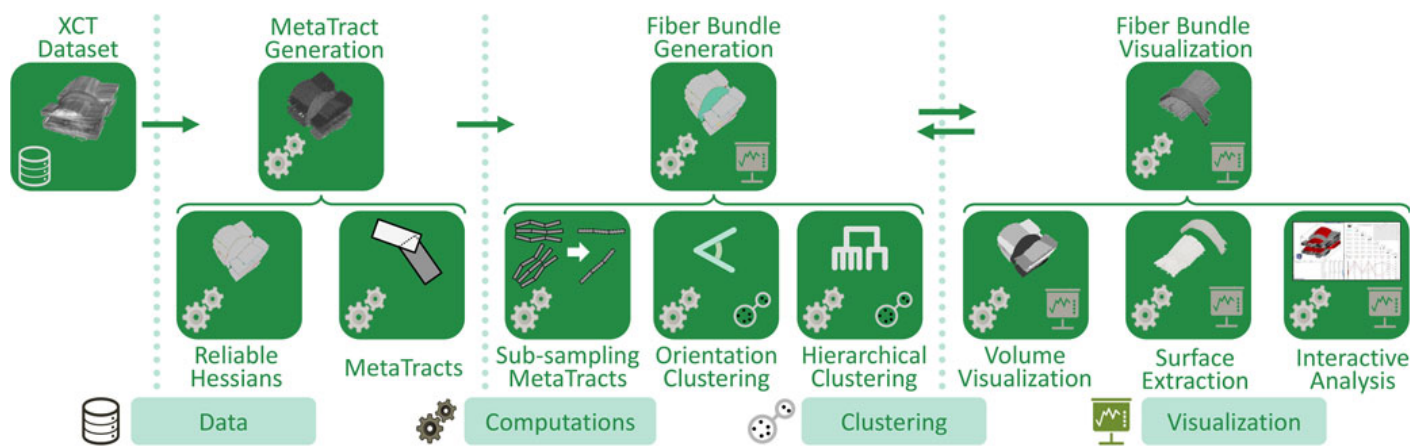
Fig. 1. Flow chart of the MetaTracts approach to fiber bundle extraction from XCT scans of CFRP datasets.

passing through the specimen get attenuated by the materials present. By transferring the X-rays in a scintillator layer into visible light, the detector records the corresponding 2D attenuation image (penetration image). The specimen is rotated and a 2D attenuation image is recorded at each angular step. The full series of attenuation images of a 360 degree rotation is utilized to generate a complete reconstruction of the data volume [3]. Cone beam XCT can reach voxel sizes below 500 nm generating high resolution volume data for comprehensive and detailed analyzes. To aid enhance reconstruction from scalar data such as industrial XCT [4] gradients have also been used.

There is unfortunately a trade-off between viewport and image resolution. The magnification reached within an XCT scan is determined by the distances between source and specimen as well as source and detector. The magnification therefore directly influences both resolution and viewport: higher resolutions decrease the viewport but show more details, lower resolutions allow for larger viewports and thus larger portions of the specimen.

In this work, we focus on datasets with larger viewports but lower resolutions where the individual carbon fibers (filaments) are indiscernible or barely visible. Our domain experts are mainly interested in visualizing the geometric structures in the weaving pattern of fiber bundles in endless carbon fiber reinforced composites instead of high resolution studies of individual fibers. Fig. 2 depicts our targeted dataset type. It shows the recurring fiber bundle pattern in the final CFRP laminate, the *unit cell*. Our work is motivated from the recent progress in two interrelated fields: first, CFRP components have gained wide application in industry because of its superior material and physical properties in comparison to conventional materials [5]. Second, recent developments in industrial 3D X-ray computed tomography (XCT) with regard to larger detectors, larger field of views, and better resolutions has opened XCT to this new application area of non destructive testing for fiber reinforced components [6]. While fiber bundles are now understood as highly important in determining component properties, the tools for visualizing the internal structure have not developed at the same pace. To the best of our knowledge, there is no current work that can resolve simple queries such as:

- How to extract and visualize the geometric structure of a particular fiber bundle?

- How to visualize the interaction between a particular pair of fiber bundles (weaving/braiding) or a unit cell?
- Which fiber bundles show a particular orientation?
- Which fiber bundles are of the same type of yarn? i.e., which bundles show similar sizes or diameters, which is the largest or smallest fiber bundle?

We separate the above queries into two major classes: geometric structure and spatial context. Queries associated with attributes of fiber bundles such as shape, size and orientation are grouped under geometric structure; while those referring to how two or more fiber bundles interact are categorized under spatial context. Spatial context answers questions such as: are these bundles in contact at a particular location in the dataset? What are the relative orientations of the contacting fiber bundles?

Providing answers to the above queries from currently common approaches such as volume rendering of the XCT datasets or visual inspection of particular 2D slices is nontrivial, even for experts. In [7] the authors presented MetaTracts, a novel approach which uses visualization techniques to gain insight into XCT scans of CFRP data. In this paper we elaborate and extend on this approach. Specifically, the extensions include a sub-sampling technique for the MetaTracts to reduce computation time and a custom interactive tool for exploration and visualization of the MetaTracts.

We interpret and advance techniques from diffusion tensor imaging as well as visual analysis to extract and visualize geometric structures from 3D X-ray computed tomography data of the woven carbon fiber reinforced composites. The main goal of this work is to expand the state of the art in non-destructive testing through extraction and interactive visualization of composite structures in *complete unit cells* of woven fabrics.

Fig. 1 shows an overview of our approach. Starting from XCT data, we first generate MetaTracts (see Section 4). Then we sub-sample and cluster the MetaTracts to generate fiber bundles (see Section 5). We discuss the visualizations we created for our domain experts (see Section 6). Section 7 illustrates an interactive tool we built for fiber bundle analysis. Section 8 summarizes the user evaluation of our method. Section 9 describes our experimental results, Section 10 presents our parameter choices. We conclude with some limitations (Section 11), conclusions and future work (Section 12).
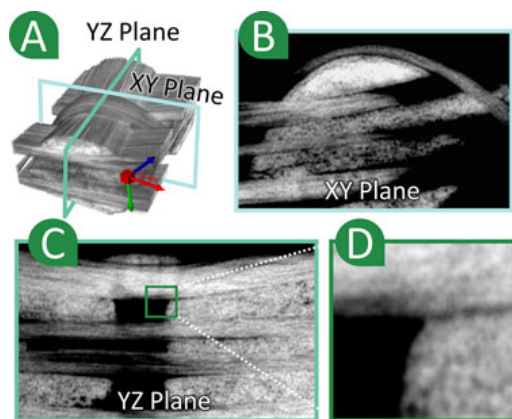
Fig. 2. Data characteristics: (a) Rendering of dataset D1. (b, c) 2D slices along Z- and X-axis. (d) Zoom in of the green region marked in (c). Multiple fiber bundles cross and are indistinguishable by visual inspection alone.

2 RELATED WORK

Diffusion Magnetic Resonance Imagining (dMRI, also referred to as Diffusion Tensor Imaging (DTI)) is a magnetic resonance imaging technique which provides three-dimensional information about the structures in cerebral white matter based on diffusion of water molecules. DTI has gained popularity in medical diagnosis within recent years; its main clinical application is found in the study and treatment of neurological disorders. DTI may reveal abnormalities in white matter fiber structure and is used for visualizing the organization of fibers in the human brain and brain connectivity. A variety of algorithms have been proposed for generating fiber-tract trajectories. In general, these reconstructions of fiber trajectories are clustered into bundles which are expected to be related anatomically or spatially. We broadly divide the related work on DTI into two parts of immediate relevance to our proposed solution: fiber tracking and fiber clustering. We next review methods for analyzing the second order local structure and the current state of the art in the visual analysis of fiber reinforced composites.

2.1 Fiber Tracking in Diffusion Tensor Imaging

A basic assumption in DTI analysis is that the principal eigenvector of the diffusion tensor is parallel to the underlying dominant fiber direction in each image voxel [8], [9], [10]. The principal diffusion direction at each discrete location is interpolated to form a continuous velocity field. Continuous tracts are generated by propagating virtual particles along the principal diffusion directions until they reach some termination criterion. This is usually done by solving a Runge-Kutta integration (typically second or fourth order). Because decisions are made locally, these methods perform poorly in noisy regions and often generate small fibers. Basser et al. [8], [11] proposed that white matter tracts could be represented as 3D curves in space. They showed that numerical methods could be used to follow fibers and fiber bundles and to generate tracts in human brain data. Mori et al. [9], [10] divided reconstruction techniques into line-propagation or energy minimization techniques. In line propagation approaches, trajectories are computed based on local neighborhoods and in energy minimization approaches the most favorable trajectory connecting two given endpoints is selected.

2.2 Fiber Clustering in Diffusion Tensor Imaging

In DTI, similarity measures such as proximity between fibers are used to group fiber tracts into bundles. Extensive research has been done on automatic DTI fiber clustering methods [12], [13], [14], [15], [16]. These approaches build on the assumption that proximity measures that compare DTI fiber trajectories can also represent anatomical relationships. Clustering requires choosing a suitable proximity measure and a method for grouping "close" fibers.

Pairwise proximity measures include endpoint distances [12] and mean of the closest distances between points on two fibers [14]. Zhang et al. [16] introduced a thresholded version of the closest distances mean, so that fibers which are close for certain distance and then diverge, are clustered separately. Brun et al. [13] use normalized cuts along with a pairwise computed distance measure using 9D fiber shape descriptors.

The choice of the clustering algorithm can be broadly divided into those approaches using hierarchical clustering [16], [17] and those using spectral clustering [13], [18], [19]. Brun et al. [12] described how a spectral non-linear dimensionality reduction technique, Laplacian eigenmaps (Belkin and Niyogi [20]), can be applied to the problem of organizing fiber tracts data. The key notion of the Laplacian eigenmaps algorithm is to represent the underlying data as a graph. Each node represents a data point and the edges connect neighboring data points. An eigenvalue problem is solved to represent the data in a lower dimensional space while preserving the local graph structure. In the case of fiber bundles, the individual points are fiber tracts. In the ideal case fiber tracts belonging to the same bundle must remain "close" to each other in the lower dimensional space. Westin et al. [15] also used spectral clustering on a Hausdorff distance measure defined as the maximum of pointwise minimum distances between two fibers. Jonasson et al. [18] ran K-means clustering on the eigenvectors of the affinity matrix defined as the co-occurrence of fibers in the data. Additionally, the agglomerative hierarchical clustering method [21] has gained popularity for proximity based fiber segregation (Zhang et al. [16], Corouge et al. [14]). An agglomerative hierarchical clustering method starts with each data point/fiber in an individual cluster. At each stage of the algorithm the two most similar clusters are merged based on some criterion. The two basic cluster similarity measures are single-link and complete-link. With the single link, the distance between the clusters is the distance between the closest pair of items. Moberts et al. [17] implemented several distance measures in their evaluation of fiber clustering and concluded that clustering methods are generally accurate in capturing fiber bundles.

There are a number of difficulties in hierarchical clustering. First, computing all pairs' distances for tracts to generate the distance matrix is time consuming [22]. Second, a "correct" distance measure to compare tracts must be chosen. Third, hierarchical clustering is best suited for similar length fibers. Spectral methods are also hindered by long matrix computations.

2.3 Second Order Local Structure

Unlike DTI, we do not have diffusion tensor data. Instead, we have a scalar volume with tubular structures embedded

in them. Analyzing curvilinear structures in volumetric images has been utilized for a variety of purposes including center line extraction [23] and vascular image enhancement as proposed by Frangi et al. [24] and Sato et al. [25]. Frangi et al. [24] introduced a method based on studying the eigenvalues of the Hessian matrix specifically for the purposes of developing vessel enhancement filters.

2.4 Visual Analysis and Modeling of Fiber Reinforced Composites

The approaches presented in visualization and analysis of composites mainly focuses on individual objects such as fiber extraction from high resolution data where the individual fibers are clearly discernible. Fritz et al. [26] proposed interactive workflows for non destructive testing practitioners to explore and quantify steel fibers in reinforced sprayed concrete. Salaberger et al. [27] introduced a pipeline to extract and characterize individual fibers of fiber reinforced composites. They encode the extracted fibers as color-coded line segments in 3D and visually identify fibers with similar orientations. Recently, Weissenböck et al. [28] presented a system for interactive exploration and analysis of fibers in fiber reinforced polymers. They use the visualization paradigms of a scatter plot matrix and parallel coordinates to select fibers according to their characteristics. The defined fiber classes can be managed in a list and are displayed with a 3D renderer. Lomov et al. [29] discuss the problems and current available solutions in geometric modeling of three dimensional composites. Modeling of the composites first starts with establishing the topology of the structure, which translates to answering if a particular bundle is in contact with another at a particular position. The second step builds the geometry of the model, answering queries relating to placement of bundles in space, their orientations and dimensions.

3 DATA CHARACTERISTICS AND ASSUMPTIONS

Fig. 2 shows dataset D1 with woven fiber bundles which is used for explaining the pipeline. The size of D1 is $450 \times 300 \times 500$ voxels with an isotropic resolution of 2 μm and 8 bit unsigned integer scalars. Fig. 2 clearly shows the recurring fiber bundle weaving pattern of the composite unit cell used for manufacturing fiber composites. Fig. 2a shows a volume rendering of the dataset. Figs. 2b and 2c show 2D slices along the X- and the Z-axis respectively. Fig. 2d shows a magnified image of the green region of interest and contains two bundles going in orthogonal directions. The low resolution makes it impossible to separate the two fiber bundles. Also the separation between two fiber bundles is barely visible. The fiber bundles may differ in terms of the amount of fibers in the bundle. Figs. 2b and 2c shows the large variation in cross section sizes among the bundles. Depending on the weaving pattern, the fiber bundles cross each other in different orientations. The number of orientations is defined by the weaving pattern and typically consists of two main orientations. The weaving pattern may cause individual bundles to be curved. In consequence, individual fibers may be adjacent in euclidean distance but belong to different bundles. We make the following *assumptions* on our data:

- The structure embedded in the data contains fiber bundles of indiscernible fibers.
- Local orientation: Each point in a fiber bundle has a local orientation parallel to the corresponding area in the fiber bundle.
- Local orientation may gradually change within the fiber bundle.
- Local orientation may be noisy and not reliable.
- Connectivity: When moving along the direction of a non-noisy local orientation in small increments, we reach another neighborhood with similar local orientation.
- Fiber bundles going in different directions only interact near the surface of contact.

4 EXTRACTING METATRACTS

Extracting MetaTracts consists of two main steps. Initially, a local orientation direction (represented as a unit vector) is computed at each grid location. Next, we compute a coarse set of poly-cylinders called MetaTracts which traverse the data constrained by the local orientation directions. Section 4.1 describes the procedure to generate reliable Hessians. Section 4.2 describes the MetaTracts and their properties. Section 4.3 details the creation of MetaTracts.

4.1 Computing Reliable Hessians

The objective of this step is to associate each grid location with a unit vector which represents the orientation in the local neighborhood and a real value [0,1] that represents a measure of reliability of the orientation computed at the given location. A reliability score of 0 means the local orientation is not credible while a score of 1 means the local orientation is correct. The input to this stage is the original scalar data, which is an uniform lattice grid in $\mathbb{R}^3$. We approximate the local orientation by eigenvalue analysis of the Hessian matrix applied locally to each voxel.

Analyzing curvilinear structures in volumetric images has been utilized for a variety of purposes including center line extraction [23] and vascular image enhancement [24], [25]. These approaches search for geometrical constructs that can be regarded as tubular structure. The local region around a pixel in an image is often approximated by the Taylor series expansion $F(x_0 + \partial x_0) = F(x_0) + \partial x_0^T \bigtriangledown_0 + \partial x_0^T H_0 \partial x_0$, where $\bigtriangledown_0$ and H_0 are the gradient and the Hessian matrix computed at x_0. The Hessian matrix captures the local second-order structures inherent in the intensity (scalar values at grid vertex) variations around each grid location. Analyzing the second order information (Hessian) has an intuitive justification in the context of detecting tubular structures [24], [25]. The second derivative of a Gaussian kernel acts like a probe that measures the contrast between the regions inside and outside in the direction of the derivative. The eigendecomposition of the Hessian matrix generates eigenvectors which represent the local curvature of the image. The eigenvector corresponding to the smallest eigenvalue gives the direction along which the curvature is smallest. This direction also termed as the principal direction, coincides with the direction of the tubular structure.

Frangi et al. [24] introduced a process that searches for geometric structures which are tubular. They defined a
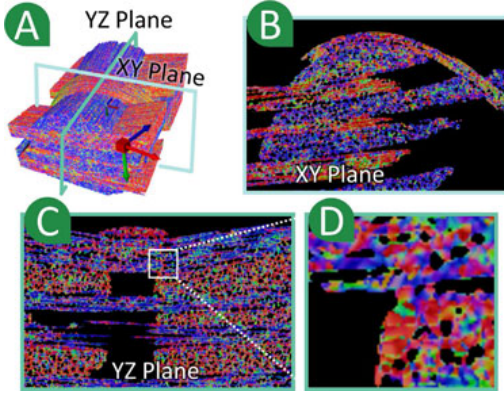
Fig. 3. Reliable Hessians. (a) MetaTracts colored according to the mean local orientation vector mapped to the RGB color scale. (b,c) 2D slices along *Z*- and *X*- axis. (d) Magnified region marked in (c).

"vesselness" criterion based on the geometric ratios of eigenvalues of the second order ellipsoid given by the local Hessian matrix. In order to determine reliable Hessians, we compute the *same* metric. We include their work here for completeness and direct the reader to [24] for details. Let λ_K be the eigenvalue with the Kth smallest magnitude. Here, $|\lambda_1| \leq |\lambda_2| \leq |\lambda_3|$ are the eigenvalues of the Hessian matrix. Specifically, a pixel belonging to a vessel region will have small λ_1 ($|\lambda_1| \approx 0$) and λ_2, λ_3 of large magnitude and of equal sign ($|\lambda_1| \ll |\lambda_2|$ and $|\lambda_2| \approx |\lambda_3|$). The sign indicates if the vessel is bright in a dark background or dark in a bright background. In our case the individual fibers are bright ($\lambda_2, \lambda_3 < 0$). The following measures are defined in [24].

$$\mathscr{R}_{\mathscr{A}} = \frac{\text{Largest Cross Section}/\pi}{\text{Largest Axis Semi-length}^2} = \frac{|\lambda_2|}{|\lambda_3|} \qquad (1)$$

$$\mathscr{R}_{\mathscr{B}} = \frac{\text{Volume}/(4\pi/3)}{(\text{Largest Cross Section Area}/\pi)^{\frac{3}{2}}} = \frac{|\lambda_1|}{\sqrt{|\lambda_2 \lambda_3|}}. \qquad (2)$$

In Equation (2), $\mathscr{R}_{\mathscr{B}}$ provides a measure of deviation from a "blob" like structure while in Equation (1), $\mathscr{R}_{\mathscr{A}}$ distinguishes between "plate-like" and "line-like" structure. Grayscale variations and close proximity of the fibers in our data make the Hessians computed at each voxels susceptible to errors. Thus, we compute reliable Hessians (R_H) to determine which locations in the volume provide reliable local orientation.

$$R_H = \begin{cases} 0 & \text{if } \lambda_2 > 0 \text{ or } \lambda_3 > 0 \\ (1 - e^{\frac{-\mathscr{R}_{\mathscr{A}}^2}{2\alpha^2}})(e^{\frac{-\mathscr{R}_{\mathscr{B}}^2}{2\beta^2}})(1 - e^{\frac{-s^2}{2c^2}}) & \text{otherwise.} \end{cases}$$

Variable s is the Frobenius norm of the Hessian matrix. The value of $(1 - e^{\frac{-s^2}{2c^2}})$ will be low in regions with no structure. The utility of the vesselness is a little different in our framework than in the work of Frangi et al. [24]. First, vesselness in biology is computed for different scales because the vessels can be of different sizes. In our case, usually the widths of individual fibers are known a priori. Second, we do not have clear tubular structures embedded in a dark contrast matrix such as in blood vessels. Instead, we are trying to associate each grid location with a probable orientation based on its local second order structure. The R_H is interpreted as a reliability measure of the local orientation.

Grid locations where the R_H is above a cutoff threshold are marked as regions with reliable orientations (see Section 10).

Fig. 3 shows the intermediate results of the local orientation computation. The principal direction represented as a unit vector has been mapped to the RGB color space. Fig. 3a shows the entire dataset. Figs. 3b and 3c provide 2D slices along the Z- and X-axes respectively. Regions with X- and Z-axis local orientation show predominant red and blue color respectively. Fig. 3d shows a magnified region of interest. The black regions within bundles are regions where the R_H is less than the threshold and have unreliable local orientation. The bundles are also not uniformly colored as the Hessians and the corresponding principal directions are noisy.

We indicate some intrinsic differences between DTI and our XCT data. Fiber traces can be generated in DTI using a standard fiber tracking algorithms following the principal direction of diffusion by employing a fourth order Runge-Kutta method [12]. The principal direction based on the Hessian matrix works best when the tubular structures in the data are well separated from the background. This is not the case for our data. The local orientations at each voxel are inherently noisier.

4.2 MetaTracts Properties

Conventional integral curve based techniques cannot be directly used to extract fiber bundle traces from reliable Hessians because of the spurious nature of the Hessian based local orientations. Thus instead of building fiber traces, we define an abstract representation of the fibers. We start from two key assumptions on the data, specifically "local orientation" and "connectivity", while taking into account the adverse effects of noise and low resolution.

This is achieved by interpreting the underlying geometric structure of the fibers as a set of connected cylinders. Hence, we formulate MetaTracts as a coarse and simple approximation of integral curves in the form of a continuous chain of cylindrical tubes in $\mathbb{R}^3$. MetaTracts traverse the fiber bundles embedded in the original data. Extending the intuition developed above, we devise the following *properties* that the MetaTracts share;

1) MetaTracts are associated with a continuous set of cylinders.
2) MetaTracts are associated with a start point at a grid vertex (C_p).
3) Individual cylinders in MetaTracts have constant lengths, radii, and start points (which are also grid's vertices).
4) Individual cylinders in MetaTracts (except the first one) are connected to their previous cylinders at their start point.
5) Individual cylinders are parallel to the local orientation vector at their start points (N_P).

4.3 MetaTracts Generation

In this section we detail the process of generating Meta-Tracts. Here we explain the process in $\mathbb{R}^2$, the procedure extends to $\mathbb{R}^3$ trivially. The output of the last (reliable Hessian) stage is input to the current step. In $\mathbb{R}^2$, each grid location is associated with a unit vector (representing the local
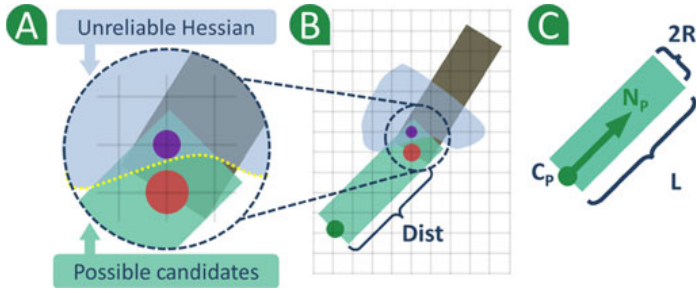
Fig. 4. MetaTracts generation. (b) MetaTracts generation process. (a) Magnified region in (b). (c) Individual MetaTract cylinder. [7].

Fig. 5. MetaTracts color-coded according to their mean orientations, along with slices of the YZ- and XY-plane.

orientation) and a reliability measure $R_H[0,1]$. Fig. 4 shows some key features of MetaTracts. In Figs. 4a and 4b the regions with unreliable Hessians are marked in blue. In $\mathbb{R}^2$ the individual components of MetaTracts are rectangles. Fig. 4c shows an individual rectangle. Let the seed point associated with this cylinder be grid point C_p (property 2 in Section 4.2). The local orientation at C_p as computed in the reliable Hessian stage is N_P and is given by the dark green arrow. The rectangle itself is of length L and radius R (properties 3 and 5 in Section 4.2).

Candidate vertices: We start with an individual rectangle (Fig. 4b) with seed point C_p, local orientation N_P and dimensions L, R. The set of grid vertices which are located within the rectangle (green region) in Figs. 4a and 4b are possible start points for the next cylinder. Among these we first discard the grid points which have unreliable Hessians (marked in blue). The remaining set of grid points are called "candidate vertices" and are potential start points for the next rectangle. Next, based on the "local orientation" and "connectivity" assumptions on our data, we rank all the candidate vertices. The rank of each candidate vertex is based on the following characteristics.

- *Orientation similarity*: The local orientation (N_p) of the start points (C_p) for the consecutive cylinders should be similar.
- *Large distance*: The MetaTracts should traverse the data using as few cylinders as possible. The distance between start point (C_p) of one cylinder and the start point for the next cylinder should be as large as possible. We measure the distance of each candidate vertex from C_p by projecting the euclidean distance between them onto N_p. For example, in Fig. 4b the distance is measured as the euclidean distance between the green and the orange vertices projected on to N_p. We refer to this perpendicular projection distance as '*projected_dist*'.

We next define a "priority" for each candidate vertex, based on the above characteristics. For each cylinder in a MetaTract, we put it's "candidate vertices" in a priority queue based on Equation (3).

$$Priority = \gamma_1 e^{(-angle^2/\eta^2)} + \gamma_2 e^{(-projected\_dist^2/\tau^2)} \quad (3)$$

γ_1, γ_2 are the weights ($\mathbb{R}_{\geq 0}$) which decide how the "priority" depends on the affine combination of the two factors. For all our cases, we use $\gamma_1 = 1/3$ and $\gamma_2 = 2/3$. In general, we suggest $\gamma_1 + \gamma_2 = 1$ and $\gamma_1 \leq \gamma_2$. At each iteration, we pick the top element in the priority queue to generate the
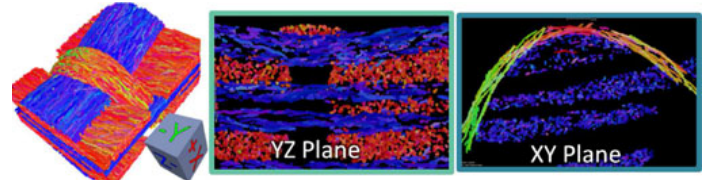
corresponding cylinder, and repeat the steps. Essentially, Equation (3) selects a grid point which is farthest from the current start point and is going in a similar direction. This approach tackles noise/errors in local orientation better than integral curves by looking at multiple choices for vertex candidates and avoiding intra-cell interpolation in an already noisy environment.

In Fig. 4b the *orange* grid vertex is selected next and the process repeated. The *purple* vertex is in a region of unreliable Hessian and is not selected even though it is further away from the seed point in terms of euclidean distance. If we generate MetaTracts that have erroneous local orientations, the size of the candidate vertex set will be small. This will create MetaTracts of small length which are then removed.

The MetaTracts generated by the above procedure are shown in Fig. 5. The MetaTracts are colored with the mean orientation direction mapped to the RGB space. Fig. 5 also shows a single slice of the YZ- and XY-plane. Consistent orientation is a key intrinsic feature in our data which is not obvious from the original grayscale images, but becomes visually pronounced in the generated MetaTracts.

Fig. 16 shows the MetaTracts of a particular bundle colored according to their individual length. MetaTracts in a given fiber bundle may extend the full length of the bundle or have different lengths and partial overlaps.

5 FIBER BUNDLE GENERATION

The MetaTracts generated in the previous section represents fragments of the fiber bundles. The MetaTracts are then clustered in order to extract the complete fiber bundles. The clustering process benefits from both the orientation and geometric proximity information inherent in the XCT scans of the CFRP fiber bundles.

Empirically, we found "orientation" information was more reliable than "geometric" proximity based approaches for MetaTracts data. For example, Fig. 5 (where the Meta-Tracts are color-coded according to mean orientation) clearly shows a separation of MetaTracts based on "orientation" of the MetaTracts. Conversely, we noticed that partially overlapping fibers (Fig. 16) created problems for "geometric" proximity based approaches. We also observed that different clustering techniques performed preferably for different measures.

We focused on the following objectives. First, we wanted a clustering approach which would take into account "orientation" and "proximity". Second, we stressed on a simple and robust approach which could be applied generally to a variety of datasets (constrained upon satisfying our data characteristic assumptions). A final goal was to assure parameters for the approach to be dependent on physical
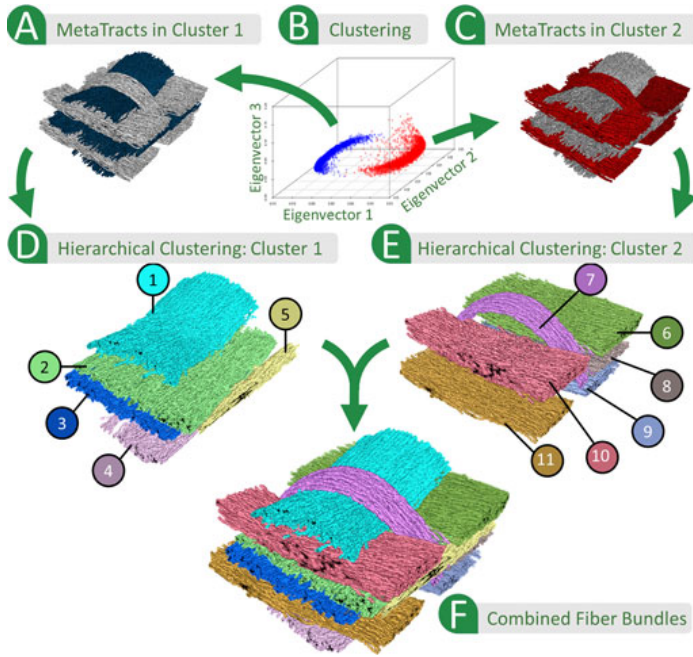
Fig. 6. Clustering results: Orientation clustering (a,b,c), distance clustering (d,e). (b) Results of K-means clustering ($K = 2$) with MetaTracts (nodes) projected to the top three eigenvectors as major axes. (a) MetaTracts belonging to orientation cluster 1 in blue. (c) MetaTracts belonging to orientation cluster 2 in red, MetaTracts in gray (a,c) show context. (d,e) Hierarchical (distance based) clustering on each orientation cluster. (f) Combined result showing 11 individual extracted clusters. [7].

parameters which our end users such as material scientist could easily grasp and manipulate. Accordingly, instead of creating a heuristic and artificially combining the orientation and geometric proximity measures, we separated the clustering process. Specifically, we first cluster based on "orientation". Each orientation cluster is then further subdivided based on "geometric" proximity. The two-step clustering process, helps making the problem more tractable and the parameters more intuitive to the end users. Section 5.3 describes associated problems with our experiments with a single-step clustering approach.

Section 5.1 describes orientation based clustering. Section 5.2 describes proximity based clustering. Section 5.3 describes our experiments with one-step clustering. Further discussion about the parameters involved can be found in Section 10.

5.1 Orientation Based Clustering

Before extracting individual fiber bundles, we first separate the MetaTracts into classes based on their major local orientations. To cluster MetaTracts going along similar local directions, we use a spectral embedding technique called Laplacian eigenmaps (originally introduced by Belkin and Niyogi [20]). An eigenvalue problem is solved to map the manifold embedded in a graph into a lower dimensional space, while preserving the graph structure. Let G be the graph, we compute the eigenvalues and eigenvectors for the generalized eigenvector problem $Lf = \lambda Df$, where D is the diagonal weight matrix and L is the Laplacian matrix. The eigenvector f_0 corresponding to the eigenvalue 0 is left out and the next m, f_1 through f_m eigenvectors are used to embed in an m-dimensional space (see Section 10 for values of m).

In our problem, each MetaTract is a node in the graph. We adopt a simple *orientation* based measure to define the

weight of the edges of the graph. Given a pair of Meta-Tracts, the edge weight between two nodes is defined as the cosine of the maximum angle between the local orientations (N_P) of all pairs of start points (C_P) between the two Meta-Tracts. The edge weights give a "distance matrix" representing the distance between each pair of nodes. Using the Belkin and Niyogi algorithm we "embed" these nodes in a low dimensional space where the euclidean distance between nodes, approximates the distance between nodes given by the original "distance matrix". Next, K-means clustering is employed in the lower dimensional space, where K is the number of major fiber bundle directions in the woven structure. K is derived from domain knowledge. For all our test cases, there are two major fiber bundle directions. Dimensionality reduction provides us some interesting advantages, by automatically handling the case of curved bundles. Laplacian eigenmaps have been used before for DTI clustering [12]. Fig. 6b shows the result of the K-means clustering with the nodes (MetaTracts) projected to the top three eigenvectors as the major axes. As expected there is a clear distinction based on fiber bundle orientation. Figs. 6a and 6c shows the MetaTracts colored according to orientation clustering results, in blue and red respectively. Each distinct cluster represents MetaTracts belonging to all fiber bundles, along an individual orientation. Note the similarity between Figs. 6a and 6c and the result of coloring the Meta-Tracts by mean orientation (Fig. 5).

5.2 Distance Based Clustering

To subdivide the oriented clusters into individual fiber bundles, we include further information about the geometric proximity between MetaTracts. We use the directed Hausdorff distance for distance based clustering. Each MetaTract is represented as a set of points (C_P). Formally, the directed Hausdorff distance from point set P to point set Q is defined as $H_{dir}(P,Q) = max_{p \in P} min_{q \in Q} d(p,q)$. The Hausdorff distance is defined as $H(P,Q) = max(H_{dir}(P,Q), H_{dir}(Q,P))$. The Hausdorff distance is a metric so $H(P,Q) \leq H(P,Q') + H(Q',Q)$ but the directed Hausdorff is not. Unfortunately, the Hausdorff distance does not work well for our application. A single fiber bundle is represented as a set of "overlapping" MetaTracts. For example Fig. 16 shows the length distribution of MetaTracts which express the fiber bundle. Consequently, if a MetaTract P covers only a part of the fiber bundle covered by Q, then $H_{dir}(P,Q)$ will be very small while $H_{dir}(Q,P)$ will be large. Thus, $H(P,Q)$ will be large, even though P and Q are in the same fiber bundle. Instead of using the Hausdorff distance, $max(H_{dir}(P,Q), H_{dir}(Q,P))$, we use $min(H_{dir}(P,Q), H_{dir}(Q,P))$. If P covers only a part of the fiber bundle covered by Q, then $min(H_{dir}(P,Q), H_{dir}(Q,P))$ is very small. Note that if P and Q overlap but do not cover the same parts of the fiber bundle, then $H_{dir}(P,Q)$ and $H_{dir}(Q,P)$ and $min(H_{dir}(P,Q), H_{dir}(Q,P))$ will be large. The directed Hausdorff distance is very sensitive to outliers in the data. However, because Meta-Tracts after orientation clustering are constructed using cylinders with similar orientations, they are not plagued by outliers. To cluster based on MetaTract proximity, we used single linkage hierarchical clustering. Hierarchical clustering has a single parameter h, the desired number of clusters. Clusters are merged until there are only h clusters left. Hierarchical clustering is intuitive since it is easy to trace how clusters are

formed and merged. Single linkage clustering finds pairs of objects $p \in P$ and $q \in Q$ where $P \neq Q$ which are closer than other such pairs, and merges the containing clusters P and Q. We found that single linkage hierarchical clustering had two major drawbacks;

- The clustering might produce some "small" clusters of just a few MetaTracts. These MetaTracts are anomalies caused by overlapping fibers and did not represent true fiber bundles.
- Second, if two distinct fiber bundles "ran" parallel for some of their length and then separated, they would sometimes be clustered into a single erroneous bundle. This occurs when a short MetaTract which was parallel to both but did not extend into the separation region forms a link between the two fiber bundles. This causes the fiber bundles to be clustered into a single bundle.

To address the problem of small clusters, we applied hierarchical clustering and then identified small clusters with few MetaTracts. We removed the MetaTracts that were in those clusters from the dataset and reapplied hierarchical clustering. To address the problem of short MetaTracts joining different fiber bundles, we applied hierarchical clustering and then removed the shortest tracts (length less than η times the median length, set to 0.6) in each bundle. We then reapplied hierarchical clustering. We repeated both steps until a steady state of clusters was reached and no new small fibers can be removed. The result of hierarchically clustering all the MetaTracts in each orientation cluster (Figs. 6a and 6c) are shown in Figs. 6d and 6e respectively.

After the clustering step, the MetaTracts are separated into well formed fiber bundles. The final result of the clustering process is shown in Fig. 6f. Eleven individual fiber bundles have been separated. Five fiber bundles were extracted from orientation cluster 1 (Z-axis) and six from orientation cluster 2 (X-axis).

5.3 Choice of Clustering Techniques

Before settling on the two-step clustering approach, we experimented with using proximity alone in a single step clustering approach for MetaTracts. We performed two separate tests. First, we used hierarchical clustering to cluster the MetaTracts. Second, we used K-means to cluster the MetaTracts. Fig. 7 shows the results.

Fig. 7a shows the results of MetaTracts that are hierarchically clustered directly using proximity alone into 10, 15, and finally 20 clusters. As discussed in Section 5.2, single linkage hierarchical clustering in the presence of overlapping MetaTracts tends to create large erroneous clusters and small (low-cardinality) outliers. When number of clusters (parameter h in hierarchical clustering) is 10, two large incorrect clusters are generated and the rest are outliers. As h increases, some appropriate bundles start to form. But even at $h = 20$, fiber bundles incorrectly cluster together. For comparison Fig. 6f shows the two-step clustering result. While hierarchical clustering is popular in clustering DTT fiber traces (sec. Section 2.2). As shown in Section 5.2 and here, hierarchical clustering using single linkage clustering has
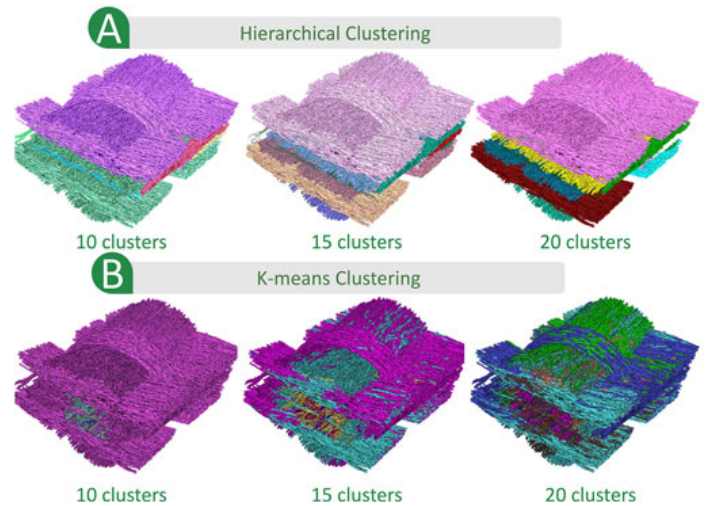

Fig. 7. Applying only (a) hierarchical clustering and (b) dimensionality reduction followed by K-means clustering, methods for various numbers of clusters (distance measure is minimal directed Hausdorffs). For comparison the results using two-step clustering is in Fig. 6f.

problems separating overlapping fiber traces and is not suitable as a single step clustering approach.

Fig. 7b shows the MetaTracts, clustered using K-means clustering by proximity alone, after being embedded in a m-dimensional (lower) space. We vary K from 10-20. After the dimensionality reduction, the lower dimensional space does not preserve the spatial context well. As a consequence MetaTracts which are in reality far away are grouped together. Even when k is set to twenty, very few correct fiber bundles are identified. In comparison, the two-step approach described above is simple, robust and extracts fiber bundles correctly. While dimensionality reduction followed by K-means based approaches have gained traction. Without explicit proximity as computed during hierarchical clustering, such close fiber bundles cannot be well separated by these approaches alone.

5.4 Sampling MetaTracts

To ensure that the MetaTracts capture the features of all the fiber bundles correctly we uniformly seed the entire volume, which generates a considerably large number of MetaTracts. Orientation clustering which performs eigenvalue and eigenvector computations on large distance matrices is particularly resource consuming. For example if M (30,000) MetaTracts are generated then the distance matrix is a $M \times M$ (30,000 $\times$ 30,000) matrix. Whereas if we subsample the MetaTracts and choose n ($n << M$), then the distance matrix and further operations on the distance matrix (clustering) becomes more time and memory efficient.

To ensure that we can handle large datasets and at the same time preserve all features, we start by uniformly seeding the entire volume and generating (M) MetaTracts. We then subsample the MetaTracts and compute all pair distances on the sub-sampled ($n, n << M$) MetaTracts and perform clustering and fiber bundle extraction on the subsampled MetaTracts.

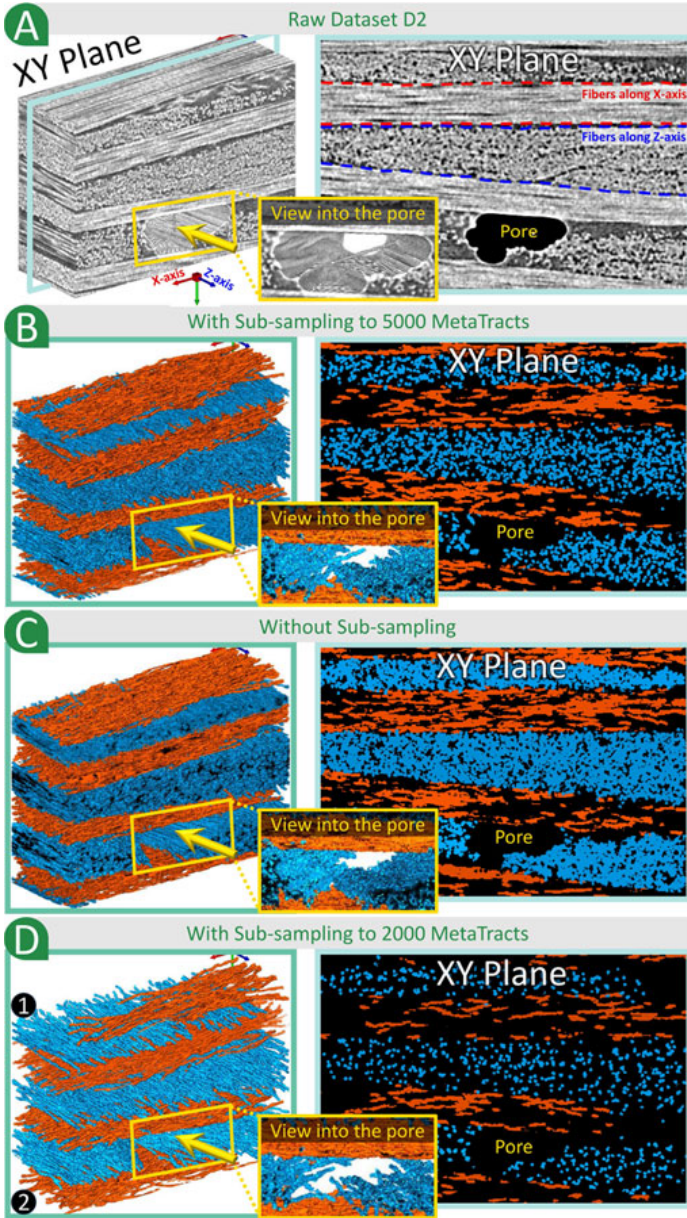The sampling algorithm is given in Algorithm 1. The sampling algorithm keeps track of a current set of

Fig. 8. Sub-sampling comparison based on dataset D2 a. b With sub-sampling to 5,000 MetaTracts, c without sub-sampling and d with sub-sampling to 2000 MetaTracts. In position 1 and 2, areas of the fiber bundles have been lost due to strong sub-sampling.

MetaTracts and in each iteration adds the MetaTract farthest from the current set.

The distance between two MetaTracts is computed as the maximum of the minimum distances between the start points of the cylinders which generate the individual Meta-Tracts. Computing all pairwise distances between two MetaTracts is an expensive operation. We bound the distances between a single MetaTract to other MetaTracts by maintaining a closest set and computing distances only when necessary. Note that in step 16 of the algorithm, we compute the distance from MetraTract M to the newly selected MetaTract M_i only if MetaTract M_i is within distance $2 \times M.dist$ of $M.closest$. The idea is that if the distance from $M.closest$ to M_i is more than $2 \times M.dist$, then $M.closest$ is closer to M than M_i so there is no reason to compute $d(M, M_i)$.

With the sampling step the user can decide the "resolution" of MetaTracts by setting the parameter n based on

their requirements and computational constraints (see Section 10). In the following example, we show the influence of the sampling step based on dataset 2 (D2) visually and provide a time comparison between sub-sampling and without sub-sampling the dataset. The dimensions of dataset D2 are $440 \times 298 \times 150$ with isotropic resolution of 2.75 μm and 8 bit unsigned integer scalars. Dataset D2 has 4 thin fiber bundles along the X-axis and 5 slightly thicker fiber bundles along the Z-axis. This dataset is especially challenging and is characterized by a hole/pore in the bottom center which was trapped during the manufacturing process. Fig. 8a illustrates a volume rendering and a 2D slice along the Z-axis of dataset D2.

Algorithm 1. Algorithm to subsample MetaTracts

---

1 $S \leftarrow$ set of all MetaTracts;
2 $n \leftarrow$ number of desired MetaTracts;
3 Pick random *MetaTract* $M_1 \in S$;
4 $S \leftarrow S - \{M_1\}$;
   /* Initialization: distances and closest bundle.   */
5 **foreach** *MetaTract* $M \in S$ **do**
6     $M.dist \leftarrow$ distance to M_1;
7     $M.closest \leftarrow 1$;
8 **end**
9 **for** $i \leftarrow 2$ **to** n **do**
10   Pick the MetaTract $M^* \in S$ with largest $M^*.dist$;
11    $M_i \leftarrow M^*$;
12   Compute the distance from M_i to every M_j, $j < i$;
13    $S \leftarrow S - \{M_i\}$;
14   **foreach** *MetaTract* $M \in S$ **do**
15       $j \leftarrow M.closest$;
16   **if** $(d(M_j, M_i) < 2 \times M.dist)$ **then**
17   Compute $dist(M, M_i)$;
18   **if** $(dist(M, M_i) < M.dist)$ **then**
19             $M.dist \leftarrow dist(M, M_i)$;
20             $M.closest \leftarrow i$;
21   **end**
22   **end**
23   **end**
24 **end**

For dataset D2 we initially computed a set of 19155 MetaTracts and two sub-sampled sets of 5,000 and 2,000 MetaTracts respectively. Figs. 8b, 8c and 8d show the clustering results. Without sub-sampling the MetaTracts produces a higher density of MetaTracts within the fiber bundles in contrast to sub-sampling (compare the 2D slices in Figs. 8b, 8c and 8d). At a sampling of 5,000 (26 percent of original number of) MetaTracts all fiber bundles are well separated, with results comparable to Meta-Tracts without sampling. Even at a severe sampling to just 2,000 (10 percent of original number of) MetaTracts the thinest fiber bundles (position 1,2 in Fig. 8d) shows loss of reconstruction, the rest of the bundles are still well separated. Note that the MetaTracts algorithm in all cases is able to cope with pores inside the dataset. Table 1 shows the time comparison between sub-sampling and without sub-sampling. Distance computation for the 19,155 MetaTracts took 72 minutes and the clustering of the 19,155 MetaTracts took 900 minutes on an Intel Xeon E5-2667 at 2.9 GHz with 256 GB RAM. Sub-sampling to

TABLE 1
Computation Time in Minutes with Sub-Sampling and
Without Sub-Sampling Performed on an Intel Xeon
E5-2667 at 2.9 GHz with 256 GB RAM

	With Sub-sampling	With Sub-sampling	Without Sub-sampling
Total Number of MetaTracts	5,000	2,000	19,155
MetaTracts Generation	41 mins	50 mins	41 mins
Sub-sampling	31 mins	21mins	–
Distance Computation	4 mins	1 min	72 mins
Cluster Computation	19 mins	3 mins	900 mins

Sub-sampling took 31 mins for Dataset D2. It reduced the number of MetaTracts from 19,155 to 5,000. Cluster computation of the 5,000 Meta-Tracts takes 19 minutes against 900 minutes when not using sub-sampling.

5,000 MetaTracts reduced the distance computation to 4 minutes and the clustering to just 19 minutes. The sub sampling itself took 31 minutes. Sub-sampling to 2,000 MetaTracts reduces the distance computation to 1 minute and the clustering to 3 minutes only.

6 VISUALIZATION OF METATRACTS

The output of the clustering step, can be used to visualize the geometric structure of the fiber bundles and answer the general queries itemized in Section 1. Apart from the direct MetaTracts visualization, we added three additional extensions which were deemed by the domain specialists as highly important and useful. Specifically,

- The first extension is to voxelize the original volume according to the clusters each voxel is associated with.
- The second extension is to extract surfaces (triangle meshes) associated with each fiber bundle.
- Finally, we added an interactive tool which allows a complete visual analysis of the fiber bundles.

6.1 Voxelization and Surface Extraction

To voxelize the entire volume based on the clustering results of the MetaTracts, we take the following "voting" approach. We compute a neighborhood around each voxel. We then create a histogram by enumerating the number of voxels of each class (cluster) in this neighborhood. The voxel is then assigned to the class with the maximum number of elements in the neighborhood. Surface extraction is often a crucial requirement for post processing of the data. While Marching Cubes [30] remains the most popular technique, other methods specific to ICT data such as MergeSharp [31] which focuses on extracting sharp edges and corners are also used. We extract the corresponding surfaces from voxel data by binarizing the volume per cluster and extracting the iso-surface associated with the largest connected component in the input binary volume.

Figs. 9a and 14d show the result of voxelization. Fig. 9b shows a single slice of the volume along the XY-plane. Fig. 9c and 9d shows examples of extracted meshes.
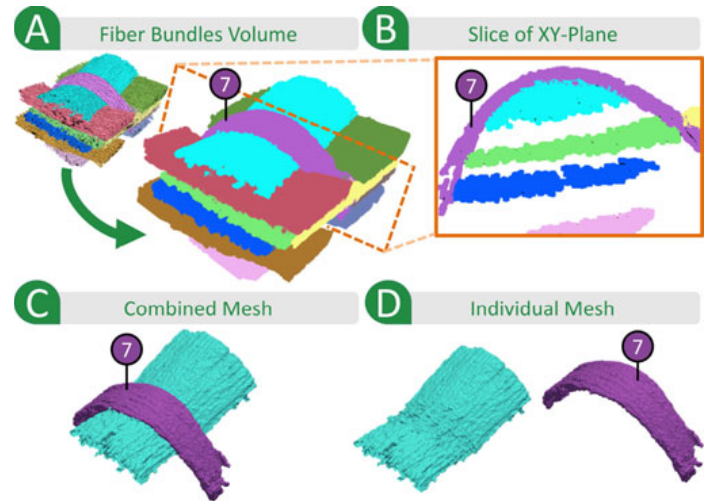

Fig. 9. Voxelization and surface extraction. (a) Voxelization of dataset 1, the inset shows the MetaTracts after clustering. (b) A single slice along the XY-Plane (c) Two of the extracted meshes together (d) The meshes rendered separately.

7 INTERACTIVE VISUAL ANALYSIS OF FIBER BUNDLES

In order to interactively analyze and explore the individual fiber bundles, we have applied the FiberScout visualization concept introduced by Weissenböck et al. [28] to the Meta-Tracts. Fig. 10 shows the necessary steps to realize the interactive fiber bundle analysis tool.

During the voxelization process (Section 6.1) a unique identification is assigned to each fiber bundle. Based on these labeled voxel data, we use ITK [32] filters to calculate multiple interesting fiber bundle characteristics. With this additional information, the individual bundles are described in much more detail. According to the work of [28] we used the following characteristics to describe the fiber bundles: the main diagonal elements of the orientation tensors (a_{11}, a_{22}, a_{33}), spherical coordinates of the orientations (φ, θ), Cartesian coordinates of the centers (X_i, Y_i, Z_i) and the *volume*. Furthermore, we calculate the X, Y, Z bounding box dimensions and the major axis length of a fiber bundle. By combining the image data and the fiber bundle characteristics we were able to create an interactive tool which allows to select, classify and color-code the individual bundles based on the calculated characteristics.

The graphical user interface of the interactive tool is shown in Fig. 11. A linked scatter plot matrix (d) and parallel coordinates (c) are used to assess the relationships between the different fiber bundle features. The parallel coordinates (PC) allow a preliminary selection of the fiber bundle characteristics. The scatter plot matrix (SPM) on the
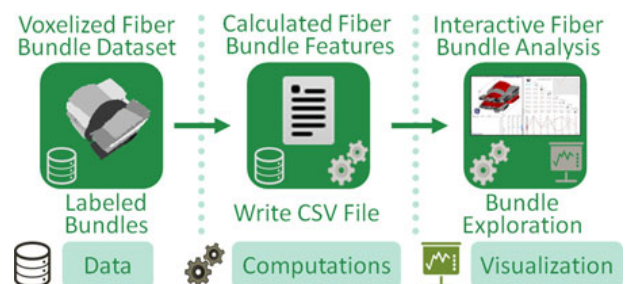

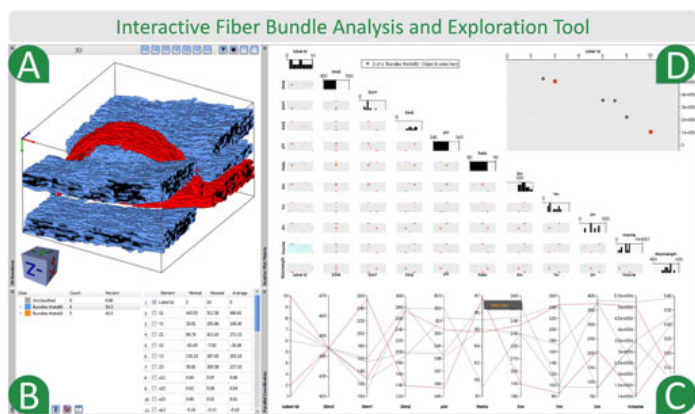Fig. 10. Flow chart of the interactive fiber bundle analysis tool.

Fig. 11. The interactive graphical user interface for a detailed analysis of fiber bundles generated with a MetaTracts approach. (a) Shows the 3D renderer with a blue colored fiber bundle class having two red bundles selected. (b) Shows the list of all defined fiber bundle classes with statistical informations. (c) Shows the parallel coordinates and (d) The scatter plot matrix with the different fiber bundle characteristics.

other hand, allows a refined selection. Based on the selected characteristics the corresponding fiber bundles are visualized. By selecting the appropriate data points on the relevant axes of the fiber bundle characteristics in the PC or SPM, domain-specific queries like:

- *which fiber bundle shows the largest XYZ-extents*,
- *which fiber bundle shows the largest volume* or
- *which fiber bundle is parallel to the Z-axis and is the thinnest*

are answered. From the fiber bundle selections, classes with user-defined colors can be created. The defined classes are managed in a list (b). In addition, statistical informations (min, mean, max) on the characteristics of a class are given. When performing a selection in the SPM or the PC as well as browsing through the classes or the sub elements of a class in the list, the fiber bundles are immediately visualized in the 3D renderer (a). All the defined color-coded classes can be shown simultaneously in the 3D renderer. By "Brushing and linking" the selections and managing the classes in a list, the dataset is systematically explored and analyzed. Thus, the domain experts are able to identify and depict interesting regions in the specimen.

Fig. 11 shows two fiber bundle classes (blue and orange) which are stored in the class list (b). The classifications are based on the characteristic *theta* (orientation to the Z-axis in degrees). The fiber bundles in the blue class are orientated around 90 degree to the Z-axis, the fiber bundles in the orange class are oriented around 0 degree to the Z-axis. The red selection presented in the scatter plot matrix (d), parallel coordinates (c) and the 3D renderer (a) defines two fiber bundles of the blue class. The selection is based on the fiber bundle volume. The bent fiber bundle at the top has a five times smaller volume than the straight bundle behind.

In addition, the interactive analysis tool makes it possible to quickly show the fiber bundle orientations and their major axis lengths as color-coded volume renderings. Informations on the fiber bundle orientations and lengths are important for the domain experts as they provide an indication of the mechanical loading capacity of the material [28]. Therefore, the angles φ (orientation in the XY-plane) and θ (orientation to the Z-axis) of the individual fiber bundles are
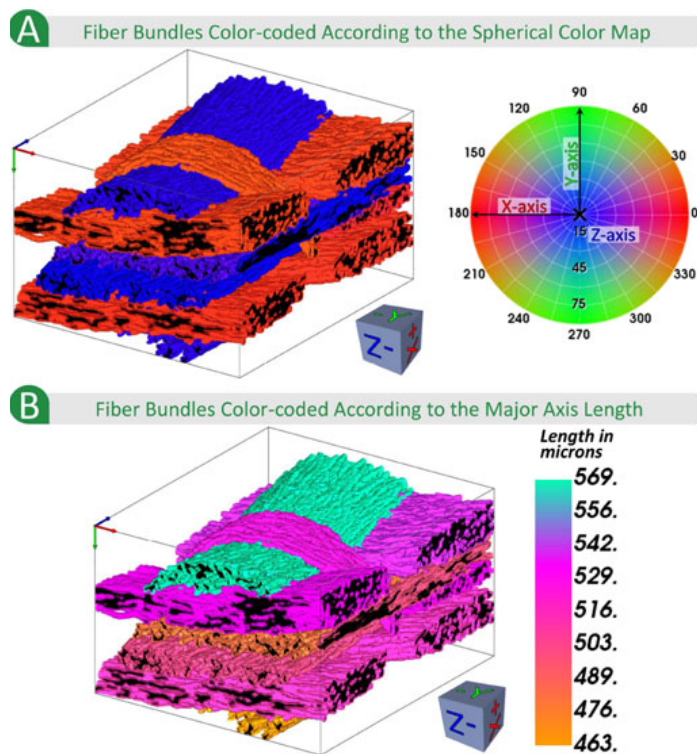

Fig. 12. (a) The spherical color map color-codes the individual fiber bundles of dataset D1 according to their X-, Y- and Z orientations. (b) Color-coded major axis lengths of the individual D1 fiber bundles.

mapped to a spherical color map where the X-, Y- and Z-orientations are color-coded in red, green, and blue. Fig. 12a shows the volume rendering of dataset D1 with the applied spherical color map. Fig. 12b shows the fiber bundles of D1 color-coded to the major axis length.

8 USER EVALUATION

We conducted a user evaluation to test the utility of our technique. Four NDT practitioners working with XCT, four material scientists experienced in analyzing CFRPs and four visualization practitioners participated in the user evaluation of MetaTracts. We set up a questionnaire, with questions on solving given tasks. The queries used Likert Scale (LS) for evaluating the performance of MetaTracts over currently utilized techniques. LS consists of five levels which range from "strongly agree" to "strongly disagree". Fig. 13 shows the results. The results are presented in the same sequential order that they appeared to the participant. The first set of tasks dealt with the effectiveness of MetaTracts in comprehending "geometric structure".

First we showed the participants a video of full 360 degree rotation of the volume rendering of D1 along the Z-axis. We tasked the user to identify the number of separate fiber bundles. The results show that the participants found it difficult to determine the number of fiber bundles from the volume rendering itself. For the second task we mapped the "top" eigenvector of the Hessian matrix to the RGB color map. We again showed a video of full 360 degree rotation of the color-mapped and asked the same query. The Hessian based mapping is a popularly used technique in fiber bundle visualization which provides more information about the major orientations than the grayscale original volume. The results show that the evaluators performed better than

Fig. 13. The user evaluation consists of a set of queries on videos of our results, volume rendering and Hessian color map. The questionnaire tests the effectiveness of MetaTracts in visualizing "geometric structure" and "spatial context". The Likert scale goes from 1-5: strongly disagree, disagree, neutral, agree and strongly agree. [7].

the simple volume rendering test (task 1). The majority of our participants agreed or strongly agreed that the Hessian color map was more effective. Finally, we showed the video of the fiber bundles extracted with MetaTracts. All participants could correctly identify the number of fiber bundles and agreed that the MetaTracts is an effective tool for perceiving geometric structure of fiber bundles, than simple volume rending or the Hessian color map. They especially liked the 2D slices of the MetaTracts (Fig. 9b, compared to Fig. 2c).

The second set of tasks dealt with the effectiveness of MetaTracts in comprehending "spatial context". The participants were given a series of tasks to select which fiber bundles were the largest, smallest or most similar to a given fiber bundle from a subset of fiber bundles. In the Likert scale, the majority of the participants agreed that the tasks were easier using MetaTracts than the volume rendering of the original data or using the Hessian color map. The majority of the participants also agreed that the extracted meshes provided better spatial context than the volume rendering of the original data.
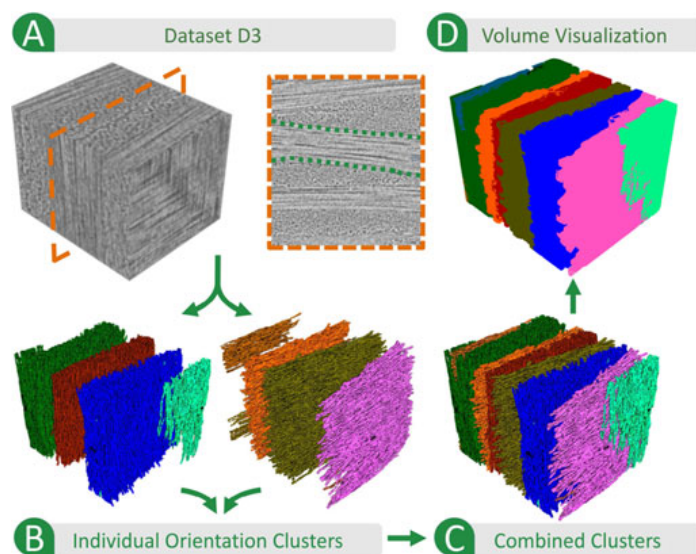

Fig. 14. Dataset D3 with flat thin and compact bundles. (a) Shows the volume rendering and a 2D slice with one of the boundaries marked in green, (b) shows the clusters according to their individual orientations. (c) Shows the complete result. (d) Shows the voxelization of (c).
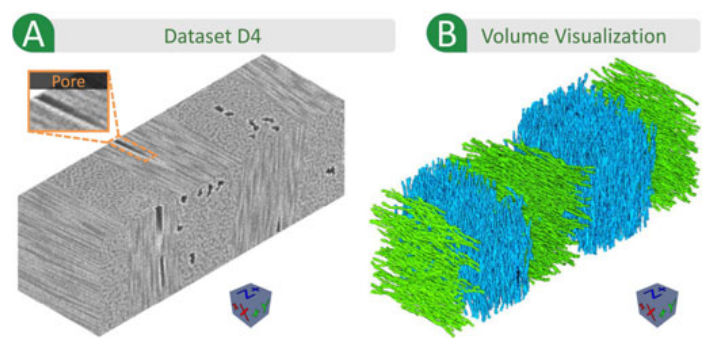
Fig. 15. Dataset D4 with dense carbon fiber bundles and pores inside. (a) Shows the volume rendering of the raw XCT dataset, (b) shows the clusters according to their individual orientations.

9 EXPERIMENTAL RESULTS

We tested our technique on datasets with varying characteristics. Dataset D1 is described in Section 3 (Fig. 2). Dataset D1 has five fiber bundles along Z-axis and six along X-axis for a total of eleven separate fiber bundles. With different cross-section sizes and varying degree of curvature of the bundles, D1 is a complicated dataset. All of the fiber bundles were identified correctly by our technique. Figs. 6 and 9 show the results of D1 decomposed into two orientation clusters with each orientation cluster further decomposed into $h = 10$ clusters followed by voxelization and mesh extraction. The reader is referred Figs. 6e and 9d where the thin and curved purple cluster bundle 7 is extracted well.

Dataset 2 (D2) was introduced in Section 5.4. D2 is characterized by a large hole/pore in a fiber bundle. Fig. 14 shows the results of our dataset 3 (D3). This CFRP dataset is characterized by dense fiber bundle arrangement, with flat and thin bundles. It also consists of two major fiber bundle orientation, there are four fiber bundles along the X-axis and five along the Z-axis. The dimensions of D3 are 300 × 350 × 300 voxels and the data type is uint16 (D1 is uint8). Fig. 14a shows the scalar data along with a single slice. The individual fiber bundles are indistinguishable. A green dotted line shows one of the bundles marked by an expert. Fig. 14b shows the result of computing MetaTracts and clustering using our two step approach. The fiber bundles belonging to the individual orientations are shown separately. Fig. 14c shows the combined results. All the fiber bundles have been separated out successfully. Fig. 14d shows the result of voxelizing the entire volume.

The results of dataset D4 are presented in Fig. 15. This dataset is characterized by dense carbon fiber bundles with

Fig. 16. (a) Length distribution of individual MetaTracts for a particular bundle (unit for length is grid cube edge length: $2 \ \mu m$).

Fig. 17. Number of MetaTracts and median, minimum and maximum length of an individual MetaTracts in the orientation cluster Fig. 6d when clustered into 10 clusters. The unit for the MetaTracts length is the grid cube length. The labeled clusters 2, 3, 4, 5, and 7 have a cardinality less than 10 and are removed. [7].

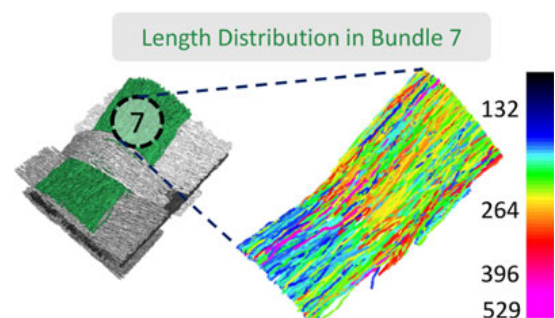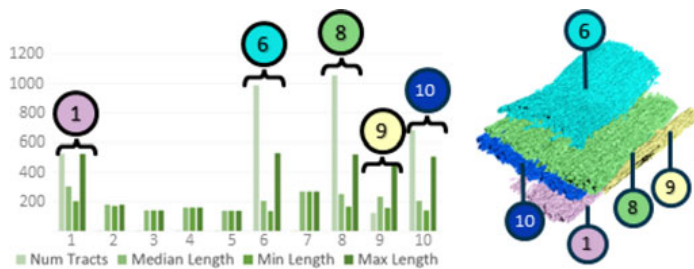pores inside. Three fiber bundles are oriented along the Y-axis and two fiber bundles are oriented along the Z-axis. D4 has a size of $600 \times 200 \times 200$ voxels, a resolution of $1~\mu m$ and the data type is uint16. The different orientations of the fiber bundles in the raw XCT dataset (Fig. 15a) are barely perceptible. In contrast, Fig. 15b shows the result of Meta-Tracts clustering. Here, the individual fiber bundles have been successfully clustered according to their orientations. The fiber bundles are separated from each other and distinguishable.

10 PARAMETER CHOICES

The critical parameters for extracting MetaTracts are K and h, where parameter K is used by the K-means during orientation clustering while parameter h which is used by the hierarchical clustering. K denotes the number of major fiber bundle directions. This is known in advance or can be estimated by considering the weaving pattern.

Robustness of Parameter h . Fig. 17 shows the number of MetaTracts in each cluster when the orientation cluster 1 (Fig. 6a) is hierarchically clustered into (h) ten clusters. It also shows the minimum, maximum and median length of the MetaTracts in each of the resulting clusters. The ground truth was five separate fiber bundles. We observe that even though the user given parameter was two times the ground truth, the major fiber bundles remain well separated in accordance with our ground truth and the small clusters (clusters 2, 3, 4, 5, and 7) have very few elements and can be easily discarded. Thus we experimentally show that our framework is robust to the choice of parameter h for hierarchical clustering. This is an appealing trait of the proximity based hierarchical clustering and thus providing good results even when exact h might be unknown. The robustness to parameter variation also reinforces our two-step approach to clustering.

Fixed Parameters. The following parameters were fixed for all the tests. We set the reliable Hessian threshold R_H to be 0.3. A R_H of 0.0 would mean all points have reliable local orientation which would cause spurious MetaTracts detection. A very high R_H would lead to a decline in number of MetaTracts produced. Coefficients α and β in R_H are as explained in Frangi et al. [24] and set to 0.5. The length and the radius parameters for the cylinders of MetaTracts decide how coarse our approximation of the fiber bundles are. These are dependent on the underlying fiber characteristic and the weaving pattern. Larger cylinders will handle noisy local orientation better as it inspects a larger number of

candidate points to extend the fiber. We used 10 and 2 for length and radius (measured in grid voxel size), respectively for all tests. A simpler geometry (e.g., D3) was experimentally found to handle larger cylinders better. η in Section 5.2 decides how quickly the hierarchical clustering converges, experimentally values 0.3 to 0.6 removed $1.2 - 5$ percent of fibers (total number of fibers $\sim$10,000) and gave similar results. Parameter n intuitively acts as "resolution" for the MetaTracts. Large n captures the features better and generates smoother fiber bundles.

η and τ in Equation (3) decide how quickly the value of the factor decays; we have used integer values between [7–10] and half the length of an individual cylinder respectively. Our number of fiber bundle directions is limited. Thus even for small m (cardinality of lower dimension in orientation clustering), the distinction between the orientation clusters is preserved quite well. We compared $m = 3, \ldots, 7$ experimentally without any change in results. Through our tests on 4 different datasets, we have experimentally shown the robustness of our parameter choices.

11 LIMITATIONS

A key assumption of the method is "connectivity" (Section 3). "Connectivity" ensures that we can travel in small increments along a fiber bundle and expect similar features (in our case orientation). If the "connectivity" criteria is not fulfilled due to noise in the image, then the generated Meta-Tracts will be inaccurate.

The clustering process also assumes that the fiber bundles have a minimum width. The orientation clustering assumes two orthogonal distinct orientations. While this might seem restrictive, in practice (and as shown in our experimental datasets) a large set of CFRP datasets share these characteristics. The interactive visualization step opens this tool for exploration of a broader range of datasets.

12 CONCLUSIONS AND FUTURE WORK

In this paper, we introduced a framework to extract and visualize fiber bundles in composite materials. We show that our framework works at comparatively low resolution and with dense fiber arrangements (when extracting single fibers might not be possible). It handles complex fiber patterns such as "cross overs", "braiding" and "holes/pores". In addition, we demonstrated a tool to interactively investigate and analyze voxelized fiber bundles generated with the MetaTracts approach.

In future, we plan to increase the precision of the extractions and include uncertainty based visualization to better portray the surface of separations. We also plan to decrease extraction times.

ACKNOWLEDGMENTS

REFERENCES

[1] C. Red, "Aviation outlook: Composites in general aviation 2011-2020," *High-Performance Composites*, May2012. [Online]. Available: http://www.compositesworld.com/articles/aviation-outlook-composites-in-general-aviation-2011–2020

[2] J. Kastner, Ed., *4th Conference on Industrial Computed Tomography*. Wels, Austria: Shaker Verlag, Aachen, Sep. 2012.

[3] C. Heinzl, "Analysis and visualization of industrial ct data," Ph.D. dissertation, Inst. Comput. Graph. Algorithms, Vienna Univ. Technol., Vienna, Austria, 2009. [Online]. Available: http://www.cg.tuwien.ac.at/research/publications/2009/heinzl-2008-thesi s/

[4] A. Bhattacharya, "Gradient dependent reconstruction from scalar data," Ph.D. dissertation, Dept. of Computer Science, Ohio State Univ., Columbus, Ohio, 2015.

[5] Y. Karpat, O. Bahtiyar, and B. Değer, "Mechanistic force modeling for milling of unidirectional carbon fiber reinforced polymer laminates," *Int. J. Mach. Tools Manufacture*, vol. 56, pp. 79–93, 2012. [Online]. Available: http://www.sciencedirect.com/science/article/pii/S0890695512000028

[6] P. J. Schilling, B. R. Karedla, A. K. Tatiparthi, M. A. Verges, and P. D.Herrington, "X-ray computed microtomography of internal damage in fiber reinforced polymer matrix composites," *Composites Sci. Technol.*, vol. 65, no. 14, pp. 2071–2078, 2005. [Online]. Available: http://www.sciencedirect.com/science/article/pii/S0266353805001879

[7] A. Bhattacharya, C. Heinzl, A. Amirkhanov, J. Kastner, and R. Wenger, "Metatracts – a method for robust extraction and visualization of carbon fiber bundles in fiber reinforced composites," in *Proc. IEEE Pacific Vis. Symp.*, Apr. 2015, pp. 191–198.

[8] P. J. Basser, S. Pajevic, C. Pierpaoli, and A. Aldroubi, "Fiber tract following in the human brain using DT-MRI data," *IEICE Trans. Inform. Syst.*, vol. 85, no. 1, pp. 15–21, 2002.

[9] S. Mori, B. J. Crain, V. P. Chacko, and P. C. Van Zijl, "Three-dimensional tracking of axonal projections in the brain by magnetic resonance imaging." *Ann. Neurology*, vol. 45, no. 2, pp. 265–269, 1999. [Online]. Available: http://www.ncbi.nlm.nih.gov/pubmed/9989633

[10] S. Mori and P. C. M. van Zijl, "Fiber tracking: Principles and strategies a technical review," *NMR Biomed.*, vol. 15, no. 7/8, pp. 468–480, 2002. [Online]. Available: http://dx.doi.org/10.1002/nbm.781

[11] P. J. Basser, S. Pajevic, C. Pierpaoli, J. Duda, and A. Aldroubi, "In vivo fiber tractography using DT-MRI data," *Magn. Resonance Med.*, vol. 44, no. 4, pp. 625–632, 2000. [Online]. Available: http://dx.doi.org/10.1002/1522–2594(200010)44:4⟨625::AID-MRM17⟩3.0.CO;2 -O

[12] A. Brun, H.-J. Park, H. Knutsson, and C.-F. Westin, "Coloring of DT-MRI fiber traces using laplacian eigenmaps," in *Computer Aided Systems Theory*, vol. 2809. Berlin, Germany: Springer, 2003.

[13] A. Brun, H. Knutsson, H.-J. Park, M. E. Shenton, and C.-F. Westin, "Clustering fiber traces using normalized cuts." *Lecture Notes Comput. Sci.*, vol. 3216/2004, no. 3216, pp. 368–375, 2004. [Online]. Available: http://www.pubmedcentral.nih.gov/articlerender.fcgi?artid=2832798 & tool= pmcentrez & rendertype=abstract

[14] I. Corouge, S. Gouttard, and G. Gerig, "Towards a shape model of white matter fiber bundles using diffusion tensor MRI," in *Proc. IEEE Int. Symp. Biomed. Imaging: Nano Macro*, vol. 1, 2004, pp. 344–347.

[15] C.-F. Westin, S. E. Maier, H. Mamata, A. Nabavi, F. A. Jolesz, and R. Kikinis, "Processing and visualization of diffusion tensor MRI," *Med. Image Anal.*, vol. 6, no. 2, pp. 93–108, 2002.

[16] S. Zhang, S. Correia, and D. H. Laidlaw, "Identifying white-matter fiber bundles in DTI data using an automated proximity-based fiber-clustering method." *IEEE Trans. Vis. Comput. Graph.*, vol. 14, no. 5, pp. 1044–1053, Sep./Oct. 2008. [Online]. Available: http://www.pubmedcentral.nih.gov/articlerender.fcgi?artid=2757786&tool =pmcentrez&rendertype=abstract

[17] B. Moberts, A. Vilanova, and J. J. van Wijk, "Evaluation of fiber clustering methods for diffusion tensor imaging," in *Proc. IEEE Visualization*, 2005, pp. 65–72.

[18] L. Jonasson, P. Hagmann, J. Thiran, and V. Wedeen, "Fiber tracts of high angular resolution diffusion MRI are easily segmented with spectral clustering," in *Proc. Int. Soc. Magnetic Resonance Med.*, vol. 24, 2005, pp. 1127–1137.

[19] L. O'Donnell and C. F. Westin, "Automatic tractography segmentation using a high-dimensional white matter atlas," *IEEE Trans. Med. Imaging*, vol. 26, no. 11, pp. 1562–1575, Nov. 2007.

[20] M. Belkin and P. Niyogi, "Laplacian eigenmaps and spectral techniques for embedding and clustering," in *Proc. Adv. Neural Inf. Process. Syst. 14*, 2001, pp. 585–591.

[21] R. O. Duda, P. E. Hart, and D. G. Stork, *Pattern Classification*, 2nd ed. New York, NY, USA: Wiley Interscience, 2000.

[22] E. Garyfallidis, M. Brett, M. M. Correia, G. B. Williams, and I. Nimmo-Smith, "Quickbundles, a method for tractography simplification," *Frontiers Neuroscience*, vol. 6, 2012, Art. no. 175.

[23] S. Bouix, K. Siddiqi, and A. Tannenbaum, "Flux driven automatic centerline extraction," *Med. Image Anal.*, vol. 9, no. 3, pp. 209–221, 2005. [Online]. Available: http://www.sciencedirect.com/science/article/pii/S1361841504000611

[24] A. Frangi, W. Niessen, K. Vincken, and M. Viergever, "Multiscale vessel enhancement filtering," in *Medical Image Computing and Computer-Assisted Intervention MICCAI98*, Berlin, Germany: Springer, 1998, vol. 1496, pp. 130–137. [Online]. Available: http://dx.doi.org/10.1007/BFb0056195

[25] Y. Sato, et al., "3D multi-scale line filter for segmentation and visualization of curvilinear structures in medical images," in *CVRMed-MRCAS'97*, Berlin, Germany: Springer, 1997, vol. 1205, pp. 213–222. [Online]. Available: http://dx.doi.org/10.1007/BFb0029240

[26] L. Fritz, M. Hadwiger, G. Geier, G. Pittino, and M. E. Gröller, "A visual approach to efficient analysis and quantification of ductile iron and reinforced sprayed concrete," *IEEE Trans. Vis. Comput. Graph.*, vol. 15, no. 6, pp. 1343–1350, Nov./Dec. 2009.

[27] D. Salaberger, K. Kannappan, J. Kastner, J. Reussner, and T. Auinger, "Evaluation of computed tomography data from fibre reinforced polymers to determine fibre length distribution," *Int. Polymer Process.*, vol. 26, no. 3, 2011, pp. 283–291. [Online]. Available: http://www.polymer-process.com/IPP2441

[28] J. Weissenböck, et al., "Fiberscout: An interactive tool for exploring and analyzing fiber reinforced polymers," in *Proc. IEEE Pacific Vis. Symp.*, 2014, pp. 153–160.

[29] S. Lomov, G. Perie, D. S. Ivanov, I. Verpoest, and D. Marsal, "Modeling three-dimensional fabrics and three-dimensional reinforced composites: Challenges and solutions," *Textile Res. J.*, pp. 28–41, 2010.

[30] W. E. Lorensen and H. E. Cline, "Marching cubes: A high resolution 3D surface construction algorithm," *SIGGRAPH Comput. Graph.*, vol. 21, no. 4, pp. 163–169, Aug. 1987. [Online]. Available: http://doi.acm.org/10.1145/37402.37422

[31] A. Bhattacharya and R. Wenger, "Constructing isosurfaces with sharp edges and corners using cube merging," *Comput. Graph. Forum*, vol. 32, no. 3pt1, pp. 11–20, 2013. [Online]. Available: http://dx.doi.org/10.1111/cgf.12088

[32] L. Ibanez, W. Schroeder, L. Ng, and J. Cates, *The ITK Software Guide*, 2nd ed. New York, NY, USA: Kitware, Inc., 2005.

Arindam Bhattacharya received the MS and PhD degrees in computer science and engineering from the Ohio State University in 2015. His research interests include computational geometry, computer graphics, scientific visualization, and image processing.

Johannes Weissenböck received the BS and MS degrees in medical informatics from the Vienna University of Technology (TU Vienna), Vienna, Austria, in 2009 and 2011, respectively. Since 2012, he has been working toward the PhD degree at the Computer Science Department, TU Vienna. He is currently a research associate at the University of Applied Sciences – Upper Austria, Wels Campus. His research interests include computed tomography, computer graphics, scientific visualization, and image processing.

Rephael Wenger received the BE degree from Princeton University in 1984 and the PhD degree from McGill University in 1988. His research interests include computational geometry, geometric algorithms, geometric modeling, computer graphics and visualization. He is author of the book "Isosurfaces: Geometry, Topology and Algorithms" on the construction of isosurfaces from scalar data sets. He is currently an associate professor in the Department of Computer Science and Engineering at The Ohio State University.

Johann Kastner received the degree in technical physics from the University of Linz and the University of Vienna. In 2012 he received the "Venia docendi" for non-destructive testing and tomography at the Institute of Materials Science and Technology of the Vienna University of Technology. He is currently the vice-president for research at the University of Applied Sciences Upper Austria. His main research interest is X-ray computed tomography for non-destructive testing and metrology.

Artem Amirkhanov received the PhD degree in computer science from the Vienna University of Technology in 2012 in the field of visualization and analysis of industrial X-ray computed tomography data. His research interests include computer graphics, scientific visualization, and image processing.
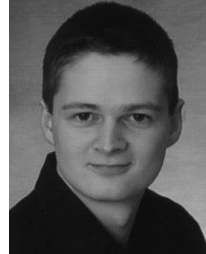
Christoph Heinzl received the PhD degree in computer science from the Vienna University of Technology in 2009 in the field of visualization and analysis of industrial X-ray computed tomography data. He is currently a head of the research center at University of Applied Sciences Upper Austria – Wels Campus. His research currently covers visual parameter space analysis, 4D analysis of time varying data, visual analysis of volume ensembles, multi modal data analysis and visualization, as well as comparative visualization for parameter studies. His research was supported by various grants which he acquired on national and on European level (NanoXCT, QUI-COM, ADAM, SmartCT, SimCT, etc.). He is a member of the IEEE Computer Society.

▷ **For more information on this or any other computing topic, please visit our Digital Library at** www.computer.org/publications/dlib.

Visual Computing
in Materials Science

Christoph Heinzl and Stefan Stappen

STAR: Visual Computing in Materials Science

C. Heinzl[1] and S. Stappen[2]

[1]University of Applied Sciences Upper Austria, Wels Campus, Austria
[2]Institute of Computer Graphics and Algorithms, TU Wien, Austria

Abstract

Visual computing has become highly attractive for boosting research endeavors in the materials science domain. Using visual computing, a multitude of different phenomena may now be studied, at various scales, dimensions, or using different modalities. This was simply impossible before. Visual computing techniques provide novel insights in order to understand complex material systems of interest, which is demonstrated by strongly rising number of new approaches, publishing new techniques for materials analysis and simulation.
Outlining the proximity of materials science and visual computing, this state of the art report focuses on the intersection of both domains in order to guide research endeavors in this field. We provide a systematic survey on the close interrelations of both fields as well as how they profit from each other. Analyzing the existing body of literature, we review the domain of visual computing supported materials science, starting with the definition of materials science as well as material systems for which visual computing is frequently used. Major tasks for visual computing, visual analysis and visualization in materials sciences are identified, as well as simulation and testing techniques, which are providing the data for the respective analyses. We reviewed the input data characteristics and the direct and derived outputs, the visualization techniques and visual metaphors used, as well as the interactions and analysis workflows employed. All our findings are finally integrated in a cumulative matrix, giving insights about the different interrelations of both domains. We conclude our report with the identification of open high level and low level challenges for future research.

Categories and Subject Descriptors (according to ACM CCS): I.3.8 [Computer Graphics]: Applications—

1. Introduction

During the past decades, a clear trend formed in industry of constantly driving research towards tailored materials for new, cost-efficient, function-oriented, highly integrated and also light-weight components with previously impossible specifications. Industries such as health care, agriculture, construction, packaging, sports equipment, automotive, aeronautics, environment, protection and others thus increasingly adopt these tailored materials to stay ahead of competition. The understanding, discovery, design and use of (new) materials as well as material systems are integral parts of materials science and permanently driven to new frontiers. Ambitious projects boost the development of novel materials for future high quality components. Some outstanding activities are for example found in the manufacturing of wall components for future fusion reactors as presented by Kim et al. [KJS*14], the design of novel anode materials for energy storage in batteries as presented by Gyulassy et al. [GKLW16], or the analysis of advanced composite components for aeronautic and automotive applications as presented by Bhattacharya et al. [BHA*15]. These projects all share the fact that only a detailed understanding of the material systems of interest ensures to met the application specific targets. Their targets are highly

divers and may range from new materials withstanding temperatures of more than 15 million degrees Celsius, deciding whether carbon nanospheres will be the anode material for future lithium ion-based batteries, to developing carbon fiber reinforced composite materials for the fuselage of a new generation of airplanes. For knowledge discovery, also simulations of material systems are of high importance when designing novel, outstanding materials. Especially simulations of the material systems in their targeted use and environments are catching up momentum: An earlier approach by Laevsky et al. [LTM01] provides an interactive visualization and computational steering tool for interactive numerical simulations of a glass pressing process. Patkar and Chaudhuri [PC13] investigate the mechanics of wetting porous solid objects by computations of fluid flows through porous media. Another technique presented by Gyulassy et al. [GKLW16] simulates the synthesis and ion diffusion of battery materials. In all these areas, visual computing generates new and previously unknown insights, supporting material scientists in understanding the material's inner structures and its behavior while in use. Aside these introductory achievements, the potential impact of visual computing is found in virtually any aspect of materials science. To demonstrate the interrelation of visual

computing and materials science we continue in our motivation for this report with a detailed consideration of an example, showing how the solution to a materials science problem was facilitated by visual computing.

2. Motivation

A strong demand is prevalent in materials science towards methods for visualizing, abstracting, combining, exploring and quantifying materials data in novel, challenging applications. We thus start with an intuitive example for visual computing enabled materials science, analyzing and simulating composites. (section 2.1).

2.1. Example: Visual Analysis of Composite Materials

Composite materials are of high interest in a broad variety of industries ranging from leisure, automotive, aeronautics to space industry and beyond. For the development and simulation of (new) composites as fiber reinforced polymers (FRP), the properties of the individual components (i.e., fibers, matrix, pores, inclusions, voids) are crucial, as they mainly determine the composite's performance characteristics in use. Due to the lack of computing power and real data, material simulations used to apply simple models: Pores and voids were approximated using ellipsoids, fibers using cylinders based on the bulk material's specifications. More recently, X-ray Computed Tomography (XCT) was applied on prototype composite materials to get a closer view on interior structures. To precisely analyze XCT scans of composite components, Weissenböck et al. [WAL*14] developed Fiberscout, a visual analysis tool exploring individual fibers as well as fiber classes (sets of fibers with similar characteristics). Fiberscout links a parallel coordinates plot and a scatterplot matrix with conventional 2D slice views and a 3D renderer as well as polar plots. As input, the tool requires pre-segmented, labeled data extracted from respective XCT scans. Despite being initially designed for fibers only, the tool was extended in a later work to pre-segmented data of pores, inclusions and other voids [WRS*14]. In this update, the computation of mean objects for classes of individual features according to Reh et al. [RGK*13] was integrated (see Figure 1). Combining these techniques, the extraction of mean objects and mean shapes of feature classes of interest became possible, in order to feed material

Figure 1: *MObjects: The individual objects on the left side are combined to a Mean Object, and a cut through of it on the right side. The blue core of the object depicts a high probability of voxels belonging to the MObject. This core is surrounded by the yellow medium probability layer which together with the outmost low probability layer forms the uncertainty cloud. ©2013 IEEE. Reprinted, with permission, from [RGK*13].*

simulations with much more precise models on the material's inner structures. The enhanced precision of the simulation now allows to produce components fulfilling the target specifications with less material (cheaper), which are even lighter (more economic). Especially in aeronautic applications this is a standing strong demand. Furthermore, these new visual analysis functionalities allow to distinguish pores, inclusions, or voids into critical and uncritical defects based on a wide variety of characteristics. Therefore, non destructive testing (NDT) engineers may now safely decide, if an 80.000 $ aeronautic component may fly or needs to be scrapped. This example impressively shows how visual computing enables solving important materials science challenges and how it opens previously impossible insights into complex materials and their behavior in use.

Aside this example, an increasing number of materials science projects make use of visual computing and especially visualization or visual analysis approaches in their research. In literature, however, there is still a huge gap observable regarding reviews analyzing of the body of work at the intersection of those two domains. Apart from earlier reviews on specific niches, such as the visualization of industrial computed tomography data for non-destructive testing as presented by Huang et al. [HMMW03], or data fusion for non destructive evaluation as presented by Liu et al. [LFK*07], or dimensional metrology using computed tomography as presented by Kruth et at. [KBC*11], to date there is no comprehensive survey available giving insight into this growing area of research. In this work our main goal is to close this gap. By analyzing visual computing approaches for materials science in a structured literature review and by integrating our own experience, we shed light on how both areas profit from each other. To analyze the body of existing work we follow the structured literature research similar to Sedlmair et al. [SHB*14] in their conceptual framework on visual parameter space analysis, Bayer et al. [BHP15] regarding GPU based large-scale volume visualization, and Alsallakh et al. [AMA*14] in terms of visualizing sets and set-typed data. We first analyze the relevant literature regarding their high level tasks, as well as their used testing or simulation techniques. We review the data characteristics as well as visualization techniques used as well as their suggested interaction concepts. We see the main contributions of our work in the following points:

1. Review and classification of the current body of literature at the intersection of visual computing and materials sciences,
2. Extraction of a cumulative matrix demonstrating the intersections of both fields,
3. Analysis of the application areas as well as their high level visual computing, visual analysis and visualization tasks for materials sciences,
4. Investigation of data acquisition methods regarding the characteristics of the different inputs vs. direct and derived outputs,
5. Discussion of the used visual metaphors as well as why they are preferred over others,
6. Discussion of the used interaction concepts as well as the corresponding analysis workflows,
7. Identification of open research challenges to guide future research endeavors in this area.

3. Method

This state-of-the-art-report is based on a structured literature review at the intersection of visual computing and materials sciences. The related literature was compiled, reviewed and clustered by two core annotators, i.e., the authors of this report, with continuous feedback from two domain experts in materials science as well as three experts in visual computing. These external advisors were continuously provided with concepts and drafts for the submission over a period of more than a year, asking for their feedback on the report, the material systems, the tasks, relevant testing and simulation techniques. In addition, the future challenges were discussed in a round of specialists from visual analysis, non destructive testing and materials science at a recent workshop. Regarding the core annotators, one of them is an expert, who is active his research at the intersection of visual computing and materials sciences for more than 12 years at the time of writing this report. He is experienced in both domains, visual computing as well as materials sciences. The second author is a high potential junior researcher also working at the intersection of visual computing and materials science. For our state-of-the-art-report the related literature at the intersection of visual computing and materials sciences was screened yielding a total of 241 research papers, which were considered as potentially interesting: We therefore started off with this initial set of contributions on the one hand from top level visualization, visual analysis and visual computing conferences and journals (e.g., IEEE Transactions on Visualization and Computer Graphics, Computer Graphics Forum etc.), and on the other hand from top level materials testing, materials simulation and materials sciences publications (e.g., Journal of Materials Science, Journal of Nondestructive Evaluation, etc.), which showed interrelations of both fields. In the next step we further extended our review to smaller conferences and venues, as well as niche topics in both areas. For the classification of the full set of papers we applied a hierarchical classification scheme: The complete set of papers was initially classified regarding relevance on a scale of zero to five stars from no relevance to core relevance. Core relevant contributions are required to reach a materials science research target through extensive use of visual computing approaches. Papers of this category include novel visual computing techniques for materials science as well as applications or adaptations of existing visual computing techniques within a specific materials sciences domain. As relevant papers contributions are considered which integrate visual computing with limited novelty for solving a materials science task. Papers, which are classified with passing relevance, focus mainly on either of the two domains and hardly interfere with the other one. As not relevant papers we classified contributions, which do not demonstrate the intersection of the two domains. This process led to 88 contributions, classified from relevant to core relevant, which are to be discussed in this report. The second level review targeted a representative overview of all papers in the form of a matrix. We thus investigated the set of 88 papers in detail using an open coding process and manually registered our findings in a dynamically growing and continuously adapted matrix of features based on the following main categories: application, high / low level tasks, material system, data acquisition and characteristics, visual computing / visual analysis aspects. To ensure a common understanding continuous discussions amongst the annotators have been carried out at least on a weekly basis during filling the matrix of features. In these discussions the main categories were also further subdivided and refined in lower levels, in order to ensure that no information is lost. After all relevant papers were encoded in the feature matrix, a manual clustering of the subcategories was carried out as next step: Subcategories of lower interest showing only limited contributions, applications or knowledge discovery for our matrix, were discussed and consequently cleared, if only passing knowledge discovery was identified. The clustering iterated until descriptive subcategories were found. The results of our literature research were integrated in a cumulative matrix which correlates the analysis tasks with the used visualization and interaction techniques. At the corresponding intersections we integrated the respective application areas as seen in Figure 2.

4. Visual Computing in Materials Science

Visual computing and especially visualization as well as visual analysis have become highly attractive to generate new, previously impossible insights for materials science by studying a multitude of different phenomena at multiple scales, dimensions, or using different modalities. In the following sections, we define materials science and its various material systems. We further define visual computing and review tasks to be solved, the simulation and testing techniques as well as the used visualization and interaction techniques. During the iterative process of analyzing the body of literature, we classified and clustered the relevant related work in a matrix revealing the different interrelations of both fields. Figure 2 outlines all relations in detail.

4.1. Definition of Materials Science

Materials science involves the subareas of understanding, discovery, design and use of (new) materials as well as material systems. As outlined by Adrian Sutton [Sut] from the University of Oxford, it is difficult to find a comprehensive definition for materials science, which covers all subtle niches of the field. Therefore, materials science is best defined by its core areas and tasks, e.g., as found in the description of Springer's Journal of Material Science. According to their definition materials science includes:

> *"... techniques for studying the relationship between structure, properties, and uses of materials. The subjects are seen from international and interdisciplinary perspectives covering areas including metals, ceramics, glasses, polymers, electrical materials, composite materials, fibers, nano structured materials, nano composites, and biological and biomedical materials ..." [Spr]*

This description outlines the broad spectrum of materials science, its diversity as well as core relevant domains. For all areas of understanding, discovering, designing and using materials, a primary objective of materials science is found gaining a profound knowledge of the material's properties (material analysis) as well as the material's performance characteristics (material simulation). Visual computing holds a large potential in retrieving and visualizing complex materials characteristics to materials scientists. For example, the properties of advanced materials are determined by material analysis techniques and visualized in order to form a mental image of regional distributions, critical areas or features of interest. Furthermore, regarding their performance, (new) materials

are increasingly modeled and simulated within their targeted usage scenario. To make sure that the generated simulation results correspond to reality, they are subsequently verified by means of destructive (DT) and non destructive testing (NDT) techniques using visual computing (see also Straumit et al. [SLW15]). While non-destructive testing enables to reuse the same specimen for tests using supplemental techniques, destructive techniques destroy the specimen during evaluation.

4.2. Material Systems

To provide an overview about promising material systems as well as the structures and features of interest, we introduce material systems in the following paragraphs, for which visual computing techniques are highly relevant:

Composite Materials are found in a wide variety of industries ranging from leisure, sports, electronics, automotive, aeronautics, to space industry. Especially, advanced composites are regarded as materials of the future in many industries, due to their tailored characteristics for their target application area. They are composed of individual components to fulfill the targeted requirements in terms of strength, stiffness, function-orientation and light weight. Composite materials feature a base matrix material, which forms the components and holds the reinforced components in place. The reinforcements are carrying the loads of the component while in use, in order to end up in a material system of superior behavior as compared to conventional materials. The main part of the reviewed literature in the area of composite materials centers around fiber reinforced materials. For example, carbon fiber reinforced polymers (CFRPs) show a low weight, but high specific stiffness and high specific strength. CFRPs are also cost effective for the properties they deliver, as stated Bhattacharya et al. [BHA*15]. CFRP is thus a promising candidate material for a large variety of new automotive, aeronautic and space components. Besides CFRPs there are many other fiber reinforced composites in industrial use. Glass fiber reinforced composites (GFRP) integrate glass fibers as reinforcements and allow the manufacturing of cheap and robust injection molded parts as indicated by Kastner et al. [KPHF08]. GFRPs are thus found, e.g., in housings of electronic or automotive components. Fiber reinforced ceramic matrix composites (CMC) withstand high temperatures and show a high resistance to thermal shocks, which opens application areas of this system for heat shields or ceramic disc brakes systems. Further reinforcement components are found in steel fibres as discussed by Fritz et al. [FHG*09] and Westenberger et al. [WEL12], biological fibers, (e.g., wood-based fibers as presented by Tran et al. [TDD*12] or hemp fibers as discussed in Placet et al. work [PMF*14]), or even ultra high molecular weight polyethylene fibers which are used in Intrater et al. [IHL*05].

Polymer Materials, especially polymer foams, are present in many advanced industrial applications due to their advantageous characteristics: Polymer foams feature stiff, strong, as well as compressible cellular cores and thus attracted significant interest for energy absorption applications. As their cellular structure shows a stochastic behavior, polymer foams require a detailed structural analysis of their foam network. Moreover, regarding the simulation of polymer foams under load, the respective mechanical properties of this material system are typically not linear but hyper-elastic as

described by Patterson et al. [PCH*15]. Even in the manufacturing of polymer foams visual computing is required, observing the plastic foaming processes under shear stress as presented by Wong et al. [WP12]. Another example of new polymer materials in need of detailed investigations are semi-crystalline polymers. As discussed by Tabatabaei et al. [TBNP14] the properties and morphology of semi-crystalline polymers need to be continuously analyzed during the crystallization process in order to reach the targeted application properties, which are mainly defined by the crystallite structures. In general, polymers are found in important material systems for future applications. For this reason this field is a highly active subarea of research inside materials science, which is especially in need for visual computing supported studies.

Non-Metal Inorganic Materials (apart from advanced composites) typically contain subcomponents such as glass (Laevsky et al. [LTM01]), concrete (Algernon et al. [AGM*08] and Marinoni et al. [MVM*09]), rock (Bimber et al. [BKA*11]), ceramics (Weber et al. [WRR*11]) or gas (Ushizima et al. [UMW*12]). As these subcomponent materials are well known, visual computing supported investigation is mainly required in this area for analyzing highly specialized material subsystems. For example, using micropowder injection molding, complex shaped ceramics or metallic parts are produced, which show a special need for visual computing supported analysis. Another example is given in Weber et al.'s work [WRR*11], who investigated the powder-binder separation using synchrotron-based microtomography and 3D image analysis. Furthermore, fused silica glass is used in the work of Galvin et al. [GGB01] for photo lithography or for first surface mirrors in telescopes. The authors analyzed surface strain and polishing artefacts using scanning electron microscopy. The determination of quantitative material properties is of high relevance in order to advance the material for future applications.

Metals and Alloys are still widely used in industry applications, leisure, automotive and aeronautics. In automotive and even in aeronautics applications, a renaissance of these conventional materials is currently being observed in the form of novel high strength, low density steels or aluminum alloys for lightweight construction. For example Al2024 is such an alloy, which is increasingly used in automotive and aeronautic industry because of its low density and high damage tolerance. Typically, metallic materials are processed in various manufacturing steps such as forging, drawing, rolling in order to tailor their characteristics to the application's requirements. As the material's micro structure and related characteristics mainly define the overall properties of the metal or the alloy, these features are crucial to be analyzed and to be controlled in manufacturing. To achieve this target, visual computing methods are used by Bhimavarapu et al. [BMBN10] to explore the compressive deformation behavior of Al2024. They encode the power density as well as the instability of the alloy in 2D and 4D maps. Ductile cast iron as a further example of this area provides high strength, high ductility and high fatigue strength depending on the micro structures of the graphite particles inside the material. These graphite micro structures are analyzed and quantified according to form and size parameters in visual analysis tools as presented by Fritz et al. [FHG*09]. In addition to the micro structure of the graphite particles they also investigate steel fibers using directional sphere histograms encoding their orientation in the material system. Another highly interest-

		Visualization				Interaction						
		Spatial Data Visualization	Spatio-temporal Data Visualization	Quantitative / Derived Data Visualization	Interactive Steering	Focus plus Context	Linking & Brushing	Filter	Translate	Rotate	Zoom	No Interaction
Material Simulation — Finite Element Simulations (FE)		Metal / Alloys: [NTJM98]; Composites: [ZSS15]	Non-Metal Inorganic: [WT10] [MTGG11] [JWJ*14] [SSJ*14] [WRK*10] [BSL*12] [BmHTF07] [LTM01]	Composites: [ZSS15]	Metal / Alloys: [NTJM98]; Non-Metal Inorganic: [MTGG11] [BSL*12]			Composites: [ZSS15]				Non-Metal Inorganic: [WT10] [JWJ*14] [SSJ*14] [WRK*10] [BmHTF07]
Material Simulation — Molecular Dynamics Simulations		Non-Metal Inorganic: [GKLW16] [GDN07]; Metal / Alloys: [FSG*11];										Non-Metal Inorganic: [GKLW16] [GDN07]; Metal / Alloys: [FSG*11];
Material Simulation — Computational Fluid Dynamics (CFD)			Non-Metal Inorganic: [LTM01] [SSJ*14]; Composites: [PC13]; Non-Metal Inorganic: [PC13] [UMW12]		Non-Metal Inorganic: [LTM01]							Non-Metal Inorganic: [SSJ*14] [PC13] [UMW12]; Composites: [PC13]
Material Analysis — Feature Extraction & Quantification		Composites: [PMF*14] [TDD*12] [YMNG05] [CFYT09] [WRS*14] [KSP*14] [HWR*14] [AFR*14] [AHKG10] [RPK*12] [KPHF08] [WEL12] [GVTA10] [WAL*14] [BHA*15] [FHG*09] [UMW*12] [BRP*16]; Biological / Biomedical: [PMF*14] [TDD*12] [KHK*12] [UMW*12] [GYL*12]; Construction / Building: [PD00] [LGKN15] [HGF14] [MKT15] [MLK*08] [AHK*13] [MHG09] [KHK*12]; Metal / Alloys: [WRR*11] [TKH13] [AKH*15] [AFK*14] [KS06] [FHG*09]; Non-Metal Inorganic: [WRR*11] [KHK*12] [UMW*12] [VCT10]; Polymers: [BDM*10] [TDD*12]	Metal / Alloys: [RAK*15]; Biological / Biomedical: [RAK*15]; Polymers: [TBNP14] [LLCD11]; Composites: [GDN*07] [Alt08]	Composites: [PMF*14] [TDD*12] [WRS*14] [KSP*14] [HWR*14] [AFR*14] [AHKG10] [RPK*12] [WEL12] [GVTA10] [WAL*14] [BHA*15] [FHG*09] [ZSS15]; Biological / Biomedical: [PMF*14] [TDD*12] [KHK*12]; Metal / Alloys: [WRR*11] [AKH*15] [AFK*14] [KS06] [FHG*09]; Non-Metal Inorganic: [WRR*11] [KHK*12]; Polymers: [BDM*10] [TDD*12] [TKH13] [TBNP14]; Construction / Building: [PD00] [LGKN15] [HGF14] [MKT15] [MLK*08] [AHK*13] [MHG09] [KHK*12]	Composites: [WAL*14] [UMW*12]; Non-Metal Inorganic: [UMW*12]; Biological / Biomedical: [UMW*12] [GYL*12]	Composites: [MVM*09] [HWR*14] [RPK*12] [GVTA10]; Metal / Alloys: [RAK*15] [AFK*14]; Biological / Biomedical: [RAK*15]; Construction / Building: [MHG09]	Composites: [MVM*09] [KSP*14] [HWR*14] [RPK*12]; Metal / Alloys: [RAK*15] [AKH*15] [AFK*14]; Biological / Biomedical: [RAK*15]; Construction / Building: [AHK*13]; Polymers: [LLCD11]	Composites: [KPHF08] [BHA*15] [FHG*09]	Metal / Alloys: [RAK*15] [AFK*14]; Biological / Biomedical: [RAK*15]; Composites: [RPK*12]	Metal / Alloys: [RAK*15]	Metal / Alloys: [RAK*15] [AFK*14]; Biological / Biomedical: [RAK*15]; Composites: [RPK*12]	Composites: [PMF*14] [TDD*12] [YMNG05] [CFYT09] [AFR*14] [AHKG10] [WEL12] [KHK*12] [GDN*07] [BRP*16] [Alt08]; Biological / Biomedical: [PMF*14] [TDD*12]; Polymers: [TBNP14]; Metal / Alloys: [WRR*11] [TKH13] [KS06]; Non-Metal Inorganic: [WRR*11] [KHK*12] [VCT10]; Construction / Building: [PD00] [LGKN15] [HGF14] [MKT15] [MLK*08] [KHK*12]
Material Analysis — Stress and Deformation Analysis		Non-Metal Inorganic: [GGB01] [MVM*09]; Construction / Building: [LGKN15] [HGF14] [SBR*15]; Composites: [IHL*05] [ZSS15]; Metal / Alloys: [CWA*09]	Composites: [PCH*15] [GDN*07] [AAS*16]; Polymers: [PCH*15] [WP12]; Non-Metal Inorganic: [FSG*11]	Metal / Alloys: [BMBN10]; Non-Metal Inorganic: [GGB01]; Construction / Building: [LGKN15] [HGF14]; Composites: [IHL*05] [ZSS15] [LBP*15]; Polymers: [WP12]				Construction / Building: [PZM*15] [SBR*15]; Composites: [ZSS15]				Metal/Alloys: [BMBN10] [CWA*09]; Non-Metal Inorganic: [GGB01] [MVM*09] [FSG*11]; Composites: [PCH*15] [IHL*05] [GDN*07]; Polymers: [PCH*15] [WP12]; Construction / Building: [LGKN15]
Material Analysis — Fatigue Testing & Damage Analysis		Ceramic: [MSM13]; Composites: [TDD*12]; Polymers: [TDD*12]; Construction / Building: [LGKN15] [MKT15] [MLK*08] [DRH15] [CHSW08] [TL13]; Biological / Biomedical: [TDD*12]; Metal / Alloys: [KS06]	Composites: [AAS*16] [YTT07]	Ceramic: [MSM13]; Composites: [TDD*12] [ZSS15]; Polymers: [TDD*12]; Biological / Biomedical: [TDD*12]; Construction / Building: [LGKN15] [MKT15] [MLK*08]; Metal/Alloys: [KS06]		Composites: [AAS*16];			Composites: [ZSS15] [AAS*16];	Composites: [ZSS15] [AAS*16];	Composites: [ZSS15] [AAS*16];	Ceramic: [MSM13]; Composites: [TDD*12]; Biological / Biomedical: [TDD*12]; Polymers: [TDD*12]; Construction / Building: [LGKN15] [HGF14] [MKT15] [MLK*08] [DRH15] [CHSW08] [TL13]; Metal / Alloys: [KS06];
Material Analysis — Dimensional Measurements		Polymers: [BDM*10] [AFR*14]; Composites: [HKG07]; Construction / Building: [HKG07] [BRP*16]; Non-Metal Inorganic: [WNG06] [BACC04] [SXJ08]; Metal / Alloys: [LKS*98]		Polymers: [BDM*10] [AFR*14]; Non-Metal Inorganic: [BACC04]								Polymers: [BDM*10] [AFR*14]; Composites: [HKG07]; Construction / Building: [HKG07] [BRP*16]; Non-Metal Inorganic: [WNG06] [BACC04] [SXJ08]; Metal/Alloys: [LKS*98]
Material Analysis — Uncertainty Quantification & Visualization		Construction / Building: [MKT15] [AHK*13]; Composites: [AFR*14] [AHKG10];		Construction / Building: [MKT15] [AHK*13]; Composites: [AFR*14] [AHKG10]			Construction / Building: [AHK*13]					Construction / Building: [MKT15]; Composites: [AFR*14] [AHKG10]
Material Analysis — Optimization		Non-Metal Inorganic: [AGM*08] [BKA*11] [Pop92] [SBSG06] [FMHH14]; Construction / Building: [FH08] [AHR*11] [MHG08] [TWM*08] [JCRA11] [PZM*15] [SBR*15]; Metal / Alloys: [AHR*11] [MHG08] [AHRG10] [JCRA11] [DBTH07]; Biological / Biomedical: [MHG08] [BKA*11] [HRN*03] [WM04] [LNA*06] [JCRA11] [GYL*12]; Composites: [AHRG10];	Polymers: [TBNP14]; Non-Metal Inorganic: [FSG*11]; Composites: [GDN*07]	Non-Metal Inorganic: [AGM*08]; Construction / Building: [FH08] [AHR*11]; Metal / Alloys: [AHR*11] [AHRG10]; Polymers: [TBNP14]; Composites: [AHRG10]	Biological / Biomedical: [WM04] [GYL*12]	Composites: [AHRG10]; Metal / Alloys: [AHRG10]	Metal/Alloys: [AHR*11]; [AHRG10]; Construction / Building: [PZM*15] [SBR*15]; Composites: [AHRG10]	Metal / Alloys: [AHR*11]; Construction / Building: [AHR*11]; Non-Metal Inorganic: [BKA*11]; Biological / Biomedical: [BKA*11] [LNA*06]	Non-Metal Inorganic: [BKA*11]; Biological / Biomedical: [BKA*11]	Metal / Alloys: [AHR*11]; Non-Metal Inorganic: [BKA*11]; Biological / Biomedical: [BKA*11]	Metal / Alloys: [AHR*11]; Construction / Building: [AHR*11]; Non-Metal Inorganic: [BKA*11]; Biological / Biomedical: [BKA*11] [LNA*06]	Non-Metal Inorganic: [AGM*08] [FSG*11] [Pop92] [SBSG06] [FMHH14]; Construction / Building: [FH08] [MHG08] [TWM*08] [JCRA11]; Metal / Alloys: [MHG08] [DBTH07]; Biological / Biomedical: [HRN*03] [JCRA11]; Polymers: [TBNP14]; Composites: [GDN*07]
Material Analysis — Risk Analysis		Construction / Building: [LZS16] [QSCZ16] [LGKN15]		Construction / Building: [LZS16] [QSCZ16] [LGKN15]		Construction / Building: [LZS16]	Construction / Building: [LZS16] [QSCZ16]					Construction / Building: [LGKN15]

Figure 2: *This matrix encodes the result of our systematic literature study at the intersection of Visual Analysis and Materials Science. In an iterative process analyzing the body of literature, we classified and clustered the relevant related work revealing the different interrelations of both fields.*

ing material system in this area is found in AlSiC, a metal matrix composite consisting of an aluminium matrix with silicon carbide particles. While AlSiC composites offer the high thermal conductivity of a metal, they facilitate to maintain the low thermal expansion of a ceramic. Reh et al. [RAK*15] presented a graph based technique for tracking those particles and other features of interest over time / over various steps of a heating / cooling process.

Construction and Building Materials as well as the corresponding material systems are typically referred to as well known materials, which have been used for ages in similar applications. Despite their seeming simpleness also construction materials often contain many different components featuring complex shapes. For example, steel fiber reinforced concrete allows to generate tailored material system for high tech applications such as the construction of tunnels. An investigation of steel fibres in such sprayed concrete was presented by Fritz et al. [FHG*09]. In contrast to the material systems described before, these materials are typically crafted for direct application in order to fulfill a specific purpose, without further processing or assembly. The application areas of construction and building materials and material systems are widespread and range from cultural heritage applications (Li et al. [LZS16]), civil engineering (Kim et al. [KHK*12] and La et al. [LGKN15]), private buildings and construction (Ham et al. [HGF14]) to electronic devices (Protopopov et al. [PD00]), printed circuit boards (PCBs) (Cicchiani et al. [CHSW08]) or even micro-electromechanical Systems (Fisher et al. [FH08]).

Biological and Biomedical Materials are used as reinforcement components for new composites. For example, plant-based fibers, such as wood-based fibers as used by Tran et al. [TDD*12], or hemp fibers utilized by Placet et al. [PMF*14], are currently tested for various applications as a promising reinforcements. In contrast, Hu et al. [HRN*03] explore biological materials as such. The authors propose an approach for the segmentation of the meiotic spindle within a mouse egg from Confocal Laser Scanning Microscope (CLSM) volume data. Their method is based on expectancy and standard deviation values of voxels extracted using a Weibull probabilistic framework for segmentation. A further application field of biological and biomedical materials deals with copying the structure of biological materials as well as their characteristics to inorganic materials.

4.3. Definition of Visual Computing

Visual computing integrates computer science disciplines dealing with the acquisition, the analysis and the synthesis of (visual) data using computing resources in applications such as industrial quality control, medical image and data analysis, robotics, multimedia systems, computer games, etc.. Aside others, visual computing thus covers aspects from image processing, visualization, computer graphics, computer vision, virtual and augmented reality, pattern recognition, machine learning, as well as human computer interaction. Furthermore, visual computing is also strongly related to other science domains such as mathematics, physics and cognitive sciences. A core aspect of visual computing is found in visualization and visual analysis. As defined in Munzner's book "Visual Analysis and Design" [Mun14], computer-based visualization systems provide visual representations of datasets, which are designed to

help people carry out their tasks more effectively. The book further indicates that visualization is especially beneficial, when there is a need to augment human capabilities rather than replace people with computational decision-making methods. This characteristic of augmenting human capabilities perfectly covers the visual computing supported materials sciences tasks discussed in section 4.4.

4.4. Tasks of Visual Computing Supported Materials Sciences

The analysis and simulation of the material systems as discussed in section 4.2 pose very different tasks and challenges on visual computing. In the following section we shed light on respective tasks and consider them in more detail. Generally, the main challenges revolve around two large topics: the simulation of material systems and the analysis the material systems.

Simulation of Material Systems is highly important for designing, manufacturing, processing and evaluating novel material systems in their application areas. Tailored visualization and visual analysis are required to solve the domain's research questions. For the simulation of material systems we identified the following three major tasks for visual computing aside the actual computation of the simulation:

- *Exploration and Visualization of Finite Element (FE) Simulations* is an important task facilitated by visual computing to explore the system of interest in its target application. Aside materials sciences, finite element models and finite element simulations are frequently used in computer graphics, robotics, special effects or virtual reality [LB15]. Typically, FE data is visualized using surface-based approaches. This is mainly due to the nature of non uniform grids as typcially used in FE simulations as well as surface based representations used for modeling the simulated domain. More flexibility is found in volumetric visualization techniques, which support the interactive exploration of the complete data. To render these datasets using ray-casting, uniformly distributed sample points are required along each viewing ray. Bock et al. introduced an approach [BSL*12], which transforms the uniformly distributed sample points into the material space for each cell using a coherency-based method, decoupling expensive world-to-material space transformations from the rendering process. Even for higher order FE models the authors achieved frame rates, which allow for interactive data exploration. Also earlier approaches as presented by Laevsky et al. [LTM01] were focused on the exploration of FE simulations using interactive steering of the simulation and monitoring the simulation's outputs. The application area of this work is found in glass being pressed in a mold, modeling glass as a Newtonian fluid. The goal of this approach, aside understanding the pressing process, is to obtain optimal shapes of new molds by a detailed evaluation of the simulation results and a feedback loop of the generated results back into the FE simulation process.

- *Visual Analytics of Computational Fluid Dynamics* marks a further crucial task in the area of simulating material systems. Of special importance in this area is the exploration of the permeability and related properties of porous media for various applications such as the storage of CO_2 in porous materials. Uzshizima et al. [UMW*12] present a framework for the analysis and quantification of porous media using multi-scale topological de-

scriptors of the underlying material of interest. In contrast to a local exploration of flow trajectories interacting with the solid structures, the authors target to extract the pore network for estimating the fluid flow using topological descriptors. The porosity is used to finally compute the permeability of the porous media. With their framework the authors facilitate to characterize synthetic material phantoms composed of packed spheres as well as 3D high-resolution X-ray computed tomography data regarding porosity. Patkar and Chaudhuri [PC13] focus on porous solid media interacting with fluids, such as cloth getting wet by a fluid jet or porous stones absorbing water. They make use of smoothed particle hydrodynamics for modeling the fluid dynamics within the specimen. In a three stage approach, they first model the fluid absorption of the object, the transport of fluid inside, as well as finally the dripping of extra fluid by oversaturated parts. They visualize the generated results in animations of the 3D domain.

- *Analysis and Visualization of Molecular Dynamics Simulations* is especially important for understanding and conditioning novel materials. Molecular dynamics simulation is a widely used technique to analyze material characteristics as well as structural changes under external forces. Gyulassy et al. [GDN*07] present an application, which uses molecular dynamics to simulate the particle impacts at various scales: In the nanometer range, particles of several thousands of atoms may be used to smooth or condition surfaces. In micro and macroscopic scales, this kind of simulation is used to mimic impact damages as well as potential materials to compensate. To understand the behavior and the interactions of the underlying materials, the authors carried out molecular dynamic simulations, which model the impact of solid grain material on low density foam. The domain specialists were interested in how the impact craters are forming for two reasons: (1) how is the structure around a crater changing and (2) how are quantitative values affected such as the overall porosity. Guylassy et al. introduced methods for the construction of distance fields, which are topologically clean in order to extract, characterize, and visualize relevant filament structures in the porous material. In a recent work, Gyulassy et al. [GKLW16] employed and extended their findings to simulate the synthesis and ion diffusion of battery materials using large-scale molecular dynamics simulations. Their technique shows how visual analysis is used to support domain specialists in the investigation and selection of novel anode materials for future batteries. Other approaches address the sheer data sizes generated by large-scale molecular dynamics simulations. Frey et al. [FSG*11] proposed a technique based on loose capacity-constrained Voronoi diagrams, which allows to replace the huge amount of simulated particles by a small set of representatives. These representatives are required to capture the main characteristics of the particle density and to exhibit coherency over time for creating visualizations, which reflect both particle distribution and geometric structure of the original data. The authors demonstrate their method on molecular simulation datasets of laser ablation from solid aluminum, compressed argon surrounded by vacuum as well as colliding liquid methane and ethane droplets.

Material Analysis denotes the second main area in materials science which makes extensive use of visual computing and thus profits from recent techniques. For this area we identified the following tasks, in which visual computing is of core relevance:

- *Feature Extraction and Quantification* is the most important task in destructive and non destructive testing. The primary goal aside the plain extraction and identification of individual features is found in the investigation of their distribution throughout the specimen as well as their individual properties. As typically the number of features is high and the characteristics of each feature may exceed 25 or more properties, visual analysis techniques are required to explore the generated data. A lot of approaches facilitating feature extraction and quantification make use of segmentation techniques in order to extract the features of interest in 3D as presented by Hu et al. [HRN*03]. Once the feature of interest is extracted, the corresponding properties may be computed and visualized in histograms, line plots, bar charts or similar representations. Features of interest may be required (e.g., fibers, particles, reinforcements, etc.) as well as undesired structures (e.g., voids, inclusions, impurities, etc.). For features such as fibers, pores and voids, typically properties as the diameter, length, volume, shape, orientation, etc. are computed and evaluated together with their distribution. Weissenböck et al. [WAL*14] employ in their approach more sophisticated visualization and interaction techniques such as parallel coordinate plots, scatter plot matrices and linked views to facilitate the clustering of interesting features. Furthermore, interactions between features of interest are investigated. They influence the overall material properties heavily as stated by Hartl et al. [HJL15], who analyze the effect of fiber orientation, stress state and notch radius on the impact properties of glass fiber reinforced polymer samples. Also Gusenbauer et al. [GRKK14] extract and quantify non metallic inclusions in steel in order to investigate their correlation with the breakage behavior in fatigue tests.

- *Stress and Deformation Analysis* is required by domain specialists to get insights into the material while being in use and under load. Aside specific properties and characteristics of materials such as flow stress, strain and strain rate, surface strain and temperature under strain, also their deformation behavior during the targeted usage are of interest. An example for stress and deformation analysis is found in the work of Lisle et al. [LBP*15], investigating the damage of woven composites under tensile and shear stress using infrared thermography and micrographic cuts. The authors computed stress-strain curves as well as temperature variation fields of the specimens encoded in 2D colormaps and used 2D scanning electron micropcopy (SEM) micrographs for verification. Also Amirkhanov et al. [AAS*16] proposed a visual analysis tool for exploring and analyzing defects and deformations occurring under increasing load conditions in glass fiber reinforced polymers by applying 4DCT interrupted in-situ tensile tests. The authors employ surface based representations as well as heat maps showing the evolution of defects and deformations over time.

- *Fatigue Testing and Damage Analysis* is a further escalation step of the previously discussed area of stress and deformation investigation. The domain specialists' tasks are to figure out where and why a material or a specimen breaks when aging. Damage analysis is for example scope of work in Marinoni et al. [MVM*09]: The authors study alkali-silica reactions in ag-

ing samples using phase contrast X-ray computed tomography (XCT) and investigate alkali-silica reactions regarding their reactive aggregate progressive dissolution together with a deposition of gel, during and after the reaction. During the aging process the specimens are deformed and they develop of microcracks in the structure. The results were compared to traditional 2D techniques such as optical microscopy and SEM. The main scope of interest was to find a method, which allows the rendering of microstructural features in the specimen. The results are presented in 2D slice images as well as 3D renderings of the segmented and colorcoded phases. Further application areas of damage analysis are found in the manufacturing of electronic devices or the construction of buildings, which suffer from similar damage types. For example, faults within printed circuit boards (PCBs) and their components are investigated by Cicchiani et al. [CHSW08]. The main goal of their work was to obtain a positive visual confirmation if a specific failure occurred in the PCB. Mayer et al. [MLK*08] target to characterize and classify indications of defects in concrete buildings and even go a step further: They target the prevention of faults by estimating cracks as well as the crack growth of concrete materials. Other types of damage are found in corrosion and delamination which are topic of research of La et al. [LGKN15] and Yashiro et al. [YTT07].

- *Dimensional Measurements*, in contrast to the previous tasks, this task centers around the traceable dimensioning and tolerancing of measurement features such as straightness, evenness, cylindricity, etc., which is essential for industrial quality control. The practitioners need to know if a specimen fulfills the required internal and external standards. Using conventional tactile or optical coordinate measurement machines, mainly plots of points, lines or surfaces are evaluated, which reflect the applied measurement strategy together with actual and nominal values as well as tolerance bands. In recent years much more information became available when X-ray computed tomography (XCT) was introduced for industrial metrology purposes. Using XCT, the uncertainty of the generated data may be estimated at every spatial position of the data, as the surfaces and interfaces characterizing a measurement feature are only implicitly given in the scanned attenuation coefficients. Information on the quality of the transition air to material or material to material is prevalent in the XCT data, which may be affected by artifacts and other irregularities. While earlier approaches are tasked to reduce and remove artefacts as presented by Heinzl et al. [HKG07], more recent techniques evaluate the datasets' uncertainty. For example, Amirkhanov et al. [AHK*13] integrate information on the uncertainty of a measurement feature as context information in commonly used visual metaphors of dimensional measurements, which is strongly related to the next task:

- *Uncertainty Quantification and Visualization* builds upon the extracted (measurement) features and targets to determine the underlying uncertainty budgets: Data acquisition and evaluation typically introduce various types of uncertainty stemming from the environmental conditions, the specimen, the measurement system, the analysis pipeline and other influences. The domain specialists require to quantify and visualize the uncertainty of their measurements in order to avoid that wrong assumptions are made on the data as stated by Amirkhanov et al. [AHK*13]. As shown by Schonfeld et al. [SB15], a lot of research efforts have been put into finding and verifying local quality measures for standard phantoms. An example of such a measure is the local quality value as presented by Flessner et al. [FMHH15], analyzing the volume data in the proximity of an extracted surface/interface point of a measurement feature. The task of uncertainty quantification and analysis was identified as separate task because of its high relevance in both application and visualization domain.

- *Optimization* of (parts of) a workflow is another task frequently found in visualization and visual analysis for materials science. Typically, methods in this area put their focus on optimizing a specific aspect of the simulation, the data acquisition or the data evaluation pipeline. Some targets in this area are for example to increase the signal-to-noise ratio, to optimize the measurement or testing parameters in order to utilize them in new materials or or to simply improve the visual representation of the underlying data. For example, Bimber et al. [BKA*11] present an approach on closed-loop feedback illumination for optical inverse tone-mapping in light microscopy. Amirkhanov et al. [AHR*11] introduce a method for projection based metal artefact reduction in XCT or Wang and Mueller [WM04] generate sub-resolution detail in images and volumes using constrained texture synthesis. In terms of optimizing the production process of materials itself, this task is also strongly related to the exploration and visualization of finite element simulations of some material or component as presented by Laevsky et al. [LTM01].

- *Risk Analysis* marks the final task we identified. For this task, mainly cultural heritage applications are of interest such as analyzing the risk, cultural heritage sites are facing because of environmental or other influences. Qian et al. [QSCZ16] propose a visual analysis technique for the assessment of the risk of deterioration, which is focusing on matching the major needs of the domain with the objectives of deterioration. They encode the risks of detoriation in spatial views, integrating techniques of visual analytics for analyzing the risk level. A similar visual analysis method is provided by Li et al. [LZS16] investigating the deterioration risk of mural paintings using site-level visualization based on a circle packing layout, a chord diagram tool and heat map encoding the overall disruption risk.

In the next section we review the different methods in materials sciences used to solve these challenges. While the FE, CFD and other simulations as well as the corresponding models for the material systems of interest are generated similarly as for other applications outside materials science and as simulations are similarly returning fields of scalar, vector and tensor data, we do not consider the simulation techniques themselves here any further but refer the reader to indicative papers of Laevsky et al. [LTM01] for FE simulation, Uzshizima et al. [UMW*12] for CFD simulation, Gyulassy et al. Gyulassy et al. [GKLW16] for molecular dynamics simulation as well as to the tasks identified in section 4.4. We put our focus in the next section on the material analysis, the respective testing techniques as well as the generated data, which are very different from each other regarding their principles and capabilities. The characteristics of the testing techniques mainly determine which visualization technique is used to solve the tasks as descibed.
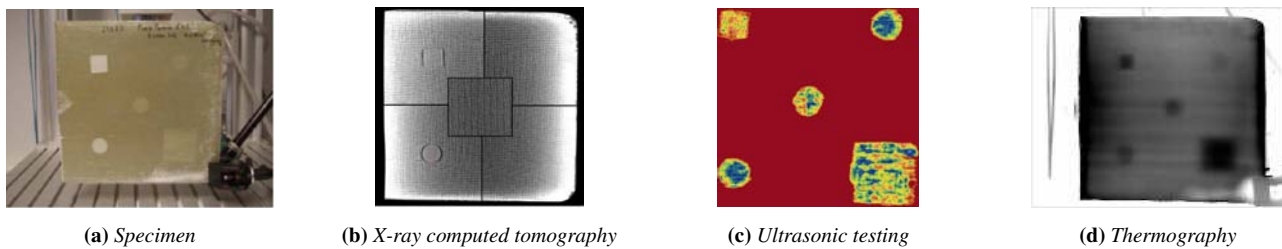
(a) *Specimen*   **(b)** *X-ray computed tomography*   **(c)** *Ultrasonic testing*   **(d)** *Thermography*

Figure 3: *Comparison of thermography, ultrasonic testing, and XCT data for the inspection of delamination in wind turbine blades made of E-glass/polyester. Reprinted from [AMLA*11], with permission from Elsevier: **(a)** **Photography** of the specimen. Teflon inserts in different dimensions and depths are used for comparing different NDT methods. Furthermore, thin but severe delaminations simulate defects. **(b)** **X-ray computed tomography**: 2D slice image of the specimen in Figure 3a. XCT did not detect thinnest delaminations due to resolution constraints. Despite this fact, such slice images or 3D reconstructions are used to find all kinds of defects, e.g., cracks, voids, inclusions, etc. in the specimen. **(c)** **Ultrasonic testing** image (C-scan) of the specimen in Figure 3a. Delamination defects are clearly visible as the back reflection intensity of the C-scan is reduced by any defect at any depth. **(d)** **Thermography** image visualizing temperatures obtained with transmissive, pulsed thermography of the specimen in Figure 3a. All five defects have been detected. Blurring in thermography images is a direct consequence of the heat of the delamination defects spreading within the specimen.*

4.5. Testing Techniques using Visual Computing supported Materials Analysis

The computationally supported study of materials is based on digital data extracted from the materials of interest. This process of data generation is also referred to as materials testing, which is subdivided in two major categories: destructive (DT) and non-destructive testing (NDT). Destructive methods, as the name indicates, destroy or modify the specimen, its structure or features of interest during the testing procedure for gaining insight into the material as well as to extract its properties. For a number of reasons, such as economic issues, functional or manufacturing issues, especially non-destructive techniques became increasingly important in materials science. Whereas the larger body of work in materials testing is currently found in the domain of non-destructive testing also destructive testing techniques are prevalent in materials sciences. The techniques explained in the following sections are highly dependent on visualization and visual analysis for data evaluation, which is the reason why we put our focus on these methods. Aside the techniques themselves we give an overview of the data generated and derived. Most of these techniques are explained on a sample as introduced by Amenabar et al. [AMLA*11], which is shown in Figure 3a. In their work they performed a comparison between active thermography, ultrasonic testing, XCT and Shearography for the inspection of delamination in wind turbine blades, which gives an intuitive example for each method regarding the generated data as well as typically used visualization techniques.

3D X-ray Computed Tomography (XCT) originated from medical applications and was adopted for NDT because of its ability to describe both inner and outer structures in detail, in a short time and without destroying the sample. The principle of XCT is based around 3 main components: the X-ray source, the detector and the rotary plate where the sample is placed on. For an XCT scan, a series of 2D penetration images is taken from the sample, recording individual attenuation images from different angles typically along a 360 degree circular trajectory. Visual computing was a key factor for the success of XCT in industrial applications. By means of reconstruction algorithms, 3D volumetric images contain-

ing scalars encoding the spatial attenuation are computed and rendered from the recorded series of 2D penetration images. Using grating based phase contrast XCT even multichannel data is generated, integrating scalars on attenuation, phase contrast and darkfield information at each spatial position of the reconstructed area. Slicing techniques facilitate detailed analyses of the generated data and rendering algorithms allow to visualize the 3D datasets. While most manufacturers of industrial XCT systems deliver their devices together with standard reconstruction and simple visualization tools, the fields of computational reconstruction as well as visual analysis of industrial XCT data is a highly active area of research. The plain 3D attenuation XCT data is used as basis to derive further information such as isolines and surfaces, complex data regarding features as well as their quantified properties, vector and tensor data in stress and strain fields, or even the dimensionality is increased to also encode time in the analysis of dynamic processes. Starting with the simulation of XCT scans for novel components and materials regarding the setup and the optimization of the scanning protocol as presented by Reiter et al. [RHS*11], or the optimization of XCT scan positions as presented by Amirkhanov et al. [AHRG10], visual computing already supports in advanced scan planning. For reducing artifacts due to strongly changing penetration lengths or attenuation coefficients during an XCT scan, Amirkhanov et al. [AHR*11] introduced a method, which accounts for the different materials present, reconstructs them individually, and fuses them to the final dataset. The major part of work about visual computing in XCT centers around the visualization and visual analysis for non-destructive testing or metrology applications. Regarding non destructive testing, for example the aeronautics industry requires tools for robust extraction of pores in fiber reinforced composite structures as presented by Heinzl et al. [HWR*14]. For metrology purposes surface models are typically extracted from the XCT data in order to compare the geometry of a specimen with its CAD model. Earlier approaches as presented by Heinzl et al. [HKKG06] focus on the extraction and comparison of surface models to CAD. More recent approaches, e.g., as presented by Flessner et al. [FMHH14] evaluate and visualize the quality of surface models determined
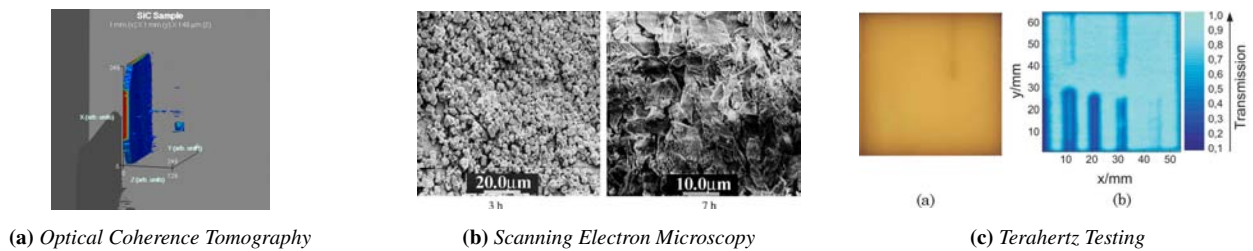
(a) *Optical Coherence Tomography*   **(b)** *Scanning Electron Microscopy*   **(c)** *Terahertz Testing*

Figure 4: *(a) **Optical Coherence Tomography**: OCT image of a silicon carbide. For the 3D representation, multiple OCT scans have been performed, each 10 μm deeper than the one before. Color encodes the strength of the backscattered signal from red (strong) to blue (weak signal). At z-values close to 0 the scattering is extreme due to the transition from air to material. Inside the material two scatterings are observed representing defects: The thin line normal to the surface and the big spot in the bottom right corner. ©1998 Optical Society of America. Reprinted, with permission, from [DBR98]. (b) **Scanning Electron Microscopy**: SEM image of a surface membrane exposed to a fouling process after 3 and after 7 hours. After 7 hours the complete membrane is covered with calcium carbonate. Even with higher resolution no empty spots are found. Reprinted from [SLKL02], with permission from Elsevier. (c) **Terahertz Testing**: THz imaging of a plastic specimen with drilled holes. (a) shows a photography of the sample. (b) shows the corresponding THz image. The drilled wholes are clearly visible using THz imaging. ©2010 Optical Society of America. Reprinted, with permission, from [JWP*10].*

from computed tomography volume data. Figure 3b shows an example of XCT data by Amenabar et al. [AMLA*11].

Ultrasonic Testing (UT) utilizes sound waves of short wavelength with a high frequency to test the wave propagation within the specimens under investigation. The wave propagation through the specimen varies depending on the material as well as through interfaces and gaps in the material. Often, the specimen is immersed in water or other liquids to improve the coupling of the ultrasonic wave with the specimen, especially when the specimen's surface is rough, and to provide a uniform contact with the specimen. In the field of non destructive testing, 2D ultrasonic techniques are state of the art, generating 2D scalar data representations encoding amplitude, brightness and other modes of the propagation of the ultrasonic waves in the specimen. While XCT for the acquisition of 3D data has been quickly adopted in non-destructive testing, 3D ultrasonic testing shows less momentum in materials science and only a few papers exist, which utilize ultrasonic wave propagation data for 3D visualization. For 3D ultrasonic testing a matrix array probe is used to scan specimens volumetrically using rotational or fan scan patterns. Sun et al. [SGW*14] indicated that visual analysis of 3D UT data dramatically speeds up the data analysis as the practitioners do not have to investigate the two-dimensional images frame by frame. An overview of how to generate 3D data from phased array ultrasonic testing techniques was presented by Kitazawa et al. [KKB*09]. An example of UT data is given in Figure 3c which is again taken from Amenabar et al. [AMLA*11]. Here, the C-scan (specific UT mode aside A(amplitude)-mode and B(brightness)-mode and others, which is formed in a plane normal to a B-mode image) of the back reflected intensity was taken, as it allows to nicely reveal the defects in the specimen.

Thermography (IR) denotes a family of different methods, which utilize thermal energy to digitize a specimen for gaining non destructive testing data. In terms of the measurement principle, the specimen is heated either from the outside through a heat lamp or a flash, or heat is generated inside the specimen through mechanical deformation of the specimen for active thermography. In contrast, in passive thermography no heat is induced and the specimen

is scanned in its current condition. Passive thermography is, e.g., used to test a specimen under stress in production environment. To analyze the thermal response, typically the infrared emission is used (infrared thermography). This infrared emission is usually encoded in 2D scalar grey scale images or using color maps encoding the thermal response. In 3D, the infrared emission data may also be visualized on the surface of the specimen as well as in subsurface regions as presented by Maldague and Marinetti [MM96]. An example image of an investigation using thermography is shown in Figure 3d as presented by Amenabar et al. [AMLA*11]: The thermography of the specimen in Figure 3a was taken using transmissive, pulsed thermography and all five different defects could be detected. As outlined by the authors, no temperature differences between the different defect types could be observed as clues regarding their thickness and depth. Therefore, the different depths and thicknesses of the defects could not be distinguished.

Optical Coherence Tomography (OCT) utilizes light to provide cross-sectional tomographic images of the microstructures of materials under test. Just as echography does with sound, an OCT system measures backscattered and backreflected light to distinguish between different layers and structures in the specimen. The utilization of light improves the resolution compared to echography by 10-100 times but reduces the penetration depth down to $\frac{1}{10}$. OCTs main application area is found in biomedical imaging. Despite the aforementioned limitations and because it is a real-time high-resolution and non-destructive technique, OCT has also been utilized in materials science in recent years. Currently, there are two main sub-techniques: Time-domain OCT (TDOCT) and Fourier-domain OCT (FDOCT). For material investigation FDOCT is the more suited due to its improved detection capabilities as stated by Placet et al. [PMF*14]. For rendering OCT images, typically color coded 2D images are used and encode the strength of the backscattered signal. An example for OCT data is provided by Duncan et al. [DBR98] in Figure 4a where subsurface samples were taken in intervals of 10 μm to a depth of 140 μm and combined to produce a 3D visualization.

Scanning Electron Microscopy (SEM) uses an electron beam to scan the surface of a specimen in a specific pattern and in order to image the signals of the electrons hitting the specimens surface. SEM generates 2D scalar data, which are often colored to focus on features of interest. The data generated in the different types of SEMs may encode the signals on secondary electrons, reflected or back-scattered electrons, photons of characteristic X-rays or light (cathodoluminescence), absorbed current (specimen current) and transmitted electrons. SEM thus facilitates also a characterization regarding the chemical decomposition of the analyzed materials aside the structural analysis, so the surface morphology and the chemical properties of a specimen can be derived in detail. To further increase the resolution of the images and therefore to gain a better insight into the specimen of interest, transmission electron microscopy (TEM) is increasingly used as stated by Bender et al. [BDM*10]. Sanderson et al. [SLKL02] use SEM to investigate 2D plus time data on the fouling and cleaning process of membranes during filtration. They further correlate ultrasonic time domain reflectometry analysis with the fouling layer of a membrane. Figure 4b shows images gathered with SEM at different scales and different states of fouling. SEM is also used together with various material removal techniques such as micro-grinding, chemical etching, or focused ion beam (FIB), in order to destructively investigate a material of interest in 3D. For example in combination with chemical etching, SEM is utilized to generate complete 3D images of the specimen as described by Lanzagorta et al. [LKS*98]. Using these material removal techniques the sample is destroyed with the primary target to remove thin layers of the material and image the revealed cross section using SEM again in order to finally get a 3D representation of the specimen. In addition, also photogrametric methods are used in order to generate 3D representations of the surface of the specimen using a low number of images which show the specimens slightly tilted.

Terahertz Testing (THz) aside its prominent applications in airport security, THz is less known to be used in materials science. THz in 3D mainly covers the data acquisition using continuous-wave terahertz computed tomography in materials science. This technique has emerged because of its useful property to facilitate imaging of transparent objects. For several techniques such as 3D-XCT it is difficult to test samples with low attenuation inner structures, e.g. the inner structure of transparent materials as plastics, wood or paper, which is due to an increased noise level, preventing from robust analyses of the features of interest. Terahertz testing overcomes these limitations because of the low absorption and large penetration depths of the transmitted THz waves, which allows to increase the local contrast. This highly desirable property opens new ways for visual material analysis as well as new challenges for visualization as stated by Balacey et al. [BRP*16]. An example provided by Jansen et al. [JWP*10] evaluates drilled holes in a plastic samples (see Figure 4c). Regarding data, THz testing generates spectral data as well as scalar data, e.g., encoding intervals in the frequency domain.

Apart from the aforementioned methods for the analysis of material systems, for sure many other destructive and non destructive techniques are existing, which are actively used in materials science. For example, hyperspectral imaging is used for inspecting artifacts from geology and cultural heritage. To discuss all remaining techniques in detail would go beyond the scope of this paper. As the contributions using other techniques play a minor role in materials science or they are on the border to other research areas such as geology, or they currently make very limited or no use of visual computing supported materials study according to our findings, these techniques are considered as out of scope for this paper and therefore not discussed any further.

4.6. Data Types

An important categorization for visual computing in materials science is the characteristics of the input, output and derived data. Regarding the categorization we adapted the types as defined by Schneiderman [Shn96] for our domain. A similar categorization can also be found in Munzner's book "Visual Analysis and Design" [Mun14]. As 1-dimensional data is typically used for extracting quantitative derived data, e.g., the overall porosity or properties of a feature in the volume, for visual computing 1D data is therefore not extensively used and thus left out in the following consideration.

2-dimensional data types are represented by 2D spatial images of testing results in many papers, e.g., in Malzbender et al. [MSM13], who use 2D images of ceramic materials to investigate crack propagation, Galvin et al. [GGB01], who image and investigate surface strain of glass surfaces at a nanometer scale, or Tanaka et al. [TKH13] who analyze the behavior of hydrogen diffusion and desorption in duplex stainless steel and Fe-30% Ni alloys with visualizations of grain boundary diffusion. 2D data representations are also used as simulation results, e.g., encoding pressure in a glass pressing simulation [LTM01].

3-dimensional data is one of the mostly used data types in the visual computing supported materials science literature. The reason is found in the 3D nature of the specimens as well as their features. 3D data types are often derived and reconstructed from many 2D images. Placet et al. [PMF*14] for example applied multiple methods such as optical coherence tomography and focused ion beam to reconstruct 3D data. Focused ion beam together with scanning electron microscopy were used by Bender et al. [BDM*10] investigating milling strategies for the structural characterization of through silicon vias. In the work of Weber et al. [WRR*11], 3D reconstructions of synchrotron-based X-ray tomography data were used to investigate micropowder injection molding in order to optimize the molding process for achieving high dimensional accuracy. For ultrasonic testing Kitazawa et al. [KKB*09] proposed a method to gather 3D data from the specimen which based on phased array ultrasonic testing.

Temporal data allows to get an insight into ongoing processes of materials science. This time component may be very discrete, as it is the case in of Patterson et al. [PCH*15] work, where synchrotron X-ray tomographic imaging is used during the compression of polymeric materials. Their goal is to analyze the mechanical properties of materials, which are important for predicting lifetime performance, damage path-ways and stress recovery. Due to required relaxing phase of the material for up to 10 minutes, which is necessary as the residual motion of the material would blur the images, the data over time is highly discrete. In contrast to this example the data may also be continuous, which allows an interactive

real-time visualization of a simulation as presented by Laevsky et al. [LTM01]. They use a tool, that operates on data streams which are directly visualized. These data streams are fed in a fluid simulation to optimize the process of glass pressing. Data is of course still discrete as it is processed by a computer, but the notion of continuity comes from the fact, that it is visualize-able in real-time.

Multi-dimensional data in materials science often comes through the investigation of material properties from data generated using more than one testing method or by deriving additional data. Multi-dimensional data is used both in terms of material analysis or in simulations, where many different properties are computed. Ota et al. [OKTM05] are using 3D-XCT to measure flows induced by shock waves in tubes for computational fluid dynamics. They extract quantities such as velocity, density, pressure and temperature in order to investigate the flow in the underlying materials. An example for derived data can be found in the work of Bhimavarapu et al. [BMBN10], where stress, strain, strain rate and temperature are obtained, combined and derived by various testing techniques for the for the investigation of alloys.

Trees and tree structures are at the moment rarely used for solving problems in materials science applications. Whereas simulation tools are frequently using trees to setup the scenery of the spatial domain, we encountered only a single usage of trees in the area of analyzing segmentation ensembles. Fröhler et al. [FMH16] are using trees as basis for clustering and navigating through similar segmentation masks. The tree in their application helps to structure the segmented datasets and to stepwise explore deeper layers of similar segmentation masks.

Networks inside materials are often of interest as means of abstraction for complex linked features (e.g., open pore networks) or as rendering in the spatial domain (e.g., closed foam networks). Due to the intrinsic nature of the specimens, those the networks influence the specimen's mechanical characteristics. Networks are typically not explicitly given but need to be derived via visual computing methods. Ushizima et al. [UMW*12] uses synchrotron X-ray computed microtomography as well as geometric and topological descriptors to derive pore networks and pore microstructures for estimating the permeability of porous media. In their work pore networks are represented by a graph, in which edges define the possible flow inside the material. These edges are assigned with a weight and augmented with their connectivity to the top of the stack, so that no flow is present in dead-end edges. Rey et al. [RMF07] represents a new node-nested Galerkin multigrid method for metal forging simulations. This method operates on 3D meshes, which are represented as networks, where nodes define the points in space and are assigned with properties such as pressure or velocity. The edges of the graph are used to define how the points of the network are spatially connected. The relationship of the nodes in space is of interest as the individual nodes can interact better with each other and overall material properties can be defined.

4.7. Visual Representations in Visual Computing supported Materials Analysis

In this section, we describe our findings concerning visualization techniques and visual metaphors used in the domain of visual computing for materials science. With regard to the tasks as discussed
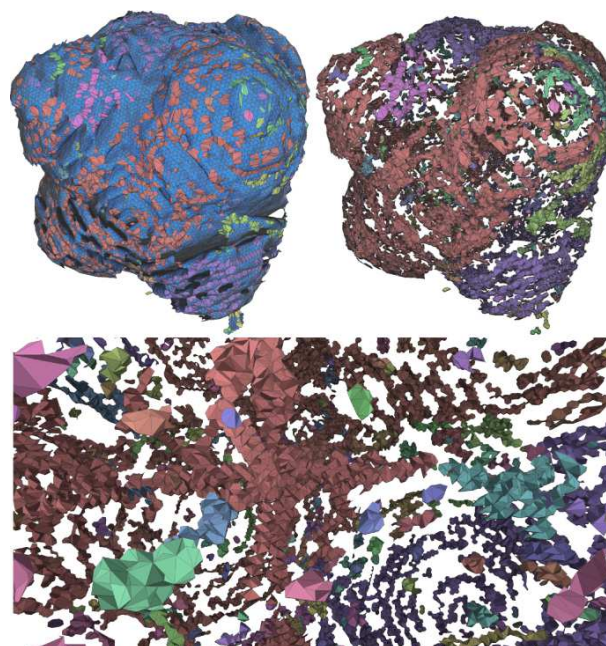

Figure 5: *Visualization of nanosphere atom rings in simulated graphite nanosphere battery materials showing blocking and non-blocking patches. Motion of lithium is controlled by the arrangement of carbon rings: while 6-member rings block lithium diffusion (top left: rings with valence of six or less clustered near the exterior), higher valence rings permit it (top right, bottom). ©2016 IEEE. Reprinted, with permission, from [GKLW16].*

in section 4.4, as well as the discussion of the data generated and derived, we subdivide the visualization techniques and visual metaphors in the following categories with respect to the domain, their respective analysis task is targeted on:

Visual Representations for Spatial Data are inherently bound to nature of the spatial domain the specimens of interest exist in. Many of such visualization and visual analysis techniques are thus found in the areas of simulating material systems as well as material analysis. Gyulassy et al. [GKLW16] use spatial visualizations of large-scale molecular dynamic simulations for evaluating simulated graphite nanosphere battery materials. The authors study the diffusion characteristics of (lithium) ions or other diffusers by employing a topological analysis of the distance function of carbon rings, and construct explicit triangulations to represent the carbon rings in the material. The carbon rings are classified as blocking or non-blocking and visualized using color coding (see Figure 5). The blue patches are part of rings with a valance of six or less, which are blocking the diffusion, while all the other patches are of rings with valance between seven and ten permitting diffusion. These patches are clustered along the exterior or along the principal axes. This allows to focus on the defects and to derive scientific findings such as, defect rings are occurring in neighbourhood of other defect rings, as there are many large components of defect patches. Further applications of simulation in combination with spatial data is found in the estimation of the permeability of porous media as presented

by Ushizma et al. [UMW*12] who provided augmented topological descriptors for analyzing pore networks. They presented 3D visualization techniques for analyzing pockets and extracting flow graphs in simulated and real world datasets of materials science. Malik et al. [MHG09] utilize techniques adapted from 2D graphical representations such as box-plots and transfer them to the 3D domain, e.g., as overlays over a spatial visualization or in a magic lense showing regions of interest. This concept yields the visualization of quantitative data to compare datasets, in their case a CAD model of the specimen with a volumetric dataset scanned by 3D-XCT. Overlays of boxplots can be used to compare data sets visually and to provide a fast overview. The main purpose of this technique is thus found in variance comparison as well as in monitoring production tolerances. Such tools are not only used in comparative visualization, but also for the investigation of the deterioration risk of mural paintings. Li et al. [LZS16] use an overlay technique based on glyphs for risk analysis of ancient frescoes. The glyphs are used to visualize the risk type, risk area size, the position and orientation of the risk area. The generated panorama view of the object, for which the corresponding risks should be determined, help the domain specialists to semi-automatically get a comprehensive view of the object. Furthermore, Wu et al. [WT10] are using overlays to visualize the simulated curvature flow (planar geometric heat flow) in materials science applications on a triangulated surface of a planar geometric object. The specific application areas mentioned in this work are found in physical simulations and materials science, where the flow plays an important role for the topology-adaptive front propagation with a curvature-dependent speed. As seen in the previous approaches, often additional information in spatial visualization is color encoded on the features of interest. Allerstorfer et al. [AHKG10] use transfer function based color-coding and opacity mapping to visualize the uncertainty of surfaces and interfaces of materials scanned with 3D-XCT data. More uncertain regions are rendered more transparently. They also apply color coded isolines as an overlay to visualize uncertainty inside the specimen. Labeling in hyperspectral imagery to distinguish between different materials in 3D is presented by Kim et al. [KHK*12]. Hyperspectral imaging is used for inspecting artifacts from geology and cultural heritage. The data is visualized in three dimensions labeling different materials with different spectra and therefore different properties. Such an encoding easily allows the investigation of the material's distribution in a specimen. Function plots such as power dissipation maps and instability maps are used by Bhimavarapu et al. [BMBN10] for the Al 2024 alloy, in order to encode the efficiency and the instability in 3D space of temperature, as well as the strain rate and strain in process maps. With this type of visualization the complete deformation behavior of a specimen can be visualized at once as the relation between a varying strain and the efficiency or the instability is shown. Takatsubo et al. [TWM*08] uses laser ultrasonic testing for visualizing the propagation of ultrasonic waves on a 3D specimen in order to gain insight into defects as well as their position: If scattering of the waves is observed, some irregularity is contained in the specimen. An experienced practitioner gains the required information on the defect from the wave propagation images. To support the visual inspection, post-processing is often applied to these images. For example, a maximum amplitude image is generated to view slits in a specimen. Such techniques are especially useful, if the testing method only supplies 2D images of a 3D object in order
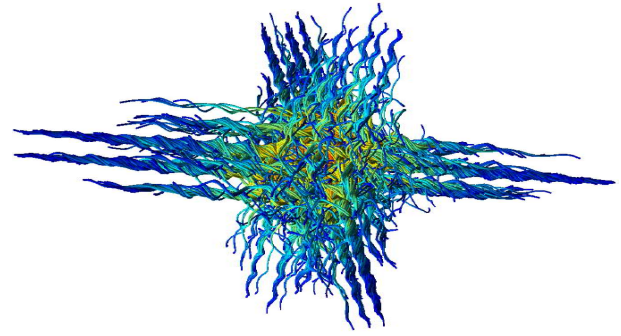

Figure 6: *Particle movement visualized as continuous path lines illustrating the structure of the flow of the Arnold-Beltrami-Childress moloecular dynamics dataset. Particle sites move smoothly over time as rendered in the path lines.* ©*2011 IEEE. Reprinted, with permission, from [FSG*11].*

to form a 3D mental model of the specimen, e.g. 2D visualizations of surfaces which are not smooth or planar.

Visual Representations for Spatiotemporal Data target to explore the temporal domain in the context of spatial data. Spatiotemporal data analysis in materials science is catching increasingly attention as the respective methods for data acquisition and processing allow for comprehensive studies gaining new, previously impossible insights. In the domain of simulation, visualization techniques are used to show the change of material systems in use within their target application. Earlier approaches as presented by Leavsky et al. [LTM01] are interactively visualizing deformation simulations. The primary target is to visualize the deformation of glass over time under the effect of heat in order to optimize glass pressing. The visual metaphors used are found in 3D animations showing the change of form of the glass materials as well as 2D animations encoding the glass velocity magnitude and the pressure in a slice of interest. In the work of Frey et al. [FSG*11] complex particle simulations are visualized by clustering in Voronoi diagrams. They reduce the visual clutter of a huge amount of simulated particles, keeping the information of particle distribution and geometric structure. To visualize the change over time for the particles, the authors use animations and visualize calculated path lines for small subsets of particles (see Figure 6). Besides lower memory consumption and less visual clutter, this approach improves rendering performance and allows for a more comprehensive view of the simulation. Spatiotemporal data visualization also integrates analyses of dynamic processes, i.e., ongoing processes, which are evaluated over time, under load or under changing environmental conditions. In order to analyze these kind of dynamic processes using (interrupted) insitu testing, most of approaches are using spatiotemporal data (i.e., 2D or 3D spatial image data plus time as additional dimension). An approach exploring dynamic heating/cooling processes of metal composites as well as drying processes of wood was presented by Reh et al. [RAK*15]. The authors introduced Fuzzy Tracking Graphs, which allow to follow the creation, continuation, split, merge and dissipation of features in a graph based representation as they evolve during the ongoing process. In an Event Explorer the extracted features of each step of the (interrupted) in-

situ test may be further investigated regarding the individual feature properties at a timestep of interest. Another example for 2D porosity investigation was developed by Tran et al. [TDD*12]. In their work, the mechanical properties of wood fiber networks are investigated using loading tests and XCT imaging in order to visualize strain over time. Using heat maps visualizing the normalized strain field, they superimpose additional information on 2D slice images, showing the local thickness of pores in the wood network, in order visually inspect the mechanical behavior and the correlations between the presence of wood, the porosity of wood, as well as strain. Further approaches generate lists of 3D spatial visualizations at key events. Key events may denote the introduction of cracks in the specimen, a maximum deformation or just at some given points in time to gain an insight into the process. Patterson et al. [PCH*15] visualize and investigate cellular materials under strain with in-situ X-ray synchroton tomography to get the mechanical properties of the material, which are important for predicting lifetime performance, damage path-ways and stress recovery. In order to explore the damage mechanisms in composite materials such as glass fiber reinforced polymers under increasing load Amirkhanov et al. [AAS*16] presented a tool for the analysis of 4D-XCT data. Aside the extraction and classification of the corresponding defects in each step of the insitu test into matrix fractures, fiber/matrix debondings, fiber pull-outs, and fiber fractures, various exploration techniques are proposed to highlight the defect regions in context of the XCT data. For example, Defect Density Maps serve as overview of the defect distributions in 2D and 3D as well as for visualizing the final fracture region, which is not explicitly given but more an estimation based on the extracted defects in the region. Another technique presented by Malik et al. [MHG10] allows to study the evolution of ongoing processes as well as ensembles of XCT data for performing parameter studies using comparative visualization techniques. Extending the idea of the checker board visualization, rendering the first dataset on the black tiles and the second dataset on white tiles, the authors propose space filling hexagons as basis for their 2D multi image view. The hexagons show a circle in the middle encoding the reference dataset. Around this circle the hexagon is divided into multiple sectors, showing all other datasets in comparison. For the comparison, the encoding may be switched from greyscale images (original data), to differences in greyvalues encoded in color, to homogeneity of the considered region as binary image. In microscopy it is often required to view the microstructure of a surface from slightly different perspectives. Since microscopes produce only orthographic images several additional steps are needed to get perspective images. Levoy et al. [LNA*06] propose a method to achieve this goal. By inserting an array of microlenses into the train of a common microscope, so that they can capture light fields, a perspective visualization may be computed in real-time. The gathered data can also be used to compute images with varying focus, so that the microstructure of the surface may be investigated in detail.

Visual Representations for Quantitative and Derived Data are required to provide additional insights into data, which may not be obvious in the spatial or spatialtemporal domain only. Methods in this area cover a large number of domains ranging from feature quantification, geometrical tolerancing, to network analyses. Therefore, examples for this category can be found both in ma-

terial simulation and material analysis. In the domain of material simulation Zobel et al. [ZSS15] propose a tool for domain specialists to verify, if and where the design of a new fiber reinforced polymer component might fail in order to improve it in additional design loops. The authors are using feature based tensor visualization to evaluate simulations of respective fiber reinforced polymer samples for virtual prototyping. Their tool presents simple and efficient overviews of the stress and strain in the complete object and introduces a new type of glyph encoding the desired fiber directions and the fiber orientation tensor. These glyphs are based on superquadrics encoding the orientations of the fibers. Furthermore, the tool indicates if the fiber orientation may cause failures using colors. Finally, the admissible fiber directions at specific regions of the specimen may be shown in the data. Quantitative data analysis of features in materials are of increasing interest. A tool facilitating the quantitative analysis of fibers in XCT scans of fiber reinforced materials was presented by Weissenböck et al. [WAL*14]. After extracting quantitative information on the fibers (e.g., length, orientation, start and endpoint) the authors are using parallel coordinates as well as a scatter plot matrix for the exploring and clustering fibers based on their characteristics. In order to ensure the maximal possible flexibility in terms of exploration and visual analysis, all views are linked with each other as well as with the representation in the spatial domain. Fritz et al. [FHG*09] and Westenberger et al. [WEL12] also evaluated fibers in XCT scans of fiber reinforced materials. After extracting each fiber and quantifying the fibers regarding their orientation in space, these approaches are using a sphere or a hemisphere as visual metaphor to encode fiber orientation distributions of fiber reinforced materials: The sphere/hemisphere allows the mapping of the orientations of the straight fibers as angles on the sphere/hemisphere. Exploiting symmetry of the orientations facilitates the simplification of the visualization from a sphere to a hemisphere, which is then azimuthal projected on a 2D plane. This is a demonstrative and innovative visualization for fiber orientation distributions as it avoids visual clutter, which direct volume rendering of the fibers would introduce. Network visualizations were also adapted for use in materials science, e.g., for the analysis of rocks as presented by Grau et al. [GVTA10]. In the spatial domain, it is often hard to determine, which nodes are near and which are far to the viewer. To solve these problems, a size may be assigned to the knots to render them smaller if they are far away. This is not always possible, as the knots are typically extended with derived properties such as pore volume etc. of the material. To solve this issue, color-coding with a legend is used to encode depth. Color-coding of the nodes can also be used to provide information about the distances removed, e.g., from a selected node, or to visualize which nodes are connected to a node. The authors use their network visualization technique to solve domain specific tasks such as finding the shortest path between two pores (see Figure 7). In the left image out-of-scope pores are ghosting. In the middle image these pores are cut away and the maximum distance is longer. In the right picture an opacity attenuation in relation to the distance is used. This also allows simulation of fluid extrusions or intrusions through the structure and therefore the visualization has an additional benefit. Another example of the utilization of network visualizations is given by Gyulassy et al. [GDN*07] regarding the simulation and visualization of porous solids hit by a projectile. Graph based visualization techniques are used by Reh et al. [RAK*15]. The authors
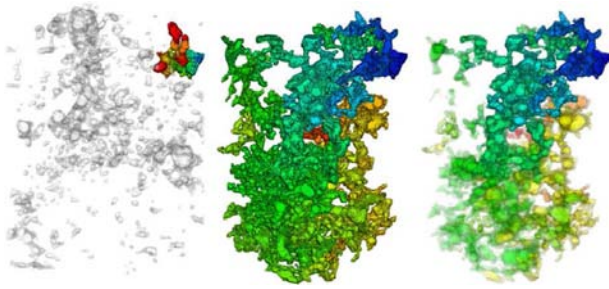
Figure 7: *Analysis of pore connectivity inside a rock. Left image: Selection of pores with distance 9, pores out of focus are ghosting. Middle image: Pores with a longer maximum distance, removing out of focus pores. Right image: Opacity of the pores encodes the distance from the selected cluster. Reprinted from [GVTA10], with permission from Elsevier.*

introduced Fuzzy Tracking Graphs visualize the evolution of features and corresponding events over time. This representative example of how complex processes can be simplified using 2D visualization techniques ensures a fast and comprehensive visual analysis for practitioners. Wireframe visualizations are used by Wang et al. [WNG06] in order to derive and visualize cloud-like structures, such as plasmapauses (boundary of a plasmasphere), from large image data, which are in motion and deforming governed by magnetic field properties. Aside being cheap to render, wireframes as visual metaphor allow to intuitively follow the structure in motion, which is only reasonable if a perspective rendering is used or if front- and backfaces are easily discernible. In addition, also the 3D visualization of derived functions are important in materials science: Data aggregations are used by Reh et al. [RGK*13] for computing MObjects, which are introduced as the mean object of a large number of features of interest such as pores, cracks, particles, voids or fibers in the data. The authors compute these mean objects in order to integrate them as precise average structures for finite element simulation purposes. Their approach is to first segment the features of interest, align them according to their center of gravity, aggregate all pore voxels and normalize all voxels in the created mean object to 1. The normalization to 1 allows for an interpretation the mean object's data as the voxels' probability of belonging to the mean object, which the authors denote as uncertainty cloud (see Figure 1).

For quantitative visualization also simpler 2D visualization techniques such as charts, plots, scatterplots, histograms etc., are widely used in materials science used for understanding complex data. As a large number of papers is building on these simpler visualization techniques, we only indicate the following examples: Bhimavarapu et al. [BMBN10] in their approach analyzing the compressive deformation behavior of the Al 2024 alloy are using function plots with level lines to visualize extracted strain rates and flow strain in relation. Froehler et al. [FMH16] use histograms as supportive techniques to explore the frequency of the parameters and derived outputs used in segmentation pipelines in materials science. As the histograms are linked to filter sliders, a quick exploration of the data will be facilitated.

4.8. Interaction Techniques

As a result of the increasing complexity of data in materials science as well as the growing demands regarding their analysis, especially passive visualizations techniques have reached their limits. For that reason interactive visualization methods are increasingly utilized to support the visual analysis process in materials sciences. For several challenges, even interactive steering is employed to influence the data generation process. We thus reviewed and analyzed the interaction techniques used in visual computing supported materials science and present our results in the following sections. Regarding the categorization of the interaction techniques we first used the categorization as proposed Yi et al. [YaKSJ07]. When coding the interaction techniques from our set of relevant literature, it turned out that this categorization was in some terms is too coarse and in others too fine grained for visual computing in materials science. As consequence, we focus in our review on those interaction techniques, which are highly relevant in visual computing based materials science and combine the proposed categories from Yi et al. [YaKSJ07] with those described by Kosara et al. [KHG03]:

Explore and Reconfigure addresses the three basic interaction techniques of translating, rotating and zooming into data, which are used in materials science for spatial, spatiotemporal and quantitative and derived data visual analysis approaches as well as interactive steering. All three basic interaction techniques fit in the category 'Explore' as defined in Yi's classification while Translate and rotate may also be categorized as 'Reconfigure'. 'Zoom', especially a semantic zoom, fits in the category of 'Abstract/Elaborate'. Despite the different approaches regarding categorization, the three basic interaction techniques of translate, rotate and zoom are frequently used in visualization systems. Especially, in the exploration and analysis of spatial data, these interaction techniques often appear in literature of visual computing supported materials science as they are easy to implement but provide huge benefits in data exploration. For example, Zobel et al. [ZSS15] use translation, rotation and zoom in order to explore, if and where the design of a new fiber reinforced polymer component might fail.

Linking and Brushing is using multiple views showing different aspects of the same data, which are connected (linked with each other) in order to interactively manipulate them all together. The term brushing refers to the categories 'Select' and 'Filter' and the term linking to the category 'Connect' from Yi's classification. Either in a single view or in all views, items may be selected, rotated, translated, zoomed, filtered by text, using sliders or other ways. As all views are linked, all views will be updated automatically once a change occurred in one of the views in order to show the selected data in context. In their Porosity Analyzer tool for the evaluation of the segmentation pipelines Weissenböck et al. [WAG*16] combined scatterplot matrices encoding the characteristics of pores with 3D spatial views of the data. With the scatter plot matrix, the masks as generated by the corresponding segmentation pipelines are evaluated regarding their input and output parameters. Results of individual segmentation-pipeline runs are selected by brushing in the corresponding scatter plot and linked to 2D slice views and 3D renderings of aggregated segmentation masks and statistical contour renderings. Qian et al. [QSCZ16] use linking and brushing to support conservators and site managers in the deterioration

risk assessment of cultural heritage. Their approach allows brushing of exogenous factors such as humidity, light, or wind, as well as endogenous factors which cause deterioration. The brushed characteristics are displayed with linked box plots, scatter plots and other charts in order to provide an overview graph for decision making in a visual analysis process.

Focus Plus Context as defined in Kosara's classification helps to visualize large data sets, which cannot be displayed or rendered at once and as a whole. In a visualization system using focus plus context, the users select a subset of data and put the focus on the analysis on this subset. The subset is then displayed in more detail and providing additional visual metaphors, e.g., rendering derived data. As context information, the complete data set is typically provided out of focus, e.g., abstracting or reducing details. There are different methods to achieve this effect. For example, the data around the focus can be geometrically distorted. Li et al. [LZS16] uses focus plus context to provide users with details (focus) and an overview as a heat map (context) describing the spatial distribution of the overall disruption risk for the deterioration risk assessment of ancient frescoes. Various applications of this technique are seen in the method of Grau et al. [GVTA10] supporting the exploration of porous structures using illustrative visualization. In their proposed graph based visualization of porous media, the user can select individual pores by clicking or within a given radius, as well as pores not reachable from the outside, at the boundary or the surface of a given model. This selection defines the focus. All other pores and the solid around those pores are rendered as context information. In their application the selected pores are rendered opaque and highlighted with color, while context pores as well as the solid material are rendered using a ghosting effect. To overcome the problem that context pores and solid overlap focus pores, they use in addition a cut-away technique for interfering pores and solid areas, which allows full focus but reduces the context in the viewing direction.

Filter is defined in both Yi's classification Kosara's classification and describes the process of searching in a data set in order to reduce the displayed data. This can be achieved via free text forms, in cases of textual or derived data sets. Another approach makes use of sliders to find all values, which feature a property of a specific range. In the workflow introduced by Fritz et al. [FHG*09] the user can filter fibers of a fiber reinforced material by their angles and other characteristics. This way, only fibers within the filter range are visible for the evaluation. Qian et al. [QSCZ16] implemented filtering as drop-down menues for constraining areas of interest, endogenous risk factors, and exogenous factors. This filtering techniques can be combined to for refinements, which demonstrates another option using filters. A combination of multiple filter types allows for an advanced interactive search facilitating complex and interactive queries.

Aside these interaction techniques also other techniques are used in visual computing for materials science such as 'Abstract/Elaborate' in the form of glyphs as in the method presented by Zobel et al. [ZSS15] or 'Reconfigure', as presented by Reh et al. [RPK*12] to identify suitable viewing angles. As these interaction techniques play a minor role in the current body of literature, they are not considered any further in this report.

4.9. Interactive Steering

Interactive steering makes use of visual representations of spatial, spatiotemporal data as well as from representations of quantitative and derived data. It also employs the interaction techniques as explained in Section 4.8. As interactive steering is considered in materials science to achieve the most benefits for a materials science problem, we also review this area from the materials science perspective: At the moment interactive steering of complex simulation and analysis techniques is a still a sparsely used method. However, in the presented approaches it already allows to generate huge benefits in materials science. Interactive Steering adjusts parameters of the data acquisition process while the acquisition process is still ongoing. It provides means to review intermediate results and uses the extracted insights in order to steer the data acquisition process using the results determined. This principle helps to explore complex phenomenons without the need of computationally expensive determination of the phenomenon's complete parameter space. Interactive steering shows the advantage, that long running simulations may be corrected and steered if they generate suboptimal results. The advantages however are overshadowed by the fact, that the corresponding data acquisition is costly and thus the interaction may end up in a tedious process. The tool of Laevsky et al. [LTM01] employs a visual steering system combining distributed computation and visualization of glass pressing simulations. The authors provide a tool enabling users to control the underlying simulation. Intermediate visualization results, such as 2D colorcoded renderings of the pressure in the form, act as a steering and visualisation front-end in order to derive parameters for a new simulation run. The interaction with the simulation is facilitated using a graphical network visualization of the dataflow. The corresponding modules in the network process data streams and represent functions such as the computation of gradients or the iso-surface extraction. Each module features its own parameters, which can be manipulated using GUI elements. The results can be visualized in 2D or 3D animations, in order to allow an interactive exploration of the simulation. Another very different approach is presented by Martin et al. [MTGG11] for performing deformation simulations with example-based materials. In their approach, the user applies pressure and strain on simulations of flexible materials. For example, a gummy bear is pressed with a spoon and the deformation may be followed interactively. The materials are represented using surface models. This allows users to adapt the underlying material parameters according to the visualized deformation. Despite this work being primarily focused on the creation of art, the authors also explain secondary applications in the domain of materials science regarding the design of new materials. Such techniques may accelerate the creation of new materials and support material scientists in their daily work.

5. Challenges for Future Work

Though a whole body of work is already found in visual analysis for materials science, there are much larger challenges to be solved in future. We combined our findings with the results of a discussion round on the topic of visual analysis for materials sciences, which took place between specialists from the domains of visual analysis, visualization, non destructive testing and materials science at a recent workshop. To solve these challenges, new collaborations and

projects are strongly encouraged, integrating end users from materials science, specialists in materials analysis and experts in visualization and visual analysis, in order to boost visual computing supported materials science. Our findings are summarized below, separated into high and low level challenges:

5.1. High Level Challenges

Regarding high level challenges, the tasks to be solved, which are of imminent need, are found in the following points:

- *The Integrated Visual Analysis Challenge* was identified as standard visualization tools are not enough to explore the generated materials science data in detail. What is required are integrated visual analysis tools, which are tailored to a specific application area of interest and which guide users in their investigations. Using linked views and other interaction concepts these tools are required to combine all data domains using meaningful and easy to understand visualization techniques. Especially for the analysis of dynamic processes, where spatial and temporal data are evaluated, e.g., when materials are being tested under load or in different environmental conditions, these kind of tools are highly anticipated. Only this concept allows to make the most out of all the data available.
- *The Quantitative Data Visualization Challenge* centers around the design and implementation of tailored visual analysis systems for extracting and analyzing derived data, e.g., as computed from extracted features over spatial, temporal or even higher dimensional data domains. Therefore, feature extraction techniques, e.g., for the extraction of flow paths through porous media, segmentation techniques, e.g., for the extraction of voids in the data, and even clustering techniques, e.g., for finding interesting feature classes, are required as prerequisites for the targeted visual analysis. As the quantification may easily end up in 25 or more properties, which are computed per feature, clustering techniques allow to distinguish the features of interest into feature classes. These feature classes may then be statistically evaluated in order to visualize the properties of the individual features as well as the properties of the different classes. Particularly, techniques from information visualization will be of interest for solving this challenge.
- *The Visual Debugger Challenge* is an idea, which uses visual analysis to remove errors in the parametrization of a simulation or a data acquisition process, in order to finally improve results. Similarly to a debugger in computer programming, which tests and identifies errors in the code and which provides hints to improve the code, a visual debugger in visual computing for materials science should show the following characteristics: It should indicate errors and identify wrongly used algorithms in the analysis. Such a tool should also identify wrongly used and incorrect parameters, which either show no or very limited benefit or provide erroneous final results. Furthermore, it should give directions on how to improve a targeted analysis and suggest suitable algorithms or pipelines for specific tasks.
- *The Interactive Steering Challenge* uses visual analysis tools to steer ongoing simulation or data acquisition systems. In this challenge, a visual analysis system should monitor a costly process and give directions in order to continuously refine its results. The main goal here is to find a reasonable solution to the problem of interest. For example, in the material analysis domain this could be a system, which provides settings for data acquisition based on the image quality achieved. If the image quality no more fulfills the target requirements, the system influences all degrees of freedom in the data acquisition in order to enhance image quality again. The same holds for the materials simulation domain. Visual analysis can help to steer target material properties in a specific application environment by predicting tendencies of costly simulation runs, e.g., using cheaper surrogate models.

5.2. Low Level Challenges

Whereas the previous section focused on specific visual analysis challenges in materials science, the following points outline more general challenges of the domain, which will help to drive collaborations as well as research in the respective areas:

- *The Common Data Repository Challenge* came up in discussions between the communities of visual analysis, visualization, non destructive testing as well as materials science, as typically the generated data is proprietary for specific end users, who do not want to share corporate secrets with competitors. Therefore, an archive of disclosed data should be created similar to the "digimorph project" (www.digimorph.org), a dynamic archive on high-resolution XCT data of biological specimens. This materials science archive should contain spatial data, spatiotemporal data as well as derived data together with descriptions of the sample as well as the analysis task.
- *The Visual Analysis Consulting Challenge* is a request of material testing and simulation specialists, who would like to provide their end users in materials science with visual analysis methods and contacts in order to solve their problems. On their daily routines, typically they can not do so, as their services end with providing the data required. Therefore, consulting services, software frameworks and methods would be required, which allow the end users of materials science to make most out of their data.

6. Conclusions

In this work we have presented the state of the art regarding visual computing for materials science. This is the first concise overview on the current state of research activities within this emerging field. After reviewing the definition of materials sciences and material systems exploiting visual computing, we analyzed the high level visual computing, visual analysis and visualization tasks for materials sciences, as well as testing techniques which are providing the data for the respective analyses. We reviewed the data characteristics as well as visualization techniques and visual metaphors used as well as the interaction concepts employed. Our review showed that about the half of all relevant literature still uses mainly passive visualization techniques. In these approaches of materials science using visual computing, simple visualization techniques as the plain output of the measured raw data or the extraction of a plot, a histogram, or even a binary value are sufficient to answer a number of problems in materials science, e.g., whether the material system is qualified for a specific application. Interactive visualization becomes a requirement if the input data dimensionality is or exceeds 2D. If input data is 3D, interactive techniques are required to

explore the data in detail. For higher dataset dimensions, e.g., the exploration of derived values, the used interaction concepts influence the quality of the data exploration results in materials science. Interactive visual steering of costly data evaluation or simulation is required by materials science in the sense of visual debuggers. These visual debuggers should support domain specialists regarding data acquisition as well as simulation processes. At the moment, despite returning the maximal benefits, these kind of systems are rarely seen. We finally concluded our report with the identification of open research challenges based in our observation results in order to guide future research endeavors in this area. We hope that our work will be the basis to establish further fruitful collaboration across the domains in order to boost research in all materials science domains as well as in visual analysis and visualization.

Acknowledgements

References

[AAS*16] AMIRKHANOV A., AMIRKHANOV A., SALABERGER D., KASTNER J., GRÖLLER M. E., HEINZL C.: Visual analysis of defects in glass fiber reinforced polymers for 4DCT interrupted in situ tests. Computer Graphics Forum 35, 3 (2016), 201–210. 7, 14

[AGM*08] ALGERNON D., GRÄFE B., MIELENTZ F., KÖHLER B., SCHUBERT F.: Imaging of the elastic wave propagation in concrete using scanning techniques: Application for impact-echo and ultrasonic echo methods. J. of Nondestructive Evaluation 27, 1 (2008), 83–97. 4

[AHK*13] AMIRKHANOV A., HEINZL C., KUHN C., KASTNER J., GRÖLLER M. E.: Fuzzy CT metrology: Dimensional measurements on uncertain data. In Spring Conference on Computer Graphics (2013), pp. 81–90. 8

[AHKG10] ALLERSTORFER M., HEINZL C., KASTNER J., GRÖLLER E.: Uncertainty visualization of computed tomography datasets from complex components using statistical analysis. In European Conference on Nondestructive Testing (2010), pp. 1–8. 13

[AHR*11] AMIRKHANOV A., HEINZL C., REITER M., KASTNER J., GRÖLLER E.: Projection-based metal-artifact reduction for industrial 3D X-ray computed tomography. IEEE Trans. Visualization and Computer Graphics 17, 12 (2011), 2193–2202. 8, 9

[AHRG10] AMIRKHANOV A., HEINZL C., REITER M., GRÖLLER E.: Visual optimality and stability analysis of 3DCT scan positions. IEEE Trans. Visualization and Computer Graphics 16, 6 (2010), 1477–1486. 9

[AMA*14] ALSALLAKH B., MICALLEF L., AIGNER W., HAUSER H., MIKSCH S., RODGERS P.: Visualizing Sets and Set-typed Data: State-of-the-Art and Future Challenges. In EuroVis - STARs (2014), Borgo R., Maciejewski R., Viola I., (Eds.), The Eurographics Association, pp. 1–21. 2

[AMLA*11] AMENABAR I., MENDIKUTE A., LÓPEZ-ARRAIZA A., LIZARANZU M., AURREKOETXEA J.: Comparison and analysis of non-destructive testing techniques suitable for delamination inspection in wind turbine blades. Composites Part B: Engineering 42, 5 (2011), 1298–1305. 9, 10

[BDM*10] BENDER H., DRIJBOOMS C., MARCKE P., GEYPEN J., PHILIPSEN H. G. G., RADISIC A.: Structural characterization of through silicon vias. J. of Materials Science 47, 18 (2010), 6497–6504. 11

[BHA*15] BHATTACHARYA A., HEINZL C., AMIRKHANOV A., KASTNER J., WENGER R.: MetaTracts - a method for robust extraction and visualization of carbon fiber bundles in fiber reinforced composites. In IEEE Pacific Visualization Symposium (2015), pp. 191–198. 1, 4

[BHP15] BEYER J., HADWIGER M., PFISTER H.: State-of-the-art in GPU-based large-scale volume visualization. Computer Graphics Forum 34, 8 (2015), 13–37. 2

[BKA*11] BIMBER O., KLOECK D., AMANO T., GRUNDHOEFER A., KURZ D.: Closed-loop feedback illumination for optical inverse tone-mapping in light microscopy. IEEE Trans. Visualization and Computer Graphics 17, 6 (2011), 857–870. 4, 8

[BMBN10] BHIMAVARAPU S. B., MAHESHWARI A. K., BHARGAVA D., NARAYAN S. P.: Compressive deformation behavior of Al 2024 alloy using 2D and 4D processing maps. J. of Materials Science 46, 9 (2010), 3191–3199. 4, 12, 13, 15

[BRP*16] BALACEY H., RECUR B., PERRAUD J. B., SLEIMAN J. B., GUILLET J. P., MOUNAIX P.: Advanced processing sequence for 3D THz imaging. IEEE Trans. Terahertz Science and Technology 6, 2 (2016), 191–198. 11

[BSL*12] BOCK A., SUNDEN E., LIU B., WUNSCHE B., ROPINSKI T.: Coherency-based curve compression for high-order finite element model visualization. IEEE Trans. Visualization and Computer Graphics 18, 12 (2012), 2315–2324. 6

[CHSW08] CICCHIANI J., HARTMULLER T., SELL C., WRIGHT R.: Fault detection and visualization through micron-resolution X-ray imaging. In IEEE AUTOTESTCON (2008), pp. 330–335. 6, 8

[DBR98] DUNCAN M., BASHKANSKY M., REINTJES J.: Subsurface defect detection in materialsusing optical coherence tomography. Opt. Express 2, 13 (1998), 540–545. 10

[FH08] FISHER R. F., HINTENLANG D. E.: Micro-CT imaging of MEMS components. J. of Nondestructive Evaluation 27, 4 (2008), 115–125. 6

[FHG*09] FRITZ L., HADWIGER M., GEIER G., PITTINO G., GRÖLLER E.: A visual approach to efficient analysis and quantification of ductile iron and reinforced sprayed concrete. IEEE Trans. Visualization and Computer Graphics 15, 6 (2009), 1343–1350. 4, 6, 14, 16

[FMH16] FRÖHLER B., MÖLLER T., HEINZL C.: Gemse: Visualization-guided exploration of multi-channel segmentation algorithms. Computer Graphics Forum 35, 3 (2016), 191–200. 12, 15

[FMHH14] FLESSNER M., MÜLLER A., HELMECKE E., HAUSOTTE T.: Evaluating and visualizing the quality of surface points determined from computed tomography volume data. In MacroScale 2014 - Recent developments in traceable dimensional measurements (2014), pp. 1–8. 9

[FMHH15] FLESSNER M., MÜLLER A., HELMECKE E., HAUSOTTE T.: Automated detection of artefacts for computed tomography in dimensional metrology. In Digital Industrial Radiology and Computed Tomography (2015), pp. 1–8. 8

[FSG*11] FREY S., SCHLÖMER T., GROTTEL S., DACHSBACHER C., DEUSSEN O., ERTL T.: Loose capacity-constrained representatives for the qualitative visual analysis in molecular dynamics. In IEEE Pacific Visualization Symposium (2011), pp. 51–58. 7, 13

[GDN*07] GYULASSY A., DUCHAINEAU M., NATARAJAN V., PASCUCCI V., BRINGA E., HIGGINBOTHAM A., HAMANN B.: Topologically clean distance fields. IEEE Trans. Visualization and Computer Graphics 13, 6 (2007), 1432–1439. 7, 14

[GGB01] GALVIN S. P., GRIFFIN B. J., BROWNE J.: Imaging of surface strain and polishing artefacts in fused silica by environmental scanning electron microscopy. J. of Materials Science 36, 23 (2001), 5683–5696. 4, 11

[GKLW16] GYULASSY A., KNOLL A., LAU C., WANG B.: Interstitial and interlayer ion diffusion geometry extraction in graphitic nanosphere battery materials. IEEE Trans. Visualization and Computer Graphics 22, 1 (2016), 916–925. 1, 7, 8, 12

[GRKK14] GUSENBAUER C., REITER M., KASTNER J., KLOESCH G.: Detection of non-metallic inclusions in steel by X-ray computed tomography and after fatigue testing. In European Conference on Nondestructive Testing (2014), pp. 1–10. 7

[GVTA10] GRAU S., VERGÉS E., TOST D., AYALA D.: Exploration of porous structures with illustrative visualizations. Computers & Graphics 34, 4 (2010), 398–408. Procedural Methods in Computer GraphicsIllustrative Visualization. 14, 15, 16

[HGF14] HAM Y., GOLPARVAR-FARD M.: 3D visualization of thermal resistance and condensation problems using infrared thermography for building energy diagnostics. Visualization in Engineering 2, 1 (2014), 1–15. 6

[HJL15] HARTL A., JERABEK M., LANG R.: Effect of fiber orientation, stress state and notch radius on the impact properties of short glass fiber reinforced polypropylene. Polymer Testing 43 (2015), 1–9. 7

[HKG07] HEINZL C., KASTNER J., GRÖLLER E.: Surface extraction from multi-material components for metrology using dual energy CT. IEEE Trans. Visualization and Computer Graphics 13, 6 (2007), 1520–1527. 8

[HKKG06] HEINZL C., KLINGESBERGER R., KASTNER J., GRÖLLER M. E.: Robust surface detection for variance comparison and dimensional measurement. In Eurographics/IEEE VGTC Symposium on Visualization (2006), pp. 75–82. 9

[HMMW03] HUANG R., MA K.-L., MCCORMICK P., WARD W.: Visualizing industrial CT volume data for nondestructive testing applications. In IEEE Visualization (2003), pp. 547–554. 2

[HRN*03] HU J., RAZDAN A., NIELSON G. M., FARIN G. E., BALUCH D. P., CAPCO D. G.: Volumetric segmentation using weibull E-SD fields. IEEE Trans. Visualization and Computer Graphics 9, 3 (2003), 320–328. 6, 7

[HWR*14] HEINZL C., WEISSENBÖCK J., REH A., KASTNER J., DIERIG T., GÜNTHER T., KIEFEL D., STÖSSEL R.: Software tools for robust extraction, analysis and visualization of porosities in XCT scans of fiber-reinforced polymers. In NDT in Aerospace (2014), pp. 1–8. 9

[IHL*05] INTRATER R., HOFFMAN A., LEMPERT G., GOUZMAN I., COHEN Y., GROSSMAN E.: Visualization of polyethylene fibers surface restructuring induced by oxygen plasma. J. of Materials Science 41, 5 (2005), 1653–1657. 4

[JWP*10] JANSEN C., WIETZKE S., PETERS O., SCHELLER M., VIEWEG N., SALHI M., KRUMBHOLZ N., JÖRDENS C., HOCHREIN T., KOCH M.: Terahertz imaging applications and perspectives. Applied Optics 49, 19 (2010), E48–E57. 10, 11

[KBC*11] KRUTH J., BARTSCHER M., CARMIGNATO S., SCHMITT R., CHIFFRE L. D., WECKENMANN A.: Computed tomography for dimensional metrology. CIRP Annals - Manufacturing Technology 60, 2 (2011), 821–842. 2

[KHG03] KOSARA R., HAUSER H., GRESH D. L.: An interaction view on information visualization. Eurographics - STARs (2003), 1–15. 15

[KHK*12] KIM M. H., HARVEY T. A., KITTLE D. S., RUSHMEIER H., DORSEY J., PRUM R. O., BRADY D. J.: 3D imaging spectroscopy for measuring hyperspectral patterns on solid objects. ACM Trans. Graph. 31, 4 (2012), 38:1–38:11. 6, 13

[KJS*14] KIM S.-K., JIN H. G., SHIN K. I., CHOI B. G., LEE E. H., YOON J.-S., JUNG Y.-I., LEE D. W., KIM D.-H.: Manufacturing and examination for ITER blanket first wall small-scale mockups with kohlt-eb in korea. IEEE Trans. Plasma Science 42, 5 (2014), 1438–1442. 1

[KKB*09] KITAZAWA S., KONO N., BABA A., ADACHI Y., ODAKURA M.: A three-dimensional phased array ultrasonic testing technique. In European Conference on Nondestructive Testing (2009), vol. 256, pp. 1–5. 10, 11

[KPHF08] KASTNER J., PFEIFFER F., HEINZL C., FREYTAG R.: Pipeline zur dreidimensionalen auswertung und visualisierung der faserverteilung in glasfaserverstärkten kunststoffteilen aus *mu*-rontgen-computertomografiedaten. In DACH-Jahrestagung (2008), pp. 1–8. 4

[LB15] LI Y., BARBIČ J.: Stable anisotropic materials. IEEE Trans. Visualization and Computer Graphics 21, 10 (2015), 1129–1137. doi:10.1109/TVCG.2015.2448105. 6

[LBP*15] LISLE T., BOUVET C., PASTOR M. L., ROUAULT T., MARGUERÈS P.: Damage of woven composite under tensile and shear stress using infrared thermography and micrographic cuts. J. of Materials Science 50, 18 (2015), 6154–6170. 7

[LFK*07] LIU Z., FORSYTH D., KOMOROWSKI J., HANASAKI K., KIRUBARAJAN T.: Survey: State of the art in NDE data fusion techniques. IEEE Trans. Instrumentation and Measurement 56, 6 (2007), 2435–2451. 2

[LGKN15] LA H. M., GUCUNSKI N., KEE S.-H., NGUYEN L. V.: Data analysis and visualization for the bridge deck inspection and evaluation robotic system. Visualization in Engineering 3, 1 (2015), 1–16. 6, 8

[LKS*98] LANZAGORTA M., KRAL M. V., SWAN J. E., SPANOS G., ROSENBERG R., KUO E.: Three-dimensional visualization of microstructures. In Visualization '98 (1998), pp. 487–490. 11

[LNA*06] LEVOY M., NG R., ADAMS A., FOOTER M., HOROWITZ M.: Light field microscopy. In ACM Trans. Graph. (2006), pp. 924–934. 14

[LTM01] LAEVSKY K., TELEA A., MATTHEIJ R.: An interactive visualisation tool applied to the simulation of glass pressing. Computing and Visualization in Science 4, 1 (2001), 31–40. 1, 4, 6, 8, 11, 12, 13, 16

[LZS16] LI H., ZHANG J., SUN J.: A visual analytics approach for deterioration risk analysis of ancient frescoes. J. of Visualization (2016), 1–14. 6, 8, 13, 16

[MHG09] MALIK M. M., HEINZL C., GRÖLLER E.: Computation and visualization of fabrication artifacts. J. of WSCG 17, 1 (2009), 17–24. 13

[MHG10] MALIK M., HEINZL C., GRÖLLER M.: Comparative visualization for parameter studies of dataset series. IEEE Trans. Visualization and Computer Graphics 16, 5 (2010), 829–840. 14

[MLK*08] MAYER K., LANGENBERG K.-J., KRAUSE M., MILMANN B., MIELENTZ F.: Characterization of reflector types by phase-sensitive ultrasonic data processing and imaging. J. of Nondestructive Evaluation 27, 1 (2008), 35–45. 8

[MM96] MALDAGUE X., MARINETTI S.: Pulse phase infrared thermography. J. of Applied Physics 79, 5 (1996), 2694–2698. 10

[MSM13] MALZBENDER J., SKIERA E., MÖNCH J.: A simple methodology to visualize crack propagation for ceramic materials. J. of Materials Science 49, 1 (2013), 403–406. 11

[MTGG11] MARTIN S., THOMASZEWSKI B., GRINSPUN E., GROSS M.: Example-based elastic materials. ACM Trans. Graph. 30, 4 (2011), 72:1–72:8. 16

[Mun14] MUNZNER T.: Visualization Analysis and Design. A.K. Peters visualization series. A K Peters, 2014. URL: http://www.cs.ubc.ca/~tmm/vadbook/. 6, 11

[MVM*09] MARINONI N., VOLTOLINI M., MANCINI L., VIGNOLA P., PAGANI A., PAVESE A.: An investigation of mortars affected by alkali-silica reaction by X-ray synchrotron microtomography a preliminary study. J. of Materials Science 44, 21 (2009), 5815–5823. 4, 7

[OKTM05] OTA M., KOGA T., TOYODA K., MAENO K.: A three-dimensional interferometric CT measurement and visualization for high-speed flow induced by shock waves discharged from open ends. In Instrumentation in Aerospace Simulation Facilities (2005), pp. 17–23. 12

[PC13] PATKAR S., CHAUDHURI P.: Wetting of porous solids. IEEE Trans. Visualization and Computer Graphics 19, 9 (2013), 1592–1604. 1, 7

[PCH*15] PATTERSON B. M., CORDES N. L., HENDERSON K., WILLIAMS J. J., STANNARD T., SINGH S. S., OVEJERO A. R., XIAO X., ROBINSON M., CHAWLA N.: In situ X-ray synchrotron tomographic imaging during the compression of hyper-elastic polymeric materials. J. of Materials Science 51, 1 (2015), 171–187. 4, 11, 14

[PD00] PROTOPOPOV V. V., DANILOV V. V.: Visualization of the surface roughness by X-ray scanning. J. of Visualization 3, 1 (2000), 63–70. 6

[PMF*14] PLACET V., MÉTEAU J., FROEHLY L., SALUT R., BOUBAKAR M. L.: Investigation of the internal structure of hemp fibres using optical coherence tomography and focused ion beam transverse cutting. J. of Materials Science 49, 24 (2014), 8317–8327. 4, 6, 10, 11

[QSCZ16] QIAN K., SUN J., CHEN H., ZHANG J.: Visual analysis method for cultural heritage site risk assessment. J. of Visualization (2016), 1–12. 8, 15, 16

[RAK*15] REH A., AMIRKHANOV A., KASTNER J., GRÖLLER E., HEINZL C.: Fuzzy feature tracking: Visual analysis of industrial 4D-XCT data. Computers & Graphics (2015), 177–184. 6, 13, 14

[RGK*13] REH A., GUSENBAUER C., KASTNER J., GRÖLLER M., HEINZL C.: MObjects–a novel method for the visualization and interactive exploration of defects in industrial XCT data. IEEE Trans. Visualization and Computer Graphics 19, 12 (2013), 2906–2915. 2, 15

[RHS*11] REITER M., HARRER B., SALABERGER D., HEINZL C., GUSENBAUER C., KUHN C., KASTNER J.: Simulation aided study for optimising device parameters of an industrial X-ray computed tomography system for non-destructive testing and materials characterisation. In Digital Industrial Radiology and Computed Tomography (2011), pp. 1–9. 9

[RMF07] REY B., MOCELLIN K., FOURMENT L.: A node-nested galerkin multigrid method for metal forging simulation. Computing and Visualization in Science 11, 1 (2007), 17–25. 12

[RPK*12] REH A., PLANK B., KASTNER J., GRÖLLER E., HEINZL C.: Porosity maps–interactive exploration and visual analysis of porosity in carbon fiber reinforced polymers. Computer Graphics Forum 31, 3pt3 (2012), 1185–1194. 16

[SB15] SCHÖNFELD T., BARTSCHER M.: Verification and application of quality measures in dimensional computed tomography. In Digital Industrial Radiology and Computed Tomography (2015), pp. 1–13. 8

[SGW*14] SUN C., GANG T., WANG C., YANG J., ZHANG X., XIA C., YAN Z., JIANG Y.: Three dimensional imaging based on ultrasonic linear phased array probe. In IEEE Far East Forum on Nondestructive Evaluation/Testing (2014), pp. 98–101. 10

[SHB*14] SEDLMAIR M., HEINZL C., BRUCKNER S., PIRINGER H., MÖLLER T.: Visual parameter space analysis: A conceptual framework. IEEE Trans. Visualization and Computer Graphics 20, 12 (2014), 2161–2170. 2

[Shn96] SHNEIDERMAN B.: The eyes have it: A task by data type taxonomy for information visualizations. In IEEE Symposium on Visual Languages (1996), pp. 336–343. 11

[SLKL02] SANDERSON R., LI J., KOEN L., LORENZEN L.: Ultrasonic time-domain reflectometry as a non-destructive instrumental visualization technique to monitor inorganic fouling and cleaning on reverse osmosis membranes. J. of Membrane Science 207, 1 (2002), 105–117. 10, 11

[SLW15] STRAUMIT I., LOMOV S. V., WEVERS M.: Quantification of the internal structure and automatic generation of voxel models of textile composites from X-ray computed tomography data. Composites Part A: Applied Science and Manufacturing 69 (2015), 150–158. 4

[Spr] Springer journal of materials science. http://link.springer.com/journal/10853. [last accessed 26.01.2017]. 3

[Sut] SUTTON A.: What is materials science? http://www.materials.ac.uk/newsletter/issue3/whatis.asp. [last accessed 26.01.2017]. 3

[TBNP14] TABATABAEI A., BARZEGARI M. R., NOFAR M., PARK C. B.: In-situ visualization of polypropylene crystallization during extrusion. Polymer Testing 33 (2014), 57–63. 4

[TDD*12] TRAN H., DOUMALIN P., DELISEE C., DUPRE J. C., MALVESTIO J., GERMANEAU A.: 3D mechanical analysis of low-density wood-based fiberboards by X-ray microcomputed tomography and digital volume correlation. J. of Materials Science 48, 8 (2012), 3198–3212. 4, 6, 14

[TKH13] TANAKA T., KAWAKAMI K., HAYASHI S.-I.: Visualization of deuterium flux and grain boundary diffusion in duplex stainless steel and Fe-30 % Ni alloy, using secondary ion mass spectrometry equipped with a ga focused ion beam. J. of Materials Science 49, 11 (2013), 3928–3935. 11

[TWM*08] TAKATSUBO J., WANG B., MIYAUCHI H., TSUDA H., TOYAMA N., URABE K.: Laser ultrasonic technique for visualizing ultrasonic waves propagating on 3-D object. In World Conference on Nondestructive Testing (2008), pp. 1–9. 13

[UMW*12] USHIZIMA D., MOROZOV D., WEBER G. H., BIANCHI A. G. C., SETHIAN J. A., BETHEL E. W.: Augmented topological descriptors of pore networks for material science. IEEE Trans. Visualization and Computer Graphics 18, 12 (2012), 2041–2050. 4, 6, 8, 12, 13

[WAG*16] WEISSENBÖCK J., AMIRKHANOV A., GRÖLLER M. E., KASTNER J., HEINZL C.: PorosityAnalyzer: Visual analysis and evaluation of segmentation pipelines to determine the porosity in fiber-reinforced polymers. In IEEE Visual Analytics Science and Technology (2016), pp. 101–110. 15

[WAL*14] WEISSENBÖCK J., AMIRKHANOV A., LI W., REH A., AMIRKHANOV A., GRÖLLER E., KASTNER J., HEINZL C.: Fiberscout: An interactive tool for exploring and analyzing fiber reinforced polymers. In IEEE Pacific Visualization Symposium (2014), pp. 153–160. 2, 7, 14

[WEL12] WESTENBERGER P., ESTRADE P., LICHAU D.: Fiber orientation visualization with avizo fire®. In Conf. on Industrial Computed Tomography (2012), pp. 99–104. 4, 14

[WM04] WANG L., MUELLER K.: Generating sub-resolution detail in images and volumes using constrained texture synthesis. In IEEE Visualization (2004), pp. 75–82. 8

[WNG06] WANG C., NEWMAN T. S., GALLAGHER D.: Synthesis of 3D model of a magnetic field-influenced body from a single image. In 3D Data Processing, Visualization and Transmission (3DPVT) (2006), pp. 1018–1025. 15

[WP12] WONG A., PARK C.: A visualization system for observing plastic foaming processes under shear stress. Polymer Testing 31, 3 (2012), 417–424. 4

[WRR*11] WEBER O., RACK A., REDENBACH C., SCHULZ M., WIRJADI O.: Micropowder injection molding: investigation of powder-binder separation using synchrotron-based microtomography and 3D image analysis. J. of Materials Science 46, 10 (2011), 3568–3573. 4, 11

[WRS*14] WEISSENBÖCK J., REH A., SALABERGER D., HEINZL C., KASTNER J.: Advanced visualization and exploration techniques for fiber reinforced polymers. In European Conference on Nondestructive Testing (2014), pp. 1–10. 2

[WT10] WU C., TAI X.: A level set formulation of geodesic curvature flow on simplicial surfaces. IEEE Trans. Visualization and Computer Graphics 16, 4 (2010), 647–662. 13

[YaKSJ07] YI J. S., AH KANG Y., STASKO J., JACKO J.: Toward a deeper understanding of the role of interaction in information visualization. IEEE Trans. Visualization and Computer Graphics 13, 6 (2007), 1224–1231. interaction methods categories. 15

[YTT07] YASHIRO S., TAKATSUBO J., TOYAMA N.: An NDT technique for composite structures using visualized lamb-wave propagation. Composites Science and Technology 67, 15-16 (2007), 3202–3208. 8

[ZSS15] ZOBEL V., STOMMEL M., SCHEUERMANN G.: Feature-based tensor field visualization for fiber reinforced polymers. In IEEE Scientific Visualization (2015), pp. 49–56. 14, 15, 16

Dynamic Volume Lines: Visual Comparison of 3D Volumes through Space-filling Curves

Johannes Weissenböck, Bernhard Fröhler, Eduard Gröller, Johann Kastner, Christoph Heinzl

Dynamic Volume Lines: Visual Comparison of 3D Volumes through Space-filling Curves

Johannes Weissenböck, Bernhard Fröhler, Eduard Gröller, Johann Kastner and Christoph Heinzl
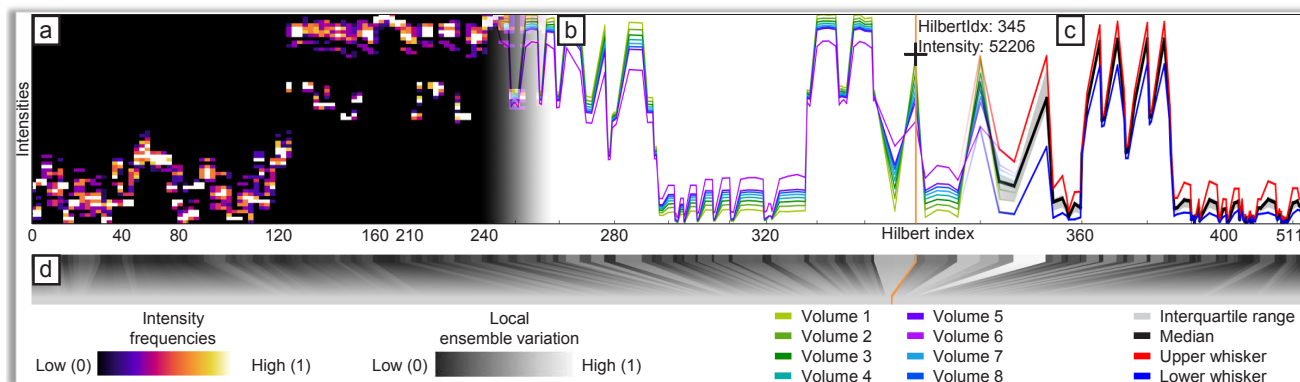
Fig. 1. *Dynamic Volume Lines* depicts sets of volumes (a) in an overview visualization, i.e., an interactive nonlinearly scaled histogram heatmap, which encodes intensity frequencies, or (b) in a detailed view, as interactive nonlinearly scaled 1D Hilbert line plots. Based on the individual 1D Hilbert line plots, functional boxplots (c) are generated on demand. The scaling widget (d) depicts the ensemble variation on each level of detail.

Abstract— The comparison of many members of an ensemble is difficult, tedious, and error-prone, which is aggravated by often just subtle differences. In this paper, we introduce *Dynamic Volume Lines* for the interactive visual analysis and comparison of sets of 3D volumes. Each volume is linearized along a Hilbert space-filling curve into a 1D Hilbert line plot, which depicts the intensities over the Hilbert indices. We present a nonlinear scaling of these 1D Hilbert line plots based on the intensity variations in the ensemble of 3D volumes, which enables a more effective use of the available screen space. The nonlinear scaling builds the basis for our interactive visualization techniques. An interactive histogram heatmap of the intensity frequencies serves as overview visualization. When zooming in, the frequencies are replaced by detailed 1D Hilbert line plots and optional functional boxplots. To focus on important regions of the volume ensemble, nonlinear scaling is incorporated into the plots. An interactive scaling widget depicts the local ensemble variations. Our brushing and linking interface reveals, for example, regions with a high ensemble variation by showing the affected voxels in a 3D spatial view. We show the applicability of our concepts using two case studies on ensembles of 3D volumes resulting from tomographic reconstruction. In the first case study, we evaluate an artificial specimen from simulated industrial 3D X-ray computed tomography (XCT). In the second case study, a real-world XCT foam specimen is investigated. Our results show that *Dynamic Volume Lines* can identify regions with high local intensity variations, allowing the user to draw conclusions, for example, about the choice of reconstruction parameters. Furthermore, it is possible to detect ring artifacts in reconstructions volumes.

Index Terms—Ensemble data, comparative visualization, visual analysis, Hilbert curve, nonlinear scaling, X-ray computed tomography

◆

1 INTRODUCTION AND MOTIVATION

Synthetic foams are widely used, for example, as packaging, as thermal insulating materials, or even as lightweight components [19]. The mechanical behavior of foamed polymers is mainly influenced by the foam density, cell size and diameter, foam hardness, and the deformation rate. For closed-cell and open-cell foams, the determination of the foam

• *Johannes Weissenböck is with the University of Applied Sciences Upper Austria, Wels, Austria. E-mail: johannes.weissenboeck@fh-wels.at*
• *Bernhard Fröhler is with the University of Applied Sciences Upper Austria, Wels, Austria. E-mail: bernhard.froehler@fh-wels.at*
• *Eduard Gröller is with TU Wien, Vienna, Austria and VRVis Research Center, Vienna, Austria. E-mail: groeller@cg.tuwien.ac.at*
• *Johann Kastner is with the University of Applied Sciences Upper Austria, Wels, Austria. E-mail: johann.kastner@fh-wels.at*
• *Christoph Heinzl is with the University of Applied Sciences Upper Austria, Wels, Austria. E-mail: christoph.heinzl@fh-wels.at*

module is important. For this purpose, the spatial distribution of the matrix material in the cell walls must be accurately described [10].

A major challenge in three-dimensional material characterization with conventional industrial 3D X-ray computed tomography (XCT) systems are low densities and thin cell walls, especially at low physical resolutions. One method that overcomes these challenges is Talbot-Lau grating interferometer XCT (TLGI-XCT) [37]. It is a non-destructive testing method, which fully delivers 3D volume information of the scanned specimen at a high resolution to precisely capture external and internal structures (e.g., cracks) in a single scan. TLGI-XCT is one of the most important X-ray technology innovations in the past ten years [28]. This method provides three complementary modalities in one scan of the specimen: (1) the attenuation contrast (AC), (2) the differential phase contrast (DPC), and (3) the dark-field contrast (DFC).

Currently, it is common practice to reconstruct the data of the three modalities separately, without simultaneously using the present and instructive complementary information. To reconstruct the data from the three modalities, the conventional filtered back-projection algorithm by Feldkamp, Davis, and Kress (FDK) is used [6]. This reconstruction algorithm is well suited for XCT data from the AC modality, as it is a fast and accurate method. However, for the DPC and DFC modalities, the FDK reconstruction is not optimal because the prior knowledge and the inherent physical effects of the different modalities

are not considered [17, 33]. Experts in the field of computed tomography reconstruction are therefore developing new algorithms based on appropriate mathematical models. These correspond to the physical characteristics of the DFC and DPC modalities in order to achieve satisfying reconstruction results with regard to conventional methods.

The domain specialists compare the results of the different reconstruction algorithms and their parameterizations with each other and with a reference reconstruction. Regions in the volume with a high ensemble variation of the intensities (e.g., feature edges on interfaces) are of great interest to the experts, as the behavior of the reconstruction algorithm can be deduced if changing specific parameters. The comparison is typically done visually. It is based on 2D gray value slices through the volumes arranged side by side. Experts perform this comparison on a case-by-case basis. They try to determine promising algorithms and suitable parameters, for instance, by checking for noise and artifact suppression. The intensity differences between the various volumetric reconstructions are typically rather small. Therefore it is difficult for an expert to judge whether a particular algorithm or parameter set provides better results (e.g., sharper edges) than another one. This problem gets even worse if several or even many different reconstruction results of an algorithm are compared (e.g., due to parameter variations).

Due to a close collaboration with reconstruction specialists, we were able to analyze their workflow and identify the following tasks when comparing many volumes in specific regions of minor intensity differences:

Task 1: Compare several reconstruction volumes with each other

Task 2: Identify interesting spatial regions based on high local intensity variations

Task 3: Reveal repeating patterns in the spatial domain, which are of high variance among all ensemble members

Task 4: Find the most suitable volume in the ensemble

To address domain-specific requirements, we introduce *Dynamic Volume Lines* for the interactive visual analysis and comparison of 3D volumes using nonlinearly scaled 1D Hilbert line plots (see Figure 1). We build upon the work of Demir et al. [3], who also use the Hilbert linearization to analyze 3D data. As space-filling curve the Hilbert curve traverses the entire 3D volume. For the line plot the space-filling curve is straightened along the horizontal axis. On the vertical axis the intensities at the specific volume positions are shown. We extend the approach of Demir et al. by an adaptive, automatic, and dynamic nonlinear scaling of the horizontal axis, which allows the user to focus on interesting regions in the volumes. The nonlinear scaling highlights regions of high variation in the ensemble and optionally hides uninteresting background regions. Abstracting and reformatting 3D volumes as line plots is chosen because the domain experts are familiar with line graphs, which they use on a daily basis. The workflow of *Dynamic Volume Lines* starts with the extraction of a region of interest (ROI), which is for each volume to be analyzed at the same position and of the same size (see Figure 2a). A Hilbert space-filling curve for the extracted ensemble volumes is generated by mapping voxel coordinates and the corresponding intensities in 3D to 1D Hilbert indices (see Figure 2b). The nonlinear scaling of a Hilbert line plot is built by summing up the local ensemble variations to formulate a cumulative importance-function (see Figure 2c), which serves as basis for the interactive visualization techniques (see Figure 2d–f). Our main contributions are:

- Design and development of *Dynamic Volume Lines*, to compare ensembles of 3D volumes, including the following key features:

  – Nonlinear scaling of the 1D Hilbert line plot, which is built from a cumulative importance-function (see Section 3.2)

  – Interactive nonlinearly scaled histogram heatmap, which encodes the intensity frequencies (see Section 3.3.1)
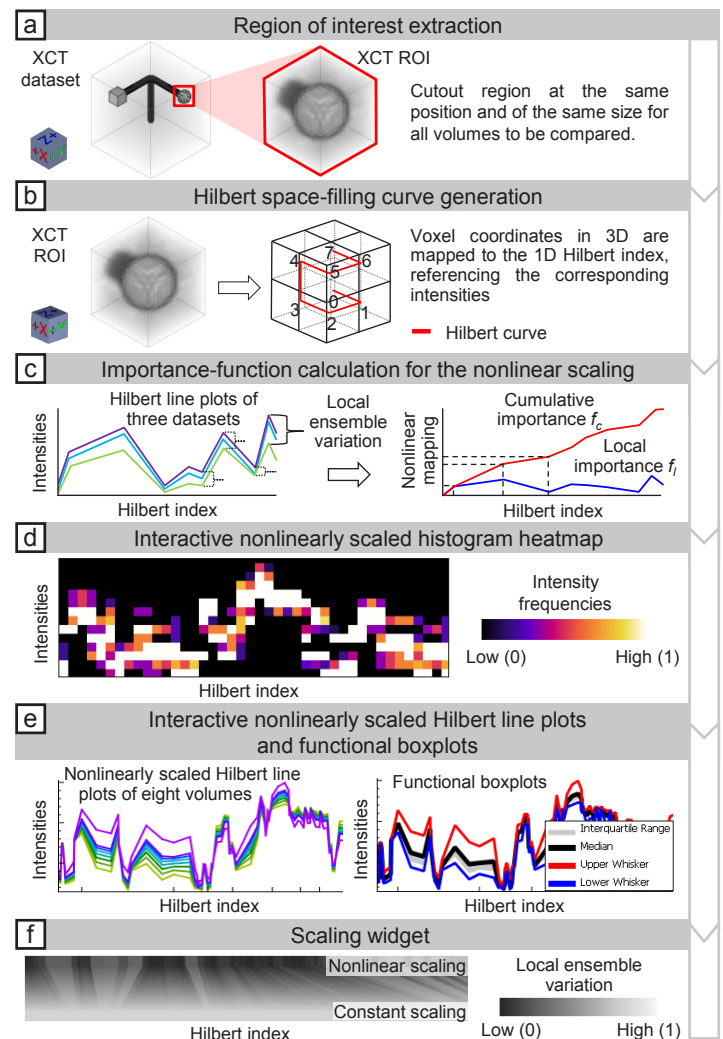

Fig. 2. The *Dynamic Volume Lines* workflow: (a) extraction of interesting regions, (b) generation of a space-filling Hilbert curve, (c) nonlinear scaling of the Hilbert line plots, (d) interactive nonlinearly scaled histogram heatmap, (e) interactive nonlinearly scaled 1D Hilbert line plots, (f) and interactive scaling widget.

  – Interactive nonlinearly scaled 1D Hilbert line plots of the individual volumes in the ensemble (see Section 3.3.2)

  – Interactive scaling widget, which illustrates the locally varying scaling factor (see Section 3.3.3)

- Evaluation of the tool based on two case studies from the XCT domain

In the subsequent Section 2 we review the related work on comparative and ensemble visualization. In Section 3 we explain *Dynamic Volume Lines*, which includes the Hilbert curve generation, the nonlinear scaling based on a cumulative importance-function, and the interactive visualization techniques. Section 4 describes the data acquisition and the used datasets. Section 5 presents the evaluation of the developed tool based on two case studies. We conclude and point out potential future work in Section 6.

2 RELATED WORK

The related work is mainly in the areas of comparative and ensemble visualization, but also in the fields of visual parameter space analysis and interactive visual analysis.

Gleicher et al. [9] provide a taxonomy to group visual designs into one of three basic categories: juxtaposition, superposition, and explicit encoding. In the work of Malik et al. [21], slices from different

volumes are compared in a hexagonal arrangement. This visual representation works only for a rather small number of datasets to be compared. Schmidt et al. [35] present a tool for the comparative visual analysis of 3D meshes, which enables the simultaneous comparison of several meshes and allows for the interactive exploration of their differences. In an earlier work [34], they present a method for visualizing differences and similarities in large sets of images. The technique preserves contextual information, but also allows the user to perform a detailed analysis of subtle variations. Based on magnetic resonance cartilage-imaging techniques, Mlejnek et al. [25] propose 3D glyphs, called *Profile Flags*, for the probing of sets of underlying curve data. Weissenböck et al. [42] introduce a system to evaluate the porosity in 3D volumes. They provide 2D slice views and 3D renderings to compare the different pore segmentation results due to varying segmentation parameters. Many of the ensembles investigated in these works result from analyzing the parameter space of some algorithm, for which Sedlmair et al. [36] present a conceptual framework to guide and systematize research endeavors.

Ensemble visualization often uses statistical summaries for the comparison of many similar datasets. *Ensemble-Vis* by Potter et al. [30] is a framework consisting of an interactively linked overview and statistical displays for the discovery and evaluation of simulated meteorology outcomes. Jarema et al. [16] provide a visual-analysis user-interface with multiple linked views to support the comparative exploration of 2D vector-valued ensemble fields. Fröhler et al. [7] present an interactive tool for exploring and analyzing the parameter space of multi-channel segmentation algorithms and the corresponding ensemble of segmentation results. Several works have been published, which embed descriptive statistics measures such as minimum, median, and maximum in functional boxplots [39], contour boxplots [43], and curved boxplots [24]. Genton et al. [8] developed *surface boxplots* for the visualization and exploratory analysis of samples of images to detect potential outliers. They use the notion of volume depth to order the images interpreted as hightfields. Raj et al. [31] examine the effectiveness of contour boxplots in the medical domain of brain atlas analysis. They extend contour boxplots to 3D to visualize and interact with ensembles of 3D isosurfaces. Demir et al. [4] determine the most central shape from a given set, to quantify a region-wise centrality, and to compute the locally most representative shape. Konyha et al. [18] and Matkovic et al. [22] focus on the interactive visual analysis of ensembles of curves called *families of curves* or *families of surfaces* using data aggregation and attribute derivation. Piringer et al. [29] extend the work on feature-preserving downsampling of 2D functions. They discuss a design study of an interactive approach for the comparative visual analysis of 2D function ensembles.

In the context of visual analysis, the state of the art report by Heinzl and Stappen [15] closes a gap between visual computing and material science. Torsney-Weir et al. [40] propose *Sliceplorer* to visually examine multi-dimensional continuous scalar functions with 1D slices. Their technique combines the benefits of topological views, i.e., screen space efficiency, with those of slices, that are a close resemblance of the underlying function. Another work of Demir et al. [3], presents *Multi-Charts*, an interface to visually analyze 3D scalar ensemble fields by linearizing the 3D data points along a space-filling curve. Our approach is similar to *Multi-Charts*, as we also use the Hilbert space-filling curve to linearize 3D volumes and represent the volumes as 1D line plots. Demir et al. represent the individual ensemble members as multiple stacked and combined bar and line charts at different levels of detail. For analyzing such regions the user has to zoom in and out. This leads to a loss of context. A significant difference in our work is the computation of a nonlinear scaling of the x-axis based on local ensemble variations. The nonlinear scaling allows us to depict all 3D volumes as 1D line plots, which can be presented in one visualization. As a result, uninteresting regions (with low ensemble variance) are compressed in the line plots, and interesting regions (with high ensemble variance) are expanded. Thereby, we can optimally use the available screen space and no zooming is necessary in the first place, as we provide insight into the interesting regions from the initial overview state. The individual line plots of the corresponding 3D volumes can be aggregated

using functional boxplots. Thus, we provide a statistical overview of the ensemble. In addition, the scaling widget indicates the nonlinear scaling of the data. Finally, we support an importance-driven selection by defining ranges based on a cumulative importance-function.

3 DYNAMIC VOLUME LINES

In this section we explain the generation of the Hilbert curve based on the 3D voxel intensities and compare the line plots of the Hilbert curve with the line plots of the scan line curve (see Section 3.1). Furthermore, we describe the nonlinear scaling of the Hilbert line plots based on local ensemble variations (see Section 3.2).

The basic motivation of *Dynamic Volume Lines* is to linearize 3D volumes along a space-filling curve. The resulting line plots are a familiar representation to engineers. Without occlusion many volumes can be compared through their line plots. A comparison of many volumes in their original 3D space that differ only slightly from each other turns out to be difficult with traditional methods. For example, a direct volume visualization of many datasets is plagued by severe clutter and occlusion problems. This effect is further reinforced by the increasing number of volumes to compare. The same is true for 2D slice views. Arranging two or four slice views of different volumes side by side would be feasible, but with an increasing number of volumes to compare, e.g., six, it is nearly impossible to find regions where the volumes differ. For example: if individual voxels differ by 5000 intensities, this difference is difficult to perceive as brightness difference, even for an expert. For a line plot in a range of 65000 intensities on the y-axis, this amplitude drop would be 7% and thus easier to recognize as positional difference. A positional encoding is much more effective than color coding to indicate subtle differences. Comparing intensities is much easier through line plots, in contrast to having first to match them in two or more 2D (or 3D) views and then comparing their color encoding. One could apply statistical aggregation to determine a volume where the voxels contain the local ensemble variances. But even in such a reduced data, rendering is affected by clutter and occlusion. For example, to make differences visible in the interior of the volume, the opacity must be set to a low value. However, larger differences are then only vaguely recognizable. Small differences will be lost. In addition, statistical aggregation volumes provide only a summary or overview and would require additional detailed visualizations to compare specific members in a region of interest. In our approach the differences between the individual members can easily be inspected by comparing line plots.

A drawback of linearizing volumes is the loss of spatial coherency. Among the many possibilities of space-filling curves we decided for one which is preserving the spatial coherency as much as possible. The wigglyness of the Hilbert curve ensures that very often neighboring voxels in the 3D volumes are mapped to nearby locations in the straightened Hilbert line plot. We compare the spatial coherence of the Hilbert curve with respect to another simple volume linearization, i.e., the scan line curve where the volume is traversed slice by slice and scan line by scan line within a slice. Switching scan lines or slices introduce large spatial incoherences. Such incoherencies appear with Hilbert curves as well, but much less.

3.1 Hilbert Space-Filling Curve Generation

In general, with space-filling curves, n-dimensional regular grids can be completely traversed and the grid points can be brought into a one-dimensional linear order. In this sense volumes are three-dimensional regular grids. There are many different space-filling curves such as the Hilbert curve, the Peano curve, or the Z-curve. An obvious approach to linearize the intensities of a 3D volume is to traverse the voxels in z-, y-, and x-axis order along a scan line curve, line by line and slice by slice (see Figure 3a). The disadvantage of this approach is that there are large jumps in the scan line curve between the last voxel of the previous row and the first voxel of the next row and the last voxel of the previous slice and the first voxel of the current slice, respectively. In contrast, the Hilbert space-filling curve traverses every point of a square, a cube, or more generally, an n-dimensional hypercube, by preserving locality much better. Points close to each other in the n-dimensional space are very often close in their order along the Hilbert curve and vice
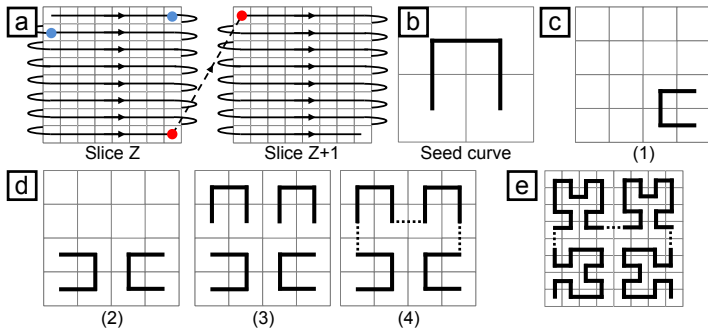
Fig. 3. (a) shows the scan line curve of a 3D volume dataset by traversing the voxels along their appearance. The blue dots mark a large jump due to a line change and the red dots mark a large jumps due to a slice change. (b) depicts the Hilbert curve of order one (initial seed curve). (c–d) illustrate the individual steps to generate a Hilbert curve of order two in 2D space. (e) shows the Hilbert curve of order three.
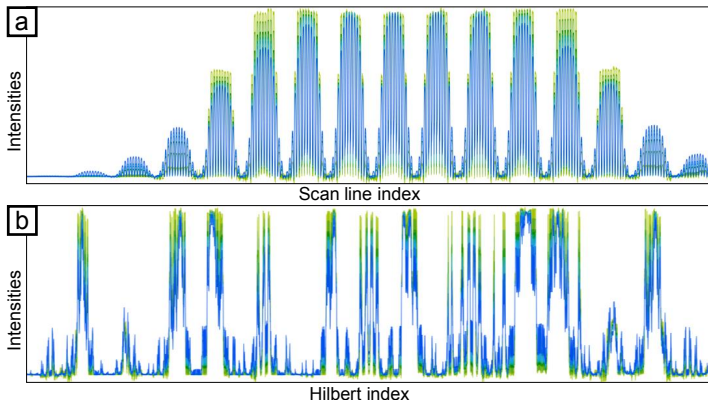

Fig. 4. Difference between the scan line curve and the Hilbert curve due to large jumps and different locality preservation. The six datasets of the artificial specimen (see Section 4.2) are represented by color-coded line plots (from light green to blue). The line plots are based on (a) the scan line curve and (b) on the Hilbert curve.

versa [11]. This results in fewer large jumps. Therefore in this work, we focus on the Hilbert curve, as it preserves the locality best [26].

In the following we describe the generation of the space-filling Hilbert curve exemplarily in 2D space [13]. Consider the initial seed curve defined on a 2×2 grid as shown in Figure 3b. It is called order 1 Hilbert curve. Based on an order k Hilbert curve defined on a $2^k \times 2^k$ grid, we define the order $k+1$ Hilbert curve on a $2^{k+1} \times 2^{k+1}$ grid according to four steps (see Figures 3c–d):

1. Place a copy of the curve in the lower right cell and rotate it 90° counter-clockwise.
2. Place a copy of the curve in the lower left cell and rotate it 90° clockwise.
3. Place a copy of the curve in each of the upper cells.
4. Connect the curves with each other.

The resulting space-filling curve visits every voxel exactly once and assigns it a scalar index resulting from the traversal order (Hilbert index). For example, Figures 3b, 3c(4), and 3e show the Hilbert curves of order one, two, and three. Figure 2b (on the right) shows the Hilbert curve of order one in 3D space.

In the case of *Dynamic Volume Lines*, all 3D volume datasets are linearized using the implementation of Hamilton and Rau-Chaplin [14]. It generates a Hilbert space-filling curve where the volumes do not need to have the same number of voxels along the x-, y-, and z-axis. The resolution along the individual axes also need not be a power of two. Figure 4 illustrates the difference between linearizing along the Hilbert curve and the scan line curve. It depicts the six volumes of the artificial

specimen (see Section 4), each represented by a color-coded line plot (from light green to blue). The scan line plots in Figure 4a fluctuate more, due to less spatial coherence, as compared to the Hilbert line plots (in Figure 4b).

3.2 Nonlinear Scaling of the Hilbert Line Plots

When generating the Hilbert curve for a dataset of $16 \times 16 \times 16$ voxels in size, 4096 Hilbert indices are created. Currently the horizontal screen resolution of a standard PC monitor is typically between 2000 and 3000 pixels. If one wants to display all the 4096 Hilbert indices as points in a 1D Hilbert line plot on the monitor, it turns out, that the horizontal screen resolution is not sufficient to assign each Hilbert index to its own pixel column. This problem becomes even more severe with increasing volume size. Linearizing a volume reduces it to a simple line plot, but with a tremendous horizontal resolution, i.e., number of voxels. This requires automatic scaling along the horizontal axis so that important regions get the screen space they need. Unimportant regions like background can be drastically reduced in their screen space or even removed. To counteract the problem of the limited screen space, we apply a nonlinear scaling to the Hilbert line plot. Since the domain experts are interested in those regions of the dataset where the variation of the intensities is high, we compute the maximum local ensemble variation V_h for every Hilbert index as follows:

$$V_h = \max_{\forall m \in M_h} Intensity_h(m) - \min_{\forall m \in M_h} Intensity_h(m) \qquad (1)$$

m defines an ensemble member of a local ensemble M_h at a discrete Hilbert index h, $Intensity_h$ defines the intensity at Hilbert index h for member m.

Inspired by the work of Mindek et al. [23] and Lindow et al. [20], we formulate the discrete local importance-function f_l based on the maximum local ensemble variation V_h:

$$f_l(h) = \left(\frac{V_h}{\max V_h} \right)^p \qquad (2)$$

To be able to filter for a specific importance-value, we do a normalization by the maximally occurring local ensemble variation. To influence the nonlinear scaling, we introduce an exponent p, which can be adapted by the user. Setting this parameter to zero means equal importance for all Hilbert indices, setting it higher than zero increases the importance-value for Hilbert indices with a high variance in the ensemble. Exponent p can be adapted by the user to fine-tune the importance-value according to the individual application scenario. By summing the local importance-function values, we define the cumulative importance-function f_c as follows:

$$f_c(h) = \sum_{i=0}^{h} f_l(i) \qquad (3)$$

The cumulative importance-function values serve as a nonlinear mapping to compress the distances between the Hilbert indices (on the x-axis). Figure 2c illustrates the calculation of the nonlinear mapping. Figure 5 illustrates the effect of nonlinearly scaling the Hilbert line plots. The regions indicated with red in Figure 5b are compressed (respectively uncompressed in Figure 5a) by the nonlinear scaling because of the low ensemble variation in these regions. In addition, we allow the user to set a threshold for intensities that are not of interest (e.g., areas of air in the dataset). For these background areas (see Figure 6) f_l is fixed to a value of 0.025. This value ensures that the background areas are still sufficiently visible, but at the same time occupy little screen space. By increasing the parameter p, the width of the background regions can be adjusted.

3.3 Visualization Techniques

Dynamic Volume Lines provides multiple linked views and follows the visual information-seeking mantra by Ben Shneiderman, "overview first, zoom and filter, then details on demand" [38]. Two charts, one with nonlinear scaling and one with constant scaling, are arranged on
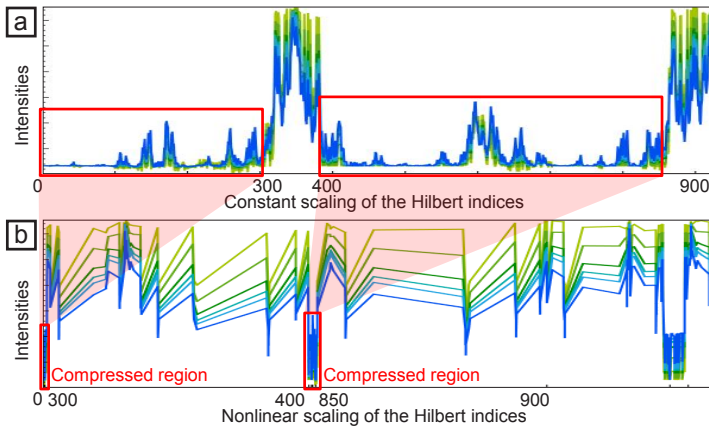
Fig. 5. Effect of the nonlinear scaling. (a) Constantly scaled 1D Hilbert line plots of six 3D volumes. (b) nonlinearly scaled 1D Hilbert line plots of the same six 3D volumes.

top of each other with a scaling widget in-between. An overview is provided through the nonlinearly scaled histogram heatmap visualization. Background regions can be filtered out. If the user zooms into the chart, details for each volume are provided through the 1D Hilbert line plots. An orientation widget displays the size and position of the currently visible chart area in light blue compared to the overall chart size, which is shown in gray (see bottom of Figures 6 and 7). In addition, we enable brushing and linking to immediately highlight the affected voxels or Hilbert indices when performing a selection in the 1D Hilbert line plots or in the 3D spatial view, respectively.

3.3.1   Interactive Histogram Heatmap Visualization

The histogram heatmap visualization provides an overview of the intensity distribution in the volume ensemble. To be able to fit the full volume into a chart with the width of the screen, we split the x-axis of the nonlinearly scaled chart into intervals of equal width. Due to the nonlinear scaling, the intervals may include a varying number of Hilbert indices. For each interval we then compute a single histogram of the intensities at the included Hilbert indices, over all ensemble members. The single histogram is visualized as a heatmap through a vertical bar, all histograms together form a histogram heatmap. The default width of each histogram bar is 10 pixels, and by default each histogram has 64 bins. These parameters can be adapted by the user to best fit the size and intensity distribution of the currently analyzed volumes. To improve the performance in computing the histogram heatmap, we adapt a segment tree [2]. A segment tree is a binary tree used for storing segments in the range $0...n-1$. Each node represents a segment and is assigned the corresponding histogram. The segment of a leave node covers only one Hilbert index (voxel), the segment of the root node covers all Hilbert indices. The segment tree partitions an arbitrary interval into a minimal set of segments (of varying sizes). With this, we avoid to compute the histogram of an interval based on single voxels. Instead we combine the histograms of the highest-level nodes, whose segments are included in the requested interval. The root node of the segment tree contains the entire segment $[0, n-1]$. A leaf node represents an elementary segment, which corresponds to one Hilbert index, i.e., one voxel. It is assigned the histogram of all the intensities at that voxel throughout the entire volume ensemble. The internal nodes merge the segments of their child nodes. The segment tree can be serialized using an array of size $n-1$. The internal nodes are stored in the first half of the array, the leaf nodes are stored in the second half of the array. The left child of each node at index i can be found at index $2*i+1$, the right child at index $2*i+2$. The segment tree is built bottom-up by taking the pairs of nodes with indices $(2*i+1, 2*i+2)$ and aggregating their histograms into the histogram of the parent at index i. The construction of the segment tree is performed for every ensemble and takes $O(n)$ time. In our case, each node of the segment tree contains the histogram for a segment of a certain contiguous range of Hilbert indices. A vertical bar of the

histogram heatmap is created by summing up each histogram of the individual volumes. Due to the nonlinear scaling, many Hilbert indices may be covered by a vertical bar of the histogram heatmap. Without the segment tree, a histogram would have to be calculated from all these Hilbert indices. With the segment tree, a histogram for a vertical bar can be generated in $O(\log n)$ time, since only a few nodes need to be traversed. The segment tree therefore supports efficient rescaling of the charts.

In the figures in this paper, the extended black body scheme proposed by Moreland [27] is used as color map for the histogram heatmap, but other predefined color maps can be selected by the user. Figure 6 shows an example histogram heatmap. White regions denote a high concentration of intensities in a single bin. This is the case if all ensemble members agree on a small range of intensities, i.e., if the variation is low in that region. In contrast, a high variation is indicated by a broader distribution in violet, red, and yellow colors from the middle of the color map. The focus in XCT images is typically on regions containing an object, therefore areas containing only background, i.e., air, are not of interest and can be ignored for the analysis. The background areas, where the intensities of all ensemble members are below a user-defined threshold, are assigned a very low importance-value and therefore are highly compressed in the nonlinear scaling. Setting the background threshold is optional, a value of zero means that the background is left out altogether. Instead of showing a histogram, these background regions are depicted by light orange boxes. In this fashion, we can identify interesting regions, i.e., those with high local variation, which addresses Task 2 from Section 1.

3.3.2   Interactive 1D Hilbert Line Plot Visualization

In the 1D Hilbert line plots, for each volume, the intensities are plotted on the y-axis over the Hilbert indices on the x-axis. Each plot is assigned a distinctive color taken from the metro color scheme of MaterialUI [1], as can be seen in Figure 7a. When zooming into the histogram heatmap, the 1D Hilbert line plots are activated automatically as soon as the range of currently visible Hilbert indices fits on the screen without aggregation. The 1D Hilbert line plots can also be shown as an overlay on the histogram heatmap. Specific ensemble members can always be activated and deactivated by clicking on them in the legend. The current mouse position is highlighted by a position marker line (the orange line in Figure 7a and c), augmented with a tool-tip displaying the Hilbert index and intensity at that position. For better visibility and to better visually link the nonlinearly scaled and the linearly scaled chart, this line is updated simultaneously in both charts. Visualizing two or more 1D Hilbert line plots side by side enables a detailed analysis and comparison of all ensemble members, addressing Task 1 and Task 4 from Section 1.

Dynamic Volume Lines provides several ways to select regions of interest. The user can perform rectangular multi-selections directly in the charts. Additionally, all Hilbert indices within a specified importance-range can be selected by defining upper and lower bounds. Furthermore, the user can perform a selection in the 3D spatial view, by marking a rectangular region with a dragging interaction. This selects all voxels inside of the cuboid region that is spanned by projecting the rectangle from the near plane of the viewing frustum along the viewing direction to the far plane. In either case, all intervals in the Hilbert line plot falling into the selected region are highlighted. They are emphasized in the scaling widget as well, and the respective regions in the selected ensemble members are displayed in a separate 3D visualization. As a result, different or similar areas in the ensemble of reconstruction volumes can be identified and thus repeating patterns in the data (e.g., ring artifacts) can be exposed. This addresses Task 3 from Section 1. Optionally, we provide an aggregated view of the individual 1D Hilbert line plots using functional boxplots [39]. The functional boxplots show statistical properties such as the lower and upper whisker, the median, and the interquartile range (see Figure 1c).

3.3.3   Scaling Widget Visualization

Dynamic Volume Lines depicts a nonlinearly scaled chart at the top and a constantly scaled chart at the bottom, both showing the histogram
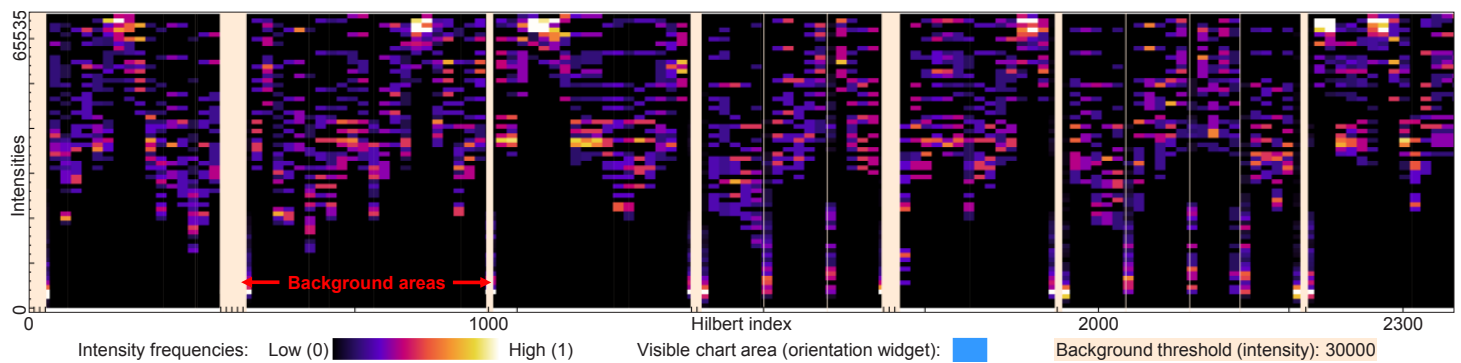
Fig. 6. The histogram heatmap overview visualization with the extended black body heatmap. White areas indicate a high concentration of intensities. This is the case if all ensemble members agree on a small range of intensities, i.e., the variation in this region is low. A high variation is indicated by a broader distribution in violet, red, and yellow. Light orange background areas hide the uninteresting intensities below 30000.
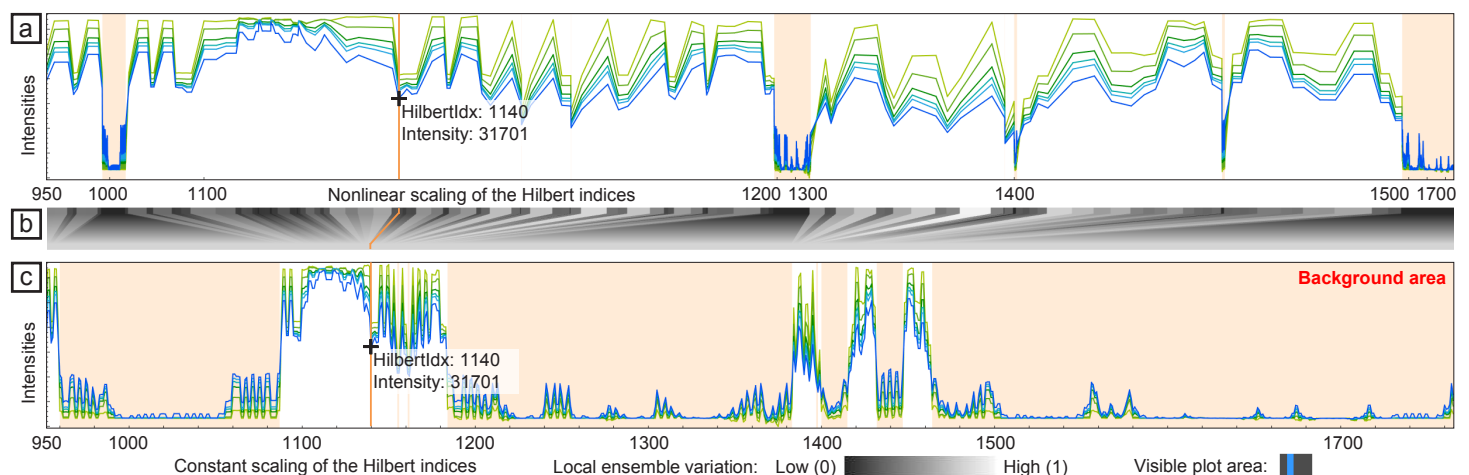

Fig. 7. (a) The nonlinearly scaled chart shows the differently colored 1D Hilbert line plots for each volume. The intensities are plotted on the y-axis over the Hilbert indeces on the x-axis. The current mouse position is highlighted by an orange position marker line, which shows the Hilbert index and intensity at that position. (b) depicts the scaling widget, which emphasizes the nonlinear scaling. (c) shows the constantly scaled chart with the individual 1D Hilbert line plots.

heatmap visualization as well as the Hilbert line plot visualization. Early prototypes just had those two charts on top of each other. When working with those early prototypes together with the domain experts, we realized that an explicit visualization of the nonlinear scaling is necessary. For this purpose, the current design includes the scaling widget, as shown in Figure 7b. Each single histogram of the histogram heatmap in the nonlinearly scaled chart is mapped to the corresponding histogram in the constantly scaled chart. If the line plots are visible, each Hilbert index in the nonlinearly scaled chart maps to the corresponding index in the constantly scaled chart. Small rectangles at the top of the scaling widget each represent a histogram or Hilbert index. Their gray values encode the local ensemble variation. Black represents a low variation, white a high variation. From these rectangles at the top, trapezoids extend to the bottom. Their color is gradually shifting to an average gray value, which represents the constant scaling applied in the lower plot. The position marker line is also shown in the scaling widget, linking the nonlinearly scaled chart at the top with the constantly scaled chart at the bottom, as shown in Figure 7.

4 DATASETS

This section briefly explains how the industrial 3D X-ray computed tomography (XCT) data is acquired (see Section 4.1) and which datasets are used (see Section 4.2).

4.1 Data Acquisition

XCT provides a volumetric representation of a scanned specimen. The specimen is placed on a rotary table between the X-ray source and the detector. While the specimen is rotating, the source emits cone-beam X-rays. The detector collects the X-rays attenuated by the specimen. The attenuation depends on the density and atomic number of the material and on the penetration thickness of the specimen. The detector converts the radiation intensity into a series of digital projection images. In the reconstruction stage, an algorithm is applied on the projection images in order to reconstruct the 3D volume of the specimen. Talbot-Lau grating interferometer XCT (TLGI-XCT) delivers, in contrast to conventional XCT, three complementary modalities, i.e., attenuation contrast (AC), differential phase contrast (DPC), and dark-field contrast (DFC) in a single scan. The three modalities are perfectly registered to each other. AC provides information on the attenuation of the X-ray beam intensity and thus is equivalent to conventional X-ray imaging. DPC is related to the index of refraction and image contrast, which is achieved by the local deflection of the X-ray beam. DFC reflects the total amount of radiation scattered at small angles, e.g., caused by microscopic structures in the sample like particles, pores, fibers, struts, or cracks. In addition, the DFC modality produces a strong signal and a high contrast at interfaces and reveals information that is undetected by AC and DPC imaging.

4.2 Dataset Description

The first ensemble consists of 3D reconstruction datasets of an artificial specimen from simulated XCT [32] of the AC modality with intensities between 0 and 65535. The size of each dataset is $128 \times 128 \times 128$ voxels and the data type is unsigned short (see Figure 8a). The artificial projection images are generated by calculating penetration lengths of primary monochromatic X-rays through the specimen. The specimen is represented by surface models of three cylinders, one sphere, and
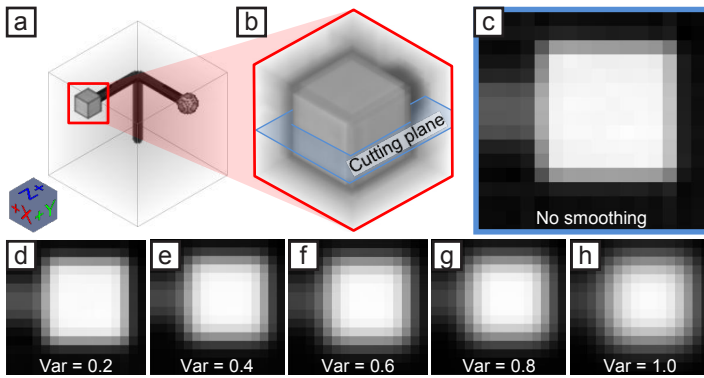
Fig. 8. (a) 3D reconstruction dataset of the artificial specimen from simulated XCT of the AC modality, (b) with an ROI cutout of a cube. (c) shows an xy-slice view of the dataset without Gaussian smoothing. (d–h) depict the xy-slice views of the five datasets with an increasing variance of the Gaussian smoothing between 0.2 and 1.0.
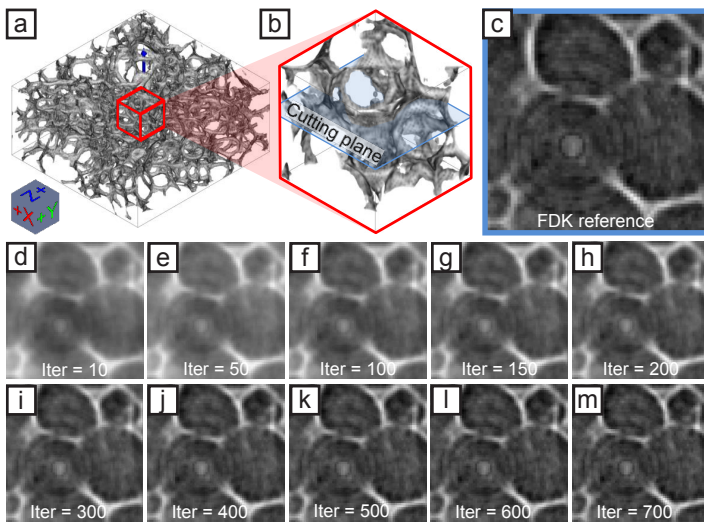

Fig. 9. (a) 3D reconstruction dataset of a real-world TLGI-XCT scanned foam specimen of the DFC modality (b) with an ROI cutout. (c) shows an xy-slice view of the FDK reconstructed reference dataset with ring artifacts in the center. (d–m) depict the xy-slice views of the SIRT datasets with iteration parameters increasing from 10 to 700 exemplarily.

one cuboid. Attenuations are calculated by applying Lambert-Beer's law. The X-ray scatter and the blurring effects were disabled for the simulation. The virtual projection images are processed using the FDK reconstruction algorithm. We applied a Gaussian filter with increasing smoothing effect to generate five additional volumes. No smoothing was applied to the first dataset. The individual variances of the Gaussian smoothing in the range [0.2, 1.0] are increased by a step of 0.2. In a preprocessing step, a user-defined ROI is selected and applied to all ensemble volumes (see Figure 8b). The resolution of the ROI cutouts are $16 \times 16 \times 16$ voxels. Figure 8c depicts an xy-slice of the dataset without smoothing. Figures 8d–h show xy-slices of the different results of the Gaussian smoothing filter.

The second ensemble consists of 16 datasets from a real-world open-cell polyurethane foam specimen, which was scanned with a Bruker Skyscan 1294 TLGI-XCT device at a resolution of 11.4 microns. The size of each dataset is $550 \times 550 \times 250$ voxels and the data type is unsigned short. To compare the individual datasets, we normalized the intensities (itk::NormalizeImageFilter) by setting the mean to zero and the variance to one. We then rescale the intensities between 0 and 65535. Figure 9a shows the thin cell walls of the foam specimen, which are revealed by the DFC modality. In the middle of the foam specimen we cut out an ROI of $64 \times 64 \times 64$ voxels (see Figure 9b). Figure 9c depicts an xy-slice of the cutout reference dataset, which

was reconstructed from 900 projections using the FDK algorithm. The center of Figure 9c shows ring artifacts. The other 15 datasets were reconstructed using the simultaneous iterative reconstruction technique (SIRT) [12] with 900 projections and the following increasing iteration parameters: 10, 50, 100, 150,...,700. Figures 9d–m present the SIRT volumes with increasing iteration parameters.

5 RESULTS

In this section we present two case studies that reflect the domain-specific requirements and present the capabilities of *Dynamic Volume Lines*. First, we analyze reconstruction data from the simulated XCT specimen, and in our second case study, we analyze the real-world XCT specimen.

5.1 Case study 1: Simulated XCT Dataset

The specimen analyzed here is an artificial dataset from simulated XCT with three cylindrical bars orthogonal to each other (see Section 4.2). Two of the bars have attachments at their ends, one of which is a sphere, the other one is a cube. Different levels of smoothing produce a volume ensemble, as shown in Figure 8. The ROI cutout for this analysis covers the end of the bar with the attached cube, as shown in Figure 10a.

The analysis goal for this dataset mainly has been to determine interesting regions, which correspond to areas where the most changes happen in the ensemble. We use a synthetic dataset in order to show the basic behavior of *Dynamic Volume Lines* under well-defined conditions. We set a filter for regions with high local variations, in this case we select an importance-range between 0.5 and 1. The 3D spatial view displays the respective regions in each member, as can be seen in Figure 10b. The voxels displayed there clearly indicate that the regions with most changes are located at the edges of the cube. The selection also gets highlighted in the nonlinearly scaled Hilbert line plot and the scaling widget shown in Figure 10c and 10d. The scaling widget visualizes the importance through the color coding (white to light-gray for the selection) and by the trapezoidal shapes, which are much broader at the top row as compared to the bottom. The background threshold is set to 30000. Intensities below this threshold correspond to air and are not of interest for this analysis. Figure 10c shows these background regions, which are marked with light orange boxes. The parameter p to influence the nonlinear scaling (see Section 3.2, Equation 2) is set to 1.4. For this dataset, this setting ensures a good balance between emphasizing regions with high variances, but still keeping background regions and regions with low variances visible.

5.2 Case study 2: Real-world XCT Dataset

We analyze the ensemble of 16 volumes from the foam specimen (see Section 4.2) as shown in Figure 9. Each volume of the ensemble is represented by a Hilbert curve of length 262144. The histogram heatmap displayed in Figure 11a shows that there is a broad variation in the lower intensities, indicated by the white region. There are less intensities in the upper range, and the histogram colors indicate lower frequencies there. This implies that most of the space is occupied by voids, the remaining space is left to the cell walls. It is also a hint that some volumes do not represent the cell walls very well.

When zooming in and viewing the 1D Hilbert line plots as shown in Figure 11b, one can see at a glance that the volumes differ vastly in their local intensity variation. The ensemble member corresponding to the bottom, dark green Hilbert line plot is nearly flat, indicating a low contrast of the intensities. The topmost, light-green plot shows highly varying intensities, revealing a high contrast. Figure 11c gives the functional boxplots of the 1D Hilbert line plots (shown in Figure 11b). The gray colored interquartile range covers the volumes with iterations from 250 to 650. The volume with 500 iterations is the median. In areas of low local intensity variation, the minimum and maximum of the functional boxplots are very close to each other. The background threshold is set to zero, because in this analysis scenario we are interested in low intensities as well. Since there is no compression due to the background, there are more voxels competing for available screen space. The parameter p to influence the nonlinear scaling (see Section 3.2, Equation 2) is increased to 2 in order to compress regions
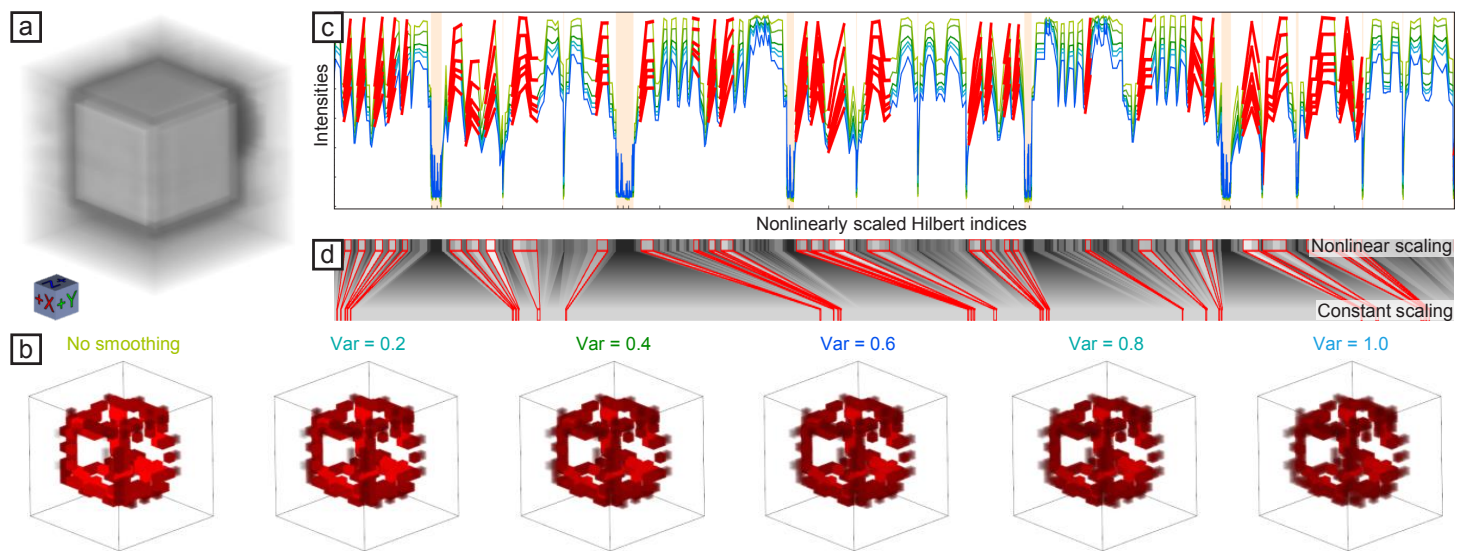
Fig. 10. (a) 3D rendering of the volume without smoothing. (b) 3D volume renderings of the selected voxels for all six ensemble members. (c) Corresponding Hilbert line plots with highly important regions selected. (d) Scaling widget with selection highlighted in red.

with low variance more and to expand interesting regions with high variance.

We select regions with an importance-value between 0.1 and 1 (high variation of the intensities). As can be seen in Figure 11d, only the cell walls show such high variations. Based on the importance-function, the cell walls can be separated easily. The selected indices are highlighted in the scaling widget shown in Figure 11e. Inspecting the Hilbert line plots (see Figure 11b) and the 3D views of the different parameter variations (see Figure 11d), we can see that the volumes produced by the SIRT algorithm with less than 250 iterations result in low contrast between cell walls and voids. Starting from approximately 350 iterations, the contrast converges to the FDK reference volume. Since doubling the number of iterations also means doubling the required reconstruction time, we can conclude that we can stop the reconstruction at 400 iterations without a major loss of accuracy.

When selecting regions with a low importance-value between 0 and 0.001 (low variation of intensities), the ring artifacts are selected, as shown in Figure 11f. This indicates that the SIRT iterations do not suppress the ring artifacts. Both FDK and SIRT are affected by them in exactly the same way. The importance-function could therefore be used to detect such artifacts. They are the only features in the volumes, which show only little variation with different reconstruction parameters. Figure 11g shows in the Hilbert line plots that in the lower intensity range there is in general a low variation in all the volumes. There is even less variation in the highlighted regions of the ring artifacts. We therefore hypothesize that there is potential to use the local ensemble variation to develop a ring-artifact reduction algorithm for the reconstructed volumes. This is an insight that would not have been possible without the knowledge gained from the analysis with *Dynamic Volume Lines*.

5.3 Performance Measurements

The experiments were performed on a desktop machine with an Intel(R) Core(TM) i7-3770 CPU, 32 GB RAM and an NVIDIA GeForce GTX 1080 with 8 GB RAM. The *Dynamic Volume Lines* were implemented in C++. ITK 4.9 has been used to perform basic image processing, to load the datasets, and to generate the Hilbert curves [41]. The 3D views were rendered with VTK 7.0. The histogram heatmap and the 1D Hilbert line plots were built with the QCustomPlot 2.0 library [5]. The scaling widget was implemented in Qt 5.8.

Computing the Hilbert curves for example for 16 datasets with a size of $64 \times 64 \times 64$ voxels (see Figure 8) takes approximately 12 seconds. This includes creating the nonlinear scaling, building the segment tree, and the initial rendering of the charts. Dragging and zooming within the charts works in real-time. The performance of selecting 1D Hilbert

line plots and rendering the corresponding 3D views depends on the number of chosen line segments and on the number of chosen volumes, but typically takes less than 5 seconds.

6 CONCLUSION AND FUTURE WORK

In this paper we introduce *Dynamic Volume Lines* for the interactive visual analysis and comparison of ensembles of 3D volumes using 1D Hilbert line plots. Volumes are linearized along a space-filling Hilbert curve. We introduce an aggregate overview visualization for volume ensembles as a histogram heatmap, which encodes the intensity frequencies. We provide nonlinear scaling to emphasize regions with high local variation, and to optimally utilize the available screen space. We illustrate the scaling in an interactive scaling widget. We investigate the usefulness of *Dynamic Volume Lines* with two case studies. Using a simulated XCT dataset, we investigate the general usefulness of the tool in detecting local variations in the ensemble. On a real-world foam dataset we showed that our importance-function, based on local variations, can be used to detect structures such as cell walls, and to discover unwanted ring artifacts.

Our domain expert collaborators were very positive about the possibility to compare multiple volumes at once, as they previously had no comprehensive tool available to support this analysis scenario. They also positively mentioned the guidance towards interesting regions, i.e., areas with high local variations. It was important for them to be able to investigate selected regions in more detail, and to retain the relation to the spatial domain. This allowed them to draw conclusions and gain insights for adaptations in their algorithm development.

Due to a technical implementation detail, the current prototype limits the maximum region of interest that can be analyzed to $256 \times 256 \times 256$ voxels. We are confident that with minor adaptations this limitation can be removed to support the analysis of much larger volumes. In general, the concept of representing an ensemble of volumes as nonlinear 1D Hilbert line plots is not limited to 3D space, but can also be applied to (abstract) n-dimensional spaces.
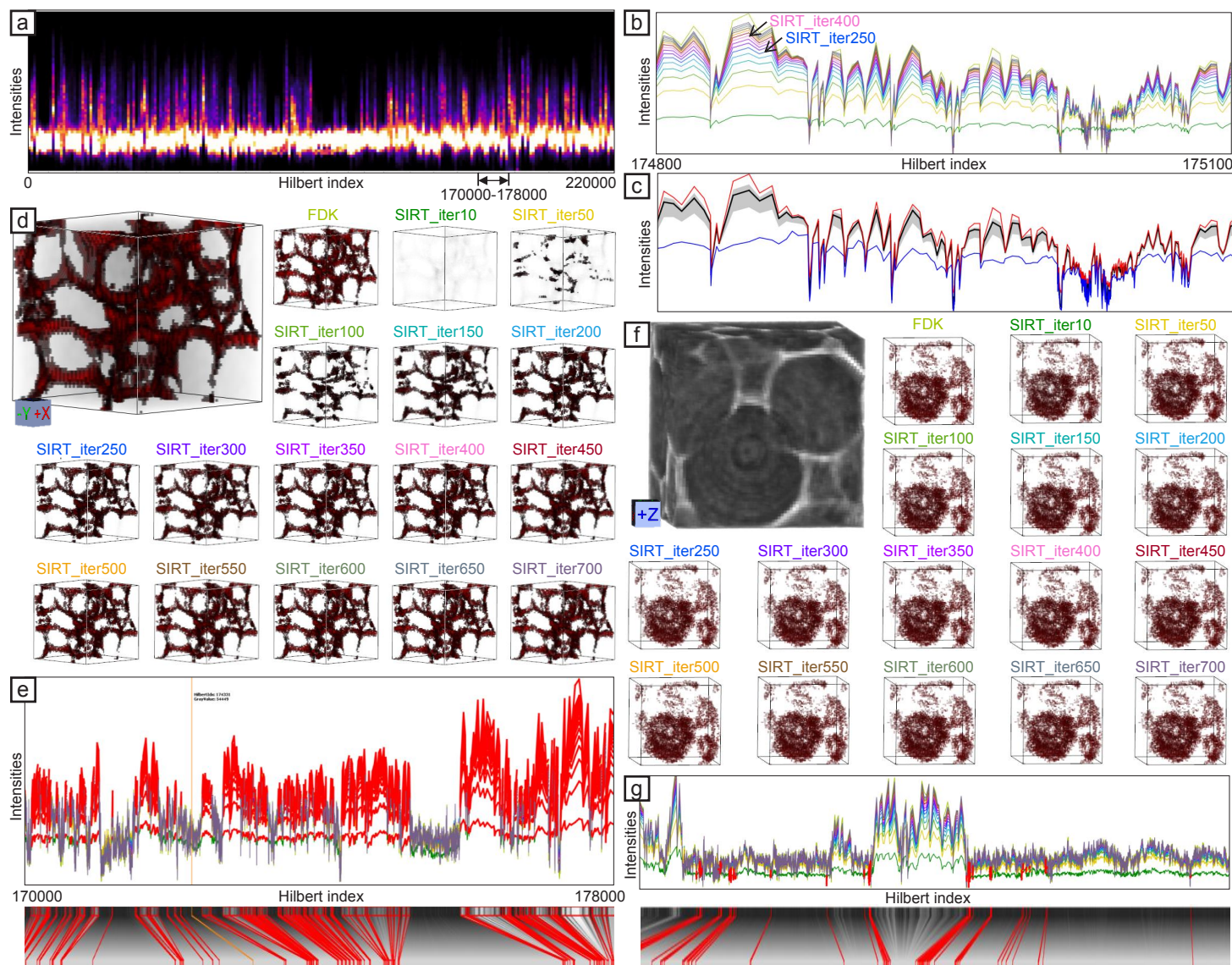
Fig. 11. (a) Histogram heatmap of the foam volumes ensemble showing most intensities in the lower range. (b) 1D Hilbert line plots zoom-in, enabling a detailed comparison of the reconstruction volumes. (c) Functional boxplots of the 1D Hilbert line plots in (b). (d) 3D views of regions with selected high importance, coinciding with the foam cell walls. (e) Regions of high importance as in (d), selected in the 1D Hilbert line plots. (f) 3D views of regions with selected low importance, coinciding with the ring artifacts. (g) Regions of low importance as in (f), selected in the 1D Hilbert line plots.

REFERENCES

[1] 7span. MaterialUI. https://www.materialui.co (accessed on 26-Jun-2018).

[2] M. de Berg, O. Cheong, M. van Kreveld, and M. Overmars. *Computational Geometry: Algorithms and Applications*, chap. More Geometric Data Structures, pp. 219–241. 2008. doi: 10.1007/978-3-540-77974-2_10

[3] I. Demir, C. Dick, and R. Westermann. Multi-Charts for Comparative 3D Ensemble Visualization. *IEEE Transaction on Visualization and Computer Graphics*, 20(12):2694–2703, 2014. doi: 10.1109/TVCG.2014.2346448

[4] I. Demir, M. Jarema, and R. Westermann. Visualizing the Central Tendency of Ensembles of Shapes. In *SIGGRAPH ASIA 2016 Symposium on Visualization*, SA '16, pp. 3:1–3:8, 2016. doi: 10.1145/3002151.3002165

[5] E. Eichhammer. QCustomPlot. http://www.qcustomplot.com/ (accessed on 26-Jun-2018).

[6] L. A. Feldkamp, L. C. Davis, and J. W. Kress. Practical cone-beam algorithm. *Journal of the Optical Society of America A*, 1(6):612–619, 1984. doi: 10.1364/JOSAA.1.000612

[7] B. Fröhler, T. Möller, and C. Heinzl. GEMSe: Visualization-Guided Exploration of Multi-channel Segmentation Algorithms. *Computer Graphics Forum*, 35(3):191–200, 2016. doi: 10.1111/cgf.12895

[8] M. G. Genton, C. Johnson, K. Potter, G. Stenchikov, and Y. Sun. Surface boxplots. *Stat*, 3(1):1–11, 2014. doi: 10.1002/sta4.39

[9] M. Gleicher, D. Albers, R. Walker, I. Jusufi, C. D. Hansen, and J. C. Roberts. Visual Comparison for Information Visualization. *Information Visualization*, 10(4):289–309, 2011. doi: 10.1177/1473871611416549

[10] R. Gosselin and D. Rodrigue. Cell morphology analysis of high density polymer foams. *Polymer Testing*, 24(8):1027 – 1035, 2005. doi: 10.1016/j.polymertesting.2005.07.005

[11] C. Gotsman and M. Lindenbaum. On the metric properties of discrete space-filling curves. In *Proceedings of the 12th IAPR International Conference on Pattern Recognition*, vol. 3, pp. 98–102, 1994. doi: 10.1109/ICPR.1994.577130

[12] J. Gregor and T. Benson. Computational Analysis and Improvement of SIRT. *IEEE Transactions on Medical Imaging*, 27(7):918–924, 2008. doi: 10.1109/TMI.2008.923696

[13] C. H. Hamilton and A. Rau-Chaplin. Compact Hilbert Indices for Multi-Dimensional Data. In *1st International Conference on Complex, Intelligent and Software Intensive Systems*, pp. 139–146, 2007. doi: 10.1109/CISIS.2007.16

[14] C. H. Hamilton and A. Rau-Chaplin. Compact Hilbert Indices: Space-filling Curves for Domains with Unequal Side Lengths. *Information Processing Letters*, 105(5):155–163, 2008. doi: 10.1016/j.ipl.2007.08.034

[15] C. Heinzl and S. Stappen. STAR: Visual Computing in Materials Science. *Computer Graphics Forum*, 36(3):647–666, 2017. doi: 10.1111/cgf.13214

[16] M. Jarema, I. Demir, J. Kehrer, and R. Westermann. Comparative visual analysis of vector field ensembles. In *IEEE Visual Analytics Science and Technology*, pp. 81–88, 2015. doi: 10.1109/VAST.2015.7347634

[17] I. Jerjen, V. Revol, P. Schuetz, C. Kottler, R. Kaufmann, T. Luethi, K. Jefimovs, C. Urban, and U. Sennhauser. Reduction of phase artifacts in differential phase contrast computed tomography. *Optics Express*, 19(14):13604–13611, 2011. doi: 10.1364/OE.19.013604

[18] Z. Konyha, A. Lež, K. Matković, M. Jelović, and H. Hauser. Interactive Visual Analysis of Families of Curves Using Data Aggregation and Derivation. In *Proceedings of the 12th International Conference on Knowledge Management and Knowledge Technologies*, i-KNOW '12, pp. 24:1–24:8, 2012. doi: 10.1145/2362456.2362487

[19] S.-T. Lee, C. B. Park, and N. S. Ramesh. *Polymeric Foams: Science and Technology*. CRC Press, 2006.

[20] N. Lindow, D. Baum, and H.-C. Hege. Perceptually Linear Parameter Variations. *Computer Graphics Forum*, 31(2pt4):535–544, 2012. doi: 10.1111/j.1467-8659.2012.03054.x

[21] M. M. Malik, C. Heinzl, and E. Gröller. Comparative Visualization for Parameter Studies of Dataset Series. *IEEE Transaction on Visualization and Computer Graphics*, 16(5):829–840, 2010.

[22] K. Matković, D. Gracanin, B. Klarin, and H. Hauser. Interactive Visual Analysis of Complex Scientific Data As Families of Data Surfaces. *IEEE Transactions on Visualization and Computer Graphics*, 15(6):1351–1358, 2009. doi: 10.1109/TVCG.2009.155

[23] P. Mindek, G. Mistelbauer, E. Gröller, and S. Bruckner. Data-sensitive Visual Navigation. *Computers and Graphics*, 67(C):77–85, 2017. doi: 10.1016/j.cag.2017.05.012

[24] M. Mirzargar, R. Whitaker, and R. Kirby. Curve boxplot: Generalization of boxplot for ensembles of curves. *IEEE Transactions on Visualization and Computer Graphics*, 20(12):2654–2663, 2014. doi: 10.1109/TVCG.2014.2346455

[25] M. Mlejnek, P. Ermes, A. Vilanova, R. van der Rijt, H. van den Bosch, F. Gerritsen, and E. Gröller. Profile Flags: a Novel Metaphor for Probing of T2 Maps. In *Proceedings of IEEE Visualization 2005*, pp. 599–606, 2005.

[26] B. Moon, H. v. Jagadish, C. Faloutsos, and J. H. Saltz. Analysis of the Clustering Properties of the Hilbert Space-Filling Curve. *IEEE Transactions on Knowledge and Data Engineering*, 13(1):124–141, 2001. doi: 10.1109/69.908985

[27] K. Moreland. Why We Use Bad Color Maps and What You Can Do About It. *Electronic Imaging*, 2016(16):1–6, 2016. doi: 10.2352/ISSN.2470-1173.2016.16.HVEI-133

[28] F. Pfeiffer, C. Kottler, O. Bunk, and C. David. Hard X-Ray Phase Tomography with Low-Brilliance Sources. *Physical Review Letters*, 98:108105, 2007. doi: 10.1103/PhysRevLett.98.108105

[29] H. Piringer, S. Pajer, W. Berger, and H. Teichmann. Comparative Visual Analysis of 2D Function Ensembles. *Computer Graphics Forum*, 31(3pt3):1195–1204, 2012. doi: 10.1111/j.1467-8659.2012.03112.x

[30] K. Potter, A. Wilson, P.-T. Bremer, D. Williams, C. Doutriaux, V. Pascucci, and C. R. Johnson. Ensemble-Vis: A Framework for the Statistical Visualization of Ensemble Data. In *IEEE Workshop on Knowledge Discovery from Climate Data: Prediction, Extremes*, pp. 233–240, 2009.

[31] M. Raj, M. Mirzargar, J. S. Preston, R. M. Kirby, and R. T. Whitaker. Evaluating Shape Alignment via Ensemble Visualization. *IEEE Computer Graphics and Applications*, 36(3):60–71, 2016. doi: 10.1109/MCG.2015.70

[32] M. Reiter, M. Erler, C. Kuhn, C. Gusenbauer, and J. Kastner. SimCT: a simulation tool for X-ray imaging. In *Proceedings of the 6th Conference on Industrial Computed Tomography*, 2016.

[33] J. Sanctorum, E. Janssens, A. den Dekker, S. Senck, C. Heinzl, J. D. Beenhouwer, and J. Sijbers. A workflow to reconstruct grating-based X-ray phase contrast CT images: application to CFRP samples. In *Proceedings of the 4th conference on X-ray and neutron phase imaging with gratings*, pp. 139–140, 2017.

[34] J. Schmidt, M. E. Gröller, and S. Bruckner. VAICo: Visual Analysis for Image Comparison. *IEEE Transactions on Visualization and Computer Graphics*, 19(12):2090–2099, 2013. Demo: https://users.cg.tuwien.ac.at/jschmidt/vaico/ (accessed on 26-Jun-2018).

[35] J. Schmidt, R. Preiner, T. Auzinger, M. Wimmer, E. Gröller, and S. Bruckner. YMCA - Your Mesh Comparison Application. In *IEEE Visual Analytics Science and Technology*, 2014. doi: 10.1109/VAST.2014.7042491

[36] M. Sedlmair, C. Heinzl, S. Bruckner, H. Piringer, and T. Möller. Visual Parameter Space Analysis: A Conceptual Framework. *IEEE Transactions on Visualization and Computer Graphics*, 20(12):2161–2170, 2014. doi: 10.1109/TVCG.2014.2346321

[37] S. Senck, B. Plank, J. Kastner, V. Revol, K. Dobes, and M. Scheerer. Non-destructive evaluation of defects in polymer matrix composites for aerospace applications using X-ray Talbot-Lau interferometry and micro CT. In *58th AIAA/ASCE/AHS/ASC Structures, Structural Dynamics, and Materials Conference, AIAA SciTech Forum*, pp. 1–9, 2017.

[38] B. Shneiderman. The Eyes Have It: A Task by Data Type Taxonomy for Information Visualizations. In *Proceedings of the IEEE Symposium on Visual Languages*, VL '96, pp. 336–343, 1996.

[39] Y. Sun and M. G. Genton. Functional Boxplots. *Journal of Computational and Graphical Statistics*, 20(2):316–334, 2011. doi: 10.1198/jcgs.2011.09224

[40] T. Torsney-Weir, M. Sedlmair, and T. Möller. Sliceplorer: 1D Slices for Multi-dimensional Continuous Functions. *Computer Graphics Forum*, 36(3):167–177, 2017. doi: 10.1111/cgf.13177

[41] N. Tustison. Why do walks with Hilbert seem to take so long? Insight Journal, 2011. http://hdl.handle.net/10380/3324 (accessed on 26-Jun-2018).

[42] J. Weissenböck, A. Amirkhanov, E. Gröller, J. Kastner, and C. Heinzl. PorosityAnalyzer: Visual Analysis and Evaluation of Segmentation Pipelines to Determine the Porosity in Fiber-Reinforced Polymers. In *Proceedings of IEEE Visual Analytics Science and Technology*, pp. 101–110, 2016. doi: 10.1109/VAST.2016.7883516

[43] R. T. Whitaker, M. Mirzargar, and R. M. Kirby. Contour Boxplots: A Method for Characterizing Uncertainty in Feature Sets from Simulation Ensembles. *IEEE Transactions on Visualization and Computer Graphics*, 19(12):2713–2722, 2013. doi: 10.1109/TVCG.2013.143

A Visual Tool for the Analysis of Algorithms for Tomographic Fiber Reconstruction in Materials Science

Bernhard Fröhler, Tim Elberfeld, Torsten Möller, Hans Christian Hege, Johannes Weissenböck, Jan De Beenhouwer, Jan Sijbers, Johann Kastner, Christoph Heinzl

A Visual Tool for the Analysis of Algorithms for Tomographic Fiber Reconstruction in Materials Science

B. Fröhler[1,3] (ID), T. Elberfeld[2] (ID), T. Möller[3] (ID), H. C. Hege[4] (ID), J. Weissenböck[1] (ID),
J. De Beenhouwer[2] (ID), J. Sijbers[2] (ID), J. Kastner[1] (ID) and C. Heinzl[1] (ID)

[1]Research Group Computed Tomography, University of Applied Sciences Upper Austria, Austria
[2]imec-Vision Lab, University of Antwerp, Belgium
[3]Data Science @ Uni Vienna, and Faculty of Computer Science, University of Vienna, Austria
[4]Visual Data Analysis Department, Zuse Institute Berlin, Germany

Abstract

We present visual analysis methods for the evaluation of tomographic fiber reconstruction algorithms by means of analysis, visual debugging and comparison of reconstructed fibers in materials science. The methods are integrated in a tool (FIAKER) that supports the entire workflow. It enables the analysis of various fiber reconstruction algorithms, of differently parameterized fiber reconstruction algorithms and of individual steps in iterative fiber reconstruction algorithms. Insight into the performance of fiber reconstruction algorithms is obtained by a list-based ranking interface. A 3D view offers interactive visualization techniques to gain deeper insight, e.g., into the aggregated quality of the examined fiber reconstruction algorithms and parameterizations. The tool was designed in close collaboration with researchers who work with fiber-reinforced polymers on a daily basis and develop algorithms for tomographic reconstruction and characterization of such materials. We evaluate the tool using synthetic datasets as well as tomograms of real materials. Five case studies certify the usefulness of the tool, showing that it significantly accelerates the analysis and provides valuable insights that make it possible to improve the fiber reconstruction algorithms. The main contribution of the paper is the well-considered combination of methods and their seamless integration into a visual tool that supports the entire workflow. Further findings result from the analysis of (dis-)similarity measures for fibers as well as from the discussion of design decisions. It is also shown that the generality of the analytical methods allows a wider range of applications, such as the application in pore space analysis.

Keywords

Simulation, parameter space analysis, ensemble visualization, industrial CT

1. Introduction

Fiber-reinforced polymers (FRPs) are in high demand for a number of manufacturing industries such as automobile or aeronautics, since they provide high strength, durability, and elasticity while being lightweight. To ascertain and optimize the targeted application-specific properties of FRPs, material scientists need to be able to quantify and model the characteristics especially of the reinforcement components, i.e., fibers. Important characteristics of a fiber are, for example, start and end point, center point, direction, length and diameter. A typical method to determine the fiber characteristics is acquiring images of an FRP specimen using X-ray Computed Tomography (CT) [KH18], and then applying customized data processing pipelines to extract the fibers and their characteristics. An overview of such methods as well as on existing analysis and visualization tools is given in Section 2.

In multiple discussions with our collaborators, both developers of fiber characterization algorithms and domain scientists using these algorithms, we found that there is a great need for a specialized tool for the analysis and comparison of algorithms for determining fiber characteristics. Our collaborators typically employ generic visualization tools, custom quantification scripts, written for example in MATLAB or Python, or resort to a manual analysis in specific cases. Each of these methods is tailored to the output format of the analyzed algorithm. Furthermore, these methods require prior domain knowledge, e.g., when setting up specific visualization pipelines in the generic tools, or when developing custom quantification scripts. Finally, each of these methods requires a considerable amount of time to set up, and does not provide inherent possibilities for comparing multiple datasets.

When analyzing the requirements of our collaborators, we found that they require support regarding the following analysis tasks:

1. to compare multiple results, specifically,
   a. to quantitatively compare average accuracy between results
   b. to qualitatively compare visual representations of results

2. to explore and identify fibers with specific properties, such as
   a. fibers growing too long in the optimization
   b. undiscovered or wrongly matched fibers
3. to visually investigate the influences of
   a. the input data itself (fiber and dataset characteristics),
   b. the input parameters (of the acquisition or fiber characterization pipeline); and finally
4. to easily create visualizations to communicate the results via scientific publications, presentations and posters.

In an iterative design process we then started designing and developing methods to address these tasks. In each step of the iteration, we discussed prototypes of our methods with our collaborators and let them experiment with these prototypes on their own data. Based on their feedback, we refined our methods. The final prototype implementing these methods is the tool for FIber reconstruction Algorithm (K/)Comparison and ExploRation (FIAKER), described in this paper.

We see our contributions in the methods and tools for analyzing fiber characterization algorithms, which we describe in Section 4. A further contribution is the evaluation of these methods in Section 5, where we analyze some synthetic and real world datasets with our methods, and indicate how they speed up the analysis of fiber reconstruction algorithms. An additional contribution described there is the evaluation of a variety of fiber dissimilarity measures, as well as explanations how to apply our methods in the similar scenario of analyzing pore characterization algorithms. Section 6 provides a discussion of the design decisions and the lessons learned during the design of FIAKER.

2. Background and Related Work

Figure 1 shows a schematic of pipelines for determining fiber characteristics from data acquired by CT. Conventional pipelines follow a sequential approach. In the CT device, X-rays are attenuated by a specimen (a) to generate projection images from multiple angles (b). From the set of acquired projections, a 3D image is reconstructed (c). Then, a variety of image processing steps are performed to extract and segment the individual fibers (d). In the last step, the characteristics of each segmented fiber are determined (e). Examples of such types of pipelines are presented in the works of Salaberger et al. [SKK*11,SJKK15]. More recently, techniques for a direct extraction of fiber characteristics from CT projection data have been proposed. For example, Elberfeld et al. [Edd*18] reconstruct volumes from a small numbers of projection angles and then estimate position, direction and length of the contained fibers using a priori knowledge of their shape, modeled as a geometric representation. This direct step is indicated by the red arrow from (b) to (e) in Figure 1. The estimates are then iteratively improved by minimizing the error that results when comparing with the original projection images. Konopczyński et al. [KRR*18] show that applying deep neural networks also can deliver reasonable results. However, a significant amount of time has to be invested for training these networks on synthetic and real-world data.

We refer to the outcome of a single parameterization of a specific fiber characterization pipeline as a *result*. We use the term *ensemble* to refer to multiple results from either different parameterizations
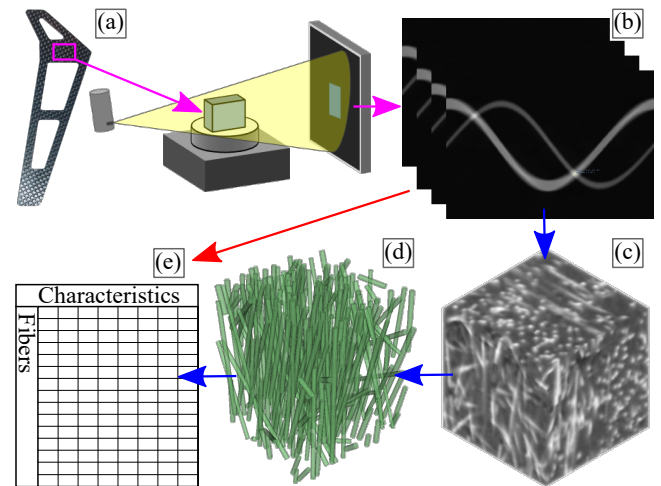

Figure 1: *Schematic of fiber characterization pipelines: A specimen (a) is scanned via computed tomography, the scanned projection images (b) are reconstructed to a 3D volume (c), which is segmented (d). The characteristics of each fiber (e) are quantified either from the segmented data or from the projection images.*

of the same pipeline or from different pipelines. When developing a new fiber characterization algorithm, one typically starts with a synthetic dataset: a ground truth with a known characterization result, which we will refer to as *reference*. In the analysis, the reference is part of the ensemble.

The use of visualization techniques to optimize these algorithms can be considered as visual parameter space analysis (VPSA) as proposed by Sedlmair et al. [SHB*14]. In the typical VPSA scenario, for each result a fixed number of global quality measures is computed. While average measures for a result can also be computed in our case, we require new approaches for analyzing and comparing the single fibers and their characteristics.

For the analysis of a single result, the methods by Fritz et al. [FHG*09] as well as by Weissenböck et al. [WAL*14] can provide insights into the distribution of fiber characteristics. Yet their methods are not suited to analyze details of the algorithms, such as intermediate steps from iterative algorithms. Furthermore, these methods only deal with a single result and cannot help in comparing multiple results or in analyzing the differences between a result and the reference. Zhang et al. [ZFS*19] provide similar capabilities for the analysis of the formation of bubbles in porous media. They analyze multiple similar pores, in volumetric data acquired via computed tomography. As their method enables the user to compare pores inside a dataset with each other, it is also targeted at analyzing a single result.

The algorithms we analyzed, model the fibers as straight cylinders. For 3D visualization, we therefore create triangle meshes in appropriate detail. Tools such as YMCA by Schmidt et al. [SPA*14] or DreamLens by Matejka et al. [MGB*18] are similar as they compare multiple 3D shapes. However, they are not required in our context because we only need the meshes for qualitative inspection and visual comparison. For the analysis of more general

polytopes, Torsney-Weir et al. [TWMSK18] explore the concept of 1D slicing. Their methods target the comparison of polytopes with more than three dimensions, and do not provide means to compare additional characteristics associated with these polytopes.

To match the fibers of the different results, we compute their similarity. For this purpose, we employ fiber similarity measures. Such measures are also used in the imaging of white brain matter through diffusion magnetic resonance imaging (dMRI). For example O'Donnel and Westin [OW07] employ a distance based on the mean closest point distance between two fibers. Quan and Vo [QV15] propose a measure based on the center of mass as well as the start and end point of each fiber. Bhattacharya et al. [BWW*17] employ distance measures for the clustering of fiber tracts of industrial fiber-reinforced materials into fiber bundles. While these measures are designed for clustering similar fibers, we are interested in determining matches of the same underlying fiber in different datasets. In our case, the ideal distance measure therefore must always rank the pair of best-matching fibers first, while for the use cases cited above, the absolute order is not that crucial. Analogously to Labra et al. [LGD*17], we utilize multiple measures with differing accuracy and performance in order to speed up our computations. While in dMRI (for an overview see e.g., Schultz and Vilanova [SV18]) the input data are tensor fields or more general orientation fields from which the fibers have to be reconstructed with numerical methods, in our case the individual fibers are explicitly given.

3. Fiber Dissimilarity Measures

For analysis purposes, we need to determine which fiber in the predefined reference matches best a particular fiber in a result. This requires measuring the dissimilarity of fibers in the reference and the result, as shown in Figure 4(c). We considered and implemented a number of different fiber dissimilarity measures:

1. Measures based on differences in the characteristics
2. Measures based on fiber point distances
3. Measures based on fiber overlap

The first category measures the dissimilarity through the difference in the fiber characteristics: the fiber center, the direction as azimuth (ϕ) and elevation (θ) angles in a spherical coordinate system, as well as the length of the fiber. The fiber dissimilarity can then be computed as the Euclidean distance in the 6-dimensional space spanned by these six fiber characteristics. Let us assume we are analyzing a result where for each fiber a we have the fiber center as a position vector $\mathbf{c}_a$, its orientation angles ϕ_a and θ_a as well as the fiber length l_a, as shown in Figure 2(a). With $\mathbf{f}_a = (\mathbf{c}_a, \phi_a, \theta_a, l_a)$ being the 6-dimensional vector of all those feature characteristics, the dissimilarity between fiber a and b is computed as

$$\check{d}_1^c(a,b) = \|\mathbf{f}_a - \mathbf{f}_b\|_2, \qquad (1)$$

where $\|\|_2$ denotes the Euclidean distance. This measure is used in the evaluation of the optimizing algorithm by Elberfeld et al. [Edd*18]. The problem with this measure is that the components of the vectors have different physical dimensions and are therefore not comparable. A methodically clean way would be the introduction of weight factors.

For this reason, we have also experimented with a normalized measure, in which we form a weighted sum of the Euclidean distance of the center points and the absolute differences of the other characteristics, the weights being used to normalize each term by its maximum possible value, so as not to over-emphasize a single characteristic. This dissimilarity measure is given as

$$\check{d}_2^c(a,b) = \frac{1}{4}\left(w_1 \cdot \|\mathbf{c}_a - \mathbf{c}_b\|_2 + w_2 \right. \qquad (2)$$
$$\left. \cdot |\phi_a - \phi_b| + w_3 \cdot |\theta_a - \theta_b| + w_4 \cdot |l_a - l_b|\right).$$

Here the coefficient w_1 is the inverse of the diagonal length of the bounding box containing the fibers from all results, w_2 and w_3 are the inverses of the maximum possible differences between two ϕ and θ angles, respectively, and w_4 is the inverse of the difference between the shortest and the longest fiber in all results.

We also evaluated three dissimilarity measures considering fiber point distances. The first is computed as the sum of the Euclidean distances between start, end and center points of two fibers:

$$\check{d}_1^p(a,b) = \sum_{\mathbf{i}\in(\mathbf{s},\mathbf{c},\mathbf{e})} \|\mathbf{i}_a - \mathbf{i}_b\|_2, \qquad (3)$$

where $\mathbf{s}$, $\mathbf{c}$ and $\mathbf{e}$ denote the start positions, centers and end positions of fibers a and b, respectively.

The measures introduced so far are not invariant to a rotation of one fiber by 180 degrees – meaning that even if fiber b in the result is exactly matching fiber a, but a is specified rotated by 180 degrees with respect to b, these measures will tell us that there is a high difference between them. As the result of structural analyses does not differ for these two cases, they should be considered equal in our tool as well. Therefore, we need to compute these distances twice, once as defined above, and a second time with the start and end position vectors for fiber b exchanged, or, for measures d_1^c and d_2^c, with direction angles ϕ and θ rotated by 180 degrees. The resulting fiber is denoted as b^-. We then use the minimum of the two distances as final measure

$$d(a,b) = \min(\check{d}(a,b), \check{d}(a,b^-)). \qquad (4)$$

We always use $\check{d}$ as an indicator that the metric d is afflicted by this orientation dependency issue.

In an attempt to overcome this limitation, we analyzed a second measure based on point distances, namely the sum of distances between all pairs of these three points:

$$d_2^p(a,b) = \sum_{\mathbf{i}\in(\mathbf{s},\mathbf{c},\mathbf{e})} \sum_{\mathbf{j}\in(\mathbf{s},\mathbf{c},\mathbf{e})} \|\mathbf{i}_a - \mathbf{j}_b\|_2. \qquad (5)$$

While this measure is not affected by the direction of the fibers, it does come with the disadvantage of being dependent on the fiber length. It cannot trivially be normalized to correct for this dependency on the fiber length.

We then sought a more mathematically grounded dissimilarity measure and came up with a measure based on the (square of) the average distance of corresponding points along the two fibers a and b. It leads to the measure

$$\check{d}_3^p(a,b) = \sqrt{\|\mathbf{s}_a - \mathbf{s}_b\|_2 + \|\mathbf{e}_a - \mathbf{e}_b\|_2 + (\mathbf{s}_a - \mathbf{s}_b) \cdot (\mathbf{e}_a - \mathbf{e}_b)}. \quad (6)$$
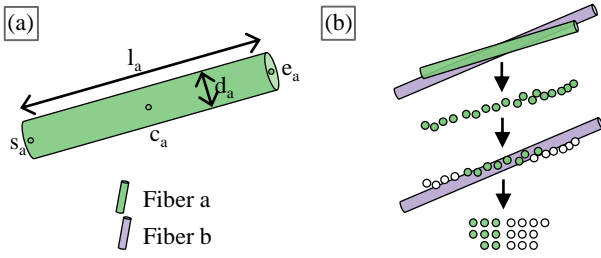
Figure 2: Fiber characteristics (a): Start point s_a, center point c_a, end point e_a, length l_a, diameter d_a. Overlap-based dissimilarity measure computation (b): Points in reference are sampled, checked for inclusion in result fiber, result is the ratio between included and total.

We can see that it depends only on the Euclidean distances between start and end points in $\mathbb{R}^3$, as well as the angle between the vectors $\mathbf{s}_a - \mathbf{s}_b$ and $\mathbf{e}_a - \mathbf{e}_b$. This measure is also subject to the orientation dependency issue; therefore the final distance is again computed with the help of Equation 4.

We also considered dissimilarity measures based on volume overlap. To compute them, we follow the procedure schematically depicted in Figure 2(b): We first sample a collection p_a of random points inside the cylinder of fiber a. We then count how many of those points are contained in the cylinder representing fiber b. The overlap is then defined as

$$o(a,b) = \frac{c(p_a,b)}{\#p_a},\qquad(7)$$

where $c(p_a,b)$ denotes the count of points in p_a that are contained in the cylinder of fiber b, while $\#p_a$ stands for the cardinality of p_a, i.e., the number of sampled points.

In an attempt to create a symmetric measure, we always sample the fiber with less volume, and check inclusion in the fiber with higher volume, since a cylinder with larger volume can never be fully included in one with a smaller volume. This leads to our first definition of an overlap-based dissimilarity measure as

$$d_1^o(a,b) = 1 - \begin{cases} o(a,b) & \text{for } v(a) < v(b) \\ o(b,a) & \text{otherwise} \end{cases},\qquad(8)$$

where $v(a)$ denotes the volume of fiber a. This measure might be sufficient for some cases, but it delivers a dissimilarity of 0 whenever one fiber is fully contained within the other one. The contained fiber could however be much smaller than the other. Therefore, we need to accommodate for their volume ratio, leading to a second overlap-based dissimilarity measure

$$d_2^o(a,b) = 1 - \begin{cases} \frac{v(a)}{v(b)}o(a,b) & \text{for } v(a) < v(b) \\ \frac{v(b)}{v(a)}o(b,a) & \text{otherwise} \end{cases}.\qquad(9)$$

We also experimented with the non-symmetric version of this metric, where we always compute the overlap in a specific direction

$$d_3^o(a,b) = 1 - o(a,b)\begin{cases} \frac{v(a)}{v(b)} & \text{for } v(a) < v(b) \\ \frac{v(b)}{v(a)} & \text{otherwise} \end{cases}.\qquad(10)$$

As noted above, these dissimilarity measures are used to compute the dissimilarity of fibers in the results to fibers in the reference result. A low value always indicates low dissimilarity, a value of 0 indicates a perfect match. Most measures are normalized to have a value in the range of $[0,1]$. It is explicitly mentioned above if this is not the case. When the reference is set, we perform the dissimilarity measure computations. For each fiber in a non-reference result, we compute the dissimilarity to all fibers of the reference. We then chose a configurable number of "best" matches, that is, those reference fibers with the lowest dissimilarity, and store them for further analysis.

4. FIAKER

FIAKER provides methods for the analysis of data resulting from fiber characteristics pipelines. The workflow realized with FIAKER is depicted in Figure 4. Input is an ensemble of results, ideally along with a reference result, as described in detail in Section 4.1. The techniques employed to visualize this information are laid out in Section 4.2.

4.1. Input Data

The input to FIAKER are the computed characteristics of the fibers in each analyzed result. As the datasets analyzed so far contained only straight fibers, FIAKER visualizes fibers as cylinders.

The cylinder geometry for each fiber is specified by the start and end point as well as the diameter. The tool can also process supplementary characteristics per fiber. All characteristics are expected in table (CSV) format, as shown in Figure 4(a). In addition, FIAKER can handle the fiber characteristics from intermediate steps of an iterative algorithm. As a preprocessing step, the user selects one of the loaded results as reference, i.e., as base for comparisons, as shown in Figure 4(b). The tool then computes for each fiber in each result the dissimilarity to all fibers in the reference. In absence of a true reference, any one of the results can be chosen as a base for comparisons.

4.2. Visualization Design

The main interface of FIAKER utilizing multiple linked views can be seen in Figure 3. Its main views are the *result list* (a) and the *spatial view* (b), as well as detail views in the form of an *iteration step chart* (c) as well as a *scatter plot matrix* (d). Additionally, a *selection view* (e), an *interaction protocol* (f) as well as a *settings view* (g) are shown when required. We recommend viewing the supplemental video for a better impression of the interactions between these views. FIAKER is available as a module in the open_iA tool [FWS*19].
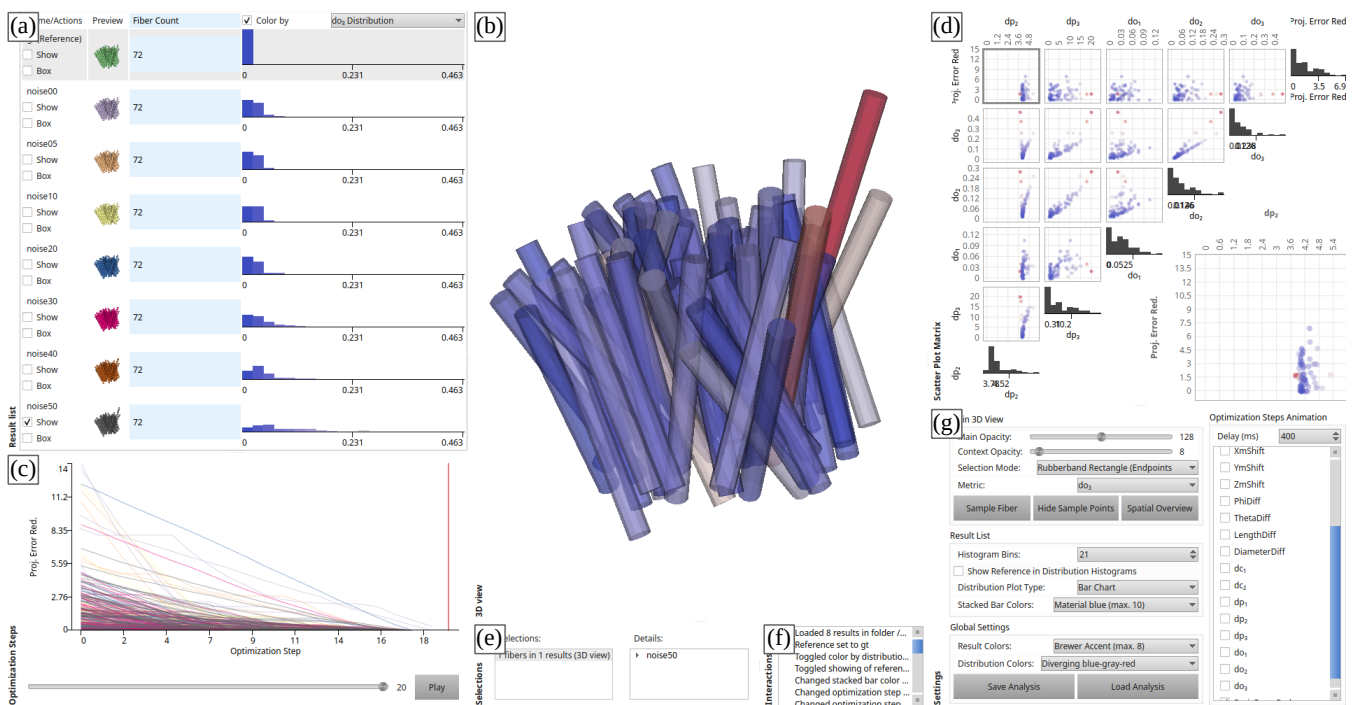
Figure 3: *The main interface of FIAKER consists of a list of all results (a), a spatial view displaying one or more results (b), which in this case is color coded by the value of the d_3^o measure for each fiber. The iteration step chart (c) provides details on the progression of iterative refinement algorithms. The scatter plot matrix (d) provides details on the characteristics of each single fiber. A selection view (e), an interaction protocol (f) and a settings widget (g) provide additional information and control where required.*

4.2.1. Result List

The result list contains the name and a 3D preview for each result, as can be seen in Figure 3(a). All fibers in a preview are assigned a color which is specific to the single result. Alongside, aggregate weighted measure bar charts in an interface similar to LineUp [GLG*13] enable ranking of the results for addressing Task 1a, the quantitative comparison of results, from Section 1. This task is supported in addition by a histogram, showing the distribution of a chosen characteristic. In addition this addresses task 3, the investigation of the influence of input data and parameters. To focus on a specific result, users can filter their analyses in the results view. Only the filtered results will then be displayed in the spatial view, and also the iteration step chart and the scatter plot matrix will be restricted to these results.

4.2.2. Spatial View

The spatial view shows a 3D visualization of all user-selected results, enabling the qualitative comparison of individual results, and thus addressing task 1b. Fibers can be color-coded by the color specific to the result which they belong to. Alternatively, the reference can be color-coded by the average dissimilarity measure value of the matches to that fiber across all results, as shown in Figure 4(d). Or, fibers can be colored by their individual match quality or all other characteristics. These color-codings enable users to identify fibers with specific properties, and thus addressing task 2b. The bars of the histogram in the result list are colored as the fibers and

serve as color map. When fibers are selected, the unselected fibers are displayed with increased transparency to provide the context, as shown e.g. in Figure 5(a). For selected fibers, the closest matches with the reference can be shown. To clarify the link between result and reference fibers, connecting lines are shown, as can be seen in Figure 6(a). Task 4, providing visualizations for communicating the results, is addressed mainly through the spatial view as can be seen in the case studies.

4.2.3. Detail Views

Users start navigating in the results list and the spatial view. Additionally, several detail views are available:

1. *Iteration step chart*, see Figure 3(c): When an iterative algorithm is analyzed, where data from each of its iteration steps is available, this data can be tracked in the iteration step chart. It shows the evolution of selected characteristics on the y-axis over the iteration steps on the x-axis. The user can switch to any iteration step through a control in this view, and the spatial view will update accordingly. In addition, an animation can be enabled that automatically loops through all iteration steps. This view supports task 1a by enabling the comparison between intermediate and final results.

2. A *scatter plot matrix*, see Figure 3(d), shows the characteristics of all fibers in the currently selected results, revealing potential correlations between the characteristics. Each dot represents a single fiber, and is colored exactly like the corresponding fiber.
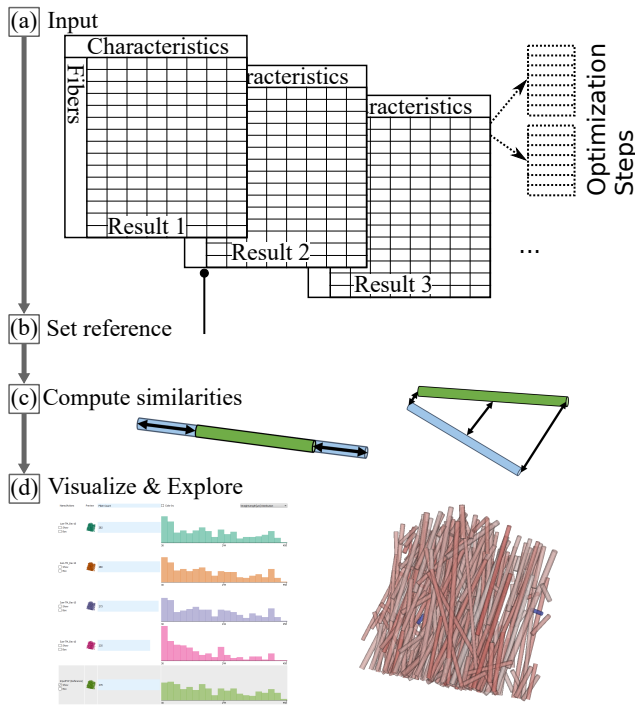
Figure 4: *FIAKER workflow: Input data (a) is loaded, then a reference is set (b), fibers in other results are matched to the reference (c), and finally exploration starts with the result list and spatial overview visualizations (d).*

It supports the analysis of the influence of fiber and dataset characteristics on the results in task 3.

3. *Selection details*, see Figure 3(e): Whenever a selection is made, its details are recorded in this two-part view. Its left part keeps a history of all selections as a list. The right part displays a tree of all fibers and the results they belong to for the current selection. Selections in general mainly address tasks 2 and 4, where users need to be able to select a subset of fibers for further analysis. In the spatial view, single fibers can be selected by dragging a selection rectangle, which selects all fibers where start or end point are in a view frustum spanned by the rectangle, or by clicking on a single fiber. Fibers can also be selected in the scatter plot matrix and the iteration step chart.

4. The *interaction protocol*, see Figure 3(f), logs all user interactions. This view, along with the selection details, makes it easy to keep track of the analysis process. Having a reproducible analysis process is crucial when providing visualizations for communicating the results, thus these views mainly address task 4.

5. A *settings view*, see Figure 3(g), provides access to visualization options such as modifying the opacity of selected and non-selected fibers, as well as specifying which fiber dissimilarity measure to use for finding the closest reference fiber.

5. Evaluation

FIAKER was developed in close collaboration with scientists working on fiber characterization algorithms. We evaluated the tool

on results from two different algorithms. One aspect of our evaluation was the iterative refinement of our methods regarding usability. The most important aspects are found in the comparison of the analysis with our tool to the analysis using existing methods, as well as the kind of insights that can be gained with our tool. We further evaluate the fiber dissimilarity measures, and finally show how the methods can be extended to support the analysis of other datasets, demonstrated by pore space analysis. Where not noted otherwise, the case studies were conducted by the tool developer, and observed and commented on by a domain expert. The domain experts were also provided the tool to play around on their own, and several of our insights in Section 6 came from the discussion of analysis sessions performed by the domain experts on their own.

5.1. Evaluated Algorithms

We evaluate FIAKER using synthetic results as well as with results obtained from datasets acquired by computed tomography. These datasets show objects made of fiber-reinforced polymer with glass or carbon fibers. The projection images from the CT device, or reconstructed volumes, that serve as input to the fiber characterization algorithms, are typically several hundreds of megabytes to several gigabytes in size. That is, there are about a hundred to a few thousand projection images of size $2\,300 \times 2\,300$ pixels, yielding reconstructed volumes of up to $2\,300^3$ voxels. Since most of our visualizations don't deal with these image or volume datasets directly, we are not limited by their size. Instead, we almost exclusively use polygonal data extracted from the characteristics computed by the fiber characterization algorithms. Thus, our algorithms are limited only by the number of fibers found. So far, we have tested our visualizations with results containing up to $400\,000$ fibers.

The datasets that served as basis in the case studies below are the result of applying two different fiber characterization algorithms. The first one, described by Salaberger et al. [SJKK15], starts with a reconstructed volume and applies a sequential pipeline of image processing operations, including template matching. Through this process, the center lines of the fibers are extracted, from which labeled fiber images are created. We will refer to this algorithm as Fiber Characterization through Template Matching (FCTM).

The second algorithm we have been evaluating, Parametric Reconstruction (PARE), has recently been published by Elberfeld et al. [Edd*18]. It directly inputs the CT projection images, performs an initial fiber characterization from a SIRT reconstruction using the ASTRA toolbox [vPC*16] and then refines this characterization by projecting the model of the recognized fibers forward (again) into the space of the projection images. The result of this forward projection is used to compute the projection error, i.e., the difference to the original projection images. The characterization is then adjusted to reduce the projection error, using a gradient descent optimization method. This minimization of the projection error is repeated for each fiber separately until no further reduction in the error is noticed, or a maximum number of iterations is reached.

5.2. Usability Evaluation and User Centered Design

We developed FIAKER over the course of approximately six months. Designs and prototypes were regularly presented to our
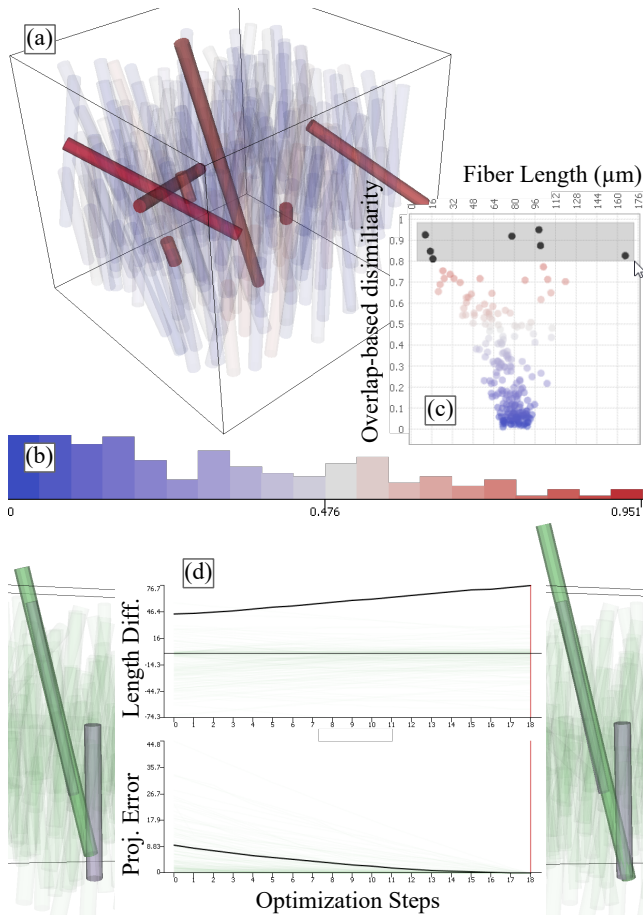
Figure 5: *Fibers of the synthetic dataset, color-coded by dissimilarity to reference (a); the color-mapping is given in the distribution chart (b). Fibers with the worst reference match are selected in the scatter plot (c). The long vertical fiber in the middle (green) and its development over the iterations is analyzed in the 3D view in comparison to closest reference fibers (grayish-violet) as well as in the iteration steps chart (d).*

collaborators on average once per week, and we discussed the direction of further enhancements that we intended to implement. It was thus a thoroughly user-centered design process, following the best practices and avoiding the pitfalls outlined in the design study methodology by Sedlmair et al [SMM12].

We continuously improved the usability of our prototype based on user input. We also conducted an interview, focusing solely on improving usability. The result of this interview was a list of items where usability was lacking in the prototype version available at the time of the interview. One such issue, for example, was that coloring single fibers by characteristics such as their length was available only through the settings dialog of the scatter plot matrix. This restriction resulted from design decisions of previous tools built in the same framework as our prototype, where the scatter plot matrix played a more central role. In our context, that was pretty counter-intuitive. The list of items, together with the suggestions

for improvement, was then discussed with the visualization experts among the co-authors, where the implementation details of each improvement where outlined and refined. This resulted in a workable, prioritized list of changes to the prototype that we were able to quickly implement in the next prototype release.

Overall, there were four collaborators involved in the development of the tool who are developing algorithms for fiber characterization or working with such algorithms on a daily basis. Furthermore, four experts on visualizations for material science lended their expertise in designing and improving the visualization techniques.

5.3. Case Study 1: Synthetic Data

This case study considers a simple synthetic ensemble consisting of only two results. One is the result of the PARE method, the other is the reference, a result artificially created to approximate the distribution of fibers in real datasets. The projection images, input to the PARE method, were generated directly from this reference. Therefore, the reference in this case is an actual ground truth.

The first goal in this case study is to test our methods on a simple dataset, and also to serve as an introduction into how to apply these methods. After defining the reference, we start by color-coding the fibers obtained by PARE by their dissimilarity to the best-matching fiber in the reference, as shown in Figure 5(a). Red indicates a bad match based on the color map depicted in (b). In (a), we already have selected the seven fibers with the worst match according to our overlap-based measure d_3^o in the scatter plot Figure 5(c). We chose these because they seem to separate slightly from the rest of the fibers. Interestingly, they come from both ends of the fiber length spectrum. It can be seen that two fibers extend beyond the bounding box of the reference, which is shown as a black wireframe box in Figure 5(a).

Now let us focus on the long, near-vertical fiber in the middle, to see why the PARE algorithm performs badly for it. We selected this fiber by clicking on it in the 3D view. Figure 5(d) shows its length difference to the best matching reference fiber (Length Diff.) as well as its contribution to the projection error (Proj. Error), the optimization criterion of the iterative PARE algorithm, over the iteration steps. The picture on the left of the charts shows the fiber in the first iteration step. Note that we view it from a slightly different camera position in (a) that is better suited for our further analysis purposes. On the right of the charts we see the same fiber in the last iteration step. From the 3D visualizations and the charts we can see that the projection error decreases, while the difference in length to the closest reference fiber actually increases. In the 3D views, the fibers are colored by their result color, green for the PARE result and grayish-violet for the reference. We can see that there is another reference fiber that is initially only touched by the green fiber, but at the end of the optimization, the start of the reference fiber is completely covered by the green fiber. On its other side, in the course of the optimization the green fiber grows out of the bounding volume of the reference, which does not adversely affect the projection error, because it outgrows the field of view and the projection error can not provide negative feedback for this change. This is actionable information for the algorithm developer. On one
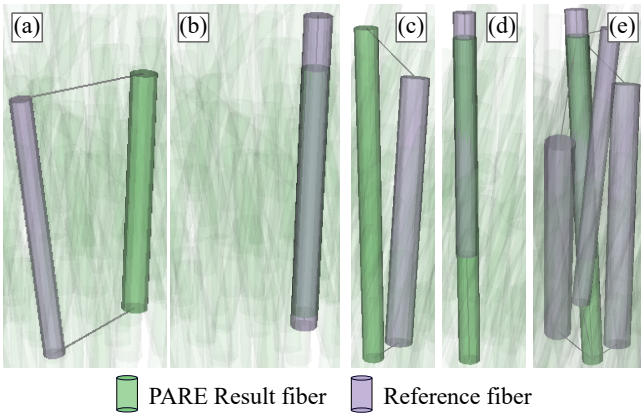
Figure 6: *Worst-case examples for dissimilarity measures. d_2^c matches fibers similar in angle and length but at a different position (a), while d_3^p matches a more suitable, shorter fiber (b). d_3^p fails for another fiber where it prefers a close position-wise match with no overlap (c), where d_3^o prefers a shorter fiber with overlap (d). However, the highest scoring fiber for d_3^o is also among the first four best matches for d_3^p (e).*

Figure 7: *List of results computed with PARE. Results lower in the list were computed from input data containing higher levels of noise. This is reflected in the average length difference to the reference (a), which increases with higher noise as well as the distribution of d_3^o across the fibers of each result (b), which is flattening with higher noise.*

hand, care must be taken to avoid generating fibers which grow to cover more than one fiber in the reference. On the other hand, it shows that reducing the projection error as an optimization criterion is not sufficient and additional constraints are required to prevent fibers from being placed outside the analyzed regions. Previous methods for analyzing this dataset involved scripts to match result to reference fibers, as well as computation of errors for the best matches. In contrast to these, with FIAKER, the fibers going outside of the optimized volume were immediately apparent.

5.4. Case Study 2: Measure Validation

To analyze the fiber dissimilarity measures we utilized the synthetic data from the previous section. Figure 6 shows examples where the first developed dissimilarity measures performed badly. For the measures based on the fiber characteristics, d^c, we quickly realized that using them would require a fine-tuned balance of weighting for all characteristic difference terms. In the example shown in (a), the length is obviously weighted too high. The reference fiber with the best match is the same size, but slightly different in orientation, and somewhat distant from the result fiber. The best measure considering only positions, d_3^p, for which the best match is shown in Figure 6(b), performs better and shows that there is a reference fiber that overlaps with the result fiber. The large difference in length is the most likely explanation for why the characteristics-based measure did not select this reference fiber as best match.

An example where measure d_3^p also does not perform well is shown in Figure 6(c), where we see that start and endpoints of the matching reference fiber are pretty close, but there is no overlap. The best match shown in Figure 6(b), computed via the overlap measure d_3^o, is the true best match, according to our collaborators. We see that there is a lot of overlap, but the length varies consid-
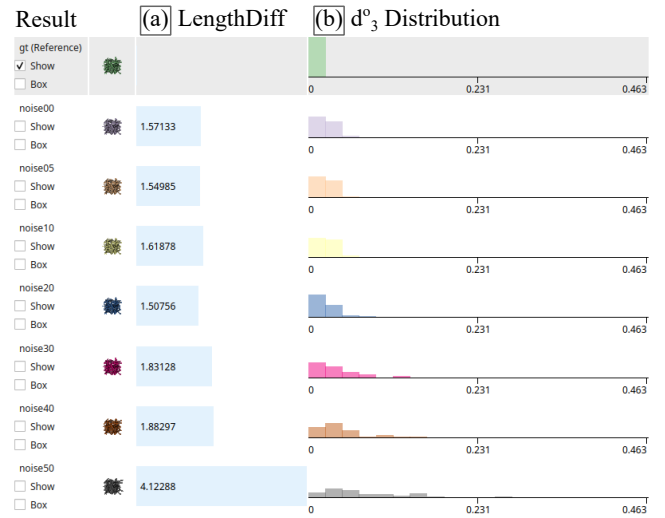
erably, which means that one of the endpoints of the reference is quite far from its counterpart on the result fiber.

When analyzing the best four matches according to measure d_3^p, which are shown in Figure 6(e), we see that it includes the best match of measure d_3^o, shown in Figure 6(d). In the examples evaluated for the synthetic dataset, it is always the case that the best match according to d_3^o is contained in the first few matches of d_3^p. Even though d_3^p does not always give the correct order, it provides a good first estimate of match quality. We can use it to optimize the computation of overlap measures, which is too expensive to be computed for each possible pairing of fibers in reference and result, especially when analyzing a large ensemble or results with a large number of fibers. We therefore only compute the overlap measures for the best 25 matches according to the d_3^p measure.

5.5. Case Study 3: Influence of Noise in Synthetic Data

We also looked at the influence of noise on the outcome of the PARE algorithm. From a ground truth, several projection images were generated with different levels of additive Gaussian noise with a mean of 0 and a sigma value of 0, 0.5, 1, 2, 3, 4, and 5. A list of the results gathered for this analysis is shown in Figure 7. We show the difference in length measure as well as the overlap-based dissimilarity measure. Even though we have a separate ground truth available again, we could also consider the 0% noise level as a baseline, as we are only interested in how the noise affects the outcome. The difference in length remains approximately the same until noise with a sigma value of 4 is generated. At sigma value 5, the difference in length begins to increase steeply. The overlap-based dissimilarity measure yields slightly more differentiated results. From noise with sigma value between 0 and 2 it varies only slightly, then
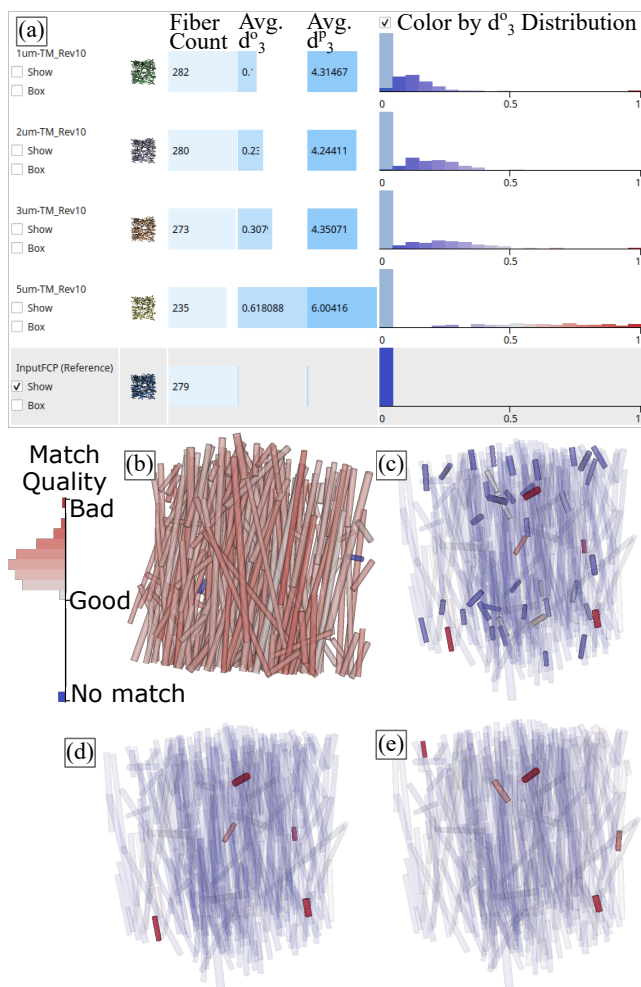
		Fiber Count	Avg. d^o_3	Avg. d^p_3	✓ Color by d^o_3 Distribution
1um-TM_Rev10 ☐ Show ☐ Box		282	0.1	4.31467	
2um-TM_Rev10 ☐ Show ☐ Box		280	0.23	4.24411	
3um-TM_Rev10 ☐ Show ☐ Box		273	0.307	4.35071	
5um-TM_Rev10 ☐ Show ☐ Box		235	0.618088	6.00416	
InputFCP (Reference) ✓ Show ☐ Box		279			

Figure 8: *Fiber characterization results computed from CT scans with different resolutions, the resolution decreases with positions further down in the list (a), reference is the last item, highlighted in gray. The reference is color coded by the match quality (b), the color map is on the left. Selections: Shortest fibers in the lowest-resolution result (c), Five worst-matching fibers in the lowest (d) and second-lowest (e) resolution results, the color map for (c-e) is encoded in the histograms in (a)*

starts to grow more rapidly. Also here, we see a sharp increase at noise created with a sigma value of 5. We conclude that the algorithm is quite robust to noise with sigma values lower than 2.

5.6. Case Study 4: Influence of Resolution Differences in Real CT Scans

The data analyzed here are based on CT scans of a small cut-out of a larger glass fiber-reinforced polypropylene structure with 30 weight-percent fiber content. The specimen was scanned four times with different resolutions, the voxel sizes of these scans were 1 μm, 2 μm, 3 μm, and 5 μm. For each of these scans, the analyzed ensemble contains the result of the FCTM approach, plus an addi-

tional manually labeled result for reference. The fibers in these datasets have an average diameter of 12 μm and a length varying widely between 30 μm and 460 μm. Before loading in our tool, this data was analyzed using some custom scripts [SJKK15] for a quantitative evaluation, in addition to a visual analysis with Fiber-Scout [WAL*14]. As each result needed to be explored separately, and quantitative evaluation was done in scripts custom-written for this purpose, the time to conduct this previous analysis was in the range of at least a week. The goal of the previous analysis was to optimize the FCTM algorithm. For our case study, the goal was to analyze whether key findings were missed in the previous analysis.

In the list in Figure 8(a) we see the results in decreasing order of resolution, except for the last entry which is the reference. We observe that the fiber count decreases with the resolution, which clearly indicates that not all fibers are detected with lower resolution. The point-based dissimilarity measure shows similar values for the first two entries, while the overlap-based dissimilarity measure correlates better with the resolution.

The spatial overview in Figure 8(b) shows two fibers in the reference, marked in blue, without matches in any of the results, not even in the highest-resolution scan. The existence of two such unmatched fibers was new to the domain expert, and was missed the first time he analyzed the data. This is remarkable given that these important findings became clear within minutes after loading the data. These two fibers clearly deserve a closer look in the input data, for which currently an external tool is needed. Another interesting detail is revealed when looking at the fibers with high dissimilarity to their best reference match according to measure d^o_3. Figure 8(d) and (e) show the five fibers with the highest dissimilarity, for the characterization performed on the 1 μm and 2 μm scans, respectively. These fibers are all very short, leading to the preliminary hypothesis that the algorithm is working better for long fibers. However, as can be seen from Figure 8(c), where all fibers of lengths between approximately 30 μm to 60 μm are selected, there is no consistent trend for all short fibers. Two fibers in (d) and (e) are the same, indicating systematic problems of the algorithm with these two fibers, as they are not well recognized in the results of two completely different scans. In the study, we found a total of four fibers that require further investigation.

5.7. Case Study 5: Feasibility Study of Analyzing Other Datasets

The goal of this section is to lay out how FIAKER can be adapted to analyze algorithms other than fiber characterization pipelines. Our methods can be applied to the analysis of multiple results, when each of those results contains a number of parametrizable objects which can be visualized through a geometric primitive. To adapt our current methods to another object type, the following modifications or extensions are required:

1. Create a 3D visualization for the geometric primitive representing an object
2. Define at least one dissimilarity measure between two objects of the given type

We have started experiments to analyze results from pore characterization algorithms, in our case generated by the FeatureAnalyzer
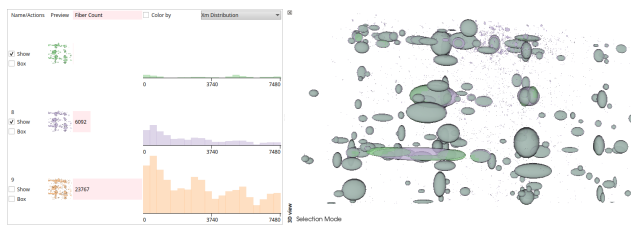
Figure 9: *Pore characterization results loaded in FIAKER*

tool [WAG*16, SWP*18]. Pores often feature a circular or elliptical shape, and may therefore be represented as ellipses. As dissimilarity measure, the distance between the center points of the two pores, combined with the difference in their extents in x-, y- and z-direction may be considered. Figure 9 shows the result list and the spatial view with the results of three differently parameterized pore characterizations. The required adaptations to our tool were done within approximately half a day by a single software programmer.

6. Discussion of Design Decisions and Lessons Learned

In the result list, initially we only showed a list of result previews. Then we implemented a simplified version of LineUp [GLG*13] for quantitative ranking. We considered implementing a design similar to WeightLifter by Pajer et al. [PSTW*17], in order to explore the weight Space more comprehensively. But we decided against this, as it was not needed for the current analysis scenarios. For comparison of value distributions across results, we added histograms.

It turned out that scatter plot matrices were not used as much as we had expected. As they play a major role in FiberScout [WAL*14], a previous tool for fiber analysis, we expected them to be a key element in the analysis again. In our case, it turned out that the main focus of the analysis is on the result list and the spatial view. We assume this is due to the fact that our tool focuses more on comparing multiple results. In FiberScout, the focus was more on correlations between different fiber characteristics.

Our users unanimously were asking for a 3D view and were thrilled to see its possibilities for visualizing the results when they first saw the prototype. This was surprising and contrary to the experience from previous work on the analysis of image processing tools in material sciences (e.g., for analyzing image segmentation results [FMH16]). The preference for 3D in this case comes, on the one hand, from the fact that we have polygonal data, not volumes, where slice images are easier to comprehend than direct volume rendering that is prone to occlusion. On the other hand, the many ways to select and thus concentrate on just a few fibers make it easy to focus in the 3D visualization on the currently interesting parts of the result. In this drill-down scenario, the majority of the fibers are rendered highly transparent so that one can focus on the few important fibers while maintaining their 3D context.

Selecting fibers in the 3D view was highly demanded by our users. However, it turned out to be quite challenging. We first implemented selection through drawing a rectangle. This selects those fibers where any of their end points is contained in the view frustum

spanned by the rectangle. We first implemented a selection mechanism by selecting those fibers whose endpoints are contained in the view frustum spanned by a user-drawn rectangle. It might have been more intuitive to select any fiber which passes through the rectangle. However, in practice, selecting only by end points already leads to selecting more fibers than wanted, as it is hard to pinpoint only the start or end point of the fibers without including others in the vicinity. In order to facilitate the selection of a particular fiber, we therefore also implemented a selection by a single click. The click selects the fiber hit first by a ray cast in viewing direction into the scene. Again, this can be problematic if the desired fiber is somewhere in the middle of the region of interest and thus occluded by other fibers. This motivated us to implement a selection view that allows the user to further refine a selection made.

An interesting lesson also was the design of the dissimilarity measures. Initial drafts had not put much emphasis on this topic. But during exploration of the datasets, we discovered problems with the initial measures. We could also verify with our tool that the measures we created as a consequence could overcome these limitations, as described in Section 5.4. This points towards the generalizability of our methods: The same methods that are helpful in understanding and debugging fiber characterization algorithms have also helped us in developing appropriate dissimilarity measures.

One potential future extension proposed by our collaborators is the ability to present the reconstructed CT volume as localized context for visualizing selected fibers for which the characterization did not work well.

7. Conclusion

We have developed FIAKER, a tool implementing methods for analyzing and comparing the results of fiber reconstruction algorithms. We refined the usability and utility of these methods by developing them in close collaboration with scientists working on fiber reconstruction algorithms or applying such algorithms on a daily basis. We evaluated the tool on the outcomes of two different fiber reconstruction algorithms, and were able to show that the tool quickly provides insight into where a fiber reconstruction algorithm still needs improvement. In addition, the methods can help to understand which algorithm performs better in comparison to a reference, both in general as well as for specific locations or specific fibers. We also showed how our methods may be generalized and applied to the analysis of any collection of objects representable by geometric primitives, and demonstrated this in our case study on pore characterization results.

References

[BWW*17] BHATTACHARYA A., WEISSENBÖCK J., WENGER R., AMIRKHANOV A., KASTNER J., HEINZL C.: Interactive exploration and visualization using MetaTracts extracted from carbon fiber reinforced composites. *IEEE Transactions on Visualization and Computer Graphics 23*, 8 (2017), 1988–2002. doi:10.1109/TVCG.2016.2582158. 3

[Edd*18] ELBERFELD T., DE BEENHOUWER J., DEN DEKKER A. J., HEINZL C., SIJBERS J.: Parametric reconstruction of glass fiber-reinforced polymer composites from X-ray projection data – a simulation study. *Journal of Nondestructive Evaluation 37*, 3 (2018), 62. doi:10.1007/s10921-018-0514-0. 2, 3, 6

[FHG*09] FRITZ L., HADWIGER M., GEIER G., PITTINO G., GRÖLLER E.: A visual approach to efficient analysis and quantification of ductile iron and reinforced sprayed concrete. *IEEE Transactions on Visualization and Computer Graphics 15*, 6 (2009), 1343–1350. doi:10.1109/TVCG.2009.115. 2

[FMH16] FRÖHLER B., MÖLLER T., HEINZL C.: GEMSe: Visualization-guided exploration of multi-channel segmentation algorithms. *Computer Graphics Forum (Proceedings of the Eurographics Conference on Visualization (EuroVis) 2016) 35*, 3 (2016), 191–200. doi:10.1111/cgf.12895. 10

[FWS*19] FRÖHLER B., WEISSENBÖCK J., SCHIWARTH M., KASTNER J., HEINZL C.: open_ia: A tool for processing and visual analysis of industrial computed tomography datasets. *Journal of Open Source Software 4*, 35 (2019), 1185. doi:10.21105/joss.01185. 4

[GLG*13] GRATZL S., LEX A., GEHLENBORG N., PFISTER H., STREIT M.: LineUp: Visual analysis of multi-attribute rankings. *IEEE Transactions on Visualization and Computer Graphics (InfoVis '13) 19*, 12 (2013), 2277–2286. doi:10.1109/TVCG.2013.173. 5, 10

[KH18] KASTNER J., HEINZL C.: X-ray tomography. In *Handbook of Advanced Non-Destructive Evaluation*, Ida N., Meyendorf N., (Eds.). Springer International Publishing, Cham, 2018, pp. 1–72. doi:10.1007/978-3-319-30050-4_5-1. 1

[KRR*18] KONOPCZYŃSKI T., RATHORE D., RATHORE J., KRÖGER T., ZHENG L., GARBE C. S., CARMIGNATO S., HESSER J.: Fully convolutional deep network architectures for automatic short glass fiber semantic segmentation from CT scans. In *Eigth Conference on Industrial Computed Tomography* (2018). URL: https://ndt.net/?id=21916. 2

[LGD*17] LABRA N., GUEVARA P., DUCLAP D., HOUENOU J., POUPON C., MANGIN J.-F., FIGUEROA M.: Fast automatic segmentation of white matter streamlines based on a multi-subject bundle atlas. *NeuroInformatics 15*, 1 (2017), 71–86. doi:10.1007/s12021-016-9316-7. 3

[MGB*18] MATEJKA J., GLUECK M., BRADNER E., HASHEMI A., GROSSMAN T., FITZMAURICE G.: Dream Lens: Exploration and visualization of large-scale generative design datasets. In *CHI Conference on Human Factors in Computing Systems* (2018), ACM, pp. 369:1–369:12. doi:10.1145/3173574.3173943. 2

[OW07] O'DONNELL L. J., WESTIN C.-F.: Automatic tractography segmentation using a high-dimensional white matter atlas. *IEEE Transactions on Medical Imaging 26*, 11 (2007), 1562–1575. doi:10.1109/TMI.2007.906785. 3

[PSTW*17] PAJER S., STREIT M., TORSNEY-WEIR T., SPECHTENHAUSER F., MÖLLER T., PIRINGER H.: WeightLifter: Visual weight space exploration for multi-criteria decision making. *IEEE Transactions on Visualization and Computer Graphics (Proceedings InfoVis 2016) 23*, 1 (2017), 611–620. doi:10.1109/TVCG.2016.2598589. 10

[QV15] QUAN T. A., VO B.: Similarity measure for fiber clustering: A constant time complexity algorithm. In *Seventh International Conference on Knowledge and Systems Engineering* (2015), IEEE, pp. 286–291. doi:10.1109/KSE.2015.48. 3

[SHB*14] SEDLMAIR M., HEINZL C., BRUCKNER S., PIRINGER H.,

MÖLLER T.: Visual parameter space analysis: A conceptual framework. *IEEE Transactions on Visualization and Computer Graphics 20*, 12 (2014), 2161–2170. doi:10.1109/TVCG.2014.2346321. 2

[SJKK15] SALABERGER D., JERABEK M., KOCH T., KASTNER J.: Consideration of accuracy of quantitative X-ray CT analyses for short-glass-fibre-reinforced polymers. *Materials Science Forum 825*, 1 (2015), 907–913. doi:10.4028/www.scientific.net/MSF.825-826.907. 2, 6, 9

[SKK*11] SALABERGER D., KANNAPPAN K. A., KASTNER J., REUSSNER J., AUINGER T.: Evaluation of computed tomography data from fibre reinforced polymers to determine fibre length distribution. *International Polymer Processing 26*, 3 (2011), 283–291. doi:10.3139/217.2441. 2

[SMM12] SEDLMAIR M., MEYER M., MUNZNER T.: Design study methodology: Reflections from the trenches and the stacks. *IEEE Transactions on Visualization and Computer Graphics 18*, 12 (2012), 2431–2440. doi:10.1109/TVCG.2012.213. 7

[SPA*14] SCHMIDT J., PREINER R., AUZINGER T., WIMMER M., GRÖLLER E., BRUCKNER S.: YMCA - your mesh comparison application. In *IEEE Visual Analytics Science and Technology (VAST)* (2014), IEEE. doi:10.1109/VAST.2014.7042491. 2

[SV18] SCHULTZ T., VILANOVA A.: Diffusion MRI visualization. *NMR in Biomedicine* (2018), e3902. doi:10.1002/nbm.3902. 3

[SWP*18] SCHIWARTH M., WEISSENBÖCK J., PLANK B., FRÖHLER B., HEINZL C., KASTNER J.: Visual analysis of void and reinforcement characteristics in X-ray computed tomography dataset series of fiber-reinforced polymers. In *13th International Conference on Textile Composites* (2018), IOP Publishing. doi:10.1088/1757-899X/406/1/012014. 10

[TWMSK18] TORSNEY-WEIR T., MÖLLER T., SEDLMAIR M., KIRBY R. M.: Hypersliceplorer: Interactive visualization of shapes in multiple dimensions. *Computer Graphics Forum 37*, 3 (2018), 229–240. doi:10.1111/cgf.13415. 3

[vPC*16] VAN AARLE W., PALENSTIJN W. J., CANT J., JANSSENS E., BLEICHRODT F., DABRAVOLSKI A., DE BEENHOUWER J., BATENBURG K. J., SIJBERS J.: Fast and flexible X-ray tomography using the astra toolbox. *Optics Express 24*, 22 (2016), 25129–25147. doi:10.1364/OE.24.025129. 6

[WAG*16] WEISSENBÖCK J., AMIRKHANOV A., GRÖLLER E., KASTNER J., HEINZL C.: PorosityAnalyzer: Visual analysis and evaluation of segmentation pipelines to determine the porosity in fiber-reinforced polymers. In *IEEE Conference on Visual Analytics Science and Technology* (2016), IEEE, pp. 101–110. doi:10.1109/VAST.2016.7883516. 10

[WAL*14] WEISSENBÖCK J., AMIRKHANOV A., LI W., REH A., AMIRKHANOV A., GRÖLLER E., KASTNER J., HEINZL C.: FiberScout: An interactive tool for exploring and analyzing fiber reinforced polymers. In *IEEE Pacific Visualization Symposium* (2014), IEEE, pp. 153–160. doi:10.1109/PacificVis.2014.52. 2, 9, 10

[ZFS*19] ZHANG H., FREY S., STEEB H., URIBE D., ERTL T., WANG W.: Visualization of bubble formation in porous media. *IEEE Transactions on Visualization and Computer Graphics 25*, 1 (2019), 1060–1069. doi:10.1109/TVCG.2018.2864506. 2